THE UNIVERSITY
of EDINBURGH

Experimental and Numerical Investigations of Geomechanical Controls on Petrophysical Changes of Carbonates During Fluid Flow

Florent Brondolo

Doctor of Philosophy

University of Edinburgh

2019

À Estelle

et

À mes parents

Peace among worlds

Rick Sanchez

Declaration

I declare that this thesis has been composed solely by myself and that it has not been submitted, either in whole or in part, in any previous application for a degree. Except where otherwise acknowledged, the work presented is entirely my own.

Florent Brondolo

September 2019

Abstract

In flooding experiments, porosity and permeability of carbonate rocks is enhanced through the dissolution of the rock matrix, which further increase the permeability as well as the inter-connection of the pre-existing porosity. Authors often refer to this process as wormholing or channelling, which define preferential pathways for any fluid circulating through the rock's matrix (Hoefner and Fogler, 1988; Fredd and Fogler, 1998; Golfier et al., 2002). A wormhole's shape and size ranges from face dissolution at very low fluid flow rates (where the reactive fluid is rapidly consumed after the injection point), to uniform dissolution (where the acid is brought to far-ends within the rock matrix, which allows the creation of a large network of connected pores). Authors have studied the factors influencing the relationship between dissolution fronts, injection rate, rock nature, and acidity of the circulating fluid (Frick et al., 1994a; Bazin et al., 1995; Fredd et al., 1996; Fredd and Fogler, 1998; Golfier et al., 2002; Egermann et al., 2006; Luquot and Gouze, 2009; Menke et al., 2015; Ott and Oedai, 2015; Barri et al., 2016; Luquot et al., 2016; Teles et al., 2016; Zhang et al., 2016). The current status of knowledge present strong connections between the reaction rate and the diffusion rate (referred to as the Damköhler number – Da Bekri et al. (1995); Egermann et al. (2010)), as well as the study between the fluid velocity and the ability for a medium to diffuse into a solvent (referred to as the Péclet number – Pe Golfier et al. (2002); Menke et al. (2015)). The Da number measures the relative importance of the reaction rate constant versus advection over some length scale, while the Pe number gives the ratio of advective to dispersive flux for a

given length scale (Zhang and Kang, 2004; Steefel and Lasaga, 1990). Large Da correspond to rapid chemical reaction in comparison to all other processes. On the other hand, smaller Da testify of very slow chemical reactions in comparison to all other processes taking place during fluid flow (Zhang and Kang, 2004). A low Péclet number suggests that transport is governed by diffusion and not by convection, and inversely at high Pe number (De Boever et al., 2012).

Along with these dynamically controlled numbers, studies have tried to unpick the relationship between rock-fluid interaction for a variety of injection fluid, as well as rock-stress interaction. These studies have been done through the analysis of key variables (resistivity, porosity, permeability, etc.), using acidic and non-acidic fluids (Hoefner and Fogler, 1988; Frick et al., 1994b; Bazin et al., 1995; Fredd et al., 1996; Fredd and Fogler, 1998; Golfier et al., 2002; Egermann et al., 2006; Luquot and Gouze, 2009; Menke et al., 2015; Ott and Oedai, 2015; Barri et al., 2016; Luquot et al., 2016; Teles et al., 2016; Zhang et al., 2016). The experimental rationales of these studies usually implies large changes in the variables representing the reservoirs conditions, such as the temperature, confining pressure, and the effective stress. A large gap has been found between the actual state of knowledge and the absolute impact of effective stress on reservoir rock alteration, at steady reservoir condition of pressure and temperature. In this study, we have created an experimental matrix where the variable representing the reservoir conditions are kept constant during an experimental flooding, while varied between experiments. By doing so, we can isolate and cross-compare the effect of each variable on the rock alteration. We have flooded a total of twelve 38 mm large diameter carbonate cores of different nature (Indiana limestones, Saturnia travertines, and pre-salt shrubs) under constant geo-reservoir condition of P-T: P_c = 50 MPa, and T= 60 °C. The effective stress and pore volume rate was varied between experiments while kept constant during each experimental flooding. We used porosity,

permeability, Ca-Mg analysis, and µCT scanning as proxies for stress state related rock matrix alteration. While it is agreed that injection rate plays a major role in carbonate dissolution, through a higher dissolution rate corresponding to a high injection rate, and our work confirms this, we also demonstrate that for a constant given confining pressure, the effective stress can have a stimulant role in rock matrix alteration and wormhole development (Indiana limestone). Inversely, effective stress has a reverse role in less consolidated, more heterogeneous rocks (travertines). The pre-salt rock samples have shown interesting and mixed results, whose behaviour falls in between the Indiana limestone's ones and the travertines' ones: the chemical response behaved like an Indiana limestone while the physical response can be compared to a travertine.

We think that our results highlight the importance of the stress state in a reservoir, and while the confining pressure cannot be varied during injection or depletion of a reservoir, the pore pressure can be affected. The processes involved behind this are not yet clarified by the experimental work, but we believe that they are time and chemistry related, with further study by the authors indicating that our results are energy-dependent. Therefore, in a carbonate sample, the expected wormhole shape and spread can be predicted thanks to the reservoir conditions, the experimental conditions, and the rock's petromorphology. Finally, our numerical work further demonstrates that the heterogeneities within the porosity arrangement and geometry drive the fluid flow and could represent the main driving variable for the creation of pore space and carbonate dissolution.

Lay Summary

Geological reservoirs can be metaphorically compared to a sponge cake; the voids in the cake - usually full of air - represent the pores of a reservoir, which usually contain a resource (oil, gas, heated water, etc.). The baked cake batter would illustrate the surrounding rock. A reservoir can also be homogeneously porous (similar to thousands of identically sized marbles put into a bucket, or a loaf of sandwich bread), or heterogeneously porous (comparable to marbles of different sizes added to the same bucket, or a healthy fruit salad). Moreover, these pores can be connected between them (e.g. a toast dipped into a cup of coffee, and getting soaked in coffee), or completely disconnected (eg. a block of Emmental cheese contains pores, while non of them are actually connected). Both the surrounding rock and the fluid contained in the pores are pressured; the rock is confined under a lithostatic pressure, represented by the overlying geological layers, while the pores, filled by a mixture of fluids, are usually less pressured than the rock. The difference between the confining pressure around a rock, and the fluid pressure within the pores and acting against the confining pressure, is named effective stress.

Geological Reservoirs are natural and valuable features used in different domains, such as hydrocarbon production, CO_2 sequestration, groundwater resource, geo-energy including geothermal energy and energy storage applications. Accessing or trapping a resource in a reservoir requires to inject or deplete it, using wells drilled through the geological layers, which usually disturbs the effective

stress, by adding or removing pressure from the reservoir. These actions, if not properly constrained, can damage the rock in an undesirable way. Conversely, some actions require to disturb the mechanical and physical integrity of the reservoir, in order to increase the volume of fluid injected or depleted. Therefore, understanding the processes taking place underground during these production and/or injection phases are of prime interest for safety, efficiency, and economic reasons.

In this PhD project, we reproduced, in a laboratory, the physical, chemical, and mechanical conditions of a reservoir sitting at 2 to 3 Km depth, which would be flooded by seawater, in order to flush the pores composing it. This flushing is representative of the processes taking place during the replacement of a resource trapped in a reservoir, by simply pushing it out through the use of another, usually non-miscible, fluid. We designed a series of observations with the aim to inject artificial seawater into a variety of rocks representing either a heterogeneous or a homogeneous reservoir. These experimental scenarios aim to study the effect of the velocity of the fluid injected through the rock (at low, medium, and high velocity), as well as the impact of effective stress, by creating a large effective stress (intense confining pressure and small pore fluid pressure), or a small effective stress (intense confining pressure and large pore fluid pressure). We used several tools and techniques to identify the impact of the nature of a rock, of the pressure, and of the fluid velocity on rock alteration: we used scanning techniques (similar to a downsized medical scanner) to observe the hidden interior of a rock prior and after an experiment. We also sampled the fluid injected through the rock and analysed their chemical composition. Finally, we measured the ability of our rocks to allow the injected fluid to pass through it (termed as permeability).

Our results show a clear link between the velocity of the injected seawater and an increase in the dissolution of the rock, as well as an increase in permeability,

and interconnection between the pores. Moreover, we observed a yet unidentified relationship between the nature of the porous media (homogeneous or heterogeneous) and its behaviour when subjected a certain effective stress. Here we noted that a low effective stress has enhanced dissolution, permeability, and pores' interconnectivity in heterogeneous rocks. Inversely, a homogeneous rock should observe similar changes under a high effective stress.

Finally, we used scanned pictures of our rocks to assess the impact of the heterogneity within a rock; i.e. how much randomly distributed pores of random shapes can affect the dissolution and the fluid flow. Artificial intelligence coupled to image analysis allowed us to observe that the principal driver, before velocity of the injected fluid, and the effective stress, appears to be the porous arrangement within a rock.

Acknowledgements

The first lines to be read and the last ones to be written. This PhD was a challenge - and more often than not - an amazing experience, whose credit can sincerely be given to many people.

I found myself lucky to land in such an incredible research group. I want to begin by thanking my supervisors: Chris McDermott, Katriona Edlmann and Ian Butler, who tirelessly helped and advised me, and always displayed a positive attitude towards this project. A special thank goes to Gus, who should have locked his door more often. Thanks mate for all the help, and I hope I'll be able to repay that one day. I would have not reached this stage without all our chats. I also thank Xander and Alex Jackson for their help, in and out the lab, during those 4 years. Big thanks to the IT guys, Ross, Magi and Justin.

I would like to thank the International Centre for Carbonate Reservoirs (ICCR) and its sponsors (Shell and Petrobras) for having funded my PhD, as well as providing the necessary resources for completing my project on time.

I have had the chance to pause my PhD during 5 month during which I realized a placement at the research centre of Total in Pau. I'd like to thanks all the friends I made there, as well as my supervisors, Fred Pivot and Chris Wibberley. This time in Pau was the mixture of relaxation and stimulation I needed prior

to write this thesis up.

I would like to acknowledge Dr. Robert H. Schor, from the University of Rochester, for his precious mentoring during the development of the LabVIEW software. I realise, by the end of my PhD, that building this software from scratch was definitely a milestone, which made my lab-life way easier, and hopefully will help future researchers.

A special thanks goes to Linda Luquot and Stuart Gilfillan who kindly accepted to be my examiners. Many told me I would enjoy this particular moment that a viva is, and indeed, I enjoyed it.

If anything, Edinburgh was obviously more than just a workplace, and was full of people that have helped me getting through this roller coaster of emotion that a PhD can be. Thank you for the friendship over the years, and in particular to Alex, Angus, Carlos, Changyou, Elo, James, John, Jonny, Julien, Matt, Megan, Phil, Sarah, Steve, as well as Yoh, Mica, and Kawa. Thank you all for the support.

I would like to thank my parents who supported me financially and morally through all those years, and never ceased to believe in me. Thank you for showing so much pride in my work. You've put me there.

Last but by no means least; I'd like to thank Estelle. I am deeply indebted to her for all the energy, patience, and the daily cat/otter/duck pictures. I couldn't write those lines if it wasn't for your indefectible support those past 3+2+4 years. Again, there is no word in French or English to describe how grateful I am.

Contents

Declaration vii

Abstract ix

Lay Summary xiii

Acknowledgements xvii

Contents xix

List of Tables xxvii

List of Figures xxix

1 Introduction 1

1.1 The Brazilian hydrocarbon exploration 1
1.2 Geological introduction to the Pre-salt 4
1.3 Context of research 5
1.4 Experimental and numerical investigation 9
1.5 Thesis structure 12

2 Background Theory 15

2.1 Introduction 15
2.2 Porosity within a porous medium 15
2.3 Fluid flow 16
2.3.1 Darcy flow and conservation of momentum 17
2.3.2 Equation of mass balance 19
2.3.3 Dissolution at the Darcy-scale 20
2.4 Injection and formation fluid properties 28
2.4.1 Thermophysical properties of seawater 29

2.4.2 Density . . . 29
2.4.2.1 Effect of temperature . . . 29
2.4.2.2 Effect of Pressure . . . 31
2.4.3 Viscosity . . . 31
2.4.4 Comparison between nitrogen permeability measurements and seawater flooding measurements . . . 35
2.5 Rocks description . . . 37
2.5.1 Travertine and travertine-like rocks . . . 38
2.5.1.1 Presentation . . . 38
2.5.1.2 Shrubs description and depositional settings . . . 38
2.5.1.3 Theory of formation . . . 40
2.5.1.4 Depositional settings of Saturnia travertines . . . 43
2.5.1.5 Geological analysis . . . 43
2.5.1.6 Presentation of the Pre-salt shrubs . . . 44
2.5.1.7 Travertine/Pre-salt comparison . . . 45
2.5.1.8 Chemical composition of the shrub framestone . . . 47
2.5.2 Indiana limestone . . . 48
2.5.2.1 General overview . . . 48
2.5.2.2 Geology of the Indiana limestone . . . 49
2.5.2.3 Depositional system . . . 50
2.5.2.4 Chemical composition . . . 51
2.6 Carbonate system and pH control . . . 51
2.7 Mechanical behaviour of a carbonate rock . . . 57
2.7.1 Forces in play . . . 57
2.7.2 Differential Effective Medium approximation . . . 61
2.7.3 Mechanical impact on permeability . . . 70
2.7.4 Influence of the pressure-solution . . . 72
2.7.5 Pore fluid effect on a rock . . . 74

3 Material and Methods **77**
3.1 Introduction . . . 77
3.2 Laboratory development . . . 78
3.2.1 Introduction . . . 78
3.2.2 Final design . . . 79
3.2.3 Detail of the equipment . . . 83
3.2.3.1 Pipework . . . 83
3.2.3.2 Pressure sensors . . . 83

3.2.3.3 Hassler cell . . . 86
3.2.3.4 Temperature probe and fluid heating unit . . . 88
3.2.3.5 Pumps . . . 88
3.2.3.6 Data Acquisition system (DAQ) . . . 91
3.2.4 Sample preparation . . . 92
3.2.5 Software development . . . 94
3.2.5.1 Summary of the previous installations . . . 94
3.2.5.2 The LabVIEW programming environment . . . 96
3.2.5.3 Example of LabVIEW controlled functions . . . 100
3.3 Numerical development . . . 106
3.3.1 Introduction . . . 106
3.3.2 ICCR-Macropore . . . 106
3.3.2.1 Presentation . . . 106
3.3.2.2 Numerical structure of a pore . . . 107
3.3.2.3 Workflow . . . 109
3.3.2.4 Input files . . . 109
3.3.2.5 Output files . . . 110
3.3.2.6 Geometrical attributes . . . 111
3.3.2.7 Ellipse simplification . . . 114
3.3.3 SVG Converter . . . 118
3.3.3.1 Presentation . . . 118
3.3.3.2 Input files . . . 118
3.3.3.3 Output files . . . 118
3.3.3.4 Limitations . . . 118
3.3.4 Slice Picker . . . 120
3.3.4.1 Rationale . . . 120
3.3.4.2 Input files . . . 121
3.3.4.3 Output files . . . 121
3.3.4.4 Slice Picker - ICCR-Macropore interactions . . . 122
3.4 µCT imaging acquisition . . . 123
3.4.1 Introduction . . . 123
3.4.2 Image processing . . . 124
3.4.3 Output data . . . 125
3.5 Experimental parameters . . . 126
3.6 Chemical investigations . . . 129
3.6.1 ICP-MS analysis . . . 129

3.6.2 Sampling process . . . 129
3.6.3 Theory . . . 130
3.6.4 Porosity evolution . . . 130

4 Observation of channel propagation at variable effective stresses and injection rates on Indiana limestone rocks 133
4.1 External Contributions . . . 133
4.2 Summary of the chapter . . . 134
4.2.1 Rationale . . . 134
4.2.2 Summary . . . 134
4.3 Introduction . . . 135
4.4 Material and methods . . . 137
4.4.1 Samples selection process . . . 137
4.4.2 Experimental design . . . 138
4.4.3 Experimental approach . . . 139
4.4.4 Flow scenarios and dissolution regimes . . . 140
4.4.5 Sample characteristics . . . 142
4.4.6 Sample preparation . . . 144
4.4.7 Measurements . . . 144
4.5 Results and discussion . . . 146
4.5.1 Laboratory analysis . . . 146
4.5.1.1 Permeability . . . 146
4.5.1.2 Calcium and magnesium evolution . . . 154
4.5.2 µCT analysis for rock alteration . . . 164
4.5.3 Porosity evolution . . . 168
4.5.4 Interpretation . . . 172
4.6 Conclusion . . . 173

5 Observation of wormhole formation at variable effective stress and injection rate on travertine rocks 177
5.1 External Contributions . . . 177
5.2 Summary of the chapter . . . 178
5.2.1 Rationale . . . 178
5.2.2 Summary . . . 178
5.3 Introduction . . . 179
5.4 Materials and methods . . . 181
5.4.1 Samples selection process . . . 181

5.4.2 Experimental design . . . 183
5.4.3 Experimental approach . . . 184
5.4.4 Flow scenarios and dissolution regimes . . . 185
5.4.5 Sample characteristics . . . 188
5.4.6 Sample preparation . . . 193
5.4.7 Measurements . . . 193
5.5 Results and discussion . . . 194
5.5.1 Laboratory analysis . . . 194
5.5.1.1 Permeability . . . 195
5.5.1.2 Calcium and magnesium evolution . . . 203
5.5.2 µCT analysis for rock alteration . . . 212
5.5.3 Porosity evolution . . . 220
5.5.4 Interpretation . . . 222
5.6 Conclusion . . . 224

6 Observation of wormhole formation at variable effective stress and injection rate on carbonate Pre-salt rocks 229
6.1 External Contributions . . . 229
6.2 Rationale . . . 230
6.3 Introduction . . . 230
6.4 Material and methods . . . 231
6.4.1 Samples selection process . . . 231
6.4.2 Experimental approach . . . 235
6.4.3 Flow scenarios and dissolution regimes . . . 238
6.4.4 Reservoir-scale presentation . . . 241
6.4.5 Core-scale presentation . . . 241
6.4.5.1 Sample characteristics . . . 242
6.4.5.2 Sample presentation . . . 244
6.4.6 Measurements . . . 245
6.5 Results and discussion . . . 245
6.5.1 Laboratory analysis . . . 245
6.5.1.1 Permeability . . . 245
6.5.1.2 Calcium and magnesium evolution . . . 252
6.5.2 µCT analysis for rock alteration . . . 255
6.5.3 Porosity evolution . . . 262
6.5.4 Interpretation . . . 263
6.6 Conclusion . . . 264

7 Prediction of location and magnitude of wormhole formation prediction in heterogeneous travertine rocks using µCT imaging and machine learning 269
7.1 External Contributions . . . 269
7.2 Summary of the chapter . . . 270
7.2.1 Rationale . . . 270
7.2.2 Abstract . . . 270
7.3 Introduction . . . 271
7.4 Materials and methods . . . 273
7.4.1 Rock sample . . . 274
7.4.2 Rock preparation . . . 274
7.4.3 Experimental procedure . . . 275
7.4.4 Experimental matrix and dissolution regimes . . . 275
7.4.5 µCT imaging acquisition . . . 275
7.4.5.1 Channel processing . . . 276
7.5 Modelling work . . . 277
7.5.1 Input data pre-processing . . . 277
7.5.1.1 Formatting . . . 278
7.5.1.2 Analysis . . . 278
7.5.2 Signature data pre-processing . . . 280
7.5.2.1 Formatting . . . 280
7.5.3 Regression and neural network modelling . . . 280
7.6 Results . . . 282
7.6.1 Permeability and calcium evolution . . . 282
7.6.2 µCT outputs . . . 282
7.6.2.1 Post-experimental results . . . 282
7.6.3 ANN outputs . . . 286
7.7 Conclusion . . . 297

8 Synthesis and discussion 299
8.1 Introduction . . . 299
8.2 Comparative work . . . 300
8.2.1 Influence of the Injection rate . . . 300
8.2.2 Influence of effective stress . . . 305
8.2.2.1 Permeability . . . 305
8.2.2.2 Chemistry . . . 309
8.2.2.3 µCT imaging . . . 314

8.2.3 Influence of the heterogeneity . . . 318
8.2.3.1 Artificial Neural Network (chapter 7) . . . 318
8.2.3.2 OpenGeoSys simulation . . . 322
8.2.4 Energy balance model . . . 325

9 Conclusion and future work 329
9.1 Conclusion . . . 329
9.1.1 Introduction . . . 329
9.1.2 Experimental and numerical development . . . 331
9.1.3 Findings . . . 332
9.1.3.1 Injection rate . . . 332
9.1.3.2 Effective stress . . . 333
9.1.3.3 Heterogeneity . . . 334
9.2 Future work . . . 334
9.2.1 Experimental work . . . 335
9.2.2 Modelling work . . . 336
9.3 Technical recommendations . . . 336
9.3.1 ICCR-Macropore . . . 337
9.3.2 LabVIEW controller . . . 338
9.3.3 Data treatment improvement . . . 339

Appendices 341

A Formation water composition 341

B Petrological analysis of the Indiana formation 343

C Indiana formation stratigraphic presentation 345

D Travertine shrub morpho-types 347

E List variables for the CNT file (ICCR-Macropore) 351

F ICCR-Macropore and Slice Picker (executables) 355

G SVG Converter: workflow 357

H LabVIEW programming architecture 359

I LabVIEW Graphical User Interface (GUI) 367

J Experimental observation of wormhole formation at variable effective stress and injection rate on carbonate samples **371**

K Prediction of wormhole formation in heterogeneous rocks using μCT imaging and machine learning **373**

L Importance hydro-mechanical coupling for fluid flow driven wormhole formation in carbonate rocks **375**

References **377**

List of Tables

1.1 Pore volume rate (PV_{rate}) and effective stress (MPa) values for the six possible flooding scenarios. The values for low, medium, and high PV_{rate} are variable between rocks. 12

2.1 Values for the bulk modulus calculation; (1) calcite / (2) dolomite / (3) quartz / (5) hematite / (6) corundum: after Mavko et al. (2009); (4) Montmorillonite: after Mondol et al. (2008). 64

2.2 Values for the shear modulus calculation; (1) calcite / (2) dolomite / (3) quartz / (5) hematite / (6) corundum: after Mavko et al. (2009); (4) Montmorillonite: after Mondol et al. (2008). 66

3.1 Timeline of the experimental work, and the membranes used throughout. The membranes have been replaced due to unexpected bursts in differential pressure and have been replaced with the available material. 85

3.2 Injection rates used for the twelve experiments (IL: Indiana limestone; Trav: travertine; PS: Pre-salt). 127

4.1 Pore volume rate (PV_{rate}) and effective stress (MPa) values for the six scenarios. 140

4.2 Chemical composition of the Indiana limestone compiled from three different studies plus an in-house XRD analysis. 1) Churcher et al. (1991); 2) Freire-Gormaly et al. (2016); 3) Powell (2004). . . 142

4.3 Petrological characteristics of the samples. The volume of solid is calculated from the difference between the volume of the cylindrical core and the volume of pore: V - V_p. 144

4.4 Sample length and total channel thickness for the six experiments. 164

5.1 Pore volume rate (PV_{rate}) and effective stress (MPa) values for the four experimental scenarios. 185

5.2 Reynold and alpha numbers calculated for the four core samples. 187

5.3 Petrological characteristics of the samples. The volume of solid is calculated from the difference between the volume of the cylindrical core and the volume of pore: V - V_p. 190
5.4 Chemical composition of a block of travertine (Saturnia - Italy) from a in-house XRD analysis. 190
5.5 Sample length total channel thickness, and wormhole length for the four experiments. 212

6.1 Petrological characteristics of the Pre-salt samples. 235
6.2 Pore volume rate (PV_{rate}) and effective stress (MPa) values for the four experimental scenarios. 237
6.3 Expected differential pressure values (MPa) for the three scenario of PV_{rate}. 238
6.4 Reynold and alpha numbers calculated for the Pre-salt core samples 239
6.5 Average proportion of mineral forming the upper sag part of the Pre-salt reservoir from Saller et al. (2016) and our in-house XRD analysis. The remaining minerals represented by 'Others' include clay, chert, sand, silts and other trace elements. 243

7.1 Summary of the key parameters used in this study and their apparent relative influence on preferential flow-path formation. . . 294

A.1 Processed formation water chemical composition. 341

List of Figures

1.1 Location of the Santos and Campos representing the main Pre-salt reservoirs. After Petrobras. 1

1.2 Elevation map of the structures of the Santos basin. After Gomes et al. (2009). 2

1.3 Prediction of the global demand by fuel type. Study realized by ExxonMobil (2018). 6

2.1 Experimental dissolution structures; A: compact dissolution; B) conical dissolution; C) Dominant channel; D) Ramified wormholes; E) Uniform dissolution. After Golfier et al. (2002). 22

2.2 Example of dissolution map suggested by Golfier et al. (2002). . . 26

2.3 Density evolution of seawater as a function of the temperature. The red dot represents the experimental limits of this study. After Sharqawy et al. (2010). 30

2.4 Phase diagram of temperature as a function of the concentration in NaCl. The red dot represents the experimental limits of this study. After Endoh and Suga (1999). 30

2.5 In-situ pressures as a function of temperature for seawater. The red dot represents the expected phase under a confining pressure of 50 MPa. After Jowitt et al. (2005). 31

2.6 Viscosity of seawater as a function of pressure at two temperatures: a): 323.15 K; b): 298.15 K. After Sawamura et al. (1992). 32

2.7 Viscosity of the seawater as a function of temperature. After Isdale et al. (1972). 33

2.8 Variation of temperature of the Hassler cell throughout each experimental run. The temperature was set to 60 °C. 34

2.9 Definition of some scientific overlaps between the three rocks used throughout this study. 37

2.10 Geological map or the sampling location of the experimental travertine core samples. The original legend has been kept for clearer comprehension of the sketch. After Ronchi and Cruciani (2015). 39

2.11 Contemporary example of travertine depositional system. After Ronchi and Cruciani (2015). 40
2.12 Illustration of porosity and permeability enhancement or reduction depending on the geological processes underwent by the rock. After Chitale et al. (2015). 47
2.13 Calcium content for meteogene (a) and thermogene (b) deposits. After Pentecost (2005). 48
2.14 Cross-bedding interpretation of the Indiana limestone located on an open outcrop (Lawrence county, Indiana - GPS location unavailable). After Swann and Willman (1961). 50
2.15 Calcium dissolution as a function of temperature. In this figure, the experimental work refers to the work of Coto et al. (2012). After Coto et al. (2012). 52
2.16 Influence of NaCl concentration on $CaCO_3$ solubility at 25°C. An average seawater contains ∼0.5 mol/l of NaCl. In this figure, the experimental work refers to the work of Millero et al. (1984). After Coto et al. (2012). 53
2.17 Bjerrum plot displaying the activities of three carbon species as a function of pH. After Zeebe (1999). 55
2.18 Main stresses acting on the core sample. $\sigma 1 = \sigma 2$. 59
2.19 Iterative construction process of the composite medium. After Norris (1985). 61
2.20 Interpretation of the bulk modulus: a force applied on the external sides of a cube of a certain composition triggers change in the cube's volume. Credit image: ESA (2009). 63
2.21 Effective bulk modulus calculation as a function of fraction of constituent of a medium. The bulk modulus should lie on the dotted line between the bounds (Mavko et al., 2009). 63
2.22 Interpretation of the shear modulus: a transverse force applied on the external sides of a cube of a certain composition undergoes a transverse deformation. Credit image: ESA (2009). 67
2.23 Permeability of limestones as a function of confining pressure. The general trend shows a diminution of the permeability as the confining stress is increased. After Ghabezloo et al. (2009). 72

3.1 Experimental rig originally designed by Edlmann et al. (2013). . . 81
3.2 Schematic diagram of the sampling unit. During flooding, A, C1, and C2 are closed, while B1 and B2 are opened, allowing the injection brine to circulate through the loop. The sampling process involves isolating the loop while letting the experiment run at pressure: A is opened first, followed by the closing of B1

and B2. C1 and C2 are then opened. Air is pushed through the loop with a syringe (D1) in order to push the fluid out, followed by a cleaning and priming of the loop by re-injecting distilled water (D2). Finally, C1 and C2 are closed; B1 and B2 are opened before closing A. 82
3.3 Hassler cell schematic. After McCraw (2016). 87
3.4 Example of switch-over between the two syringes of an ISCO pump, producing a constant line pressure (example from the Indiana limestone $HFR\ HES$ experiment; chapter 4). 90
3.5 NI DAQ wired to the equipment and the computer, and composed by three modules: outline in blue: the chassis; outline in red: the temperature input module; outline in purple: the voltage input module. 92
3.6 Example of function written in LabVIEW G-code (Read function): the VISA (ID number of the pump) is used to communicate with the hardware. In this case the command 'CC' is sent to the pump, which answers with a string. The string is then converted into a double and a float which is then transferred to a data cluster. . . 98
3.7 General structure of the program. The red areas represent the equipment (connected to the computer via RS-232 cables or via the NI DAQ), data, and data cluster's initialization. The blue areas are the five main loops. The green area represents the closing functions for queues and equipment. 99
3.8 Pressure set-up function, written in G-code. 101
3.9 Pressure set-up path for a) a low pore pressure experimental scenario, and b) a high pore pressure experimental scenario. . . . 102
3.10 Pressure release function (true 'if' case), written in G-code. 103
3.11 Pressure release function (false 'if' case), written in G-code. . . . 103
3.12 Pressure release path for a) a low pore pressure experimental scenario and b) a high pore pressure experimental scenario. 104
3.13 Fluid sampling tool interface present on the reading panel. By clicking on the 'sample' button, the user resets the volume to zero. 105
3.14 Fluid sampling function: a) after a sampling is done, the user should reset the volume of fluid that has flooded the sampling loop; b) the user has not sampled any fluid. 105
3.15 Simplified UML diagram presenting the main classes of the ICCR-Macropore, as well as the relationship between them. 108
3.16 General workflow for the ICCR-Macropore. Three input types are necessary (a CNT file, a comm file, a text file, and the SVG pictures). The tool generates three types of output files (mesh file, geo files, and geometrical data). 109

3.17 a) Slice from a travertine sample used in this study ($LFR\ LES$ - cf. chapter 5); b) Isolated porosity after ICCR-Macropore processing. 111
3.18 Aspect ratio (a/b) of four samples of heterogeneous nature (travertine and Pre-salt). 113
3.19 Steps for the detection of a link between two pores (black shapes). Step (A) represents the area of influence applied around a pore through a multiplier of the original pore area. The case (B) shows two non-overlapping pores; Case (C) displays a case of overlapping ellipses. 115
3.20 Sketch of an overlap detection (blue square) between two pores (black) defined by area equivalent of a) rectangles and b) ellipses. The ellipse simplifications of the pores allow a finer rendering than the rectangles. 116
3.21 Visual rendering of the 2D connections between pores forming a network of interconnected vugs. Three different 'area of influence' have been used: 5, 10, and 15. 117
3.22 SVG Converter user interface: a) selection of the folder containing the PNG pictures; b) the list of pictures to convert is displayed in the box; c) selection of the destination folder; d) & e) original size of the slices for resizing. 119
3.23 Input files of the Slice Picker. The three input units are the ICCR-Macropore, the Slice.txt file, and the Comm file. 121
3.24 Programming logic and communication between the Slice Picker and the ICCR-Macropore. The Comm file is used as an intermediate file. 122

4.1 Experimentally calculated $\triangle P$ as a function of predicted $\triangle P$ for Indiana limestone rocks. The predicted $\triangle P$ is calculated by solving Darcy equation and using the pre-experimental $k_{nitrogen}$. The experimental $\triangle P$ represents the first log of the differential pressure transducer during a core flooding experiment. 138
4.2 $Da - Pe$ map for the six core samples flooded. The boundaries have been suggested by Golfier et al. (2002) for a HCl-calcite system. 141
4.3 µCT slice of the $MFR\ HES$ core sample. Each sample used in this chapter have been cored from the same homogeneous block of Indiana limestone, and present similar petromorphological characteristics. Image size: 3.8 cm by 3.8 cm. 143
4.4 Example of skeletonization operation from the $MFR\ LES$ sample (AutoSkeleton function under Avizo® 9): a) 3D rendering of the experimentally generated wormhole; b) Corresponding simplified

wormhole's skeleton. In this example, the fluid was injected from top to bottom. 145

4.5 Permeability output. The permeability calculation is derived from Darcy law. All randomly selected LES samples ended up displaying a larger $k(0)$ than the HES samples. The breakthrough onset windows are distributed according the PV_{rate}, and as follows: HFR, MFR, and LFR. 148

4.6 Permeability evolution normalized against the permeability value recorded at $t = 0$ min. Left: untreated data; right: the plain curves display the data outside the error region, while the dashed lines are the extrapolated data. The linear extrapolations are based on the recorded data sitting in between the marks of figure 4.9 and the last valid recorded value. 149

4.7 Derivative of the permeability with respect to time. Each major peak represents the maximum permeability generation during the breakthrough. Per family of PV_{rate}, the HES experiment has peaked before the LES one. The influence of the PV_{rate} is clear, with the HFR experiments peaking before the MFR ones, themselves peaking before the LFR floodings. Interestingly, the permeability is generated quicker as we increase the PV_{rate}. 150

4.8 Normalized permeability generated as function of pore volume injected. Regardless of the PV_{rate} in use, each experiment have seen its breakthrough onset happening within a k/k_0 window spanning from 3 to 6 times the original permeability of the samples. 152

4.9 Differential pressure analysis and relative permeability evolution for the six experiments. The blue marker indicates the time at which a breakthrough begins. We observe the clear behavior of $\triangle P$ on k. 153

4.10 Pore volume to breakthrough as a function of constant PV_{rate} used for the six experiments. The values for PV_{bt} have been derived from the markers of figure 4.9, while the PV_{rate} values are given in table 4.1. 154

4.11 pH measurements for 5 of the 6 experiments. All measures have been done on sub-samples of the fluid before ICP analysis. 155

4.12 Volume of calcium derived from the effluent fluids sampled directly out of the Hassler cell and normalized against the original volume of rock of the core sample (Ω). The low flow rate experiments have been discarded with regards to the abnormally high content values. The curves splits in two families, with the HFR experiments on top of the MFR experiments. Within a family of PV_{rate}, the HES experiment has dissolved more Ca than the MFR one. 157

4.13 Volume of magnesium derived from the effluent fluids sampled

directly out of the Hassler cell and normalized against the original volume of rock of the core sample (Ω). It appears that Mg has largely reacted to a larger effective stress with the HES experiments on top of the LES ones. 158

4.14 Concentration of calcium derived from the effluent fluids. The low flow rate experiments have been discarded with regards to the abnormally high content values. The impact of the effective stress is visible with the HES group gathering on top of the LES one. Within each group, the influence of PV_{rate} is respected, so that a higher flow rate generates more Ca. 159

4.15 Concentration of magnesium derived from the effluent fluids. Mg has largely reacted to a larger effective stress: the HES group is displaying larger [C] in Mg than the LES one. Within each group, the influence of PV_{rate} is respected, so that a higher flow rate generates more Mg. 160

4.16 Dimensionless capability of calcium to be removed from a carbonate rock during water flooding. The low flow rate experiments have been discarded with regards to the abnormally high content values. A high effective stress (blue curves) appears to be more capable of dissolving calcium, assisting the flow rate which remains the prime variable. 162

4.17 Dimensionless capability of magnesium to be removed from a carbonate rock during water flooding, at different PV_{rate} and effective stresses. A high effective stress (blue curves) appears more capable of dissolving magnesium, assisting the flow rate, which remains the prime variable. Mg seems to be very reactive to the effective stress, particularly visible with the $LFR\ HES$ experiment more 'capable' than the $HFR\ LES$ one ($PV_{rate\ HFR\ LES}$ is 3 times larger than $PV_{rate\ LFR\ HES}$). 163

4.18 Cumulative thickness of the main wormholes and channels. The cumulative thickness has been calculated from the skeletons of the wormholes left after each experimental flooding. The red arrows show the flow direction. 165

4.19 Density plot of the dissolution pattern. Each picture displays the nodes forming the skeleton shape of the wormhole left after flowing. Left subplots show the HES experiments; right subplots show the LES experiments. The color-scale displays the amount of nodes in the Z axis. Each square is 3.8 cm by 3.8 cm. 167

4.20 Porosity evolution calculated from Ca and Mg mass balance. . . . 168

4.21 µCT scans of the HFR experiments. The 3D volumes have been computed under Avizo® 9. The fluid was injected from bottom to top (red arrow). 169

4.22 µCT scans of the MFR experiments. The 3D volumes have been computed under Avizo® 9. The fluid was injected from bottom to top (red arrow). 170
4.23 µCT scans of the LFR experiments. The 3D volumes have been computed under Avizo® 9. The fluid was injected from bottom to top (red arrow). 170
4.24 Suggested new boundaries for the dissolution map of Golfier et al. (2002). The new boundaries have been shifted after a qualitative assessment of the experiments presented in this chapter, and correspond to a seawater-calcite system. The red line is supposedly affected by the stress state while the arrow indicates the shift direction. 171
4.25 2D sketch of an homogeneous rock before experimental flooding. The blue arrows represent a low fluid pressure, the red arrows a high confining pressure, and the red lines are regions of likely dissolution. 172
4.26 2D sketch of an homogeneous rock during/after experimental flooding. The blue arrows represent a low fluid pressure, the red arrows a high confining pressure, and the red lines are regions of likely dissolution. 173

5.1 Experimentally calculated $\triangle P$ as a function of predicted $\triangle P$ for travertine rocks. The predicted $\triangle P$ is calculated by solving Darcy equation and using the pre-experimental $k_{nitrogen}$. The experimental $\triangle P$ represents the first log of the differential pressure transducer during a core flooding experiment. 183
5.2 Distribution of the major axis lengths of the ellipse shape of the pores after analysis of 100 slices in the Z direction, and using the ICCR-Macropore (bin size = 60). 186
5.3 $Da - Pe$ map for the four core samples flooded. The boundaries have been suggested by Golfier et al. (2002) for a HCl-calcite system. 187
5.4 µCT slices of each travertine core sample used in this study. A: $LFR\ LES$; B: $MFR\ HES$; C: $HFR\ LES$; D: $HFR\ HES$. Image size: each slice is 3.8 cm by 3.8 cm. 189
5.5 Pre-experimental µCT scan analysis of the $HFR\ HES$ experiment. The volumes represent the connected network of pores, while the non-connected cluster have not been displayed. The image respects the initial size ratio of the sample. Image size: 3.8 cm by 7.1 cm. 191
5.6 Pre-experimental µCT scan analysis of the $HFR\ LES$ experiment. The volumes represent the connected network of pores, while the

non-connected cluster have not been displayed. The image respects the initial size ratio of the sample. Image size: 3.8 cm by 6.8 cm. 191

5.7 Pre-experimental µCT scan analysis of the $MFR\ HES$ experiment. The volumes represent the connected network of pores, while the non-connected cluster have not been displayed. The image respects the initial size ratio of the sample. Image size: 3.8 cm by 7.3 cm. 192

5.8 Pre-experimental µCT scan analysis of the $LFR\ LES$ experiment. The volumes represent the connected network of pores, while the non-connected cluster have not been displayed. The image respects the initial size ratio of the sample. Image size: 3.8 cm by 8.1 cm. 192

5.9 Example of skeletonization operation, from the $MFR\ HES$ sample (Centerline Tree function under Avizo® 9): a) 3D rendering of the wormhole experimentally generated; b) Corresponding simplified skeleton. In this example, the fluid was injected from bottom to top. 194

5.10 Permeability outputs, derived from Darcy law. Although all experiments appear to enter the limit of $\triangle P$ detection at different time, we observe a clear influence of the PV_{rate}. 197

5.11 Permeability evolution normalized against $k(t = 0)$. Left: untreated data; right: the plain curves display the data outside the error region, while the dashed lines are the extrapolated data. Each linear extrapolation is based on the recorded data logged between the mark of figure 5.14 and the last valid recorded value. Both plots highlight the large influence of a LES on the permeability evolution of travertines. 198

5.12 Derivative of the permeability with respect to time. The grey area displays a larger k generation for the lower injection rate experiment. 199

5.13 a) Normalized permeability generated as function of pore volume of seawater injected. From left to right: most economic to least economic scenario with regard to the injection fluid, and as a mean to generate permeability. b) Relative contribution each pore volume injected has had on the creation of permeability. The lower flow rate experiments have been able to create more permeability per PV injected. Per family of injection rate, the LES experiments might have a secondary positive impact. 200

5.14 Differential pressure analysis and relative permeability evolution for the four experiments. The blue marker indicates the time before which the $\triangle P$ had a maximum impact on the permeability generation. 201

5.15 PV_{maxK} as a function of constant PV_{rate} used for the four experiments. The values for PV_{bt} have been derived from the markers of figure 5.14, while the PV_{rate} values are given in table 5.1. 202

5.16 pH measurements for the 4 experiments. All measurements have been done on sub-samples of the fluid before ICP analysis. 203
5.17 Volume of calcium derived from the effluent fluids sampled directly out of the Hassler cell and normalized against the original volume of rock of the core sample (Ω). The influence of the PV_{rate} is apparent, and drives the Ca dissolution for the four experiments. 204
5.18 Volume of magnesium derived from the effluent fluids sampled directly out of the Hassler cell and normalized against the original volume of rock of the core sample (Ω). The influence of the PV_{rate} is apparent, and drives the Mg dissolution for the four experiments. 205
5.19 Concentration of calcium derived from the effluent fluids. The impact of the PV_{rate} is visible with the lower flow rate group gathering on top of the HFR experiments. Within each group, the influence of the effective is perceptible, with the LES displaying higher Ca concentration than the HES. 207
5.20 Concentration of magnesium derived from the effluent fluids. The impact of the PV_{rate} is visible with the lower flow rate group gathering on top of the HFR experiments. Within each group, the influence of the effective is perceptible, with the LES displaying higher Mg concentration than the HES. 208
5.21 Dimensionless capability of the effective stress to remove calcium from a carbonate rock during water flooding. Per family of effective stress, the lower flow rate appears more capable of dissolving calcium. Regardless of the flow rate, a lower effective stress is more capable to dissolve calcium. 210
5.22 Dimensionless capability of the effective stress to remove magnesium from a carbonate rock during water flooding. Per family of effective stress, the lower flow rate appears more capable of dissolving magnesium. Regardless of the flow rate, a lower effective stress is more capable to dissolve magnesium. 211
5.23 Main wormhole thickness displayed by effective stress and computed from the Centerline Tree function of Avizo® 9 (Sato et al., 2000). The red arrows show the flow direction. 214
5.24 Main wormhole thickness displayed by injection rate and computed from the Centerline Tree function of Avizo® 9 (Sato et al., 2000). The red arrows show the flow direction. 215
5.25 Density plot of the dissolution pattern. Each picture displays the nodes forming the skeleton shape of the wormhole left after flowing. The left subplots show the HES experiments; the right subplots show the LES experiments. The color-scale displays the amount of nodes in the Z axis. Each square is $\sim$2.5 cm by $\sim$2.5 cm. . . . 217

5.26 Dissolution pattern of the $HFR\ HES$ experiment. Blue = pre-existing porosity amongst the wormhole; white: post-flooding dissolution. The fluid was injected from right to left (red arrow). . 218
5.27 Dissolution pattern of the $HFR\ LES$ experiment. Blue: pre-existing porosity amongst the wormhole; white: post-flooding dissolution. The fluid was injected from right to left (red arrow). . 218
5.28 Dissolution pattern of the $MFR\ HES$ experiment. Blue: pre-existing porosity amongst the wormhole; white: post-flooding dissolution. The fluid was injected from right to left (red arrow). . 219
5.29 Dissolution pattern of the $LFR\ LES$ experiment. Blue: pre-existing porosity amongst the wormhole; white: post-flooding dissolution. The fluid was injected from right to left (red arrow). . 219
5.30 Slice (perpendicular to the sample axis) of the $HFR\ HES$ experiment showing the dissolution pattern at the pore scale. The clear zones represent the pre-existing pores; the blue outlines represent the post-experimental porosity enhancement. The image side length is 1.9 cm by 1.9 cm. 220
5.31 Porosity evolution calculated from Ca and Mg mass balance. . . . 221
5.32 Suggested new boundaries for the dissolution map of Golfier et al. (2002). The new boundaries have been shifted after a qualitative assessment of the experiments presented in this chapter, and correspond to a seawater-calcite system. The red line is supposedly affected by the stress state while the arrow indicates the shift direction. 222
5.33 2D sketch of an heterogeneous rock before experimental flooding. The orange arrows represent a high fluid pressure, the red arrows a high confining pressure, and the red lines are regions of likely dissolution. 223
5.34 2D sketch of an heterogeneous rock during/after experimental flooding. The orange arrows represent a high fluid pressure, the red arrows a high confining pressure, and the red lines are regions of likely dissolution. 224

6.1 Experimentally calculated $\triangle P$ as a function of predicted $\triangle P$ for travertine and Pre-salt rocks. The predicted $\triangle P$ is calculated by solving Darcy equation and using the pre-experimental $k_{nitrogen}$. The experimental $\triangle P$ represents the first log of the differential pressure transducer during a core flooding experiment. 233
6.2 Pre-experimental pictures of the $HFR\ HES$ sample. Scale: 1 cm. 234
6.3 Pre-experimental pictures of the $HFR\ LES$ sample. Scale: 1 cm. 234
6.4 Pre-experimental µCT scan analysis of the $HFR\ LES$ sample.

The volumes represent the connected network of pores. The image respects the initial size ratio of the sample. Image size: 3.8 cm by 5 cm. 236
6.5 Pre-experimental µCT scan analysis of the $HFR\ HES$ sample. The volumes represent the connected network of pores. The image respects the initial size ratio of the sample. Image size: 3.8 cm by 6 cm. 236
6.6 Distribution of the major axis lengths of the ellipse shape of the pores after analysis of 100 slices in the Z direction, and using the ICCR-Macropore (bin size = 20). 240
6.7 $Da - Pe$ map for the Pre-salt core samples. The boundaries have been suggested by Golfier et al. (2002) for a HCl-calcite system. . 240
6.8 µCT slices of the two core sample used in this study. A: $HFR\ LES$; B: $HFR\ HES$. Image size: each slice is 3.8 cm by 3.8 cm. 243
6.9 Preparation of the $HFR\ LES$ sample; left: Teflon-tape wrapped sample + Teflon-tape inserted within the major vugs (non-visible on the picture). Right: sample wrapped in duct tape in order to keep the Teflon-tape in place during the experiment. Scale: 1 cm. 244
6.10 Permeability (m^2) of the $HFR\ HES$ (blue) and $HFR\ LES$ (orange) experiments. The large decrease in k during the $HFR\ HES$ experiment (∼5,000 min) is due to a pausing of the experiment after a technical issue with the back-pressure regulators. 247
6.11 Permeability evolution normalized against the permeability value recorded at $t = 0$ min. Left: untreated data; right: the plain curves display the data outside the error region, while the dashed lines are the extrapolated data. The linear extrapolations are based on the recorded data sitting in between the marks of figure 6.14 and the last valid recorded value. By assuming a linear increase of the permeability for both scenarios, $HFR\ LES$ should have generated a larger k/k_0 than $HFR\ HES$. 248
6.12 Derivative of the permeability with respect to time. 249
6.13 a) Normalized permeability generated as a function of pore volume of seawater injected; b) Relative contribution each pore volume injected had on the permeability generation. 250
6.14 Differential pressure analysis and k/k_0 evolution. The blue marker indicates the time before which the $\triangle P$ has had a maximum impact on the permeability generation or at which a breakthrough was initiated. 251
6.15 PV_{maxK} and PV_{bt} as a function of constant PV_{rate}. The values for

PV_{maxK} and PV_{bt} have been derived from the markers of figure 6.14, while the PV_{rate} values are given in table 6.2. 251
6.16 pH measurements for the Pre-salt experiments. All measures have been done on sub-samples of the fluid before ICP-MS analyses. . . 252
6.17 Concentration of calcium and magnesium derived from the effluent fluids. For both ions, the $HFR\ HES$ scenario has generated more Ca and Mg. The shapes of the curves largely differ, which might be due to two different processes taking place during each experiment. 254
6.18 Volume of calcium and magnesium derived from the effluent fluids sampled directly out of the Hassler cell and normalized against the original volume of rock of the core sample (Ω). $HFR\ HES$ has dissolved ∼6 times more Ca and ∼5 times more Mg than the $HFR\ LES$ scenario. 255
6.19 Post-experimental $HFR\ HES$ sample. The three smallest pieces of rock (right part) have been cleaned out and kept as displayed on the figure, while the largest bloc has been cast in epoxy resin for further µCT scanning. 256
6.20 Top view of the post-experimental µCT scan reconstruction of the $HFR\ HES$ sample. Side length: 3.8 cm by 3.8 cm. 257
6.21 Side view of the post-experimental µCT scan reconstruction of the $HFR\ HES$ sample. Side length: 6 cm by 3.8 cm. The fluid was injected from right to left (red arrow). 257
6.22 Dissolution pattern of the $HFR\ LES$ experiment. Blue: pre-existing porosity amongst the wormhole; White: post-flooding dissolution. Image size: 3.8 cm by 5 cm. The fluid was injected from right to left (red arrow). 259
6.23 Dissolution pattern of the $HFR\ HES$ experiment. Blue: pre-existing porosity amongst the wormhole; White: post-flooding dissolution. Image size: ∼1 cm by ∼0.6 cm. The fluid was injected from right to left (red arrow). 260
6.24 Prediction of dissolution based on µCT images and geometrical features ($HFR\ HES$ experiment). The features present on both pictures are likely signs of a branched dissolution pattern. 260
6.25 Slices from the µCT volumes showing the dissolution pattern at the pore scale. The clear zones represent the pre-existing pores; the blue outlines represent the post-experimental porosity enhancement. Images side length: 1.9 cm by 1.9 cm. 261
6.26 Porosity evolution calculated from Ca and Mg mass balance. . . . 262
6.27 Suggested new boundaries for the dissolution map of Golfier et al. (2002). The new boundaries have been shifted after a qualitative

assessment of the experiments presented in this chapter, and correspond to a seawater-calcite system. 263

7.1 Data acquisition workflow. The two sub-sampled cuboids are of the same size. Both stacks have been re-sliced a hundred times in two orthogonal directions. A & B: input data acquisition; C & D: signature data acquisition; E & F: input and signature data are attributes for the ANN. 277

7.2 Signal data and their respective post-experimental cross-sectional direction ($LFR\ LES$). The fluid was injected from bottom to top (red arrow). 283

7.3 Signal data and their respective post-experimental cross-sectional direction ($MFR\ HES$) The fluid was injected from bottom to top (red arrow). 284

7.4 Signal data and their respective post-experimental cross-sectional direction ($HFR\ LES$) The fluid was injected from bottom to top (red arrow). 285

7.5 Signal data and their respective post-experimental cross-sectional direction ($HFR\ HES$) The fluid was injected from bottom to top (red arrow). 286

7.6 Linear regression weights for all features. The outlying weight on feature 12 is -6.22. 288

7.7 Visual representation of the capacity of the ANN solution to predict the location of the forthcoming dissolution in a rock sample. Color scale: yellow = high confidence; pale blue = low confidence. 289

7.8 Measured data (red) overlain on density plot of 3,000 trained neural networks' blind test predictions for the $LFR\ LES$ experiment. The white curve represents a linear regression applied to the same dataset, and which comparatively shows the better fit of the neural network solution. Color scale: yellow = high confidence; pale blue = low confidence. 290

7.9 Measured data (red) overlain on density plot of 3,000 trained neural networks' blind test predictions for the $MFR\ HES$ experiment. The white curve represents a linear regression applied to the same dataset. Here the linear regression still fails to find the right magnitude of material removal but appears to relatively accurately shows the zone of material removal. Color scale: yellow = high confidence; pale blue = low confidence. 291

7.10 Measured data (red) overlain on density plot of 3,000 trained neural networks' blind test predictions for the $HFR\ LES$ experiment. The white curve represents a linear regression applied to the same dataset, and which comparatively shows the better fit of the neural

network solution. Color scale: yellow = high confidence; pale blue = low confidence. 292

7.11 Measured data (red) overlain on density plot of 3,000 trained neural networks' blind test predictions for the $HFR\ HES$ experiment. The white curve represents a linear regression applied to the same dataset, and which comparatively shows the better fit of the neural network solution. Color scale: yellow = high confidence; pale blue = low confidence. 293

8.1 Absolute permeability generation for the three rock-types experimentally tested, and showing similar trends: the flow rate is the dominating variable for k generation. 302

8.2 Normalized volume of Ca per volume of solid rock (Ω) for the three rock-types experimentally tested. A trend seems to appear for the Indiana limestone experiments, where an uncoupling between experiment sharing the same PV_{rate} appears. Calcium dissolution within Travertines and Pre-salt rocks is controlled by the injection rate and the sample petromorphology. 303

8.3 Normalized volume of Mg per volume of solid rock (Ω) for the three rocks experimentally tested. A trend is clearly visible for the Indiana limestone experiments, where an uncoupling between experiment sharing the same PV_{rate} seems to show the large effect of the HES on Mg dissolution. Magnesium dissolution within Travertines and Pre-salt rocks is controlled by the injection rate and the sample petromorphology 304

8.4 Normalized permeability evolution for the three rocks experimentally tested. The Indiana limestone curves show a clear arrangement which depends upon the PV_{rate} and the effective stress. The travertine and Pre-salt cores seems to have been affected by the low effective stress scenario. An interesting uncoupling of the processes is visible within the set of travertine experiments, were the lower flow rates appear to have generated larger k/k_0. 307

8.5 PV_{maxK} and PV_{bt} as a function of constant PV_{rate} for HFR experiments of travertine and Pre-salt rocks. The values for PV_{maxK} and PV_{bt} have been derived from the markers of figures 5.14 and 6.14, while the PV_{rate} values are given in tables 5.1 and 6.2. We observe that similar processes took place during the four experiments, which could have been influence by the effective stress in place. 309

8.6 Ca normalized Ω values for Indiana limestone and travertine rocks. No normalization is needed for the Pre-salt samples due to a similar PV_{rate}. The effect of the stress state is clearly visible: HES had a

positive impact on the Indiana limestone and Pre-salt rocks, while a LES had one on travertine samples. 311

8.7 Mg normalized Ω values for Indiana limestone and travertine rocks. No normalization is needed for the Pre-salt samples due to a similar PV_{rate}. The effect of the stress state is clearly visible: HES had a large positive impact on the Indiana limestone and Pre-salt rocks, while a LES had a large one on travertine samples. 312

8.8 Ca concentration values for Indiana limestone, travertines, and Pre-salt rocks. From the standpoint of a high Ca dissolution, scenarios tending towards a $HFR\,HES$ were preferable for Indiana limestone and a Pre-salt rocks, whereas scenarios tending towards a $LFR\ LES$ were preferable for a travertine rock. 313

8.9 Mg concentration values for Indiana limestone, travertines, and Pre-salt rocks. From the standpoint of a high Mg dissolution, scenarios tending towards a $HFR\,HES$ were preferable for Indiana limestone and a Pre-salt rocks, whereas scenarios tending towards a $LFR\ LES$ were preferable for a travertine rock. 314

8.10 Main wormholes thicknesses for the travertine HFR experiments and Pre-salt $HFR\ LES$ experiment. The red arrows show the flow direction. 316

8.11 Density plot of the dissolution pattern. Comparison case for the HFR experiments involving a shrub framestone. The color-scale displays the amount of nodes in the Z axis. From three comparable rock samples, the LES experiments have undergone more damage than the HES one. 317

8.12 Signal data plotted under their respective cross-sectional direction for the travertine $LFR\ LES$ experiment. 319

8.13 Signal data plotted under their respective cross-sectional direction for the travertine $MFR\ HES$ experiment. 320

8.14 Signal data plotted under their respective cross-sectional direction for the travertine $HFR\ LES$ experiment. 320

8.15 Signal data plotted under their respective cross-sectional direction for the travertine $HFR\ HES$ experiment. 321

8.16 Signal data plotted under their respective cross-sectional direction for the Pre-salt $HFR\ LES$ experiment. 321

8.17 Comparison between pre- and post-experimental 2D slice of image stack, and the stress map. The interest of this 2D model is two-fold: 1) it validates the 2D network of pore presented in chapter 3, and 2) it validates the impact that the heterogeneities have on the fluid flow. 324

8.18 Comparison between the experimental permeability and the

model-based permeability for Indiana limestone. The model renders well the curves ordering as well as the relative magnitude until $\triangle P$ becomes too low (end of an experimental flooding). 327

8.19 Comparison between the experimental permeability and the model-based permeability for travertine. While the model catches the mains trends (difference of magnitude between higher and lower PV_{rate}), it fails in finding the relative ordering between the $LFR\ LES$ and $MFR\ HES$ experiments. 327

C.1 Detailed Mississippian stratigraphic nomenclature. The Salem formation correspond to the Indiana limestones .After: Ramaker et al. (2015). 346

D.1 1/2 - Classification of shrubs' morphology (micro and macro scale). Shrub samples from Denizli, Turkey. After Claes et al. (2017). . . 349

D.2 2/2 - Classification of shrubs' morphology (micro and macro scale). Shrub samples from Denizli, Turkey. After Claes et al. (2017). . . 350

H.1 Loop 1: Event-Driven and producer loop. The user's physical action are caught by this structure, before sending an order to the loop 2. a) LabVIEW queuing functions; b) pre-defined user events; c) data-cluster generation. 363

H.2 Loop 2: consumer of loop 1 and producer of down loops. This structure represents a State-Machine whose actions are triggered according to the data-clusters received from the loop 1. a) data-cluster dequeued and split in two variables (a Boolean and a string command); b) 'if' structures; c) tailored functions. Red area: equipment and enqueue initialisation. 364

H.3 Loop 3: first of the two display loops. This loop consumes the data generated by the loop 2 before displaying them in GUI structures. a) data-cluster dequeued and split into variables; b) tailored functions. 365

H.4 Loop 4: second of the two display loops. This loop consumes the data generated by the loop 2 before displaying them in GUI structures. a) data-cluster dequeued and split into variables; b) 'if' structures. 366

H.5 Loop 5: the recording loop consumes the data generated by the loop 2, and save them in a text file. a) creation of the text file; b) tailored data averaging function. 366

I.1 Control panel of the tailored LabVIEW software. 368

I.2 Reading panel of the tailored LabVIEW software. 369

Chapter 1

Introduction

1.1 The Brazilian hydrocarbon exploration

Located in the Santos and Campos basins (figure 1.1), the Pre-salt reservoirs lay 300 km south east of São Paulo.

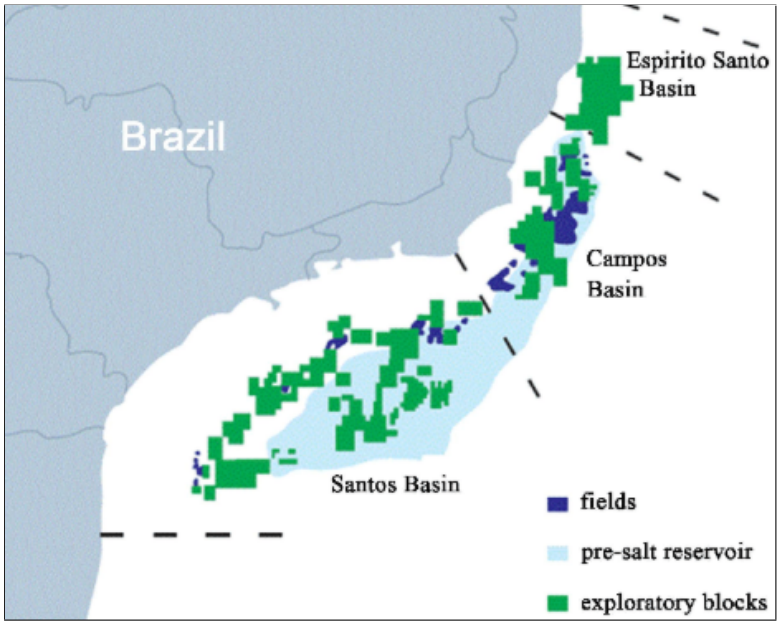

Figure 1.1: Location of the Santos and Campos representing the main Pre-salt reservoirs. After Petrobras.

Several small fields, dated from Neocomian/Barremian (145.5 Ma to 125 Ma), were discovered during the mid-1950's. The 1960's saw the onset of the exploration of giant oilfields with the discovery of the Sergepie Basin (Carminatti et al., 2008). Until early 2000's, the efforts where periodic and permitted to raise an industrial interest in this area, by recognizing the potential of the Outer high (broad region around the Santos basin - figure 1.2). The Outer High is a structural province which forms a 4-way closure at the Aptian geological level and is fully sealed by evaporate salts. This geological structure contains two elevations called Sugar Loaf and Tupi. A well drilled in the Santos basin in the mid 2000's confirmed the geologic models which predicted the presence of gas and oil within the Pre-salt formations, and marked the onset of a new exploration and production trend, as until then, oil in the Brazilian gulf was produced from the more conventional sub-salt layers (Beasley et al., 2010). The economic interest that these unconventional reservoirs represents have encouraged the industry to put additional efforts into innovative technologies in order to reach these ultra-deep reservoirs (Naveiro et al., 2015).

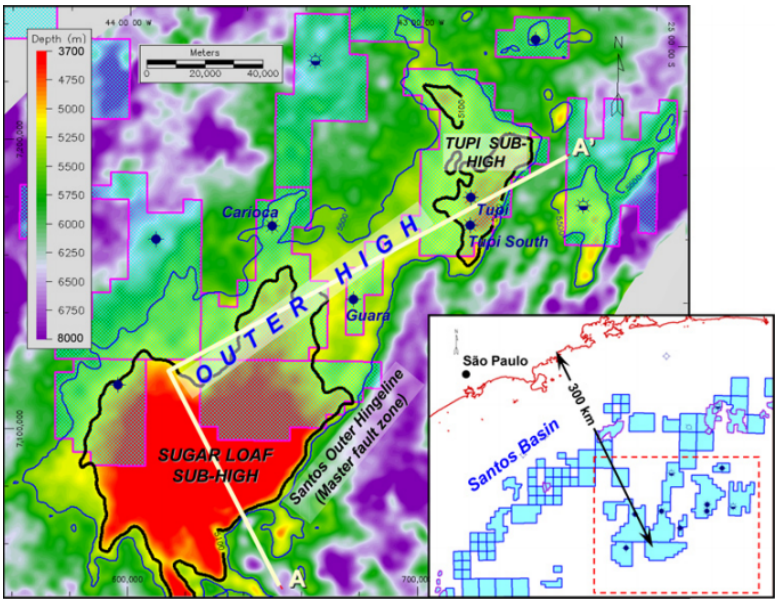

Figure 1.2: Elevation map of the structures of the Santos basin. After Gomes et al. (2009).

The Pre-salt reservoirs are considered as unconventional, or more precisely transitional (Balouga, 2012). Transitional oils have an ordinary composition but are extracted in unconventional ways. The Pre-salt fields are offshore reservoirs, where the wells are considered ultra-deep (> 1,500 meters of water depth - Rocha et al. (2003)). The oil is held in complex microbial carbonate reservoir facies displaying a large degree of heterogeneity. Diagraphic well data suggest a high vertical heterogeneity in permeability amongst the reservoir, where flow rates appear to be high with no barrier in the bedding direction. Nakano et al. (2009) summarized the characteristics of the reservoir as follows:

- Depth: 5,000 to 5,500 m from sea level.
- Water depth: 2,200 m.
- Microbial carbonate (referred to as SAG and RIFT reservoirs) + coquina section.
- Reservoirs are supposed to contain a recoverable volume of oil comprised between 0.8 to 1.27 billion m^3.
- Salt layer thickness: up to 2,000 m.
- Oil API: 28.
- Gas/oil ratio: 220-240 m^3/m^3.
- Oil viscosity: 1.14 cP.
- CO_2 content: 8 to 12 %.

The oil in the Santos basin is light (28 to 30 API) with a high gas content, and displays a high CO_2 content. Pressure is high, while temperatures are lower than expected for the reservoir depth. This is due to the high heat conductivity of the overlying salt layer (∼60 °C).

1.2 Geological introduction to the Pre-salt

The Pre-salt defines a stratigraphic and tectonic structure which refers to the strata deposited before an evaporite layer, and dated early to mid-Aptian. The oldest layers have been deposited in half grabens, while the following Barremian-Neocomian-Early Aptian beds are linked to lacustrine and fluvial to paralic-marine environments (estuaries, bays, lagoons). The onset of the Pre-salt deposit is dated 160 million years ago, and is in connection with the break-up of Gondwana, which led to the formation of the new African and South American continents. Deposition of sediments occurred during the rifting phase: as the rifting proceeded, the sea water began to fill the existing lakes, creating low energy and high salinity environments, suitable for stromatolites. The combined effects of the stromatolites secretion and the carbonate salts formed the microbialite carbonates, now known as the hydrocarbon reservoir in the Pre-salt strata. The following environment represents a radical climate change as the lakes started to see the dissolved salts to precipitate, forming a thick layer of salt (Formigli et al., 2009). The overlying layers of salt began to seal the carbonate Pre-salt layers and the rifting faults by Mid-Aptian times. The accommodation space which permitted the deposition of the salt has been generated by the thermal subsidence which accompanied the opening of the Atlantic sea (Versfelt et al., 2009).

Three characteristics tend to make this geological structures industrially interesting (Gomes et al., 2009):

- Prolific and mature source rocks.
- Syn-rift structures that played both migration and trapping roles.
- Evaporites (salts) sealing the reservoir.

1.3 Context of research

Most of the progress and invention throughout human history is closely related to the exploitation and use of energy (Hall et al., 2003). Currently, and because of the environmental issues we face, we observe large scale changes in our energy production; shifting from hydrocarbons to more renewable ways of harvesting energy. While this shift is necessary due to the environmental threat we are facing, hydrocarbons currently remain the most important source of energy, hence forcing oil & gas companies to enhance their exploration and production technologies, in order to find economically interesting fields, while further exploiting those already in production.

Several reasons can explain the relative stability in the use of fossil energies:

- It represents one of the simplest energy to store.
- The announced decrease slope which should have occurred after the oil peak is less steep than expected due to efforts for improving Enhanced Oil Recovery methods (EOR), or by finding alternative resources (non-conventional reservoirs). Rogner (1997) observed that if the technological advancements progress in a similar rate as observed in the past, it is unlikely to see the hydrocarbon production to decrease during the twenty-first century.
- As of 2019, the demand in oil and gas is still high (figure 1.3).

Rogner (1997) summarized the current economic situation by reflecting on the current hydrocarbon exploration, production and development rate, which grows by 1 % per year. This rate seems to approximate the average long-term growth rate of the sector.

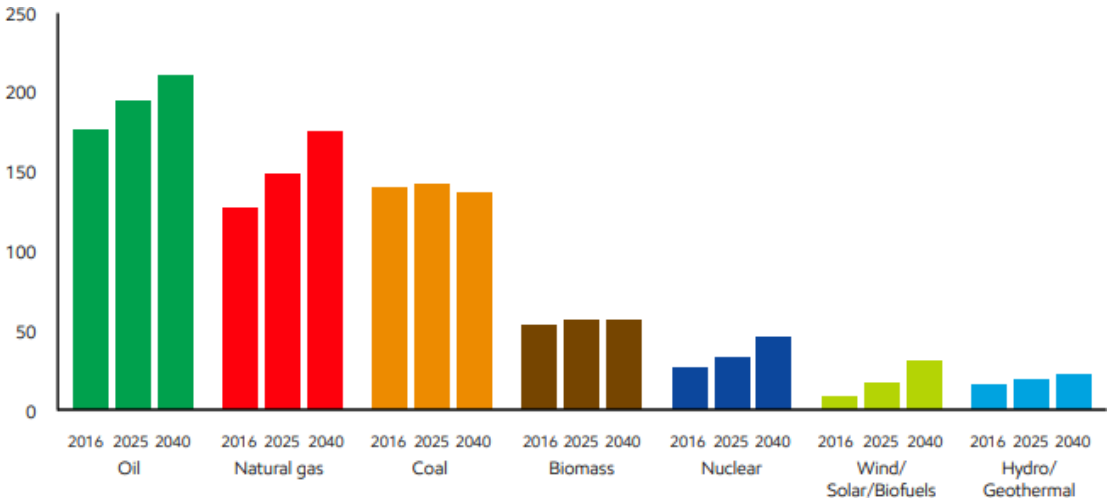

Figure 1.3: Prediction of the global demand by fuel type. Study realized by ExxonMobil (2018).

The increasing demand for oil over the next two decades (Al Adasani and Bai, 2011), the reduction in conventional resources, and oil prices have led to more research into EOR methods (Kamari et al., 2014). EOR can be used at any stage of an oil field development when classic techniques are inefficient for extracting oil from a reservoir. Since the beginning of the Pre-salt reservoir life-cycle (Pizarro et al., 2012), industry players are using Water Alternating Gas (WAG) techniques for oil extraction from the offshore carbonate reservoirs, by alternating between CO_2 injections and seawater flooding. While implementing EOR methods on the Pre-salt reservoirs has been proven beneficial (Pizarro et al., 2012), injection of fluids and production of hydrocarbons from carbonate reservoir rocks involve variations in pore pressure within the reservoirs (Al-Harthy et al., 1998a; İşcan et al., 2006), as well as fluids mixing: over time, the pore space of the rocks has been filled with a mixture of fluids which interact with the rock and affect the matrix through mechanical and chemical alterations (Davies et al., 1999; Jaeger et al., 2009). These pressurized fluids circulating within a reservoir act against the overburden loading. This steady-state can be mechanically altered leading to a stress disequilibrium, for example during extraction or injection of

fluid(s). This inevitably leads to multi-chemical and physical problems eventually affecting the rock's petrophysical and chemical properties, such as hydraulic conductivity or permeability (Sun et al., 2016). This is also reinforced by the effect of local permeability and in-situ heterogeneities within the flow system. Pore pressure should decrease during fluid depletion from a reservoir, causing variation of the permeability, and further leading to changes in production rate and increase of recovery issues (Ghabezloo et al., 2009). Ignoring the effects of the local or global pressure changes during injection/production can causes serious deviations from fluid recovery estimations (İşcan et al., 2006).

The ability to ground truth multi-physic models of the behaviour of carbonate reservoir material under in-situ reservoir conditions of temperature, polyaxial stress, and fluid flow is vital for the reduction of risk and enhancement of underground fluid injection and/or production. Studies have experimentally assessed the above mentioned variables, through single or multi-phase flow (Hoefner and Fogler, 1988; Bazin et al., 1995; Fredd et al., 1996; Golfier et al., 2002; McDuff et al., 2010), and the results point toward a relationship between dissolution and injection rate (Buijse et al., 1997). Extensive work has been done using acidic injection fluids (Hoefner and Fogler, 1988; Bazin et al., 1995; Fredd et al., 1996; Golfier et al., 2002; McDuff et al., 2010), which induce rapid permeability and porosity changes within the first pore volumes injected. It also results in shorter experimental flooding time spent at reservoir P-T conditions. We believe that the effect of effective stress on a rock has been neglected, while little effort has been made to address the coupled effect of stress state and injection rate on carbonate rock matrix alteration. For the first time, we have produced experimental and numerical work designed to understand the impact of effective stress on carbonate rocks, and by assessing the following research questions:

- What is the effect of the injection rate on permeability and porosity evolution of carbonate rocks ?

- How does the stress state affect the permeability and porosity evolution of carbonate rocks during seawater flooding?
- What are the key chemical controls during mixing between fluid and rock, and what can we infer from the amount of dissolved matter?

Experimental work has been undertaken, allowing the study of seawater flooding through a specific set carbonate rock samples. Due to the prime nature of this work, we first observed the effect of variable effective stress and injection rate using homogeneous Indiana limestone samples, whose results were used as a comparative baseline. We then proceed to recreate similar experimental conditions using Pre-salt and Pre-salt analogue rock samples (travertine). The experimental flooding rig was composed of a set of pumps (for injection and back-pressure), a series of sensors (pressure and temperature), and a high pressure polyaxial Hassler cell able to accommodate 3.8 cm diameter core samples.

Analytical tools have been developed and used to investigate structural and chemical alterations as a result of fluid injection. We have used physical sensor recording, ICP-MS fluid analysis, and µCT scanning techniques as a way to estimate carbonate reservoir sweep efficiency. A new tool (the ICCR-Macropore software) has been developed to provide numerical meshes of a core sample structure, as well as important statistical characteristics of the void arrangement. This has allowed us to further analyse the evolution of the pore network during the experimental work. This ICCR-Macropore has also been used as a pre-processor of data for other modelling tools: parts of the models have been solved using the open source coupled processes software tool OpenGeoSys (OGS), while another model has been developed using the machine learning packages offered by Matlab, with the aim of developing numerical tools capable of capturing dominant coupled process behaviour. This thesis presents the experimental development and results, the pore geometry analysis and the numerical tools and modelling results that have been achieved over three and a half years of research

and development.

This project, named GeoMeChem, involved Dr. Christopher McDermott, Dr. Katriona Edlmann, Dr. Ian Butler, Dr. Andrew Fraser-Harris, and Prof. Gary Couples. GeoMeChem belongs to the International Centre for Carbonate Research group (ICCR), whose aim was to investigate the poorly known Brazilian Pre-salt reservoir. Projects spread from the pore scale to the reservoir scale, and from purely theoretical research to fully experimental work. This PhD observes the Darcy-pore scale using a mixed experimental and numerical approach. Most of the work done during this PhD, as well as the ideas developed throughout were the result of a team effort, while the outputs, the developed tools, and the methods were disseminated to ICCR members.

1.4 Experimental and numerical investigation

The rig used by Edlmann et al. (2013) and further developed by McCraw (2016) has been modified for the purpose of our experimental flooding. While in working condition, the injection pump had to be replaced for a Teledyne CP-class pump, whose operating pressure and injection rate range matched our experimental conditions. A pair of Teledyne ISCO 100DX pumps used as a back-pressure regulator have been refurbished and fixed, partially due to extensive use of corrosive fluids during previous studies, and resulting in pressure and fluid leaks. A Validyne P365D high line differential pressure transducer has finally be added to the rig. The differential pressure transducer, along with the ISCO and CP-class pumps were designed for direct control and use through a programming language named LabVIEW. As a way to facilitate experimental controls and data gathering, an extensive control software has been developed. This controller allowed to remotely perform actions on the equipment, gather the data in a uniform and frequency-controlled way, and allowed the loading and unloading

of the sample under controlled confining and pore pressure. The controller is further presented in chapter 3 and appendices H and I. One experimental challenge consisted in flooding at high flow rate and high pressure conditions while being able to sample the fluid for chemical analysis. For this purpose, a sampling loop has been designed for simultaneously allowing continuous flooding and fluid sampling while preserving a relatively stable pore pressure within the system (further described in section 3.2.2). The experimental approach consisted in flooding a range of cylindrical core samples of 38 mm diameter and similar length. The rock flooding experiments have been done by injecting an artificial seawater of known chemistry (30.5 g NaCl per litre of distilled water) and pH (∼7). The experiments have been carried under geo-reservoir conditions of pressure, temperature, and representative chemistry (temperature T = 60 °C, pore pressure P_p = 10 MPa or 40 MPa, confining pressure P_c = 50 MPa - table 1.1). The main difference between each experimental scenario resided in using a different pore volume rate and effective stress. The effective stress in this study refers to the work of Terzaghi (1951). The run-time for an experiment varied between ∼800 min (travertine) to more than 6,000 min (Pre-salt) of continuous flooding. Fluid samples for chemical analyses were taken every one to two hours. Except for one Pre-salt sample, the experiment were terminated when the delta in pressure across the rock samples was constantly close to 0 Pa. Post-processing of the data were done in an orderly way (one experiment at a time) using a pre-designed excel spreadsheet containing the main mathematical functions (eg. permeability calculation).

Carbonate samples of different rock nature have been investigated through this PhD project:

- The homogeneous Indiana limestone, which represents a baseline work for comparative analysis.

- The heterogeneous Italian travertine rock (Saturnia, Italy), which was used as an analogue for the Pre-salt reservoir rock.

- The heterogeneous Pre-salt rock, cored from non-destructive wells offshore Rio de Janeiro (Brazil).

The prime aspect of this project resided in using an experimental matrix allowing vertical and horizontal comparison between each flooding: table 1.1 presents the six experimental scenario available in this study. Each scenario resides in a coupling between a flow rate (low flow: LFR; medium flow: MFR; high flow: HFR) and an effective stress (low effective stress: LES; high effective stress: HES). Moreover, we have developed new numerical tools allowing a coupled experimental and numerical investigation of the variables affecting rock alteration under constant injection rate and stress state.

The numerical investigation was two-fold:

- An extensive C++ tool has been further developed by Dr. Christopher McDermott and I. The software, known as the ICCR-Macropore, is able to extract key geometrical data from µCT images of rock samples. Outputs were used for analysis and modelling works. The tool also creates mesh files of 2D slices rock samples, and 2D network of pore connectivity. The meshes have been used by Dr. Christopher McDermott and Dr. Andrew Fraser-Harris for 2D modelling of fluid flow through heterogeneous carbonates. Their work completes the research undertaken during this PhD as it highlights the role of the heterogeneity and porosity, as well as the predictability of poro-permeability development.

- A solution using the Deep Learning Toolbox of Matlab has been developed with the help of Phil Cilli (PhD candidate within ICCR - University of Edinburgh). This numerical work requires to uses the ICCR-Macropore

as a pre-processor of experimental results in order to study the effect of heterogneities on poro-permeability development.

		Flow expressed as pore volume		
		Low	Medium	High
σ'	Low	n1 PV/min m1 MPa	n2 PV/min m1 MPa	n3 PV/min m1 MPa
	High	n1 PV/min m2 MPa	n2 PV/min m2 MPa	n3 PV/min m2 MPa

Table 1.1: Pore volume rate (PV_{rate}) and effective stress (MPa) values for the six possible flooding scenarios. The values for low, medium, and high PV_{rate} are variable between rocks.

1.5 Thesis structure

Within this thesis, the following chapters are presented:

Chapter 2 presents the background theory and reading. This section encompasses the broad scope of the research, by also underlining the key equations and concepts that were further used during this work. In this chapter, the relevance of the models used throughout this project is also succinctly discussed.

Chapter 3 outlines the experimental and numerical development, by presenting the hardware, software, and workflows used and followed during this project. The numerical tools developed during this PhD are also presented, along with the underlying mathematics, key functions, and usefulness.

Chapters 4, 5, 6, and 7 are the results chapters. Three out of four chapters have been written for the purpose of being publicly published in scientific reports.

The material and methods for chapters 4, 5, and 6 were similar and allowed a comparison of the results within and between each chapter. Chapter 7 focuses on a non-linear modelling approach of the heterogeneities of travertine rocks used in chapter 5.

Chapter 8 is a closing chapter that aims at cross-comparing the results gathered during the previous sections, and approaches them in an objective way in order to highlight the main features that could lead to answer the research questions of this PhD.

Chapter 9 closes this thesis and suggests new ideas for future work, as well as discussing potential flaws and bugs that have been encountered during the experimental and numerical development.

Chapter 2

Background Theory

2.1 Introduction

This section aims to describe the chemical and mechanical processes of carbonates undergoing different stress states and flow regimes. The fundamental laws governing these processes are described in this chapter as well as a brief geological description of the samples used for the fluid flow and effective stress experiments.

2.2 Porosity within a porous medium

Porosity is one important variable studied in this work. Whether it is in an oil reservoir, an aquifer, or in a restricted laboratory experimental study, the fluid flow takes place within a connected network of pores. One way to define the porosity is by considering the rock to be a solid matrix with holes. Bear (1972) defined the porous medium as a portion of space occupied by one or more liquid or gaseous phases (i.e. at least one phase is not solid). In the case of an oil reservoir or an aquifer, it would be the fluid in place. That space within a medium is called void space. One feature of a porous medium is that at least some of the void space should be interconnected. This interconnected voidage can be referred to as the effective pore space. In opposition to this

connected network of pores, the unconnected pores were considered as parts of the solid matrix by Bear (1972). A third category of pores is called the blind-porosity which refers to the dead-end formed by a channel, and which eventually makes the path ineffective as very little to no flow circulates through it.

The porosity formed by the voids, or pores, is defined as a ratio of volume of the void space (U_v) to the bulk volume (U_b) of the porous medium (Bear, 1972):

$$n = \frac{U_v}{U_b} = \frac{U_b - U_s}{U_b} \tag{2.1}$$

Where U_s is the volume of solids of the sample. The porosity n is a dimensionless ratio, while also often represented as a percentage. The equation is valid for the total porosity, also called absolute porosity. As described above, a porous medium is composed of interconnected and unconnected voids. Therefore we must introduced a revised version of the aforementioned equation which takes into account the effective porosity n_e, defined as the ratio of interconnected voids, $(U_v)_e$, to the total volume of the medium:

$$n_e = \frac{(U_v)_e}{U_b} \; ; \; (U_v)_e + (U_v)_{n_e} = U_v \tag{2.2}$$

For this study, the mentioned porosity (laboratories measurement, triple weighing, and computed porosity) refers to the effective porosity.

2.3 Fluid flow

This section introduces and discusses mass conservation and momentum conservation within a dynamic fluid flow system, the principles of which are implied by Newton's second law.

2.3.1 Darcy flow and conservation of momentum

The Navier-Stokes equations represent the principle of mechanics for viscous fluids, and therefore cover gases and nearly every liquid flow through a medium. The velocity of any fluid Q (m^3/s) is proportional to the area A (m^2) of a porous media and to the pressure gradient $\frac{\partial P}{\partial x}$ or hydraulic head $\triangle h/L$ (Pa/m) and inversely proportional to the viscosity μ (Pa.s). Bear (1972) stated that the Navier-Stokes equations were not applicable in practice as they did not inform about the behaviour of the fluid pressures and velocities in the pores at the microscopic scale. Darcy law was later introduced as a macroscopic law which may be used on the scale of the porous medium and which linked pressure, velocity of the fluid, and forces in play. Whitaker (1986) related the law formulated by Darcy to the equations of fluid mechanics and validated Darcy law as a form of the conservation of momentum equation that remains valid for laminar flow of viscous Newtonian fluids through a porous medium (Bear, 1972; De Marsily, 1986):

$$u = \frac{Q}{A} = -\frac{k}{\mu}(\nabla P + \rho g \nabla z) \tag{2.3}$$

Where u is the Darcy velocity (m/s). Frick et al. (1994a) offer a revised version of the Darcy velocity, by adding the rock porosity, leading to the pore velocity formula:

$$u = \frac{Q}{A \cdot \phi} \tag{2.4}$$

The equation 2.3 shows the two main drivers for a fluid displacement in a porous media: the pressure gradient ∇P and the external gravity forces $\rho g \nabla z$. Here, k is introduced as the intrinsic permeability of the porous media (m^2). As described in chapter 3, the gravity term g can be removed from this equation as the design of our experimental set-up injects the fluid from the bottom of the sample, while the fluid exits at its top. Therefore ∇z becomes largely inferior to

∇P (i.e. horizontally bedded aquifer or laboratory conditions - Bear (1972)). The laboratory conditions being limited by definition, De Marsily (1986) showed that equation 2.5 suggested, but did not prove, that a flow Q of an incompressible fluid through a sectional area A subjected to a pressure gradient ∇P or $\frac{\partial P}{\partial x}$ respected the following form:

$$Q = -A\frac{k\nabla P}{\mu} = -A\frac{k}{\mu}\frac{\partial p}{\partial x} \tag{2.5}$$

Where:

$$\nabla = \begin{bmatrix} \frac{\partial}{\partial x} \\ \frac{\partial}{\partial y} \\ \frac{\partial}{\partial z} \end{bmatrix} \; ; \; \frac{\partial}{\partial y} \; \& \; \frac{\partial}{\partial z} \approx 0 \tag{2.6}$$

With $\nabla P = \frac{\partial P}{\partial x} = (P_{in} - P_{out}/L)$, and P_{in} the downstream pressure (Pa/m), P_{out} the upstream pressure (Pa/m), and L the length of the sample (m). We can write the following equation which has been used during this study as a way to obtain the permeability evolution of rock samples over time (m^2):

$$Q = -A\frac{k \triangle P}{\mu L} \tag{2.7}$$

Darcy law remains valid for three-dimensional flow through a porous, fluid-saturated, and permeable media, provided there is a linear relationship between the fluid velocity and the differential pressure. The equation is applicable if it meets two criteria. The first validity check concerns the ratio between the average pore length l (m) of a flooded sample - later referred to as the characteristic length - and the length L of the core sample (m) (Whitaker, 1986):

$$\alpha = \frac{l}{L} \tag{2.8}$$

Where α is a dimensionless number that should remain largely below unity for each core experimentally flooded (Whitaker, 1986). The second condition requires

a small Reynold number (Re - Stokes (1851); Fourar et al. (2004)). The Reynold number is a dimensionless number that gives an indication of the behaviour of the fluid flow and its pattern in a medium, and is defined as (De Marsily, 1986; Fourar et al., 2004):

$$Re = \frac{\rho_{fluid} \cdot u \cdot l}{\mu} \tag{2.9}$$

Where ρ_{fluid} is the density of the injection fluid ($\sim 1,030$ kg/m^3), μ is the viscosity of the fluid ($\sim 5.45 \times 10^{-4}$ Pa.s for seawater at 60 °C), and u is the Darcy velocity of our injection fluid (m/s - equation 2.4). A small Re number describes a laminar behaviour, while it characterizes a turbulent regime at higher values. The threshold between laminar to turbulent flow regimes is not clear and is greatly dependent upon the pore arrangement and connectivity. Nevertheless, studies present a series of values partitioning laminar flow and turbulent regime for a homogeneous medium represented by packed spheres, which ranges from 1-10 (Fourar et al., 2004), to more than a hundred (De Marsily, 1986; Seguin et al., 1998). De Marsily (1986) stated that laminar flow was achieved when $Re < 2,000$.

2.3.2 Equation of mass balance

An equation of mass balance, or continuity equation, for fluid flow through a volume of porous media is based on the principle of mass conservation. It states that mass cannot be created or destroyed, and was popularized by Lavoisier in 1774. Its common and most simple form is given by De Marsily (1986):

$$\nabla(\rho u) + \frac{\partial \rho}{\partial t} = 0 \tag{2.10}$$

Where ρ represents the density of the fluid (kg/m^3), and t is the time (s). As highlighted by McCraw (2016), the equation states that the rate of change of mass within a given region is mathematically linked to the mass flux entering or

leaving this region. Our experimental scenarios were taken under steady-state conditions. Thus, the rate of change of the mass of seawater within a sample is negligible, leading to a 1:1 ratio between the mass of seawater entering and leaving the sample. McCraw (2016) also noted that dissolution of the rock matrix can lead to pore interconnection. Although the release of water trapped within a previously unconnected pore, as well as the mass of calcite dissolved during flooding could affect the mass flux, we did not take these values into account in this work as no data on the trapped water chemistry and/or volume has been gathered prior to the experiments.

2.3.3 Dissolution at the Darcy-scale

From the standpoint of fluid flow through carbonate rocks, one can expect chemical reactions to occur, leading to a further increase in the effective porosity and permeability, assuming that no precipitation occurs. The common effect of chemical dissolution due to fluid injection into a carbonate rock sample is called channelization, or wormholing (Hoefner and Fogler, 1988; Frick et al., 1994a; Fredd and Fogler, 1998; Golfier et al., 2002; Barri et al., 2016). This process generates preferential pathways that increase the fluid conductivity and allow the injection fluid to flow more easily (Fredd and Fogler, 1998). This process is often referred to as matrix stimulation (Barri et al., 2016). The main variables controlling and triggering the formation of preferential pathways are the pre-existing heterogeneities of the porous medium and the rate of dissolution of the flooded material (Hoefner and Fogler, 1988; Fredd and Fogler, 1998; Kalia and Balakotaiah, 2009; Izgec et al., 2010). The former implies that even two very similar and homogeneous samples might not respond exactly identically to the same experimental flooding conditions, while the latter is dependent upon a combination of factors implying rock-fluid interactions, injection rates, and the rock fabric.

Preferential pathways, in addition to the dissolution of the rock matrix, allow more fluid to flow through the sample. This leads to the formation of dominant channels which are usually associated with an increase in permeability, eventually leading to an increase in mass-transfer, which itself contributes to more dissolution (Golfier et al., 2002). The growth of a channel is influenced by different variables. Amongst them we can list the rate of the fluid which is injected into a rock, the nature of this fluid, the nature of the rock, the architecture of the rock, the permeability of the system, the stresses undertaken by the rock, and the fluid-to-mineral reaction kinetics (Hoefner and Fogler, 1988; Lucia, 1995; Mavko and Nur, 1997; Fredd and Fogler, 1998; Yale et al., 1998; Crawford et al., 2002; Panga et al., 2005; McDuff et al., 2010; Barilaro et al., 2012; García-del Cura et al., 2012).

Fredd and Fogler (1998) and Golfier et al. (2002) qualified the channelization process as injection rate and the fluid properties dependent, and described several dissolution-types:

- Compact dissolution (figure 2.1A): at low injection rates, the maximum dissolution is seen at the inlet flow face of the sample where the reactant fluid is mostly consumed, resulting in face dissolution. The system usually does not present a significant increase in permeability as the whole medium is not affected by the dissolution.

- Conical dissolution (figure 2.1B): At slightly higher injection rates, the reactant starts to enter the matrix and can enlarge pores allowing fluids to flow more easily. A significant amount of reactant is still consumed at the entrance of the sample and on the walls of the flow channel leading to the formation of conical-shaped wormholes.

- Dominant channel (figure 2.1C): at intermediate flow rates, the unconsumed reactant reaches the larger pores, leaving the small porosity untouched and leading to the formation of a dominant wormhole channel. The formation

of a dominant flow-path is considered as part of matrix stimulation as it effectively increases the permeability of the system.

- Ramified wormholes (figure 2.1D): at high flow rates, the flow channel becomes more ramified as the fluid is forced into smaller pore structures. The dissolution front spreads into as many heterogeneities as it can reach. A higher amount of material dissolution is expected.

- Uniform dissolution (figure 2.1E): this type of dissolution is rarely seen experimentally as it requires very high injection rates. This physical forcing allows the majority of the porosity to be reached by the injection fluid. The dissolution front is uniformly spread over the length of the core.

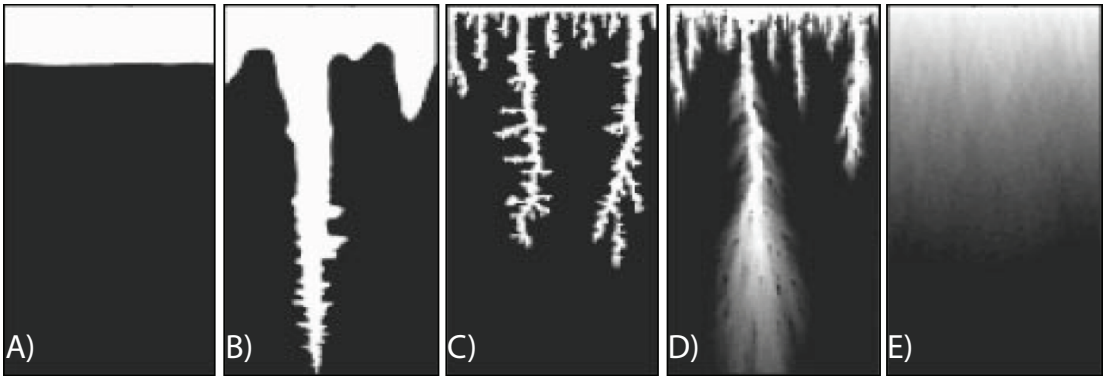

Figure 2.1: Experimental dissolution structures; A: compact dissolution; B) conical dissolution; C) Dominant channel; D) Ramified wormholes; E) Uniform dissolution. After Golfier et al. (2002).

Due to the high chemical reactivity of carbonate rocks (Ehrenberg and Nadeau, 2005), both porosity and permeability can be affected in different and unrelated ways. When relating both variables, studies observed a power law relationship (Luquot and Gouze, 2009; Handhal, 2016), while others described a linear relationship (Nelson et al., 1994). A poro-permeability relationship is rock-nature dependent (Saar and Manga, 1999), and also relates to other variables such as clay content, or presence of micro-structures. In this PhD, they were assumed

independent (Baechle et al., 2004), therefore the optimum matrix stimulation requires an increase of the permeability as well as an increase in porosity. For each experiment undertaken, the channelling type and the way it propagates can be described as a function of two dimensionless numbers, which are correlated to the injection rate, the acidity of the injected fluid and the way the rock reacts to it: the Damköhler number, and the Péclet number (Lasaga, 1984; Fredd and Fogler, 1998; Golfier et al., 2002). The Damköhler number defines the ratio of acid consumed and the acid transported by convection, while the Péclet number represents the ratio between the convective transfers over the diffusional transport (Golfier et al., 2002). The Damköhler number is controlled by the slowest process in place: if the characteristic time of the chemical reaction is short compared to the characteristic time of transport ($Da < 1$), then the process is mass-transfer limited. Inversely, if the hydrodynamic renewal of the reactive fluid is low ($Da > 1$) the reaction is controlled by the mass-transfer rate at the fluid-mineral interface and is called reaction-rate limited. Assuming a variable injection rate and a virtually infinite reaction rate, the Damköhler number can cross different families of dissolution patterns: at slow injection rates, the acid of the fluid is consumed on the walls of the core (compact dissolution), where at higher flow rates the acid penetrates deeper in the sample and the dissolution pattern should range from a conically shaped wormhole to a more tubular wormhole.

On the other hand, the Péclet number combines the diffusivity of a fluid (which is a function of the molecular diffusion and convective flow) and the injection rate, which represents the advective time scale. These numbers are mathematically different but imply similar ideas. Assuming a fixed diffusivity, the only way to vary the Péclet number is to increase the injection rate. From the standpoint of the injection rate only, the Damköhler number reacts by increasing the Péclet number: a compact dissolution results from a very low flow rate, followed by

a more conically shaped wormhole if the injection rate is increased. The final achievable stages are a tubular wormhole at intermediate flow rates and finally a uniform dissolution, driven either by very high flow rates (forcing the fluid to enter the entire porosity), or by a chemically aggressive fluid.

Several studies have worked on the Da number (Fredd et al., 1996; Fredd and Fogler, 1998; Golfier et al., 2002; Szymczak and Ladd, 2009; Menke et al., 2015). While different version of this number have been worked out by scientists (Alexeev et al., 2015), we used a classic version cited by most (Golfier et al., 2002; Menke et al., 2015; Ott and Oedai, 2015):

$$Da = \frac{kl}{u} \tag{2.11}$$

Where u is the Darcy velocity (cf. equation 2.4), and l the characteristic pore length. We have opted for a µCT imaging approach for computing the characteristic pore length. Per sample, we have taken ∼100 slices perpendicular to the radial axis of the core sample, and analysed them using the ICCR-Macropore (cf. chapter 3.3.2). For a sample, the chosen characteristic pore length corresponds to the average size of the pore-size distribution, based on the length of the major axis of the ellipse-shape of each pore (further described in chapter 3). Pore length values are further described in respective results chapters (4, 5, and 6). In equation 2.11, k is the reaction rate constant which is the kinetic action of the hydrogen protons at the calcite/water interface (m/s). Several studies present values for the reaction rate k (Compton et al., 1989; Wilkins et al., 2001; Morse and Arvidson, 2002; Bouchelaghem, 2010), but in order to remain as close as possible the rock-brine interaction encountered within the scope of this study, we have calculated our own reaction rate constant following the formula given by (Menke et al., 2015):

$$k = \frac{\pi \cdot r}{n \cdot l} \tag{2.12}$$

Where r is the dissolution rate (mol/m^2/s), and n the molecular mass of calcite (mol/m^3). The value for n can be solved using the following equation Menke et al. (2015):

$$n = \frac{\rho_{calcite} \cdot (1 - \phi)}{M_{calcite}} \tag{2.13}$$

For simplification purposes, we assumed that the samples used throughout this study to be purely made of calcite, with a density $\rho_{calcite}$ equal to 2710 kg/m^3, and $M_{calcite}$ the molecular mass of calcite (∼0.1 kg/mol). The values for n have been calculated for each sample used throughout this project and averages at 2.4×10^4 mol/m^3. Most studies are using dissolution rates corresponding to CO_2-water of HCl-water systems (Menke et al., 2015; Peng et al., 2015), while very few studies have calculated the reaction rate for pH neutral experimental flooding. Morse and Arvidson (2002) gave a value of 1×10^{-6} mol/m^2/s (in the presence of pure calcite at pH 3), where Pokrovsky et al. (2005) presented a reaction constant of 3.6×10^{-7} for pH 7-8 systems with 0 P_{CO_2}, which better represents our system.

The Pe number is rather consistently given under the same expression (Golfier et al., 2002; Egermann et al., 2006; Luquot and Gouze, 2009; Menke et al., 2015; Ott and Oedai, 2015):

$$Pe = \frac{ul}{D_{aq}} \tag{2.14}$$

Where D_{aq} the diffusivity constant (m^2/s). The diffusivity is a proportionality constant between the flux induced by a molecular diffusion and the gradient in the concentration of species. The aqueous diffusion coefficient for NaCl displays a value of 1.61×10^{-9} m^2/s (Robinson and Stokes, 1955).

Golfier et al. (2002) proposed a map of expected dissolution patterns based on the

Da and *Pe* numbers (figure 2.2 - the expected dissolution patterns are plotted in the respective results chapters).

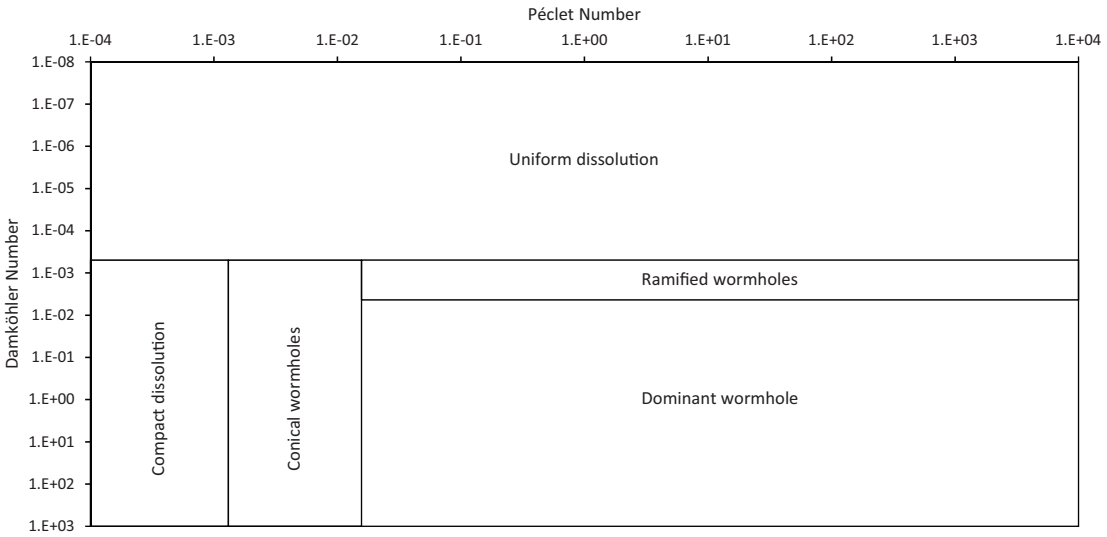

Figure 2.2: Example of dissolution map suggested by Golfier et al. (2002).

Boundaries on the map have been set by the authors and are representative of an acid/calcite setup (closer to a mass-transfer limited system), and were the results of qualitative observations. Golfier et al. (2002) used unsaturated NaCl injection fluid in a porous medium made of compacted salt grains. This setup was comparable to a limestone matrix stimulated using acid (mass-transfer limited) and displayed an acid capacity number (Nac) of 4.66×10^{-2}. The acid capacity number can be described by the amount of acid present in the pore space against the acid required to dissolve the accessible mineral. In order to calculate the Nac value of our injection fluid we need to solve the following equations (Daccord et al., 1993a):

$$N_{ac} = \frac{C \cdot M}{\beta(1-\phi)\rho} \tag{2.15}$$

With C the concentration of reactive fluid (mol/l), M the molecular mass, ϕ the porosity (-), and β the stoichiometric coefficient in the reaction:

$$fluid + mineral \longrightarrow products \tag{2.16}$$

The molecular mass is equal to 100.08 for $CaCO_3$, and the stoichiometric coefficient is equal to 1. We used a density of 2,300 kg/m^3 and a porosity of 7 % (0.07). The concentration of reactive fluid is given by the following equation:

$$[H^+] = \frac{pH}{\gamma} \tag{2.17}$$

Where γ is the activity coefficient for an ion. We have measured the pH of our injection fluid at ∼7 by using a Hanna instruments model HI 2210, at ∼20 °C (room temperature). The Debye-Hückel theory is a model that allows activity coefficients for a single ion to be calculated based on the effect the ionic interactions should have on free energy. Davies and Shedlovsky (1964) proposed the following equation to calculate γ:

$$-log\gamma = A_z^2 \left(\frac{I^{1/2}}{1 + I^{1/2}} - 0.2 \cdot I \right) \tag{2.18}$$

Where A is a constant related to the temperature and the dielectric constant of the solvent. A value of 0.51 for water at 25°C was given by Misra (2012). The coefficient z is the charge on the ion and is equal to 1, and I is the Ionic strength of the solution which expresses the concentration an electrolyte solution. The ionic strength is defined as:

$$I = 0.5 \sum_{n}^{1=1} c_i z_i^2 \tag{2.19}$$

Where c_i is the concentration of an ion in moles per litre and z_i its charge. The sum takes into consideration all the ions of the solution. Our injection solution was made of 0.52 mol/l of sodium (electric charge of 1) and 0.56 mol/l of chloride (electric charge of -1). Solving equation 2.19 gives a value of 0.54 mol/l. Solving equation 2.18 outputs $log\gamma = 0.16$, and therefore $\gamma = 10^{-0.16} = 0.69$. Equation

2.17 can now be solved. The expected concentration of protons for the injection fluid is $\frac{10^{-7}}{0.69} = 2.9 \times 10^{-7}$ mol/l. Knowing the concentration in protons, we can substitute it to equation 2.15, which gives a value of $Nac = 1.16 \times 10^{-5}$. Our result is three orders of magnitude lower than the Nac values given by Golfier et al. (2002). We are confident in this result as the injection fluid should not be more acidic than the distilled water was. Moreover, adding NaCl buffers the acidity of the solute. One implication of such a difference between the model-based Nac and the Nac of this work is that we should expect to work with shifted boundaries on the dissolution map presented by Golfier et al. (2002) (figure 2.2). These limits are supposedly not fixed and uncertainties are associated with the frontiers.

2.4 Injection and formation fluid properties

The reproducibility of the injection water was of prime importance as large quantities were injected during core flooding experiments, and to minimize the amount of biological contamination (Kester et al., 1967). Two artificial types of seawater have been prepared for our experimental purposes. The first one recreated the formation fluid of the Pre-salt rocks, whereas the other one was used as an injection fluid. The constraints for each fluids were as follows:

- The injection water should be chemically close to the one used by the industry during the injection phases.
- The formation water had to be as chemically equilibrated as possible with our core samples.

All fluids used in the experiments were analogues to the fluids involved during the EOR process within the fields of the Santos Basin, offshore Brazil. The chemical composition for each of the fluids has been provided by the sponsors, and each of these fluids was simplified for reproducibility and financial purposes. The formula

for the formation water is available in appendix A, while the injection fluid was composed of 30.5 g NaCl/l of distilled water.

2.4.1 Thermophysical properties of seawater

Described in the section 2.3, the laws of fluid motion explain that the physical properties of a fluid circulating through a porous medium play a role into the general behaviour of the system: temperature and pressure impact the viscosity, the density, or the phase of a fluid, and therefore impact its ability to be displaced through a core sample. This section focuses on the simplified seawater used as an injection fluid during the experiments.

2.4.2 Density

The fluid density (ρ) is defined as the mass of this fluid per unit volume (Bear, 1972). It usually varies accordingly with the pressure (P) and the temperature (T) of the system, so that:

$$\rho = \rho(P, T) \tag{2.20}$$

2.4.2.1 Effect of temperature

For simplifying the experimental preparation, a seawater density of 1,035 kg/m^3 (at 20 °C) was used during this study. Sharqawy et al. (2010) and Endoh and Suga (1999) have studied the thermophysical properties of seawater according to its NaCl concentration. Figures 2.3 and 2.4 present the expected density and phase of our injection water according to our experimental P-T conditions. The injection seawater was expected to remain within a single and liquid phase under the experimental reservoir condition, while the density should remain at ∼1,035 kg/m^3 ($P_c = 50$ MPa - $P_p = [10 - 40]$ MPa - T = 60 °C).

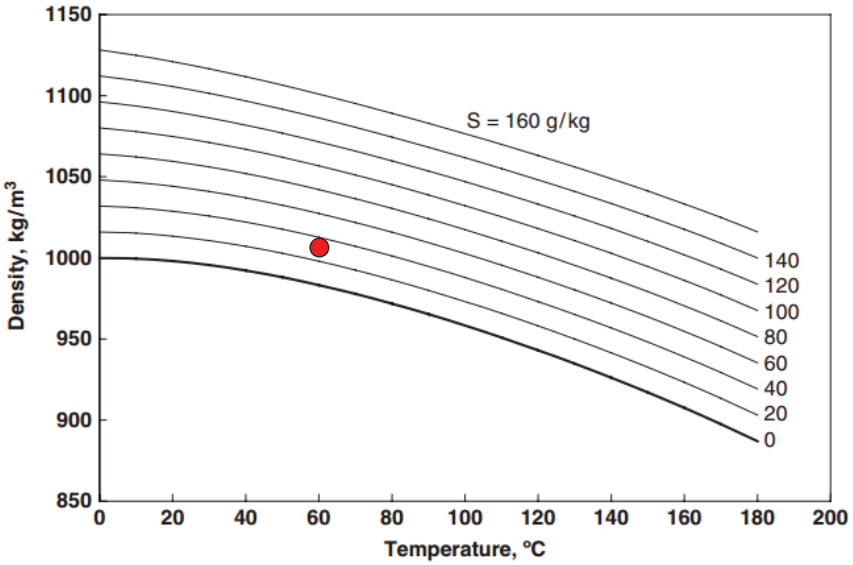

Figure 2.3: Density evolution of seawater as a function of the temperature. The red dot represents the experimental limits of this study. After Sharqawy et al. (2010).

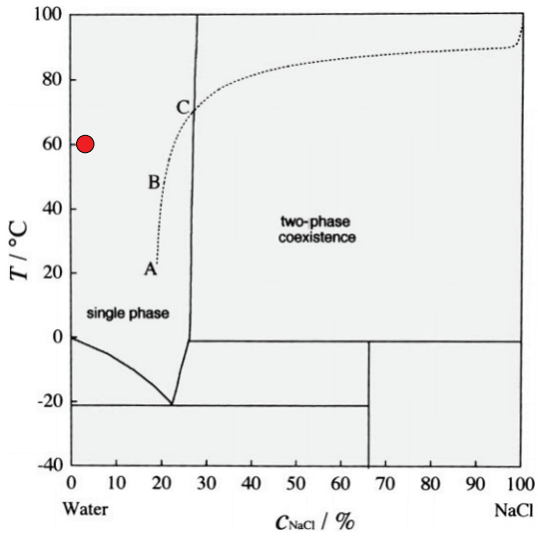

Figure 2.4: Phase diagram of temperature as a function of the concentration in NaCl. The red dot represents the experimental limits of this study. After Endoh and Suga (1999).

2.4.2.2 Effect of Pressure

Sharqawy et al. (2010) studied seawater at atmospheric pressure (0.1 MPa) while it is unspecified by Endoh and Suga (1999). While the phase diagram of pure water is well known and has been widely studied by many, it was complex to find similar work based on seawater. Jowitt et al. (2005) offered a P-T diagram for a 3.2 wt % NaCl seawater, comparable to the composition of the injection water in this study, the difference in weight between the two waters being ∼4.5 %. Figure 2.5 presents a phase diagram of seawater as a function of the pressure state.

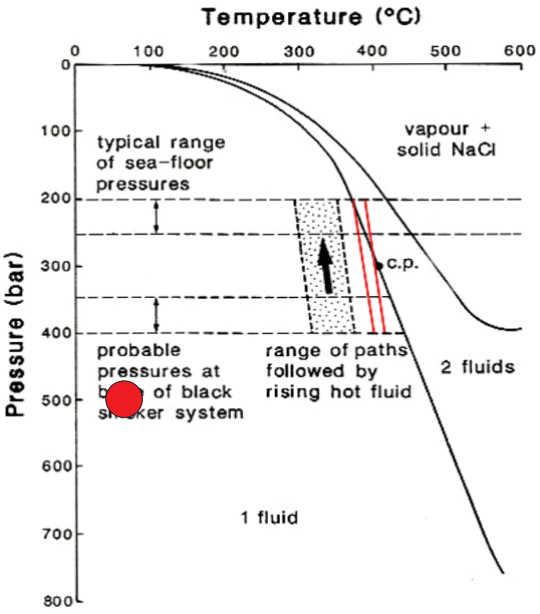

Figure 2.5: In-situ pressures as a function of temperature for seawater. The red dot represents the expected phase under a confining pressure of 50 MPa. After Jowitt et al. (2005).

2.4.3 Viscosity

Bear (1972) described a fluid as a material that continues to deform as long as a shear stress is applied. This is a referred to as continuum deformation, while the capacity of that fluid to resist any deformation is known as the viscosity. Through this study, we used two different scenarios of pressure state, while the

temperature was kept constant. Sawamura et al. (1992) studied the influence of pressure on the viscosity of seawater, and although their study did not cover the whole range of our experimental conditions (cf. table 1.1 in chapter 1), we used it as a reliable source which indicates that despite affecting the viscosity of seawater, the pressure should not induce significant changes under any of our experimental stress scenario (line pressure of 10 MPa to 40 MPa). Figure 2.6 shows the variation of viscosity of seawater at different concentrations (0, 0.5, 1, 2 and 3 mol/kg NaCl; approximately 0 g, 29 g, 58.5 g, 116.8 g, and 175.3 g NaCl per litre of water), and different temperatures (293.15 K and 323.15 K, respectively ∼25 °C and ∼50 °C). We observe that, while the viscosity seems to be affected at very high pressures (150 MPa and more), the expected operating pressures during our experiments results in negligible changes in the viscosity of the injection fluid.

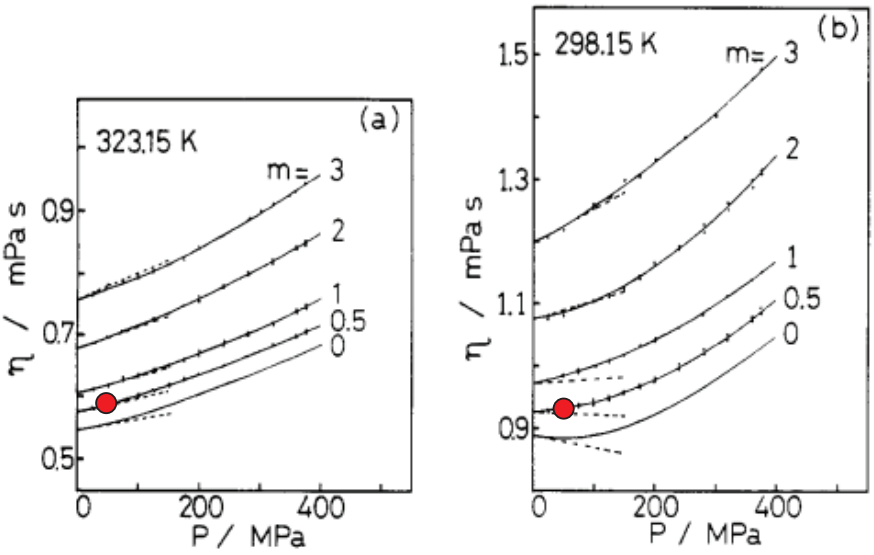

Figure 2.6: Viscosity of seawater as a function of pressure at two temperatures: a): 323.15 K; b): 298.15 K. After Sawamura et al. (1992).

Considering that the temperatures within the Hassler cell might change slightly (variations in temperature during the experiments given in figure 2.8), we have

implemented a function to account for the viscosity change of the injection fluid (figure 2.7). Isdale et al. (1972) proposed the following relationship, which describes the viscosity evolution of a water (cP) displaying a concentration of 30 g NaCl/l:

$$\mu = -0.482\ ln(T) + 2.4859 \tag{2.21}$$

Where μ the viscosity and T the temperature recorded by our sensor (°C).

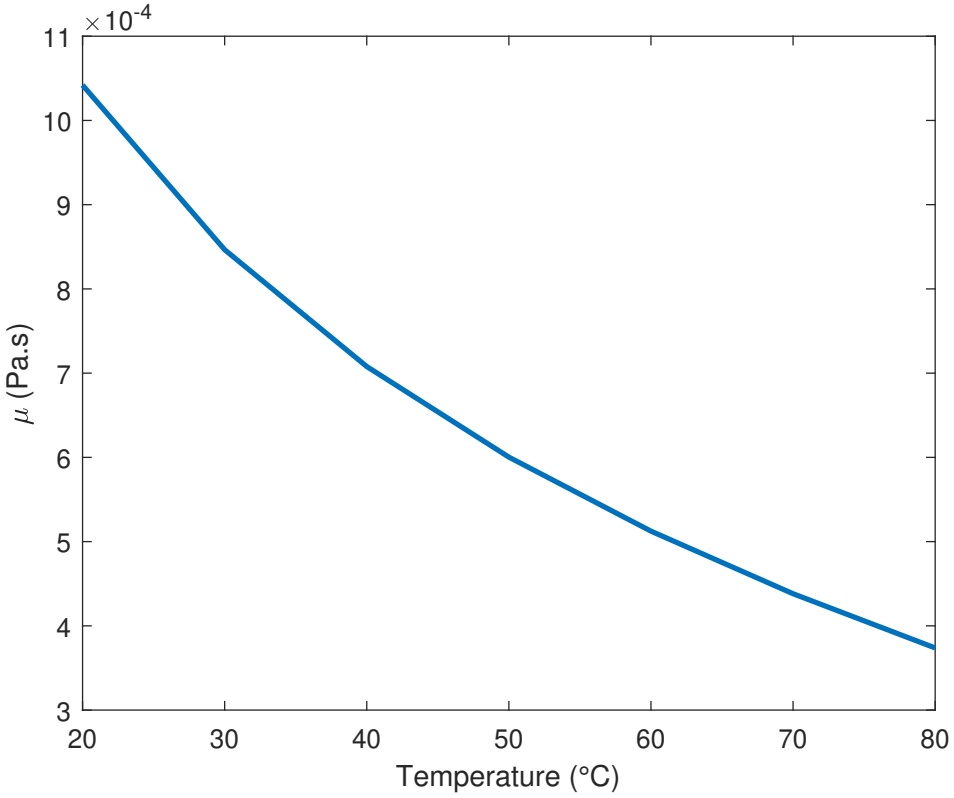

Figure 2.7: Viscosity of the seawater as a function of temperature. After Isdale et al. (1972).

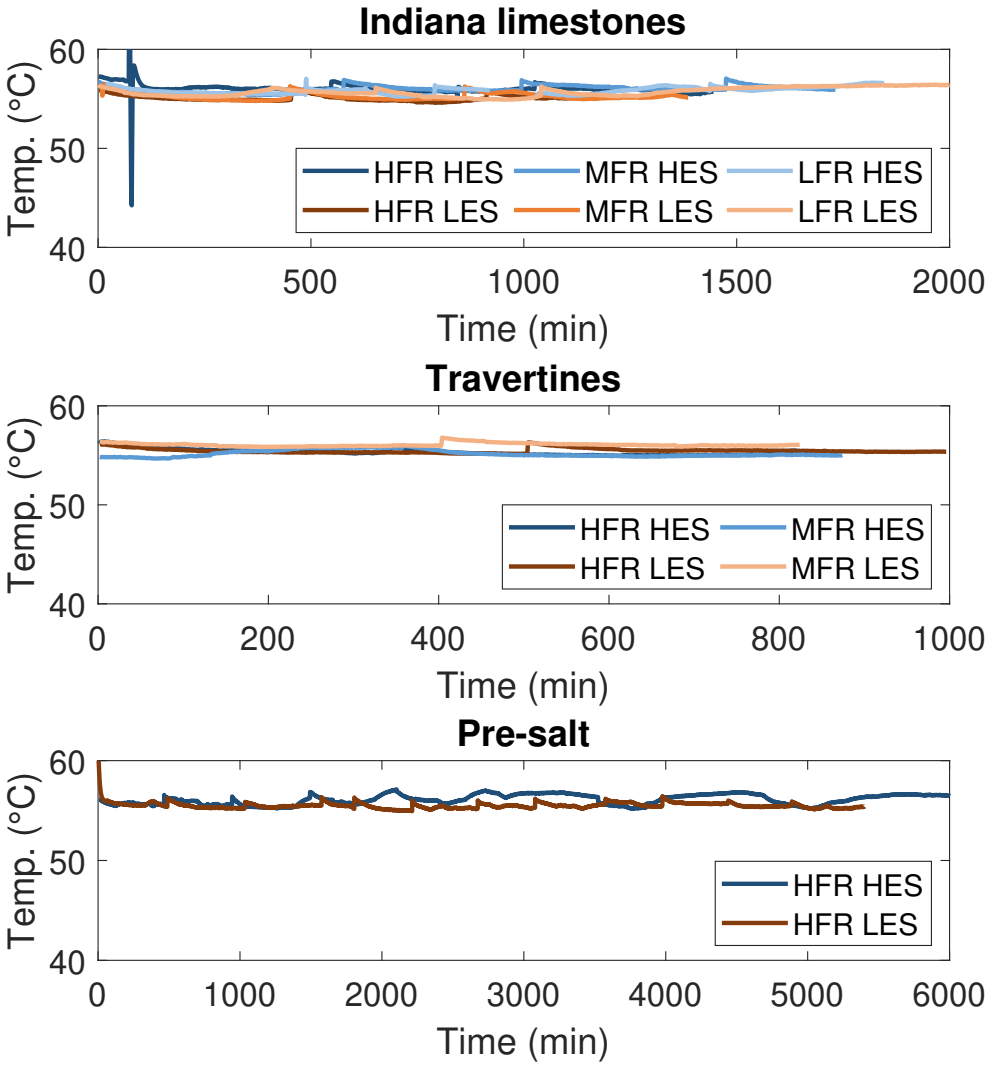

Figure 2.8: Variation of temperature of the Hassler cell throughout each experimental run. The temperature was set to 60 °C.

2.4.4 Comparison between nitrogen permeability measurements and seawater flooding measurements

The intrinsic permeability, often referred to as the permeability, is a controlling parameter of fluid flow through a porous medium. It is believed that permeability does not depend on the type of fluid flowing through the rock, as it is a measure of the ability for a fluid to move within a tortuous path, hence that variable should only be related to geometrical factors: pore shape, pore size, pore distribution, cementation, and tortuosity. The permeability calculation is of prime importance during core flooding experiments as it gives an important indication about the changes of the rock; i.e. how much a dynamic system affects the dissolution of the sample. Klinkenberg et al. (1941) discovered that a gas flow calculated permeability of any medium appears higher than the ones using a more vicious fluid, i.e. water in the case of this study. This effect, called 'slippage', represents the behaviour of a gas near the wall of a porous medium, which eventually influences its permeability: water displays an apparent zero velocity near the wall of a pore while gas displays a finite velocity at the same surface. Following Klinkenberg's work, Heid et al. (1950) demonstrated that in absence of any electro-kinetic reactions (eg. with the use of nitrogen) the difference in permeability between gas and water is generally the result of slippage of gas molecule at the rock walls. The outcome is an apparent higher permeability when measured using nitrogen rather than water.

Each sample of this study has been chosen based on a preliminary assessment of its permeability using nitrogen permeability calculations. This first permeability evaluation was used as a way to discard samples displaying a permeability higher than $\sim$15 mD, as higher values would have likely resulted in a free-flow through the samples, preventing from observing any permeability evolution during water flooding. The nitrogen calculations were not corrected for the Klinkenberg effect, and were expected to display a larger permeability than expected. Ziarani and

Aguilera (2012) showed a rather simple equation to calculate the Knudsen number (Kn), which is a dimensionless number that facilitates the classification of the flow regimes within the pores of a core sample:

$$Kn = \frac{\gamma}{r} \tag{2.22}$$

Where γ is the molecular mean free path (nm) and r the pore radius (nm). Using the ICCR-Macropore (cf. section 3) we obtain $r_{travertine} = 5.7 \times 10^5$ nm and $r_{Pre-salt} = 3.66 \times 10^5$ nm (with $r = \frac{l}{2}$, and l the averaged characteristic pore length of the rock core samples). Due to technical limitations, we have not been able to obtain a characteristic pore length through µCT analysis of the Indiana limestone scans. Freire-Gormaly et al. (2016) gave $l_{Indiana} = 5 \times 10^{-5}$ m, so $r_{Indiana} = 2.5 \times 10^4$ nm. We have used $\gamma = 177$ nm for nitrogen at 20 °C (Maurer et al., 2003). The equation 2.22 outputs the following:

- $Kn_{Indiana} = 7.1 \times 10^{-3}$
- $Kn_{travertine} = 9.2 \times 10^{-4}$
- $Kn_{Pre-salt} = 4.8 \times 10^{-4}$

Ziarani and Aguilera (2012) showed that Darcy law was applicable for $Kn < 0.01$, and a laminar flow was expected during a permeameter nitrogen calculation, implying that no correction should be required. As $\gamma \ll r$ for this study, we assumed that the Klinkenberg effect was minimal. If minimal or no correction was required for the nitrogen permeability, due to the slip effect of gas flow, a water flow measurement should display a smaller permeability. Ziarani and Aguilera (2012) have compared nitrogen and water permeability over different sandstone core samples, at the same effective stress. Results showed that the gas permeability was two to ten times larger than the water permeability. In this study a first assessment of rocks permeability has been done using nitrogen

permeability, while the syn-experiment permeability evolution has been calculated using water flooding and the Darcy equation.

2.5 Rocks description

This section presents the three different rocks studied in this project. The first type is an Indiana limestone that displayed a very high homogeneity in permeability and porosity. In this study, the Indiana limestone was used as an experimental baseline to be compared against more complex heterogeneous rocks. The second batch of samples used have been quarried from the Saturnia travertine formation (Italy), and represented an experimental analogue for the Pre-salt shrub framestone. Finally the last rock presented in this section is the shrub Pre-salt rock, which have been sampled from well cores. Figure 2.9 shows the scientific overlaps between the three rock types.

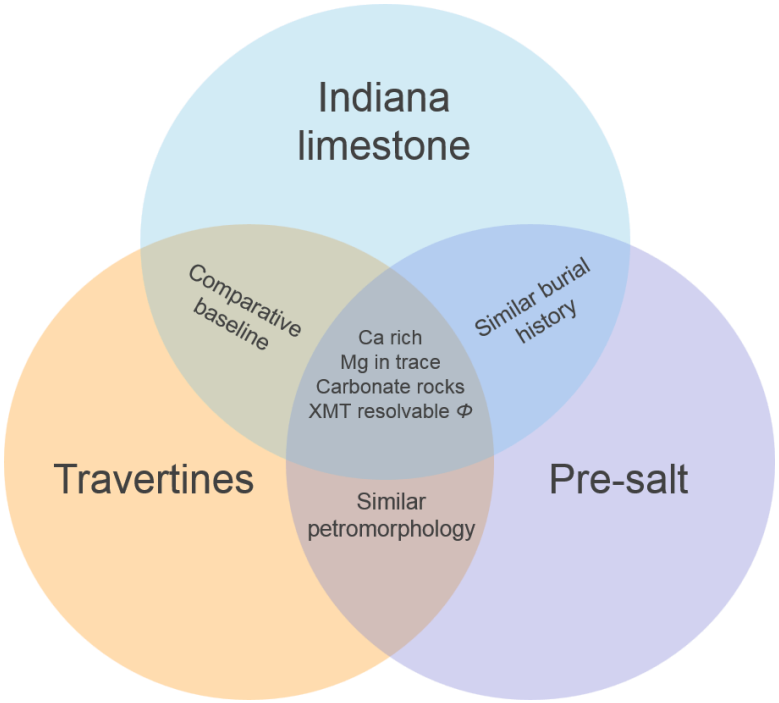

Figure 2.9: Definition of some scientific overlaps between the three rocks used throughout this study.

2.5.1 Travertine and travertine-like rocks

2.5.1.1 Presentation

This section describes the Saturnia travertines and the Pre-salt rocks that are studied in this project. The analogue samples (travertines) have been collected from large blocks of rocks quarried from an outcrop located in Italy (the Pleistocene Saturnia travertine – cf. figure 2.10) while the Pre-salt samples have been sampled from the Brazilian reservoir.

The terminology 'travertine' describes a deposit derived from calcite-rich hydrothermal waters or springs. There is no strict definition for a travertine rock, and authors are still debating over the terminology (Pentecost, 2005; Jones and Renaut, 2010). Some authors emphasize on the temperature of the depositional system, while others accentuate on the hydrological settings or the formation processes. One short and meaningful definition was given by Emig (1917): 'A travertine is the result of a deposition from water of springs or streams holding calcium bicarbonate in solution'. While this definition is lacking few elements, it accurately describes the geological context of travertine deposition.

2.5.1.2 Shrubs description and depositional settings

While no analogue fully corresponds to the Pre-salt shrub framestone (Erthal et al., 2017), modern day travertines and subsequent shrubs are considered excellent analogues for the Brazilian Pre-salt shrubs (Borghi et al., 2013; Ronchi and Cruciani, 2015; Schröder et al., 2016; Wright and Barnett, 2015; Claes et al., 2017; Erthal et al., 2017). Kitano (1963) first introduced the term shrub after studying Japanese travertine systems. Later, Chafetz and Folk (1984) described shrubs as short and shrubby crystalline masses of $CaCO_3$ that expand upwards by irregular branching.

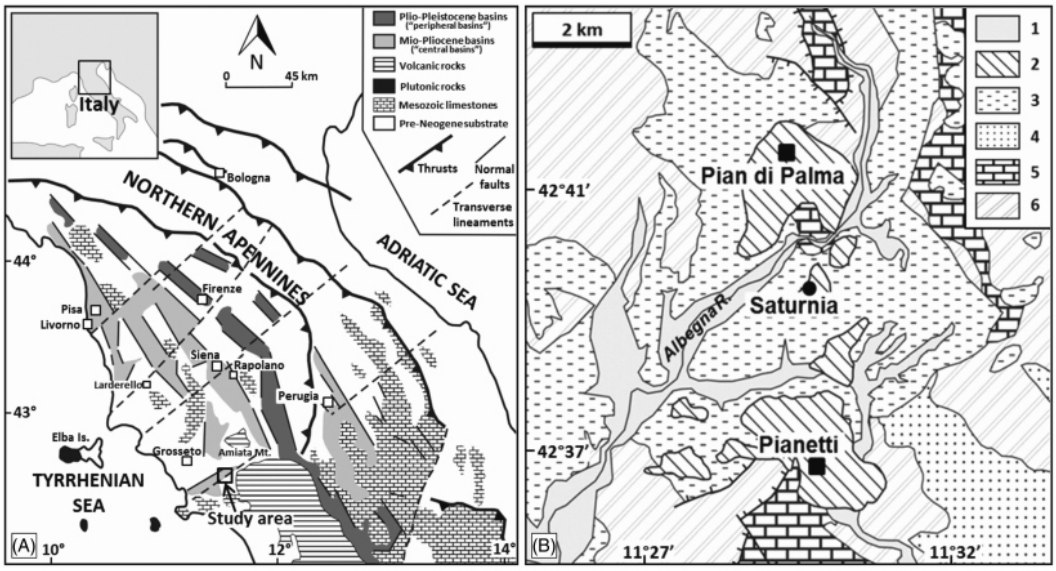

Figure 1. Study area. (A) Location map of the study area. Modified after Martini and Sagri (1993). (B) Schematic geological map of the Saturnia area with quarry location. After 1:10,0000 tectonic scheme of the Tuscany Region; (1) alluvial deposits; (2) travertine deposits; (3) Pliocene deposits; (4) Miocene deposits; (5) Tuscany domain; and (6) Ligurian domain.

Figure 2.10: Geological map or the sampling location of the experimental travertine core samples. The original legend has been kept for clearer comprehension of the sketch. After Ronchi and Cruciani (2015).

Shrubs usually form in shallow pools (Borghi et al., 2013) which are themselves located on the top of mounds of calcite (figure 2.11 - Chafetz and Guidry (1999); Kele et al. (2008); Ronchi and Cruciani (2015)). Chafetz and Guidry (1999) identified three types of shrub: bacterial, crystal, and ray crystal; respectively from a fully bacterial controlled formation process to a coupling between bacterial and abiotic processes.

Travertines are characterised by their rapid variation in texture (within millimetre to centimetres) whose apparent layering reflects the rapid and dynamic depositional system (Borghi et al., 2013; Virgone et al., 2013; Chitale et al., 2015). A layer height ranges from less than 1 cm to ∼4 cm, and can extend horizontally for several meters. A description of shrubs' facies morpho-types is

given in appendix D.

The thickness of the shrubs is a direct consequence of the amount of available calcium within the depositional pool. The typical dendritic growth pattern is not well understood yet, but is probably related to the high deposition rate and preferential growth of crystal aggregates on sharp protuberances (Pentecost, 1990). The orientation of the shrubs is an indicator of the depositional setting as they are always pointing upwards and perpendicular to their depositional surface (Kele et al., 2008; García-del Cura et al., 2012). Finally, García-del Cura et al. (2012) defined the shrubby travertines as a porous material (by opposition to the low porous micrite or the highly porous tufas). Their porosity is intercrystalline and is related to the growth framework (Pentecost, 2005; García-del Cura et al., 2012).

Figure 2.11: Contemporary example of travertine depositional system. After Ronchi and Cruciani (2015).

2.5.1.3 Theory of formation

The formation of travertines involves reactions between carbon dioxide and calcium bicarbonate solution leading to the precipitation of calcium carbonate in a lacustrine environment (Fouke et al., 2000; Pentecost, 2005; Terra et al., 2010; Borghi et al., 2013; Boyd et al., 2015; Chitale et al., 2015; Rezende and Pope,

2015; Wright and Barnett, 2015). Travertines are formed in thermal water (i.e. warmer than ambient temperature; Kele et al. (2008)). Due to its formation process, the physical and chemical signature of any travertine rock depends on variables such as the composition of the infiltrating solution, the migration path and depth, the residence time, the migration pathway, the rock/water interaction during the formation, the climatic conditions, the water level and its pH, and the overall salinity (Borghi et al., 2013; Boyd et al., 2015; Chitale et al., 2015). We should assume that even if a travertine rock does not chemically and physically widely differ from another, the experimental responses are not expected to be similar to the Pre-salt ones.

The processes responsible for the deposit of nearly all travertines on Earth is rather constant and does not widely vary depending on the location or age of the formation. Although there are differences amongst the type of travertines, the general process includes the degassing of surfacing carbon dioxide-rich groundwater containing more than 80 ppm of calcium per litre (Pentecost, 2005).

The first depositional reaction is represented by the reverse of the chemical equation 2.23. Carbon dioxide is lost from solution in contact with the atmosphere, whose CO_2 concentration is lower than the concentration of the underground solution. The Saturnia travertines are thought to be partially formed by this type of reaction:

$$Ca(OH)_2 + CO_2{}^{\uparrow} + H_2O \rightleftharpoons Ca^{2+}(aq) + 2\,(HCO_3)^- \tag{2.23}$$

The second type of depositional reaction is rarer (equation 2.24). It occurs between atmospheric carbon dioxide and hyperalkaline groundwater. The CO_2 is not provided by the ground but by the atmosphere:

$$Ca(OH)_2 + CO_2 + H_2O = CaCO_3(s) + H_2O \tag{2.24}$$

The third reaction is named groundwater alkalinisation and is observed when a calcium rich groundwater mixes with an alkaline surface water (equation 2.25). Hydroxyl ions in the lake react with HCO_3^- to form carbonates (CO_3^{2-}) followed by the precipitation of the calcium carbonate. This reaction corresponds to what could have occurred during the Pre-salt formation as it happens mainly within saline lakes with high OH^- concentrations. Because they are not formed due to a transfer of CO_2 from or to the atmosphere, they are not strictly travertines but travertine-like rocks.

$$Ca(HCO_3)_2 + OH^- = CaCO_3 + HCO_3^- + H_2O \tag{2.25}$$

The fourth and last process is called common ion effect. This reaction occurs when groundwater infiltrates evaporites, which leads to a saturation of the waters with gypsum or anhydrite. When reaching Ca-bicarbonate waters, the water becomes calcium-supersaturated and starts to precipitate. This precipitation takes place underground and, therefore, is not representative of the Pre-salt or the Saturnia travertine.

Pentecost (2005) divided the travertines in two main families: carbonates of meteogene origins or thermogene origins. Both terms define the origin of the CO_2 carrier:

- Meteogene: the carbon dioxide is of meteoric origin. Cold water springs are surrounded by carbonates or more rarely gypsum (Pentecost, 1994). Source waters can go deep underground, get heated up and surge back as hot springs (thermo-meteogene - Pentecost (1995)).

- Thermogene: although it can contain some meteoric CO_2, most of it is provided by thermal processes within the Earth's crust. The thermally generated CO_2 remains dissolved in the groundwater due to the considerable pressure, resulting in high CO_2 concentrations, capable of dissolving a large

amount of carbonate rocks. The waters surge as hot springs, and form hydrothermal circuits. The resulting system usually displays higher calcium concentrations than the meteogene one. Those systems are usually associated with volcanism and/or tectonic activities. The Saturnia travertines probably partially belong to that type of carbonates due to the tectonic and volcanic activities likely responsible of heating up the source water (Ronchi and Cruciani, 2015).

The Saturnia travertines are genetically linked to the faults which are migration pathways for groundwater. Carbon 13 analyses made on the Shrubby facies of the Saturnia region give credit to a mantle driven carbonation of the groundwater rather than an organic sourcing (Ronchi and Cruciani, 2015).

2.5.1.4 Depositional settings of Saturnia travertines

Ronchi and Cruciani (2015) published a review of the geological formation of the Saturnia travertines. Despite evidences of meteogenic traits, they are the results of tectonic and volcanic activities. The Italian set-up and the actual Mediterranean basin are geologically complex and related to the formation of the Thetis Ocean, followed by the late Cretaceous/early Miocene orogenic phase provoked by the collision between the African and the European continent, and finally by an extensional regime (late Miocene). The Pre-salt travertines have been formed during the break-up of Gondwana and the formation of the Atlantic Ocean: a series of alternation between compressional and extensional regimes created a set of faults and basins which have been alternatively filled up by fluvial, marine, and lacustrine deposits (Pliocene/Pleistocene).

2.5.1.5 Geological analysis

A travertine rock is composed by several different types of facies where each one displays a variable porosity. The porosity of the travertines is poorly sorted, with a wide range of pore diameter and shape in each facies. The porosity is spread

between centimetre large vugs to microporosity (which can be smaller than our µCT imaging resolution). On average, the porosity of the shrubs within the Saturnia travertines is < 10 %. Ronchi and Cruciani (2015) raised the question of a representative volume for studying a core sample. As we focused on the shrub framestone, our representative volume might be small, and easier to find. Due to the restricted growth length of the shrub framestone, each core has been sampled vertically so that the radial axis of our core sample was taken parallel to a shrub layer.

2.5.1.6 Presentation of the Pre-salt shrubs

Continental carbonate research became of major interest in the last decade due to the discovery of giant hydrocarbon reservoirs (Campos and Santos basins in south Atlantic - Erthal et al. (2017)). This project aims to study the shrub framestone found within the upper part of the Pre-salt (named 'sag' and of Aptian age - Chitale et al. (2015); Erthal et al. (2017)). Modern day Pre-salt rift-like systems are associated with great lakes, such as the Bonneville lake (east African rift – great lake system) which are considered analogues to the Brazilian Pre-salt lacustrine reservoirs formation (Borghi et al., 2013). The earliest formation, called Coquieros Formation, was deposited in an environment supplied by fresh to brackish water, and displays a large amount of bivalve's fossils (Chitale et al., 2015). This depositional setting was characterized by fan, deltaic, and lacustrine deposits (Rezende and Pope, 2015). The following depositional system, called Macabu, has been set in a restricted and highly saline system which allowed the formation of travertine-like rocks (Rezende and Pope, 2015), whose most common facies is represented by the shrub framestone (Chitale et al., 2015). Along with the common shrubs, the Macabu formation presents beds of stevensite and spherulite, deposited at depth (Alabi et al., 2014; Chitale et al., 2015). Alabi et al. (2014), Chitale et al. (2015), and Wright and Barnett (2015) described

the hydrodynamical and chemical context of the Pre-salt facies (from oldest to earliest):

- Laminates that contains ostracods and vertebrates have been produced by short-lived pluvial events causing expansion of the shallow lakes.
- Spherulites are the results of later evaporation of the pluvial events. They triggered Mg-silicate to precipitate and calcite nucleation to produce spherulites.
- Shrub-like rocks grew after the spherulite nucleation stopped. Calcite growth, less inhibited, produced shrub structures resembling those seen in today's travertines.
- Coquinas were deposited during a phase of rift, that provoked mixing of fresh and brackish waters into the depositional basins.

2.5.1.7 Travertine/Pre-salt comparison

Choquette and Pray (1970) and Barilaro et al. (2012) have split the porosity of travertine-like rocks into two large families:

- Fabric selective, also called depositional porosity (representative of most modern day travertines).
- Non-fabric selective, or secondary porosity (vuggy meteoric dissolution, fractures).

Pre-salt shrubs and current day analogues display some petromorphologic differences, mainly driven by the limited diagenetic evolution of the former. Only the Pre-salt shrub has witnessed an intense burial history which has created or enhanced the primary porosity through karstification (generation of porosity due to intense dissolution - Rezende and Pope (2015)), or hydrothermal activity (associated with faults and fractures - Borghi et al. (2013)). The

poro-permeability can also be negatively affected through dolomitization and compaction (calcite and silica occur as a replacement phase - Rezende and Pope (2015)). Pre-salt rocks also display an intermediate state which lies halfway between the poro-permeability alteration spectrum, and has been described as 'hybrid pore system' by Rezende and Pope (2015), which is not seen amongst modern day travertines. Hybrid pore systems can see their poro-permeability diagenetically enhanced or reduced (figure 2.12).

While sharing different geological histories, some petrological similarities between travertines and Pre-salt rocks can be highlighted: the common and wide variation of the poro-permeability testifies of a similar depositional system, whose complex petromorphology has been preserved throughout the diagenetic evolution of the Pre-salt shrubs (Rezende and Pope, 2015; Claes et al., 2017; Rochelle-Bates et al., 2018). Chitale et al. (2015) explained that the main difference between the modern travertines and the Pre-salt rocks relies on the diagenesis underwent by the Pre-salt largely overprinting the rock's chemistry and poro-permeability. Indeed, the rapid changes in textures and compositions are interpreted as an effect of the diagenesis, which is also responsible for a larger dissolution-dolomitization and silicification leading to a high degree of textural heterogeneity (micro to macro scale). These extreme petromorphological changes are not necessarily observed within the Saturnia travertines.

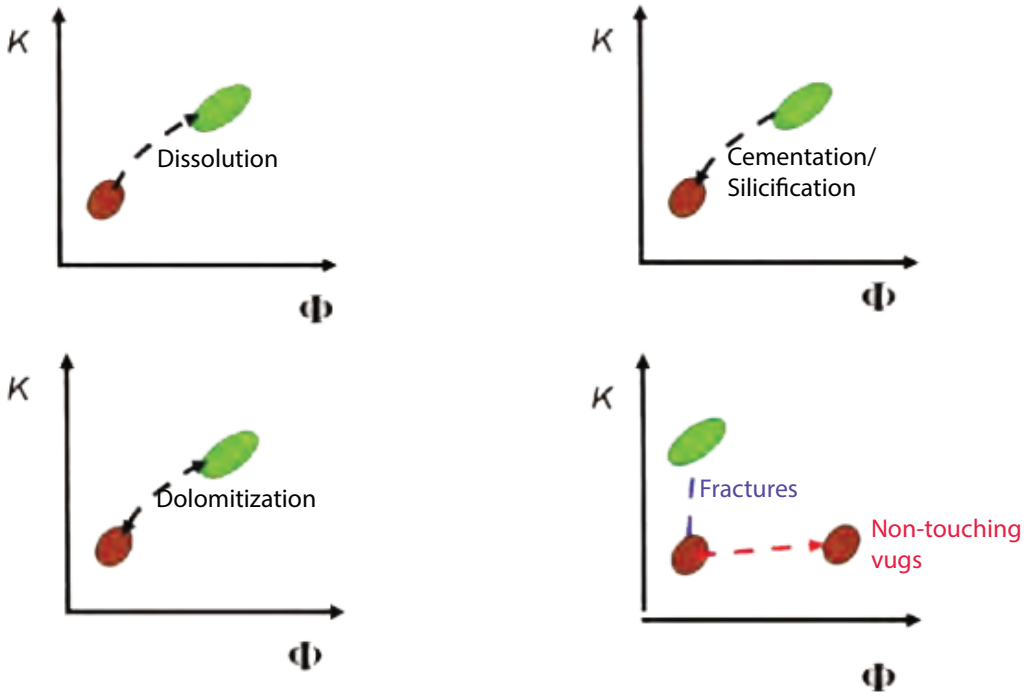

Figure 2.12: Illustration of porosity and permeability enhancement or reduction depending on the geological processes underwent by the rock. After Chitale et al. (2015).

2.5.1.8 Chemical composition of the shrub framestone

The calcium content of a travertine, whether they are of meteogene or thermogene origin, is rather high (on average $> 90\%$ $CaCO_3$ - cf. figure 2.13). The remaining constituents being trace elements. The main representative one is magnesium, and is found in the form of magnesium calcite, dolomite, or magnesium carbonate. Travertines are usually low-magnesian calcite (Chafetz and Folk, 1984; Pentecost, 2005; Kele et al., 2008; Erthal et al., 2017). Boyd et al. (2015) studied the Pre-salt travertines, and stated that they were mainly composed of limestone, dolomite, silica, and varying amount of Mg-rich clays (ex. Stevensite). For each rock experimentally flooded during this study, we have ran an XRD analysis, whose results are displayed in chapters 4, 5, and 6.

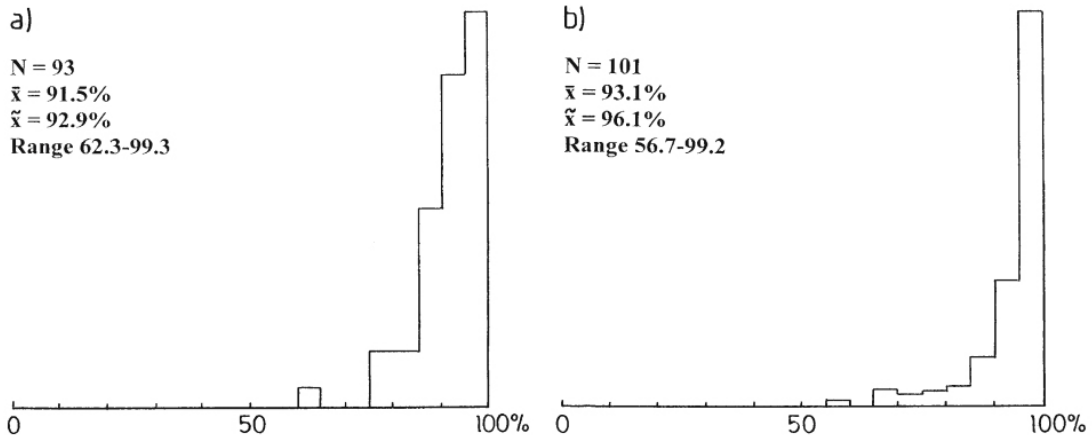

Figure 2.13: Calcium content for meteogene (a) and thermogene (b) deposits. After Pentecost (2005).

2.5.2 Indiana limestone

This section describes the Indiana limestone rocks which have been used as a comparative rock in this study.

2.5.2.1 General overview

The Indiana limestone deposit, also known as the Bedford or Salem limestone, is a geological formation located in Indiana, USA. Contrary to the travertines, they are highly homogeneous in permeability, porosity, and composition. The noticeable difference between the Indiana limestone and the Pre-salt and/or travertine shrubs lies in that the former is made of fossil organisms which provided the skeletal material (bryozoans, echinoderms, and endothyra – Seminar (1966); Smith (1966)). The most abundant fossil found in these formations are the bryozoans, followed by the echinoderms. Other species are present but are not quantitatively important (Smith, 1966). The thickness of the formation ranges from several centimetres (northern limits) to nearly a hundred meters (southern

limits). Folk (1959) described the limestone unit as a biomicrite and biosparite mainly made of sand-sized marine fossils.

2.5.2.2 Geology of the Indiana limestone

The onset of the deposit of the Indiana limestone unit (formally named Salem formation) is dated back to the middle Mississippian (Viséan - 346-330 Ma). The depositional setting involved shallow water environments, suggested by its horizontal and vertical irregularly distributed cross-bedded structures found throughout the record (Seminar (1966); Swann and Willman (1961) - cf. figure 2.14). The Illinois basin, directed northeast-southwest, is surrounded by the Ozark Dome (west), the Cincinnati Arch (east), and the Kankakee Arch on the northeast side (Seminar, 1966). The basin extends to Indiana state on its eastern margin, where the Indiana limestone is quarried (Brown et al., 1990). The initial bedrock is thought to have subsided, creating space for the further deposits. Black shales followed by siltstones are found prior to the Indiana limestone sequence, in the eastern and north-eastern parts of the Indiana basin. Central to this basin lies homogeneous and relatively pure carbonates of middle Mississippian age (Indiana limestone quarries). The late Mississippian displays layers of shales between larger beds of limestone and sandstone. There is little evidence that the calcite has been precipitated through chemical forcing (Baxter, 1960). Instead, the depositional history can be explained by the reworking of particles made of livings parts. A more detailed presentation of the stratigraphy of the Indiana formation is given in appendix C.

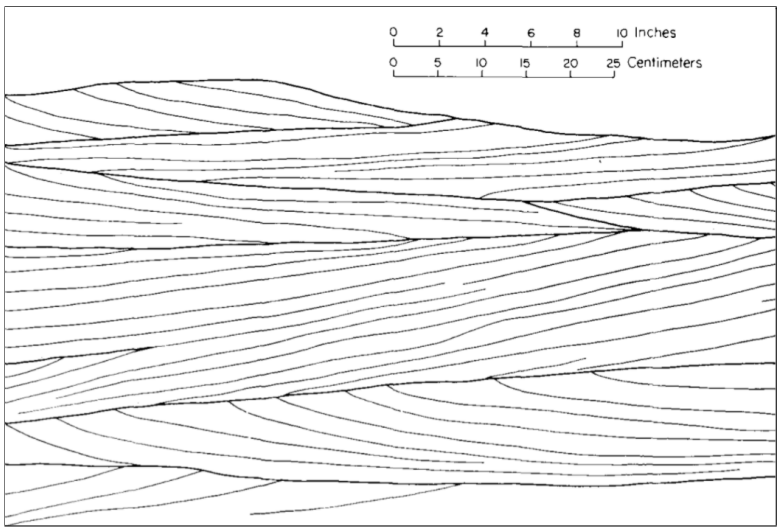

Figure 2.14: Cross-bedding interpretation of the Indiana limestone located on an open outcrop (Lawrence county, Indiana - GPS location unavailable). After Swann and Willman (1961).

2.5.2.3 Depositional system

Deposit of calcite units can be of eolian or marine origins. The records display skeletal micritic limestones, indicating that transporting currents were of marine origins rather than eolian in this setting (Seminar, 1966; Smith, 1966). Moreover, the important thickness of the unit (up to 100 m) is likely to be linked to a shallow marine environments (Seminar, 1966).

Analysis of the angles of the cross-bed deposits indicates a marine environment, as the usual eolian related deposits angles (i.e. dunes) ranges from 30° to 35°, whereas the ones present in the Indiana limestone display angles ranging from 10° to 25°. Usually, the nature of the cross-beds and their sizes indicates that most transport happened via small sand-waves, which also had a winnowing effect on the fossil particles (Seminar, 1966). This wave effect as also been recognized by Powell (2004) who described the bryozoans of this formation. Bryozoans used to live in quiet and low energy environments. The fact that they compose most

of the formation implies that they have been carried away form their original – quieter – habitat. Moreover the partially broken - but recognisable - nature of the parts, suggests that they were not living far from their depositional settings (Smith, 1966). The deposition rate of the Indiana limestone is thought to be rapid with an estimate of up to 35 cm/y of material deposited (Brown et al., 1990). A detailed petrological analysis of the Indiana formation is given in appendix B.

2.5.2.4 Chemical composition

The Indiana limestone is low in magnesium and high in calcium, with a low terrigenous content (Swann and Willman, 1961). Most chemical analysis shows a high $CaCO_3$ content (> 97 %) plus traces of $MgCO_3$. A detailed analysis of the chemical composition of the Indiana limestone is presented in table 4.2 (chapter 4).

2.6 Carbonate system and pH control

The pH of most of waters (including seawater) is controlled by chemical reactions involving carbonate systems such as calcite. Calcite is one of the most commonly precipitated minerals at the surface of the Earth, and as such, contributes the most to carbonate geochemical data. When exposed to a solution which is under-saturated with respect to $CaCO_3$ relative to their host mineralogy (eg. rainwater), carbonate rocks undergo surface dissolution. The rate of calcite dissolution decreases as temperature increases (Panthi, 2003; Pokrovsky et al., 2009; Coto et al., 2012) (figure 2.15), while the saturation index becomes lower at higher temperature. Calcite under-saturation is inversely linked to temperature and likely thermodynamically controlled (Garcia-Rios et al., 2014). Dissolution of $CaCO_3$ dissolves under the following reaction:

$$CaCO_3(s) \rightleftharpoons {Ca_2}^{+} + {CO_3}^{2-} \tag{2.26}$$

Followed by the hydrolysis of the carbonate ion, which produces HCO_3^-:

$$CO_3^{2-} + H_2O \rightleftharpoons HCO_3^- + OH^- \tag{2.27}$$

The hydrolysis of the carbonate ion generates alkalinity which reacts with, and increases the acid-buffering capacity of the reactant solution. Therefore, carbonate dissolution via increased $CaCO_3$ solubility leads to the generation of carbonate ions and elevates the pH. The injection fluid used in this project is a slightly low salinity artificial seawater (~30 g/l NaCl dissolved into distilled water). Sodium chloride is a base compound falling at the centre of the pH spectrum: dissolution of NaCl increases the pH in an acidic solvent, and decreases it if introduced into a basic solvent. Coto et al. (2012) demonstrated that while NaCl has no major impact on the pH of a solute, it does influence the solubility of calcium carbonate (figure 2.16). Coto et al. (2012) established that 1.25 mol/l NaCl (~ 73.0 g/l) represents the optimum concentration for $CaCO_3$ solubility.

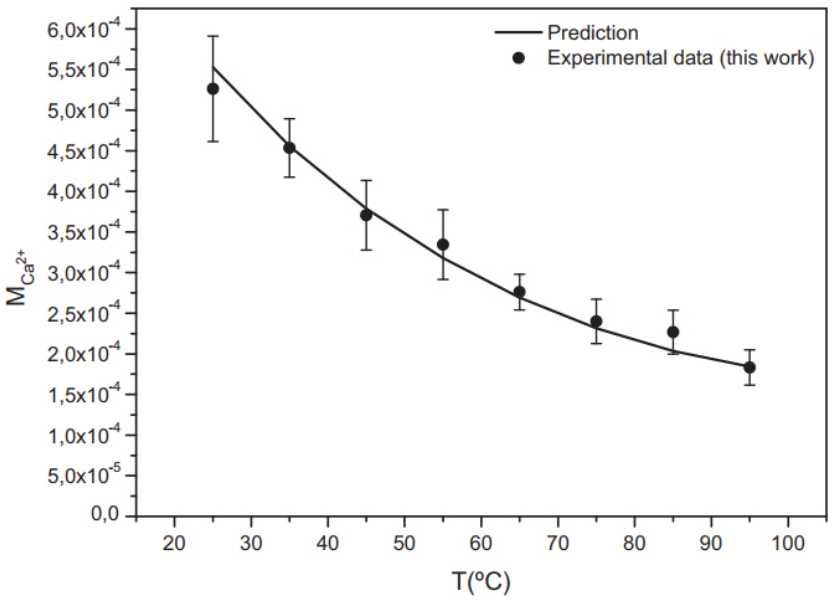

Figure 2.15: Calcium dissolution as a function of temperature. In this figure, the experimental work refers to the work of Coto et al. (2012). After Coto et al. (2012).

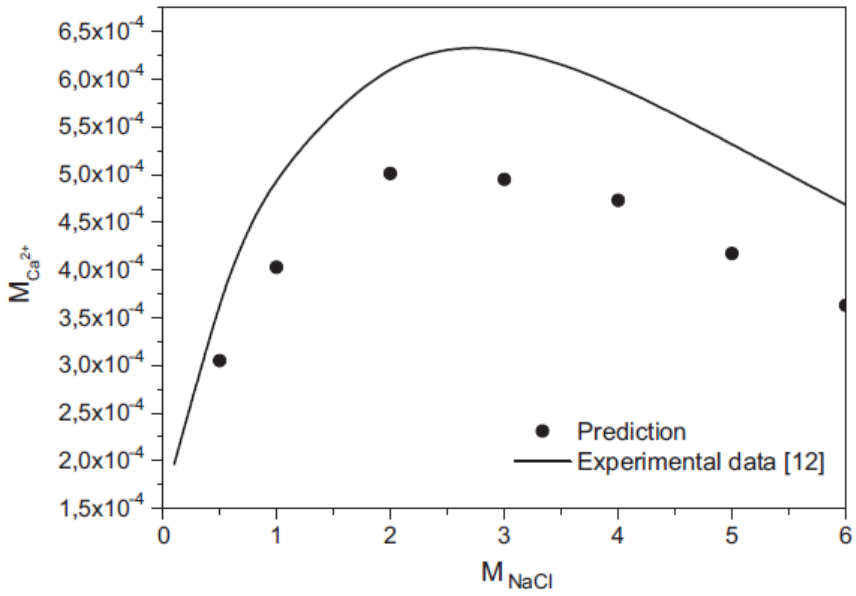

Figure 2.16: Influence of NaCl concentration on $CaCO_3$ solubility at 25°C. An average seawater contains ∼0.5 mol/l of NaCl. In this figure, the experimental work refers to the work of Millero et al. (1984). After Coto et al. (2012).

The pH of our solute should reach higher values after passing through a carbonate rock sample due to the absence of external CO_2. The pH value can exceed 8.2 for a water-calcium carbonate system. This correspond to the dissolution process of carbonates in a gas free solution with virtually no head space, where the partial pressure of air or any other gas is zero. We can assume that pH of the solvent should not be affected through the use of an injection fluid displaying a slightly lower salinity than the average oceanic seawater. In theory, a plug of pure calcite plunged into distilled water of pH 7 should not induce any chemical reaction and should be left intact due to the absence of CO_2. However, some carbonate ions combine with H_2O to form HCO_3^- (equation 2.28) which eventually leads to more calcium carbonate dissolution. Bicarbonate molecules further react to make carbonic acid, freeing more OH^- making the solution more alkaline (equation 2.29):

$$CaCO_3 + H_2O = Ca^{2+} + HCO_3^- + OH^- \tag{2.28}$$

$$HCO_3^- + H_2O = H_2CO_3(aq) + OH^- \tag{2.29}$$

The convention is to refer to the dissolved carbon dioxide as carbonic acid (H_2CO_3). Carbonic acid forms and dissociates in the presence of bicarbonate ions and protons following:

$$H_2CO_3 \rightleftharpoons H^+ + HCO_3^- \tag{2.30}$$

For which the equilibrium constant can be formulated as follows:

$$K1 = \frac{[H^+][HCO_3^-]}{[H_2CO_3]} \tag{2.31}$$

So that:

$$\frac{[K1]}{[H^+]} = \frac{[HCO_3^-]}{[H_2CO_3]} \tag{2.32}$$

Bicarbonate ions form and dissociate as a protons and a carbonate ions:

$$HCO_3^- \rightleftharpoons H^+ + {CO_3}^{2-} \tag{2.33}$$

For which the equilibrium constant can be formulated as follows:

$$K2 = \frac{[H^+][{CO_3}^{2-}]}{[HCO_3^-]} \tag{2.34}$$

So that:

$$\frac{[K2]}{[H^+]} = \frac{[{CO_3}^{2-}]}{[HCO_3^-]} \tag{2.35}$$

The concentration of the three carbonate species is pH dependent, since the pH determines the amount of H^+ available, so that pH $= -log_{10}[H^+]$. Values of

$pK1$ and $pK2$ are given by Plummer and Busenberg (1982), with $pK = -log_{10}K$, $pK1 \approx 6.3$, and $pK2 \approx 10.3$ at 25 °C. These variables present the pH at which the concentration of one specie equilibrates with another. When $[HCO_3^-]$=$[H_2CO_3]$, we can note $\frac{[K1]}{[H^+]} = 1$, which leads to K1 = $[H^+]$. Therefore, pK1 = pH^+ = pH = 6.3. The same applies when $[CO_3^{2-}]$=$[HCO_3^-]$, which leads $\frac{[K2]}{[H^+]}$ to equal 1. This brings pK2 = pH^+ = pH = 10.3. Figure 2.17 is a representation of a Bjerrum plot that displays the carbonate species present in a fluid as a function of the pH of the solvent. We can easily observe an equilibrium of carbonate species at pH ∼6.3 and ∼10.3.

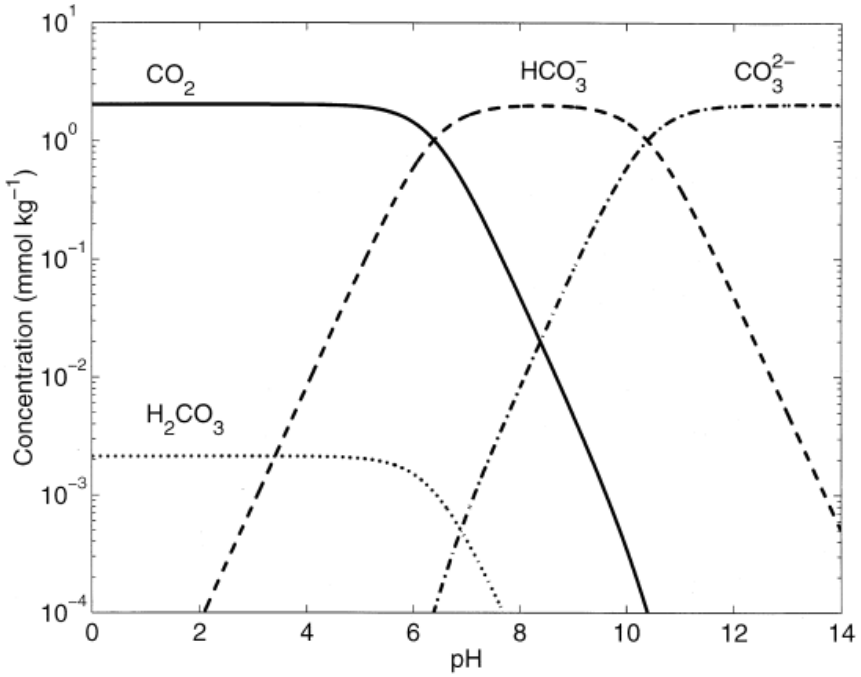

Figure 2.17: Bjerrum plot displaying the activities of three carbon species as a function of pH. After Zeebe (1999).

Garcia-Rios et al. (2014) explained that in the case of calcite flooding, dissolution occurs exclusively at the first rock-brine contact if strong acids is used, which should increase the pH of the exiting fluid, and stabilizes at 7, limiting further dissolution. Inversely, using a weak acid should keep a constant - lower than 7 - pH, which enhances dissolution at a slower rate. Some carbonic acid might

eventually escape the dissolved phase to form a gas, producing carbon dioxide vapour pressure, or P_{CO_2}. Partial pressure of carbon dioxide plays a major role in calcium carbonate dissolution. Our current rig design implies that the injection pump draws the artificial seawater from a container which replaces the exiting fluid by the surrounding air. This partially air-filled tank can lead to acidification of the injection fluid as the CO_2 naturally present in the air partially dissolves in the water. The amount of dissolved CO_2 depends on the pressure and temperature of the tank, which equals the laboratory's P-T conditions ($P \approx 0.1$ MPa and $T \approx 20 - 25$°C). We approximated the pH of our injection water following Henry's law, which describes the amount of dissolved gas proportional to its partial pressure. Atmospheric CO_2 reaches values of ∼400 ppm (0.04% of the total atmospheric composition), therefore:

$$P_{CO_2} = \frac{0.04}{100} \cdot 1\ Atm = 4 \times 10^{-4}\ Atm \tag{2.36}$$

And:

$$K_{CO_2} = 3.3 \times 10^{-2}\ mol/l \cdot Atm \tag{2.37}$$

The expected concentration of CO_2 is:

$$[CO_2(aq)] = K_{CO2} \cdot P_{CO2} = 3.3 \times 10^{-2} \cdot 4 \times 10^{-4} = 1.32 \times 10^{-5}\ mol/l \tag{2.38}$$

Where $[CO_2(aq)] = [H_2CO_3]$. The first acidity constant is given by:

$$K1 = \frac{[H^+][HCO_3^-]}{[H_2CO_3]} = 4.47 \times 10^{-7}\ mol/l \tag{2.39}$$

CO_2 naturally dissolves into water following:

$$CO_2(g) = H_2O(l) = HCO_3^-(aq) + H^+(aq) \tag{2.40}$$

As the concentration of protons and bicarbonate ions in solution is equal, we can simplify the system:

$$K1 = \frac{[H^+]^2}{[CO_2(aq)]} \tag{2.41}$$

Therefore:

$$[H^+] = \sqrt{K1 \cdot [CO_2(aq)]} \tag{2.42}$$

By solving equation 2.42 we obtain a value of $[H^+]$ equal to 2.4×10^{-6} mol/l. The expected pH for our injection water is mathematically ~ 5.6. In reality, due to the buffering effect of the NaCl on the pH, the pH of our injection fluid varied between 6.5 and 7. Referring to the Bjerrum plot, we injected a quasi-perfect mixture of carbonic acid and bicarbonate. Pokrovsky et al. (2009) and Garcia-Rios et al. (2014) developed on the effect of P_{CO_2} in a H_2O-CO_2 system: partial pressure of CO_2 has been found to be of second importance compared to the direct effect of the pH and the amount of HCO_3^- and H_2CO_3 present in the fluid. The decrease in pH observed in system with P_{CO_2} was mainly due to the pH decrease followed by CO_2 dissolution in water as an effect of H_2CO_3. As a weak acid, H_2CO_3 acts as a pH-buffer and allowed to maintain a circumneutral low pH over a longer period of transitional time, as opposed to a strong acid. If the same system was displaying a similar P_{CO_2} but was maintained at neutral pH, we could expect a decrease in the rate of dissolution.

2.7 Mechanical behaviour of a carbonate rock

2.7.1 Forces in play

A force F is a physical vector which quantifies, when unopposed, the energy necessary to change the motion of an object. It is expressed in Newtons (N) of dimension kg.m.s^{-2}, and results from the product of mass m (kg) and acceleration

a (m.s^{-2}): $F = ma$. The direction of the vector F is dictated by the direction of the vector acceleration, a. Any volume V of mass m accelerates in the direction of the Earth's gravity following $m = V\rho$. Therefore, a one meter large cube of limestone displays an average mass of 2,700 kg, which corresponds to a density (ρ) of 2,700 kg/m^3.

Stress, denoted σ and given in pascal (Pa), is defined as a force applied per surface area (dimension analysis of F/A). Depending on the field of study, a pressure applied perpendicular to a plane is defined as positive in a compressive environment, and negative in a tensile one. Stress applied around a solid core sample results in elastic (reversible) or plastic (irreversible) deformation, and is known as strain ϵ (dimensionless) which in 2D is the ratio of the change in length, following the compression related deformation, $\triangle L$, such as $\epsilon = \triangle L/L$.

The stress/strain relationship is linear for most intact rocks, and is expressed by the Hooke's law as $\sigma = E\epsilon$, where E is the Young's modulus, a constant describing the elasticity of a rock. High E implies high stiffness, hence low deformability. Usual values for limestone varies between 15 GPa to 55 GPa. Indiana limestones are given a Young's modulus of ∼30 GPa (Hart and Wang, 1995) whereas travertines display a Young's modulus ranging from ∼ 35 to ∼ 45 GPa (Yagiz, 2009).

Figure 2.18 shows the three different stresses applied around a core sample during an experiment. Our experimental rig was composed of a triaxial cell (type Hassler cell; cf. chapter 3) which applies a controlled confining pressure P_c or σ_c distributed around a core sample through the use of a rubber sleeve which contributes equally to $\sigma 1$ and $\sigma 2$. The pore-fluid was introduced through small holes in the stainless steel end–pieces that were fixed at the core's ends (Coyner, 1984). Assuming the radial strain negligible in this study, the differential stress

($\sigma 1 - \sigma 3$) was not calculated as the cell did not permit to control the axial load besides the stress induced by the fluid pressure acting on the axial platens, added to the potential rock deformation by the action of confining pressure around the sample.

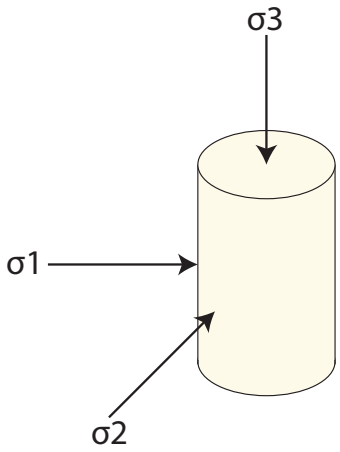

Figure 2.18: Main stresses acting on the core sample. $\sigma 1 = \sigma 2$.

A sedimentary rock undergoes different stress regimes through its depositional history. Mechanical compaction starts immediately after deposition and is driven by the effective stress. The modern idea of effective stress in a fluid-saturated porous media has been introduced by Terzaghi (1951) after his experimental studies on the uniaxial consolidation of fully saturated samples. Terzaghi stated that the main control on this property was the difference between the overburden compaction or lithostatic pressure (or confining stress) and the pore pressure (or fluid pressure):

$$\sigma' = \sigma_c - P_p \tag{2.43}$$

Where σ' refers to the effective stress, σ_c describes the confining pressure (also referred to as P_c), and P_p the pore fluid pressure acting against the walls of the voidage of the rock. This equation remains valid for fluid-saturated sample and does not require any further modification as our experimental set-up does

not include the injection or production of gas through the sample. Moreover, this simple equation has been described as sufficiently accurate for engineering purposes (Skempton, 1960).

The concept of effective stress is central for pressure-related studies as it allows, to a certain extent, to control the behaviour of a rock. Following Terzaghi (1951), Biot (1955) has introduced the coefficient n (equation 2.44), also called the pore pressure coefficient, the effective stress coefficient, or the Biot-Willis coefficient (Ghabezloo et al., 2009; Vasquez et al., 2009). In this case, the true effective stress is equal to the confining pressure minus n times the pore pressure, with n equal to 1 in Terzaghi's definition of a stress regime, which implies that the confining stress and the pore pressure have similar but inverse effect (Ghabezloo et al., 2009). The factor n should be constant for linearly elastic mediums, and is generally inferior or equal to 1 if grain compressibility is small (McCraw, 2016).

$$\sigma' = \sigma_c - n \cdot P_p \tag{2.44}$$

The coefficient n can be assessed by the following equation (Gurevich, 2004):

$$n = 1 - \frac{K}{K_s} \tag{2.45}$$

Where K is the bulk modulus of the rock and K_s is the bulk modulus of the solid grain (Pa). Values for K and K_s can be found for carbonates but despite an important literature review, no reliable value for K_s have been found for travertines.

A way to solve equations 2.44 and 2.45 is to proceed to an in-depth analysis of the two different rocks used in this study in order to find both moduli (cf. section 2.7.2).

2.7.2 Differential Effective Medium approximation

Differential Effective Medium approximation (DEM) is used to analytically describe a macroscopic medium by averaging the values that characterise it. It was first introduced by Norris (1985) whose work was based on Bruggeman (1935). The theory behind the DEM states that despite their apparent differences and disorder, two sets of rocks as contrasted in shape and structure as the Indiana limestones and the travertines, gather in fact some unifying statistical characteristics. A classic representation of a DEM solving for the characteristics of a medium is to virtually create a composite material from the properties of an initial and existing one by incrementally adding inclusions of a phase into the matrix one, through a series of iterations, and until the porosity of the last composite material matches the porosity of the studied rock (figure 2.19 - Cleary et al. (1980); Norris (1985); Zimmerman (1990)). The construction process and the properties of the composite material depend upon the construction path taken and not just the final result.

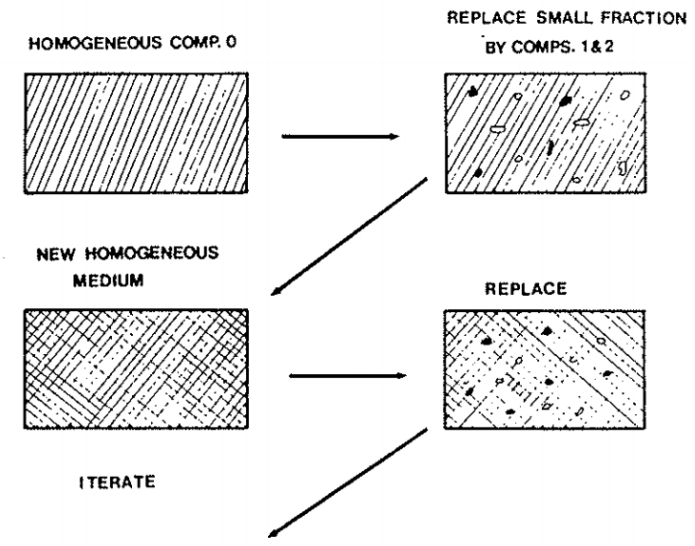

Figure 2.19: Iterative construction process of the composite medium. After Norris (1985).

The script used for solving for the DEM approximation is provided by the

University of Stanford and is called 'dem1' (Mavko et al., 2009). The model is fed with an initial material of known properties:

- Bulk and shear modulus of the background matrix.
- Bulk and shear modulus of the inclusion.
- The aspect ratio of the inclusions; fixed at 0.1, and by only taking the background porosity into account (Kumar and Han, 2005; Xu and Payne, 2009; Kittridge, 2015).
- The critical porosity.
- The porosity.

The bulk modulus of a medium (gas, fluid, or solid) represents the relative change in volume of this medium by unit of compressive stress; i.e. acting uniformly over its surface in the case of this study (figure 2.20). It defines how compressible, or resistant to the compression, a medium is. It is defined by the following formula:

$$K = -V\frac{dP}{dV} \tag{2.46}$$

Where K is the bulk modulus (Pa), P the applied pressure (Pa), V is the volume (m^3), and dP/dV is the derivative of the pressure with respect to the change in volume of the rock. We used the Voigt-Reuss-Hill average method to estimate the bulk moduli of both travertines and Indiana limestones (Mavko and Nur, 1997). Knowing the volume fractions and the constituent moduli, the Voigt-Reuss-Hill average method can provide us with a theoretical effective bulk modulus. For a given volume fraction of constituents, the effective modulus falls between the two bounds defined by the Voigt upper bound and the Reuss lower bound. The upper bound represents the modulus of a rock under uniaxial tension while the lower bound displays the bulk modulus values for a sample is loaded perpendicular to the rock fibres.

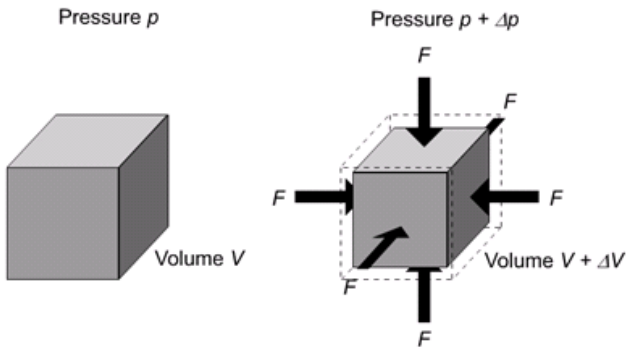

Figure 2.20: Interpretation of the bulk modulus: a force applied on the external sides of a cube of a certain composition triggers change in the cube's volume. Credit image: ESA (2009).

The Voigt-Reuss-Hill average method is a simple arithmetic average of the two boundaries (figure 2.21).

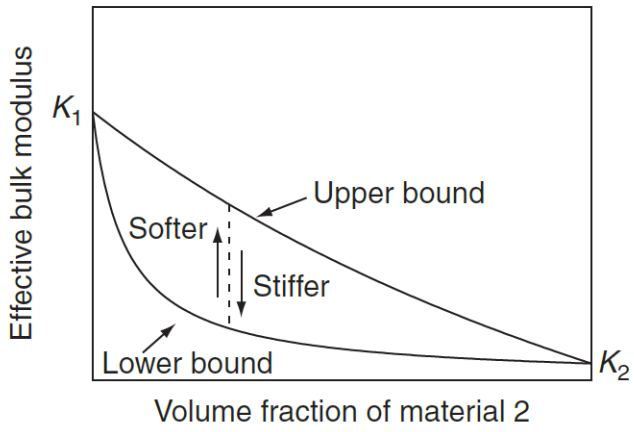

Figure 2.21: Effective bulk modulus calculation as a function of fraction of constituent of a medium. The bulk modulus should lie on the dotted line between the bounds (Mavko et al., 2009).

This averaging can be done with any moduli. In the case of this study we average the bulk and shear moduli by proceeding as follows:

$$Y_{VRH} = \frac{Y_v + Y_r}{2} \tag{2.47}$$

Where:

$$\begin{aligned} Y_v &= \sum_{i=1}^{n} fiYi \\ \frac{1}{Y_r} &= \sum_{i=1}^{n} \frac{fi}{Yi} \end{aligned} \tag{2.48}$$

And Yi and fi are the moduli (bulk or shear) and the volume fraction of the ith component of the rock. Values for the bulk moduli are summarized in table 2.1.

Species	(1)	(2)	(3)	(4)	(5)	(6)
	76.8	94.9	37	37.8	100.2	252.9
	63.7	69.4	36.6		154.1	
Values (GPa)	70.2	76.4	36.5			
	74.8		37.9			
	68.3					
Average Values (GPa)	**70.8**	**80.2**	**37**	**37.8**	**127.15**	**252.9**

Table 2.1: Values for the bulk modulus calculation; (1) calcite / (2) dolomite / (3) quartz / (5) hematite / (6) corundum: after Mavko et al. (2009); (4) Montmorillonite: after Mondol et al. (2008).

The Saturnia travertines are composed as follows (data collected from in-house XRD analysis and Pentecost (2005)):

- ∼99.6 % calcite.
- ∼0.4 % dolomite.
- Traces of quartz and montmorillonite (∼0.1 %).

The Indiana limestones are composed as follows (data collected from in-house XRD analysis and Churcher et al. (1991); Freire-Gormaly et al. (2016); Powell (2004)):

- ∼98 % calcite.
- ∼0.8 % quartz.
- ∼0.7 % alumina.
- Traces of iron oxide (∼0.1 %).

Finally, in-house XRD analyses of the Pre-salt samples used in this study show the following composition (the values have been averaged over the two samples):

- ∼17.5 % quartz.
- ∼65.5 % calcite.
- ∼17 % dolomite.

Therefore:

- $K_{voigt-Indiana} = 71.8 \times 10^9$ Pa.
- $K_{voigt-travertine} = 70.83 \times 10^9$ Pa.
- $K_{voigt-Pre-salt} = 66.48 \times 10^9$ Pa.
- $K_{reuss-Indiana} = 70.6 \times 10^9$ Pa.
- $K_{reuss-travertine} = 70.83 \times 10^9$ Pa.
- $K_{reuss-Pre-salt} = 62.1 \times 10^9$ Pa.

And:

- $K_{VRH-Indiana} = 71.3 \times 10^9$ Pa.
- $K_{VRH-travertines} = 70.83 \times 10^9$ Pa.
- $K_{VRH-Pre-salt} = 64.29 \times 10^9$ Pa.

The shear modulus describes the deformation caused by shear strain (figure 2.22). This value is intrinsic to the studied medium, and is described as follows:

$$G = \frac{F \cdot L}{A \cdot \triangle x} = \tau \frac{L}{\triangle x} \tag{2.49}$$

Where G is the shear modulus (Pa), F is the force (N), L the thickness of the medium (m), A the area (m^2), and $\triangle x$ the lateral displacement. The variable τ represents the shear stress and is given in Pascal. Values for the shear moduli are summarized in table 2.2.

Species	(1)	(2)	(3)	(4)	(5)	(6)
	32	45	44	17.1	95.2	162.1
	31.7	51.6	45		77.4	
Values (GPa)	29	49.7	45.6			
	30.6		44.3			
	28.4					
Average Values (GPa)	**30.3**	**48.8**	**44.7**	**17.1**	**86.3**	**162.1**

Table 2.2: Values for the shear modulus calculation; (1) calcite / (2) dolomite / (3) quartz / (5) hematite / (6) corundum: after Mavko et al. (2009); (4) Montmorillonite: after Mondol et al. (2008).

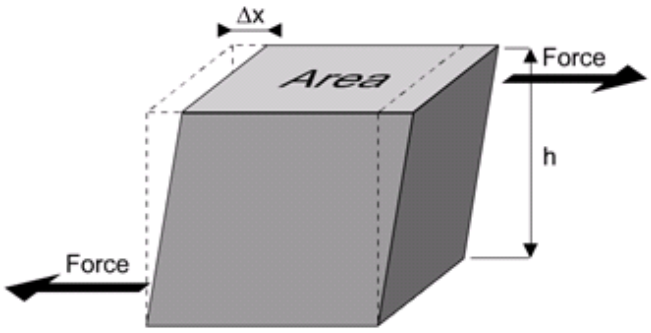

Figure 2.22: Interpretation of the shear modulus: a transverse force applied on the external sides of a cube of a certain composition undergoes a transverse deformation. Credit image: ESA (2009).

Therefore:

- $G_{voigt-Indiana} = 31.4 \times 10^9$ Pa.
- $G_{voigt-travertine} = 30.37 \times 10^9$ Pa.
- $G_{voigt-Pre-salt} = 35.96 \times 10^9$ Pa.
- $G_{reuss-Indiana} = 30.6 \times 10^9$ Pa.
- $G_{reuss-travertine} = 30.36 \times 10^9$ Pa.
- $G_{reuss-Pre-salt} = 34.46 \times 10^9$ Pa.

And:

- $G_{VRH-Indiana} = 30.9 \times 10^9$ Pa.
- $G_{VRH-travertines} = 30.36 \times 10^9$ Pa.
- $G_{VRH-Pre-salt} = 35.21 \times 10^9$ Pa.

Both bulk and shear moduli can be calculated by solving for the equations 2.47 and 2.48, or by running the 'bound' script (Mavko et al., 2009)).

The critical porosity, noted ϕ_c, is defined by Nur (1992) and Mavko and Nur (1997) as a threshold below which the mineral grains are load-bearing, and above which the rock 'falls apart' and forms a suspension. This concept is directly related to the effective porosity which is usually characterized by calculating the porosity of the flooded core sample by using the triple weighing method instead of a Nitrogen permeameter. Kittridge (2015) explained that the percolation porosity is not related to any pore shape parameter and considers this variable as the only adjustable parameter of the DEM approximation, and might be related to the geology and the texture of the rock. The current state of research does not provide any values for the rocks used in this study. Nevertheless, Mavko et al. (2009) provide values for calcite ($\phi_c = 0.4$), dolomite ($\phi_c = 0.6$) and quartz ($\phi_c = 0.4$). A simple weighting of the rocks composition is realised in order to calculate the percolation porosity:

- Indiana limestones weighted ϕ_c: $0.975 \cdot 0.4 + 0.012 \cdot 0.6 \approx 0.4$.
- Saturnia travertines weighted ϕ_c: $0.996 \cdot 0.4 + 0.02 \cdot 0.6 \approx 0.41$.
- Pre-salt weighted ϕ_c: $0.175 \cdot 0.4 + 0.17 \cdot 0.6 + 0.655 \cdot 0.4 \approx 0.43$.

The last variables are the bulk and shear modulus of the inclusion (seawater in the case of this simulation; respectively 2.34×10^9 Pa and 0 Pa), the pore aspect ratio (fixed at 0.15 - Kittridge (2015); Xu and Payne (2009)), and the porosity ϕ of the rock ($\phi_{Indiana} \approx 0.17$; $\phi_{travertine} \approx 0.15$; $\phi_{Pre-salt} \approx 0.12$). Having gathered all the parameters needed for running the 'dem1' script, we can solve for the bulk moduli and shear moduli. For this study we obtain:

- $K_{Indiana} = 8.07 \times 10^9$ Pa.
- $G_{Indiana} = 3.53 \times 10^9$ Pa.
- $K_{travertine} = 9.95 \times 10^9$ Pa.
- $G_{travertine} = 4.95 \times 10^9$ Pa.

- $K_{Pre-salt} = 1.44 \times 10^{10}$ Pa.
- $G_{Pre-salt} = 8.97 \times 10^{9}$ Pa.

Equation 2.45 can now be solved:

- $n_{Indiana} = 1 - (K_{Indiana}/K_{VRH-Indiana}) \approx 0.9$.
- $n_{travertine} = 1 - (K_{travertine}/K_{VRH-travertine}) \approx 0.85$.
- $n_{Pre-salt} = 1 - (K_{Pre-salt}/K_{VRH-Pre-salt}) \approx 0.8$.

Following Terzaghi's work on effective stress (Terzaghi, 1951), several studies stated that the coefficient n should be equal to one (Gardner et al., 1965; Zimmerman, 1990; Jaeger et al., 2009; Mavko et al., 2009). In reality this coefficient is dependent upon the mineralogy of the rock, the method used to solve for the moduli, and some approximations made in order to provide the parameters needed by the 'dem1' function (eg. 3D pore aspect ratio). As seen by equation 2.45, it is unlikely that the coefficient n should strictly equal unity, except if the rock frame is homogeneous and composed by only one solid material (Berryman, 1992). Gurevich (2004) supported the idea that, despite a lack of consensus around the effective stress coefficient, a value of one should be used for calculating an effective stress. Since $n_{travertine}$ and $n_{Indiana}$ display values relatively close to one, and relatively close to each others, this study uses the original Terzaghi's law of effective stress.

The above calculated bulk and shear values can be further used for assessing the pressure exerted on the flat ends of the samples once confined in the Hassler cell. The pressure applied around the rock should slightly deform the sample. The amount of deformation relates to the Poisson's ratio ν, expressed as follows (Birch, 1960; Mavko et al., 2009; Kittridge, 2015):

$$\nu = \frac{3K - 2G}{2(3K + G)} \tag{2.50}$$

Once solved, equation 2.50 displays $\nu_{Indiana} \approx 0.3$, $\nu_{travertine} \approx 0.29$ and $\nu_{Pre-salt} \approx 0.24$. These values are in accordance with the literature, which observes $0.28 < \nu_{Indiana} < 0.36$ (Hart and Wang, 1995), and $0.28 < \nu_{travertine} < 0.33$ (Soete et al., 2015).

In case of isotropic stress applied around a sample, $\sigma 3$ can be expressed as follows (Jaeger et al., 2009):

$$\sigma 3 = \nu(\sigma 1 + \sigma 2) \tag{2.51}$$

With $\sigma 1 = \sigma 2 = 50$ MPa (cf. figure 2.18), and assuming $\epsilon_3 = 0$. Solving equation 2.51 highlights the pressures exerted on the end platens of the Hassler cell during experimental flooding at constant P-T, with $\sigma 3_{Indiana} = 30$ MPa, $\sigma 3_{travertine} = 29$ MPa, and $\sigma 3_{Pre-salt} = 24$ MPa.

2.7.3 Mechanical impact on permeability

Assessing the permeability of a medium is of prime importance in many geological processes and crucial for engineering field work. This parameter can vary over several order of magnitude for the same type of rock. In-situ, the permeability of a rock is hard to evaluate due to local anisotropy amongst a field, such as fractures or layers of impermeable shale. Therefore, a core sample tested for its permeability in laboratory display values which might not be representative of a larger geological reservoir system.

Permeability is a physical quantity that relates to the pore structure and stress state (İşcan et al., 2006), which implies that while chemically similar, the pore structure of an Indiana limestone and a travertine sample, being genetically different, should observe variable permeability responses for an identical experimental scenario of P-T and injection rate. Permeability is dependent

upon the confining pressure and the pore pressure (Zoback and Byerlee, 1975). Understanding this coupling allows to better understand and weight how these variables affect the rock matrix during stress changes in a reservoir. For example, production of fluid from a field often reduces the pore pressure, leading to an increase in the effective stress state (İşcan et al., 2006). Al-Harthy et al. (1998b) stated that reservoir pore pressure decreases with the production of the fluids. Thus, there exists an increment in the effective stress of any engineered reservoir. This dependence between production of fluids and reservoir stress state is even more important at great depth where the pore pressure can have a significant impact on the hydraulic conductivity (Coyner, 1984). As a general rule, increasing the confining pressure decreases the permeability of a rock. Besides geomechanical plays, other external actions can lead to permeability alterations, such as thermal loading, or dissolution and precipitation of minerals during advective transport within the pore space (Selvadurai and Głowacki, 2008).

A set of experiments ran by Ghabezloo et al. (2009) determined the permeability on white limestones from Nîmes (France). Contrary to the experimental plan of this study, where the confining pressure is kept constant, their tests have been performed by varying eight times the confining pressure by 1 MPa steps, and at three different pore pressures during each confining pressure change. Their results showed an increase of the permeability when the confining pressure and the pore fluid pressure were low (figure 2.23), i.e. when the pore pressure is relatively high.

Vairogs et al. (1971) noticed that low permeability samples (< 0.1 mD) were more reactive to confining pressure changes, which appeared to be the controlling variable for permeability change. Effective stress and temperature are classified as secondary variables for permeability changes (Sun et al., 2016; Zhou et al., 2016). The experimental plan of Sun et al. (2016) was rather similar to the work undertaken in this study in that the confining pressure was kept constant, while only the

pore pressure was varied. The thermo-hydro-mechanical test was accomplished by varying the temperature several times. Results showed a correlation between permeability variations and effective stress and/or temperature variations.

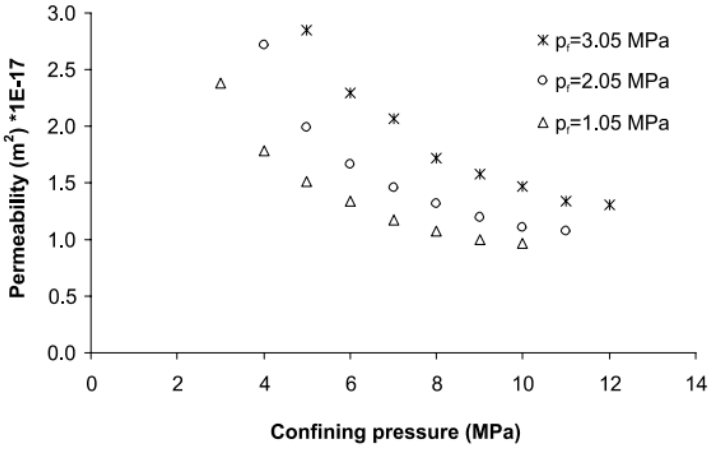

Figure 2.23: Permeability of limestones as a function of confining pressure. The general trend shows a diminution of the permeability as the confining stress is increased. After Ghabezloo et al. (2009).

2.7.4 Influence of the pressure-solution

Despite dissolution caused by pressure, or pressure solution, being a well known phenomena, there is no overall agreement on the best approach to model pressure solution. This is due to the fact that although detailed mathematical models can be put forwards, the key limiting factor is normally knowledge about the geometry of the system, which in this study is limited to homogeneous or heterogeneous. During compaction four different mechanisms are proposed leading to a reduction in volume of the material being compressed, that is stress corrosion causing the growth of sub-critical fractures, dissolution at the surface of contact, diffusion of the dissolved solid from the surface contact and precipitation. It is known in carbonate rocks that the main factors influencing carbonate pressure solution are stress, temperature, grain size, geometry, advective transfer, diffusive transfer and pore fluid composition. Pressure solution can be considered a dominant

mechanism by which a change in permeability can be achieved and elevated concentrations of species in the effluent could be obtained. A further problem is that in principle pressure solution is compacting two surfaces together, potentially reducing the permeability, but chemical solution is widening the gap between two surfaces, potentially enhancing the permeability. We attribute any dissolution to the widening of the space available for fluid flow, and attribute pressure solution to assisting the dissolution of the carbonate into the fluid and the increase in permeability. A comparison of the similarities and the key differences between the characteristics of pressure solution and chemical dissolution can be expressed as follows:

- Both pressure solution and chemical dissolution are kinetically controlled, as such both chemical dissolution and pressure solution are be impacted by the flow rate, which means practically that the higher the flow rate the more material should be removed.
- Both pressure solution and chemical dissolution are effected by temperature in a similar way.
- Only pressure dissolution is limited by a critical value stress value (cf. equation 2.52) under which pressure solution does not occur, or is at least extremely limited. Chemical dissolution is not limited by a critical value.
- Both pressure solution and chemical dissolution are controlled by the area of across which the process is operating. In chemical dissolution this area provides a face where dissolution is occurring. In pressure solution the contact area between two surfaces is critical providing local stress enhancement as well as delimiting the surface area over which pressure solution will occur.

The effective stress at the contacts between the grains can not exceed a certain critical value, discussed by Revil (1999); Polak et al. (2004). Where less stress than this occurs, no further pressure solution can happen. This is given by:

$$\sigma_{cr} = \frac{E_m \left(1 - \frac{T}{T_m}\right)}{4V_m} \tag{2.52}$$

Where σ_{cr} is the critical pressure solution (MPa), where E_m and T_m are the heat and temperature of fusion respectively (5.7 kJ mol^{-1} and 1603 K), T is the system temperature in kelvin (333 K) and V_m is the molar volume (4.61×10^{-5} m^3/mol). Solving for σ_{cr} suggests the limiting pressure can be calculated to be approximately 25 MPa. The range of the experimental work has been both below (LES experiments) and above (HES experiments) the theoretical critical value for pressure solution. Given the degree of uncertainties expressed it is difficult to deconvolute the pressure and chemical dissolution in any theoretically meaningful manner.

2.7.5 Pore fluid effect on a rock

As the rock undergoes burial, the pore space of the rocks is filled with a mixture of gradually pressurised fluids. These pore fluids interact with the rock and can affect it in two ways (Jaeger et al., 2009):

- Through mechanical alteration.
- Through chemical interactions.

A common way of representing the pore fluid pressure is by describing the pressure inside the pore space acting against the lithostatic pressure acting in the opposite direction. The more istotropic the rock is, the more istotropic the outward pressure should be. Both fluid pressure ($P_p = \rho_{fluid} \cdot g \cdot z$) and lithostatic pressure ($P_c = \rho_{rock} \cdot g \cdot z$) are lower than expected within the Pre-salt reservoir, due to a thick layer of salt of a lower density deposited on top of the carbonate rock. In such case, the pressures do not follow a linear trend, but can be calculated by integration:

$$P_c = \int_z \rho_{litho}(z) \cdot g \; dz \tag{2.53}$$

$$P_p = \int_z \rho_{fluid}(z) \cdot g \; dz \tag{2.54}$$

During this study, and respecting the in-situ conditions ($\rho_{litho} > \rho_{fluid}$), the pore pressure should never reach or exceed the confining pressure (Weijermars, 1997). A controlling parameter of pressure is called the coefficient of fluid pressure λ (Weijermars, 1997), and is the ratio of the pore pressure over the confining pressure:

$$\lambda = \frac{P_p}{P_c} \tag{2.55}$$

For in-situ wells, λ should be kept close to 1. Overcoming unity would lead to damaging the casing of a well. The same applies for this study, so that if $\lambda \geq 1$, our confining oil could contaminate the injection fluid. On the other hand a small fluid pressure relative to the confining pressure can trigger in-situ blow-outs and borehole crumbling. This situation should not be experimentally reproducible (Weijermars, 1997). Throughout this study, we used a constant $P_c = 50$ MPa, while two P_p scenarios were investigated ($P_p = 10$ MPa and 40 MPa), respectively referred to as the High Effective Stress scenario (HES), and the Low Effective Stress scenario (LES). HES displays a λ value of 0.2, while LES displays a λ value of 0.8.

Chapter 3

Material and Methods

3.1 Introduction

This section introduces the equipment, whether it was already in place or modified throughout this project, as well as the methods employed. Extensive work has been realized by Edlmann et al. (2013) and McCraw (2016) to develop, test, and deliver an experimental rig. Several updates and calibration have been done as part of this PhD in order to adapt the equipment to high pressure and constant temperature flooding. A large part of the modification undertaken by the author focuses on switching from a semi-manual rig, with several logging devices, to a remotely controlled solution, centralizing the displays as well as the logging system.

The second part of this chapter describes the numerical software developed during this PhD. Firstly, the ICCR-Macropore (section 3.3.2) has been developed as a pre-processor of the OpenGeoSys (OGS) software (Kolditz et al., 2012), as well as a 2D slice of rock analyser. A second software has been coded (section 3.3.3) and coupled with a neural network solution in order to study the predictability of zones of dissolution in vuggy carbonate samples (chapter 7).

Finally, this section ends by presenting the physical, chemical and µCT methodologies that have been used as part of the PhD work.

3.2 Laboratory development

3.2.1 Introduction

This section details the update of a pre-existing rig which was originally designed for two-phase flow. The working rig has been updated to meet the requirements of single phase brine flow through carbonate rocks, at high confining and line pressures, while efforts were put into updating the command and logging system. The early version of the rig was designed to allow multi-phase flow (CO_2-water) through 38 mm diameter cylindrical core samples at pre-selected temperature, while including a series of security valves, heating systems, and fluid mixer appliances (Edlmann et al., 2013; McCraw et al., 2013; McCraw, 2016).

Extensive work has been realized prior to this project in order to develop a functioning and stable flow rig which has been originally designed during the MUSTANG EU FP7 project (Edlmann et al., 2013), and further developed during the PhD project of McCraw (2016). This study re-uses the same Hassler cell, manual confining oil pump, fluid heater, back-pressure regulators, oven, and several pressure sensors placed along the line. We have simplified the rig by removing unused parts, while replacing damaged and/or outdated equipment:

- Due to the aggressive nature of the fluids used during early work, the entire stainless steel line has been replaced due to the presence of rust.
- Two of the proxies used for rock alterations were based on the permeability evolution during fluid flow, as well as the evolution of the calcium and magnesium present in the effluent fluid. Initial versions of the rig, during this study, did not include a differential pressure transducer. Darcy's

permeability during early experiments was based on the pressure difference calculated between two Omega sensors placed at the inlet and outlet of the core holder. This set-up produced inaccurate $\triangle P$ measurements, especially when the sample was showing a high initial permeability, or during a low flow rate experimental scenario. We have updated the rig with a differential pressure transducer, while keeping the Omega pressure sensors as controls.

- The injection pump used as an upstream pump at the initial stages of the rig (Edlmann et al., 2013; McCraw et al., 2013; McCraw, 2016) has been replaced by a programmable pump that meet the needs of this project (HPLC steady injection rate at high line pressure).

- A fluid sampling loop as been designed and installed at the outlet of the core holder.

3.2.2 Final design

The current experimental design is displayed in figure 3.1. It includes the Hassler cell which can hold a 3.8 cm core sample up to 8.5 cm in axial length, and can apply a radial confining pressure around the sample through the use of a mineral oil surrounding an elastomer sleeve. The injection system has been updated by installing a new pump (Teledyne CP-class constant pressure dual-headed piston pump) which has been chosen in order to meet the pressure, injection rate, and corrosion requirements (cf. section 3.2.3.5). A differential pressure transducer (Validyne P365D high line pressure) has been introduced with a membrane allowing a maximum differential pressure across the sample $\triangle P$ of $\sim$ 8 MPa, while rated to withstand a line pressure of $\sim$69 MPa (cf. section 3.2.3.2). The easy access to the parametrization and control of the pump and pressure-transducer through a LabVIEW-ready library of commands and DAQ acquisition system (cf. section 3.2.3.6) was one of the primary feature for the system upgrade.

A fluid loop allowing the sampling of the effluent fluid at desired interval of time has been designed and installed at the outlet of the rock core sample. The fluid sampling unit had to meet the following requirements:

- The pore pressure has to be preserved before and after a sample was taken out of the line.
- An experimental flooding should not be paused while sampling the fluid.
- The effluent fluid should be taken directly at the outlet of the Hassler cell, as opposed to be sourced from the back-pressure regulator, in order to avoid any mixing of the fluids within the cylinders of the back-pressure regulator.
- Each sample should not be contaminated by the previous one or contaminate the following one.
- A fluid sample should contain at least 5 cm^3 of brine.

Figure 3.2 shows a diagram of the sampling unit. The only limitation of this unit concerned the pore pressure which, even if kept high, was still slightly disturbed after a sample was taken. As such, we limited the amount of interaction with the experiment in order to have a clearer $\triangle P$ signal. The balance between fluid sampling and clean physical recording was directly dependent on the injection rate Q. This is attributed to the distilled water being introduced into the loop at atmospheric pressure (further described in figure 3.2). These 5 ml of under-pressured tubing were quickly be pressurized to the set pore pressure at high injection rate, while it could take up to one hour at lower rates to recover a stable pressure signal. The logging and controlling structures have also been updated by switching from an analogue-based logging apparatus and semi-manually-controlled system to a LabVIEW-controlled rig. This automation couples a National Instrument™ (NI) DAQ that collects the signals gathered by the different pieces of equipment (section 3.2.3.6) to a tailored software used for remote control, display, and pre-processing of the data (section 3.2.5).

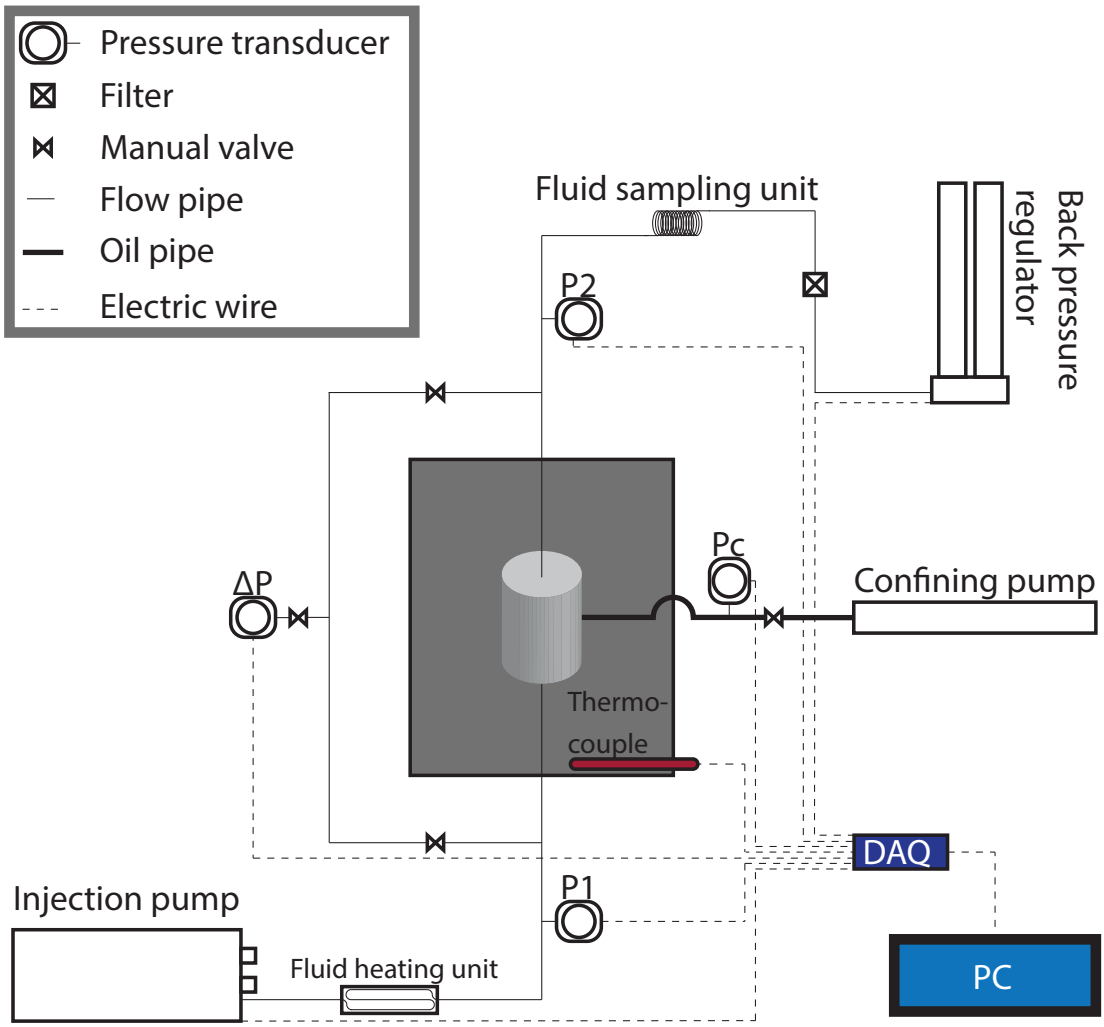

Figure 3.1: Experimental rig originally designed by Edlmann et al. (2013).

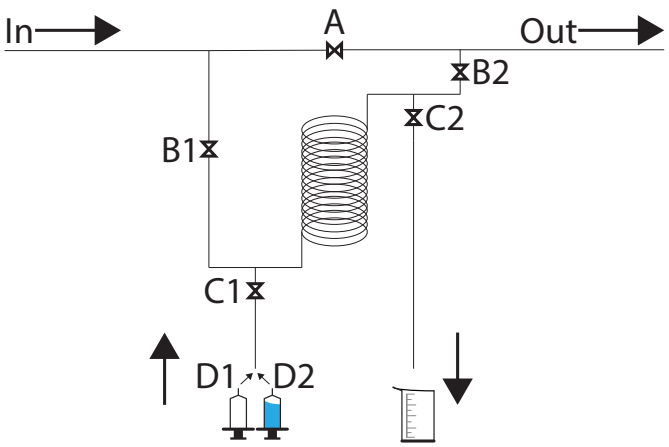

Figure 3.2: Schematic diagram of the sampling unit. During flooding, A, C1, and C2 are closed, while B1 and B2 are opened, allowing the injection brine to circulate through the loop. The sampling process involves isolating the loop while letting the experiment run at pressure: A is opened first, followed by the closing of B1 and B2. C1 and C2 are then opened. Air is pushed through the loop with a syringe (D1) in order to push the fluid out, followed by a cleaning and priming of the loop by re-injecting distilled water (D2). Finally, C1 and C2 are closed; B1 and B2 are opened before closing A.

The rig is rated to provide at least:

- 50 MPa radial confining pressure ($\sigma 2 = \sigma 3$).
- 40 MPa pore pressure.
- System temperature of 60 °C.
- $\triangle P$ of 5.5 MPa.
- Pulsation free injection rate from 0.01 cm^3/min up to 24 cm^3/min.

The actual design of the rig includes the following sensors:

- Pressures:

  - Upstream: injection pump sensor and Omega sensor.
  - Downstream: back-pressure sensor and Omega sensor.
  - Differential pressure transducer.
  - Confining pressure: Omega sensor.

- Temperature: probe.
- Fluid rate:
  - Upstream: injection pump sensor.
  - Downstream: back-pressure sensor.

3.2.3 Detail of the equipment

3.2.3.1 Pipework

The metallic frames used by McCraw (2016) as a structure for the rig have been re-used in this study. The stainless steel tubing and fittings have been replaced by Swagelock 1/8" (3.2 mm) outside diameter (OD) tubing (0.9 mm tube walls), rated to a pressure of 75.2 MPa (10,900 psi). The fittings are rated to withstand pressure up to 75.8 MPa (11,000 psi). A number of valves have been replaced before and during the experimental work due to leaks and normal wear of the material. We have installed Top Industrie stainless steel needle valves (910.10.0), which have the advantage of being smaller than similar Swagelock products, while being rated to hold a pressure of 69 MPa (10,000 psi).

3.2.3.2 Pressure sensors

A total of four in-line pressure sensors were present along the rig. Three of the four pressure sensors were Omega General Purpose 100 millivolt output pressure sensors (PX302). They were used for measuring the inlet line pressure, the outlet line pressure, and the confining oil pressure. These sensors are rated to provide

accurate pressure reading within the range of 0 to 68.9 MPa (0-10,000 psi; 0.25 % accuracy; ± 25 psi or 0.17 MPa). The output voltage is gathered by the NI DAQ and converted to digital values with a millivolt to pressure conversion. Due to inaccurate measurements at low injection rates, the values gathered by the two sensors have been used as controls only. these inaccuracies were mainly due to the uncoupling between both sensors as well as the impossibility to obtain a perfect pressure calibration between them. Therefore, and at low $\triangle P$, the downstream pressure sensors could read a pressure higher than the upstream one, leading to erroneous permeability calculations. A fourth pressure sensor has been installed, under the form of a differential pressure transducer. The P365 high line pressure transducer has been chosen as it is a fully customizable product (original part number: P365D4K2XXW8A; explained below), with the possibility of replacing the pressure membrane in case of over-pressuring or experimental matrix evolution. Moreover, the pressure transducer is NI DAQ compatible. Due to technical issues related to the LabVIEW software (cf. section 3.2.5) and the back-pressure regulator (cf. chapter 9), several membranes have been damaged and replaced. Table 3.1 shows the membranes used for each experiments presented in this thesis, and the associated error. The part numbers have been meticulously selected so that the final design of the transducer meets our experimental requirements:

- 4: electrical connector for direct plug into the NI DAQ digital modules.
- K: kalrez O-rings were the safest option for a seawater saturated environment.
- 2: calibrated output option. In our case, we measured a differential pressure from an output voltage ranging from -5 v to +5 v at minimum and maximum $\triangle P$ allowed by the membrane.
- XX: serial number of the differential pressure membrane, originally rated to measure a $\triangle P$ of up to 800 psi (serial number 58; 5.5 MPa), and temporarily

replaced by a 320 psi (2.2 MPa) differential pressure membrane (serial number 54). The output shift due to static pressure does not exceed 3 % of full scale, up to a line pressure of 10,000 psi (68.9 MPa), while the accuracy of the measurements reads ± 0.5 %.

- W: complete temperature range. We opted for the wide range (-53 to 120 °C).
- 8: inconel sensor, which was the most suitable option for brine flooding. Inconel is a nickel-chromium superalloy.
- A: 1/8" (3.2 mm) NPT female fitting, which could be adapted to the rig's tubing.

Rock type	Experiment	Date	Membrane & $\triangle P$
IL	$MFR\ HES$	11/08/2017	58 - 800 psi
	$HFR\ HES$	19/09/2017	
Trav.	$LFR\ LES$	04/10/2017	
IL	$MFR\ LES$	28/11/2017	
	$HFR\ LES$	04/12/2017	
Trav.	$HFR\ HES$	19/12/2017	
	$HFR\ LES$	09/01/2018	54 - 320 psi
	$MFR\ HES$	16/02/2018	
IL	$LFR\ HES$	21/02/2018	58 - 800 psi
	$LFR\ LES$	26/02/2018	
Pre-salt	$HFR\ HES$	21/03/2018	
	$HFR\ LES$	12/04/2018	

Table 3.1: Timeline of the experimental work, and the membranes used throughout. The membranes have been replaced due to unexpected bursts in differential pressure and have been replaced with the available material.

3.2.3.3 Hassler cell

The Hassler core holder cell designed and used by McCraw (2016) has been used in this study (figure 3.3). It is a uniaxial cell holding a 3.8 cm diameter large and up to 8.5 cm long cylindrical rock core sample. The core was confined within an elastomer sleeve around which a pressured mineral oil produced a confining pressure. The elastomer sleeve also allowed the injection fluid to circulate through the rock matrix by isolating the edges of the samples, providing a confining stress value superior to the line pressure. Both inlet and outlet of the sample were coupled with the cell using end-platens. The upstream platen is locked in place using a clover-leaf mechanism, while the downstream platen is screwed onto the Hassler cell. Both end-platens were provided with a 1/8" Swagelock fluid entry port:

- The inlet port is connected to the injection pump.
- The outlet port is connected to the back-pressure regulator.

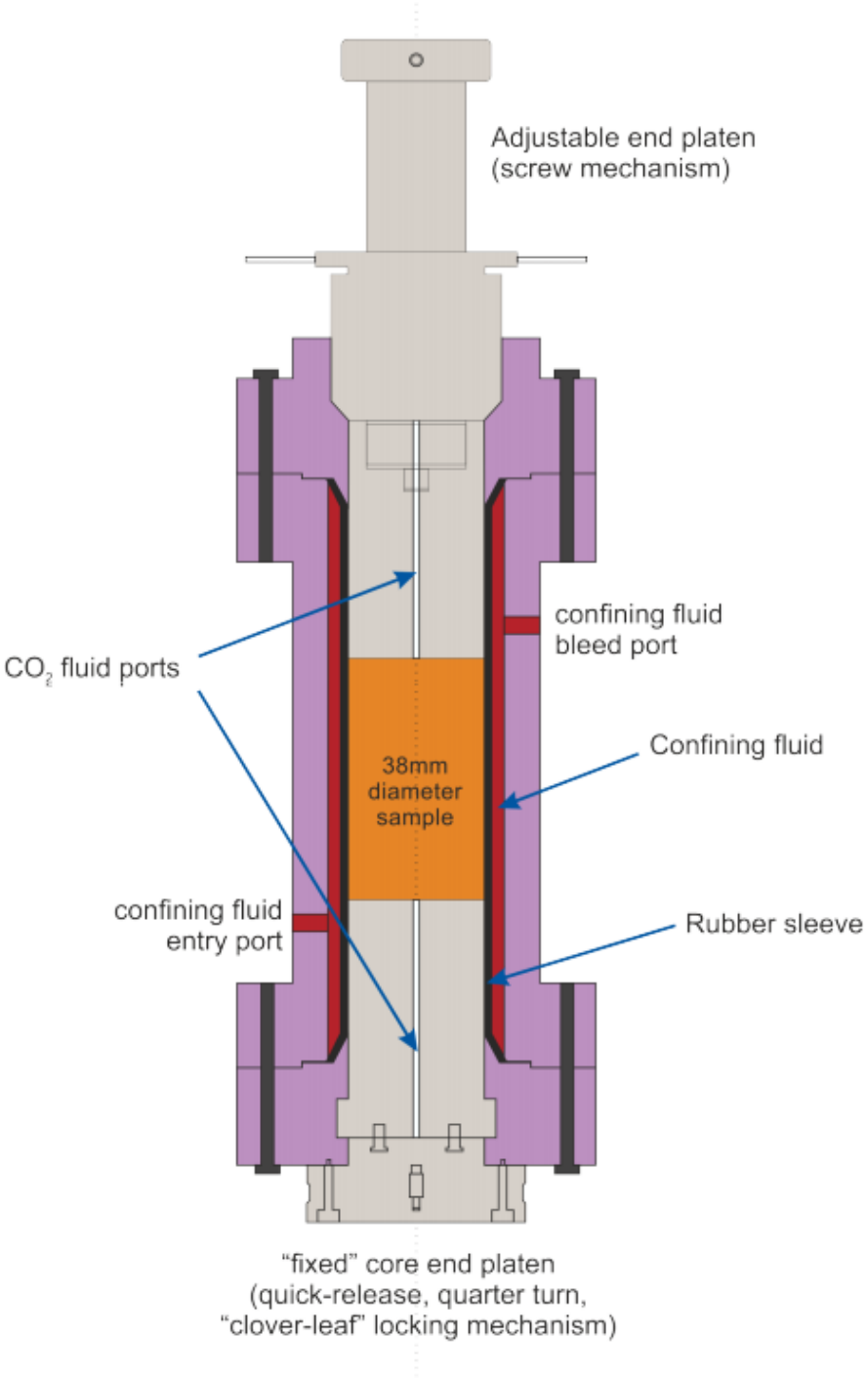

Figure 3.3: Hassler cell schematic. After McCraw (2016).

3.2.3.4 Temperature probe and fluid heating unit

Experiments have been carried out at constant fluid and oven temperature of 60 °C. The fluid heater unit system is a Thar model 04626-1, which has been installed in between the injection pump and the Hassler cell, providing a pre-heated upstream fluid at oven temperature.

The temperature within the oven is recorded using an Omega self-adhesive iron thermocouple (J-type) rated to 375 °C (±1.5 °C). The probe is connected to the thermocouple NI DAQ module where the analogue voltage was recorded at a frequency of 2 Hz.

3.2.3.5 Pumps

Three different pumps were used during an experimental flooding: a Teledyne CP-class pump (injection pump), a paired set of Teledyne ISCO pumps (back-pressure regulator), and a Sunex 4 Ton hydraulic hand pump (confining stress).

CP-Class pump

A CP-Class pump (part number: CP024SFX1C; described below) is a programmable dual headed, positive displacement piston, pressure controlled pump which cover a flow rate range of 0.01 to 24 cm^3/min at line pressure of up to 69 MPa (10,000 psi). The stainless steel fluid path is able to withstand brine flooding assuming thorough cleaning after each experimental flow. The pump is connected to the computer through a bespoke RS-232 cable for direct communication via a tailored LabVIEW software (section 3.2.5, and appendices H and I). Several variables can be recorded from the pump, such as the injection rate (cm^3/min) and the line pressure (psi). While the line pressure was used as a control, we used the injection rate provided by the injection pump for further permeability calculations. The pump has been customized as follows:

- 24: flow rate range (0 - 24 cm^3/min at 10,000 psi - 68.9 MPa max).
- S: stainless steel fluid path.
- F: self-flush piston wash, necessary to avoid internal clogging of the pump due to salt deposits.
- X: pressure and leak sensor option.
- 1: standard piston seal.
- C: inlet and outlet ports: 1/8" - 3.2 mm (outside diameter), compatible Swagelock.

ISCO pump

We have used the paired ISCO 100DX high pressure syringe pumps already in place for back-pressure operations. The syringes have been refurbished at the beginning of this project, due to extensive use during previous studies, involving corrosion after CO_2 flooding. The refurbishment involved a deep cleaning of the cylinders of the tanks, a greasing of the internal and external gears, and a replacement of all O-seals which proved to be permeable once put under pressure. A pump is constituted of two paired syringe tanks, allowing a constant line pressure throughout an experimental flooding (figure 3.4). The pump has been set under continuous constant pressure receiver mode, so that the injection pump alternatively refilled both syringes, while the ISCO pump calculated the rate at which the syringe should be refilled in order to maintain a pre-defined line pressure. Once a syringe was 80 % full, the ISCO pump observed a switch-over phase during which both syringes were sharing half of the injection rate for a short period of time, before the second syringe took over and operated as the leading back-pressure while the first syringe emptied its tank at a rate of 50 ml/min, until the remaining volume of fluid contained in the syringe reached 20 % of the total volume. Dumping rate, maximum tank volume, and minimum tank volume

were empirical values that worked for our set-up. The ISCO syringe pump can operate within a flow rate range of 0.00001 to 24 cm^3/min, and with a flow rate accuracy of ±3 %. The pressure capability ranges from 0.06 MPa (10 psi) to 69 MPa (10,000 psi). The pumps were programmable with a set of LabVIEW-ready commands which have been used in order to communicate with the pump through a RS232 cable connected to the computer.

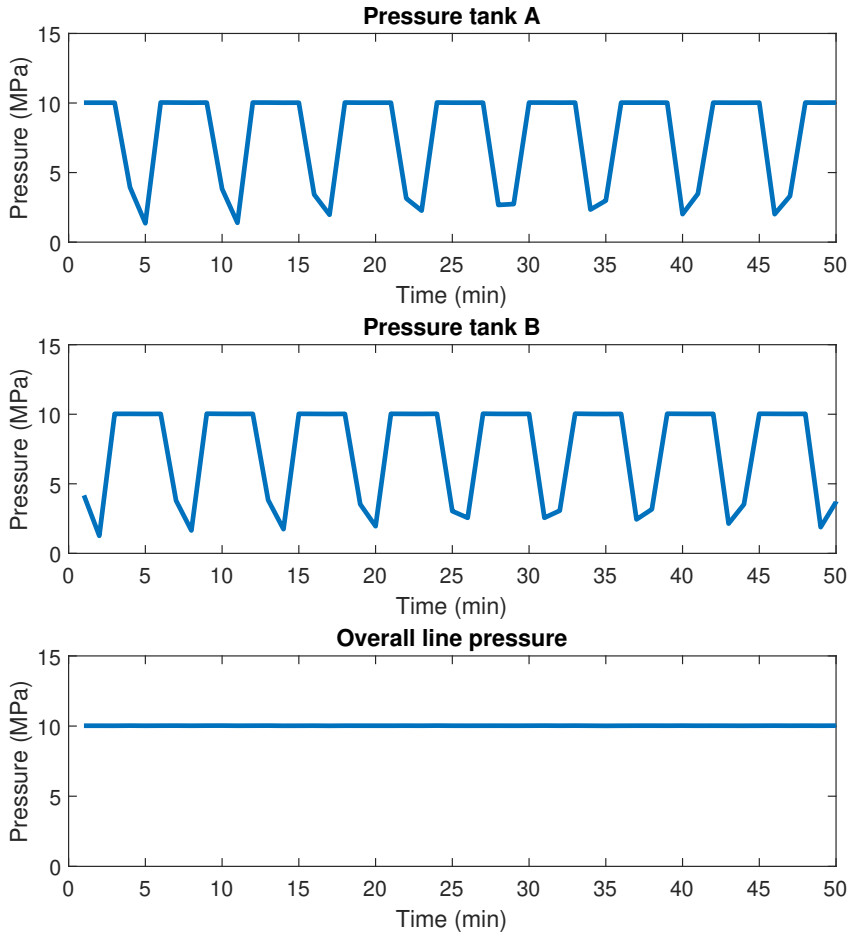

Figure 3.4: Example of switch-over between the two syringes of an ISCO pump, producing a constant line pressure (example from the Indiana limestone $HFR\ HES$ experiment; chapter 4).

Confining oil pump

The confining oil pump is a manually controlled tool. The oil was pumped towards the sleeve of the Hassler cell through a Swagelock tube. Once the desired confining pressure was reached, a Top Industrie valve was closed preventing the oil from returning towards the pump. Section 3.2.5.3 describes issues relative to the oil expansion due to the temperature increase within the oven. The method used for raising the confining pressure consisted in applying a small confining pressure during the set-up of an experiment, followed by the activation of the oven. This small confining pressure would later increase due to the thermal dilatation of the confining oil. Final adjustments were made in order to reach a confining pressure of 50 MPa.

3.2.3.6 Data Acquisition system (DAQ)

A National Instrument (NI) DAQ has been added to the system (figure 3.5). The acquisition of data represents the process of sampling physical measurements. A DAQ allows the user to centralize all physical analogue waveform measurements to one sampling unit in order to convert them into digital numeric values. A DAQ, coupled with a LabVIEW software, received the digital values prior to sending them to a computer where a tailored software was used for post-processing work, display, and logging (3.2.5). Our DAQ is composed of three elements:

- DAQ USB chassis (cDAQ-9174): controls the timing, the synchronization, and the data transfer between the different NI modules.
- Temperature input module (NI-9211): 4-channel thermocouple for temperature recording. The module is provided with a noise immunity filter.
- Voltage input module (NI-9205): 32-channel module used for analogue input recording (pressure sensors).

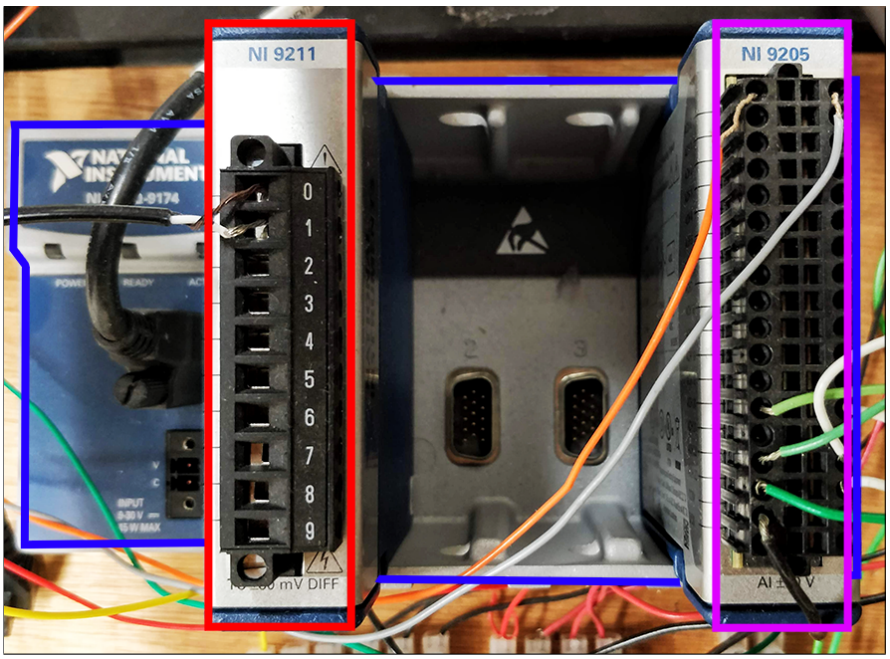

Figure 3.5: NI DAQ wired to the equipment and the computer, and composed by three modules: outline in blue: the chassis; outline in red: the temperature input module; outline in purple: the voltage input module.

3.2.4 Sample preparation

Special attention has been given to strictly follow the same preparation process for all core samples flooded during this project. Travertine and Indiana limestone samples have been cored from blocks, while the Pre-salt samples were provided as pre-cored 38 mm samples. The coring of the blocks has been achieved using a pedestal wet-drill with a 38 mm diameter diamond impregnated cylindrical core drill bit. The raw plugs were edge trimmed using a rock cutting circular saw, and polished using an abrasive rotating disc. These three steps produced fines which could later alter the chemical and physical outputs. Therefore, each core plug of rock has been placed in a sonic bath, and cleaned using distilled water. We repeated this until there was no evidence of fines in the distilled water. The clean core samples were then dried in a Memmert UNB500 oven

for at least one week, at 65 °C. The porosity of each sample was measured using the triple weighing (TW) method and using pH neutral distilled water as a saturating medium, and a Highland® HCB 1002 balance (± 0.01 g) for dry, saturated, and immersed weightings. The decision was made to use TW due to the unreliability associated with our µCT imaging acquisitions to be able to efficiently resolve the micro porosity of our rocks: as demonstrated by Lai et al. (2015), a significant part of the rock's porosity can be missed using µCT imagery at 1 µm resolution. Considering that our µCT scanning facilities displayed a 40 µm resolution, we opted for alternative methods which could reliably and consistently be used on each type of rock in this project. As such, the TW method, by its robustness appeared to be an excellent choice for assessing the accessible porosity. The general framework of the experimental procedure for sample preparation and conditioning is described in the steps below:

- Sample preparation:

    1. Coring of a 38 mm diameter large sample from a rock. We ensured that the ends of each sample were trimmed, flattened and squared within 0.025 mm as per the standards.
    2. The sample was trimmed and flattened using a diamond disk.
    3. Cleaning: sonic bath with distilled water.
    4. Measurement of the volume of the core.
    5. The core was dried in an oven at 65 °C.
    6. Nitrogen poro-permeability measurements.
    7. Dry weight measurement.
    8. Vacuum saturation of the core with distilled water.
    9. Wet and submerged weight measurements.
    10. The core was dried in an oven at 65 °C.

- Sample conditioning:

  1. Pre-experimental µCT scanning of the sample.
  2. Vacuum saturation of the sample with a formation water (composition given in appendix A, table A.1).
  3. The core was coated according to the nature of the rock:
     (a) Indiana limestone: the samples were heat shrink coated.
     (b) Travertine: a fine layer of cement was applied before coating the samples with a heat shrink membrane. The process is further described in section 5.4.6.
     (c) Pre-salt: particular treatment was applied to either samples due to the special rock nature of the Pre-salt. The process is further described in section 6.4.1.

- Experimental procedure: the core was put into a Hassler cell and connected to the flow rig, followed by a flooding until the permeability evolution reaches stability.

- Post-experimental procedure:

  1. Sonic bath of the sample using distilled water.
  2. The core was dried at least 1 week in an oven at 65 °C.
  3. Post-experimental µCT scanning of the core sample.

3.2.5 Software development

3.2.5.1 Summary of the previous installations

The recording system used prior to this study (Edlmann et al., 2013; McCraw et al., 2013; McCraw, 2016) has been updated to a numerically and remotely controlled system. Part of the recording was based on a Omega OM-CP data logger, connected to digital panel gauges (Omega DP25 S - discontinued). The

signal received by the panels for display was sent back to the computer for logging through the Omega OM-CP-OCTPROCESS data logger, which was recording the Omega pressure sensors values at 5 second frequency, with an accuracy of ± 1 minute per month. The back-pressure ISCO pumps were logged via a dedicated pump controller provided by Teledyne® ISCO. Flow data and pressure data were logged from a software and exported as a ASCII text file with a 5 second frequency. Due to software limitations, only one instance of the ISCO software could run at a time on a computer, which forced McCraw (2016) to use two computers in order to run an experimental flooding. The upstream pump was manually controlled, and was not part of the logging system, while the injection rate was assumed constant and not logged. The temperature throughout an experimental run was recorded from a USB thermocouple data logger (Omega OM-EL-USB TC) which was rated to hold 32,000 readings. McCraw (2016) determined that logging the temperature at 10 s frequency would provide 3 days and 16 hours of log, after which the data logger would go full and needed a reset. As the equipment was manually controlled, one of the post-viva suggestions of McCraw (2016) concerned the necessity of developing a data acquisition tool, along with the requirement of centralizing the commands of the equipment behind one united software. Early on during this study, it was decided to entirely re-think and develop the acquisition and control system of the experimental rig, which has been done by the author as part of the PhD project. After some research, the LabVIEW development suite appeared to be a convenient way to develop a solution. Several reasons motivated our choices:

- The injection pump, the back-pressure pump, the pressure sensors, and the differential pressure transducer were LabVIEW-ready or LabVIEW-compatible tools.
- A parallel experimental study uses a similar equipment set-up (Fraser-Harris et al., Submitted). The coupling between both experimental works justified investing in a LabVIEW programmed environment.

- The active and helpful online community of LabVIEW.

3.2.5.2 The LabVIEW programming environment

The Laboratory Virtual Instrument Engineering Workbench (LabVIEW) is a data-flow-designed development environment provided by National Instruments ™ (NI). The graphical languages supported by LabVIEW is named G-code, and was released for Apple in 1986. Nowadays, the language is supported by a vast majority of OS, including Microsoft Windows, macOS, and several versions of Linux.

The early version of our program, while functioning, was not stable enough to provide a steady logging of our variables. The cache memory of the computer would quickly go full due to a sequential architecture, which resulted in command delays (eg. seconds to minutes between a user click and a software response). The decision was made to postpone all experiments of this study during 6 month to focus on the re-development of a LabVIEW command and logging system following NI's standards and design patterns. Figure 3.7 displays the entire structure of the G-code (further described in appendix H). Our code uses the following programming architectures and design pattern:

- Data cluster: they are comparable to objects in Oriented-Object Programming. Figure 3.6 displays an example of simple data cluster used within the Read function of the injection pump. The light blue rectangle represents the format of the data cluster (two Doubles in this case), while the green rectangle is the data cluster, gathering the pressure and the injection rate read from the pump.

- Functions: a well designed function should observe the simplest structure. In this project, most functions have two input variables and two to three output variables. The equipment serial reference (called VISA) and the

error handler are, for most functions, inputs and outputs (figure 3.6 - yellow and purple wires), while a data cluster should be the third output (green rectangle).

- State-Machine design pattern: used for user interfaces and complex logical cases. This pattern revolves around the state, the event, and the action:
  - The state is the status of the program, for example: normal run state (true) or action from the user (false).
  - The event: example of events are running a pump, stopping a pump, resetting the total volume of fluid injected, etc. This bespoke LabVIEW controller allows a total of eight actions the user can execute that counts as actions (i.e. communicate with an equipment). Once any of these events are triggered by the user, the program receives a data cluster under the form of a Boolean (true: no event detected; false: an event is detected), and the name of action to trigger, under the form of a simple string command (eg. 'RUN CP', 'STOP').
  - The action is the task to be executed by the program.

- Event-Driven user interface: this architecture can be coupled with a state-machine for GUI purposes. An event-driven program runs orders determined by the user during a running session of the software. Contrary to the State-Machine design pattern, the event-driven pattern catch physical actions, such as a mouse click.

- Master-Slave architecture: used for smooth data-flow and data queuing. This pattern is used as long as more than one process runs simultaneously. The usual purposes for asynchronous processes are data acquisition, visualisation, and logging. Executing these three tasks within the same structure (referred to as 'loop') would result in severe timing issues. The entire

program was designed following this architecture(figure 3.7): loops 3 (displaying), 4 (displaying) and 5 (writing) are slaves of the master loop 2 (sampling), itself slave of the master loop 1 (event catching).

- Producer-Consumer: is coupled with the above architecture, for the purpose of data sampling and data visualization. This design pattern asynchronously attributes different tasks (sampling data, small or heavy calculations, display, etc.) without losing in respective loop frequency. This architecture should be coupled to a queued state-machine with event-driven actions: each event or data are enqueued by the producer loop and dequeued by the consumer loop. The relationships between loops are as follows (figure 3.7):
  - Loop 1 is a producer.
  - Loop 2 is a producer and a consumer.
  - Loop 3, 4, and 5 are consumers.

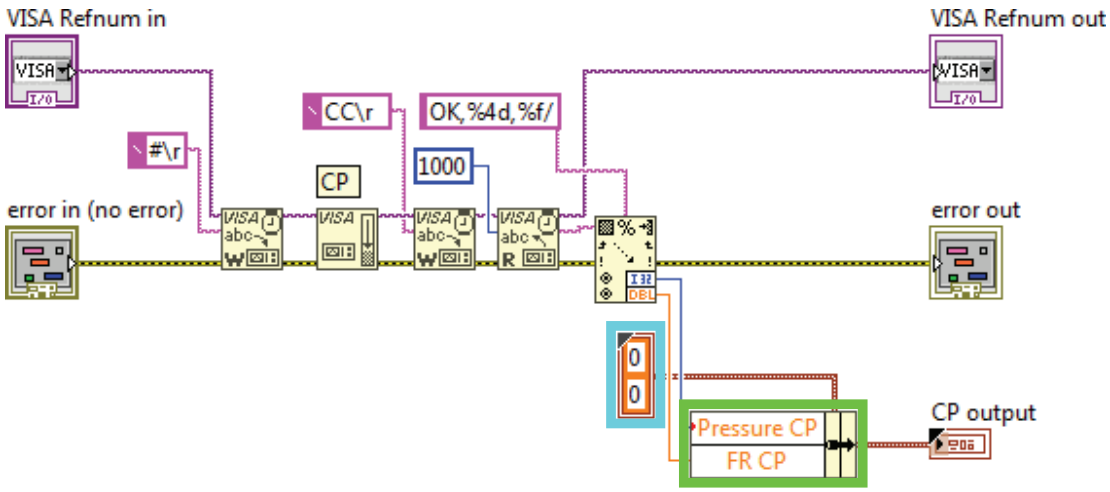

Figure 3.6: Example of function written in LabVIEW G-code (Read function): the VISA (ID number of the pump) is used to communicate with the hardware. In this case the command 'CC' is sent to the pump, which answers with a string. The string is then converted into a double and a float which is then transferred to a data cluster.

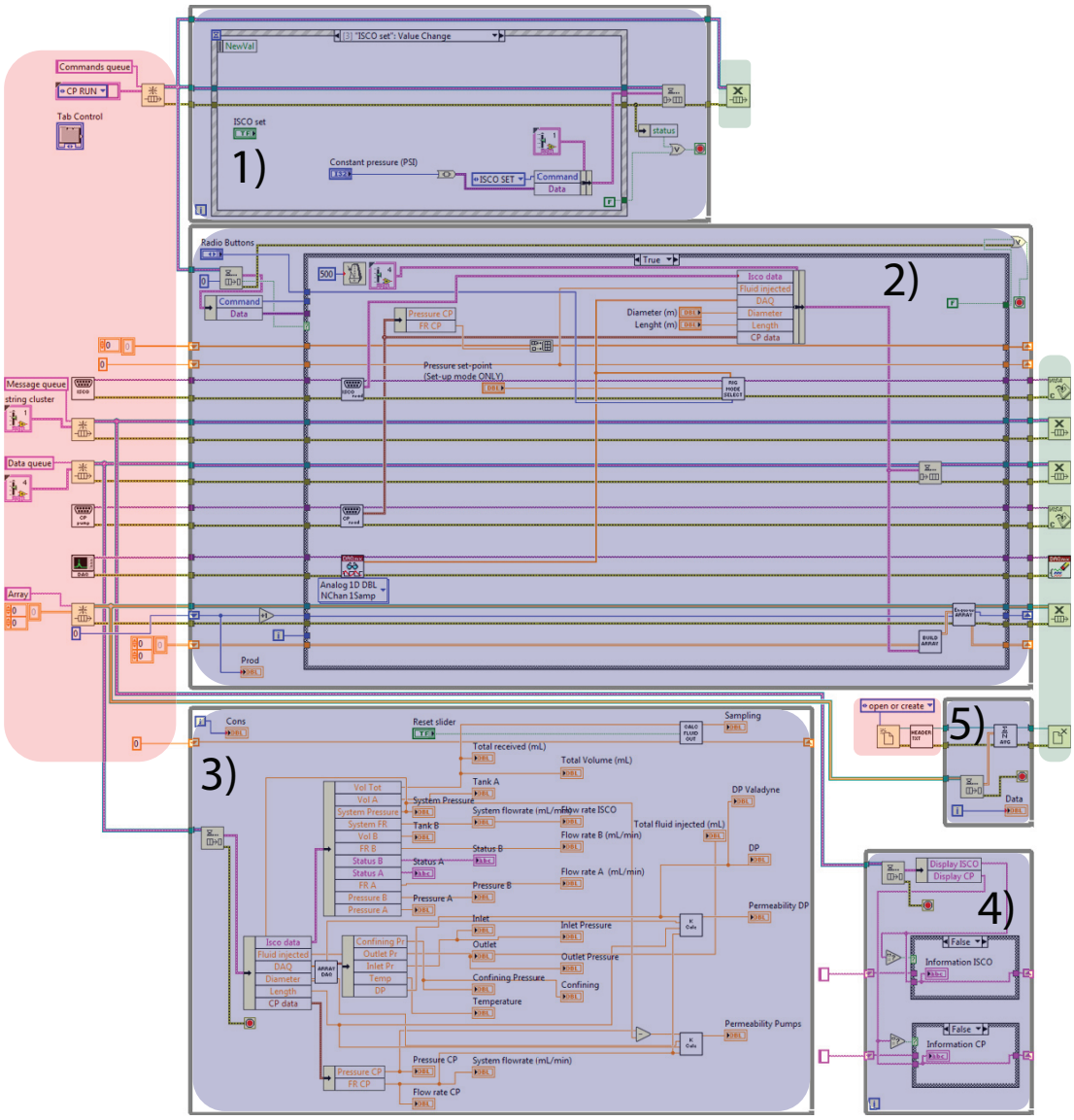

Figure 3.7: General structure of the program. The red areas represent the equipment (connected to the computer via RS-232 cables or via the NI DAQ), data, and data cluster's initialization. The blue areas are the five main loops. The green area represents the closing functions for queues and equipment.

The combination and the respect of these architectures are accepted by the LabVIEW community, while it is seen as a good programming practice as the code is easily transferable and readable by a third party. Moreover, a coupling of these architectures allows a smooth and steady data-flow throughout an execution of the software, and minimizes timing issues. We have calculated the timing deviation from the longest flooding experiment of this study (Pre-salt carbonate rock sample; presented in chapter 7). This rock sample has been flooded for 8 days (including overnight breaks) without switching off the system. The LabVIEW program presented a delay of 0.009 s over the course of this experiment ($S^2 = 0.01$ s). This would represent a delay of 0.03 s over the course of a month. The user can control the experimental logging and set-up through a Graphical User Interface (GUI) presented in appendix I.

3.2.5.3 Example of LabVIEW controlled functions

The important coupling between LabVIEW functions and the equipment has been used in different ways. Due to time limitations, several options have not been explored, but have been edited in section 9.3. This section presents three examples of useful interactions between LabVIEW and the equipment.

Set-up function

One limitation of our experimental rig concerned the manual confining pump, as it represented the only manual and non-connected piece of hardware of the set-up. As shown in section 3.2.2, we used a mineral oil in order to apply a radial confining stress around our cylindrical rock samples. This oil was injected into a Hassler cell, itself placed into an oven. The thermal properties of the mineral oil involves that it expands in volume as the temperature increases, leading to an increase in the force applied around the rubber sleeve used to confine the rock sample. This unsolicited increase in confining stress can be partially controlled through the use of an intermediate pressure sensor, placed on the confining oil

line (figure 3.1). A LabVIEW function has been coded to accompany the pore pressure during the raise of the confining pressure due the uncontrollable thermal expansion of the confining oil. Figure 3.8 presents the pressure set-up function: at the beginning of an experiment, the user selects the radio button 'Set-up' mode on the control panel (figure I.1 in appendix I) which triggers the pressure set-up function. The user also sets the pressure set-point that should be reached and maintained. The program reads the confining pressure from the pressure sensor placed on the line, and controls that the pressure sits between 0 and 10,000 psi. If so, the function calculates a line pressure corresponding the 90 % the value of the confining pressure. If that value is less or equal to the pressure set-point previously set by the user, then the function sets the back-pressure to a value corresponding to 90 % the value of the confining pressure, otherwise the software sets the back-pressure value to the pressure-set point value entered by the user prior to running the software.

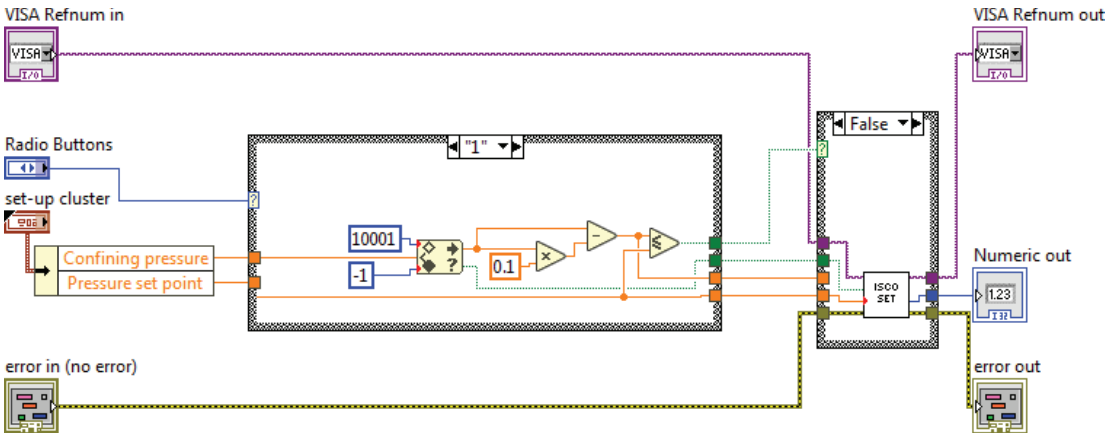

Figure 3.8: Pressure set-up function, written in G-code.

Figure 3.9 presents two experimental pressure set-ups. Figure 3.9a represents a high effective stress experimental set-up (HES), while figure 3.9b shows the pressure line accompanying the confining pressure in order to preserve a low effective stress (LES).

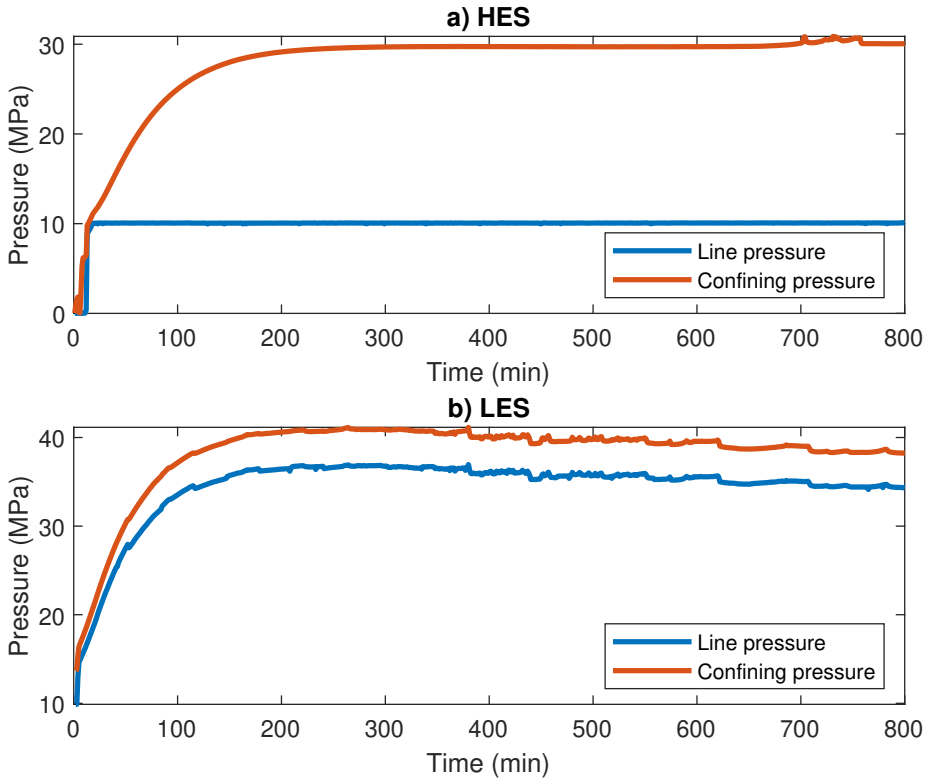

Figure 3.9: Pressure set-up path for a) a low pore pressure experimental scenario, and b) a high pore pressure experimental scenario.

Pressure release function

Following a similar process to the one described for the Pressure Set-up function, a Pressure Release function has been programmed. Once an experimental flooding was terminated, part of the equipment was switched off, including the oven. The temperature rapidly decreased to reach room temperature, involving a quick decrease in confining pressure, due to a reduction in the mineral oil volume. This function has been written as a way to preserve the rock matrix of a core sample until its complete unloading. The function checks whether 80 % of the confining pressure value remains above the pressure set-point value. If so, the pressure set-point defines the line pressure, and the back-pressure regulator is updated with

this value (figure 3.10). Otherwise, and once the confining pressure value becomes too low, the back-pressure regulator is updated with a value equal to 80 % the value of the confining pressure (figure 3.11).

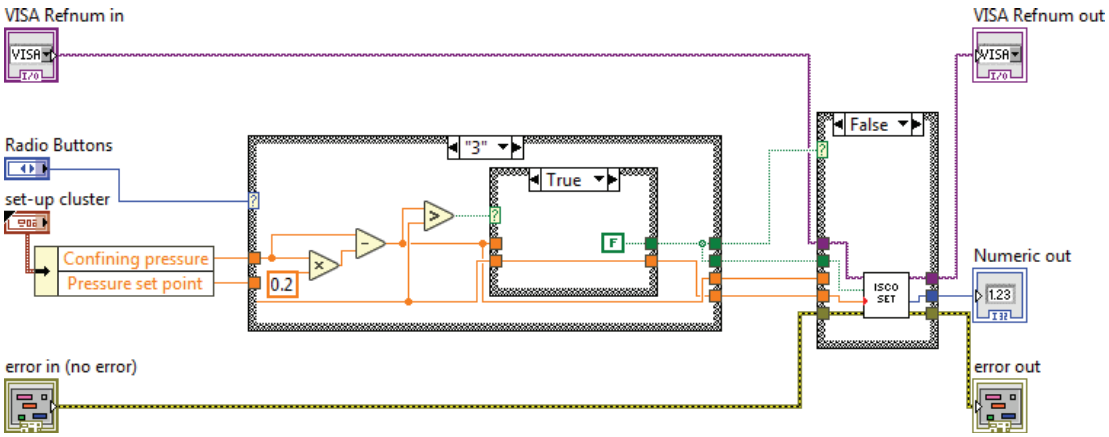

Figure 3.10: Pressure release function (true 'if' case), written in G-code.

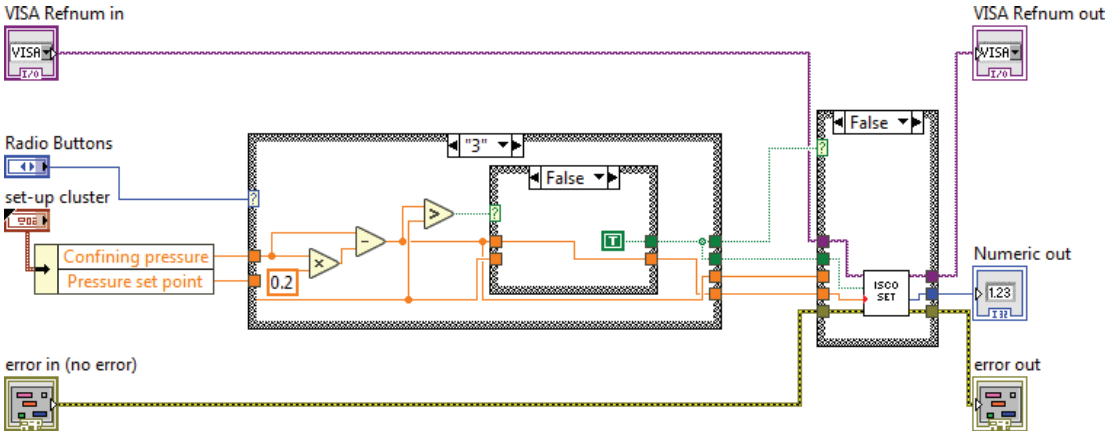

Figure 3.11: Pressure release function (false 'if' case), written in G-code.

Figure 3.12 displays two examples of line pressure release: a) shows an example of high effective stress scenario. Here the pressure set-point is kept low to preserve the experimental pore pressure. Only after ~1,000 min (opening of the confining oil valve, for fast release) the confining pressure value takes over the pressure set-point. Figure 3.12b shows a case of a low effective stress scenario: the pore pressure being already high, the pressure set-point defines the line pressure only

for a very short period of time, and is quickly taken over by 0.8 times the value of the confining pressure.

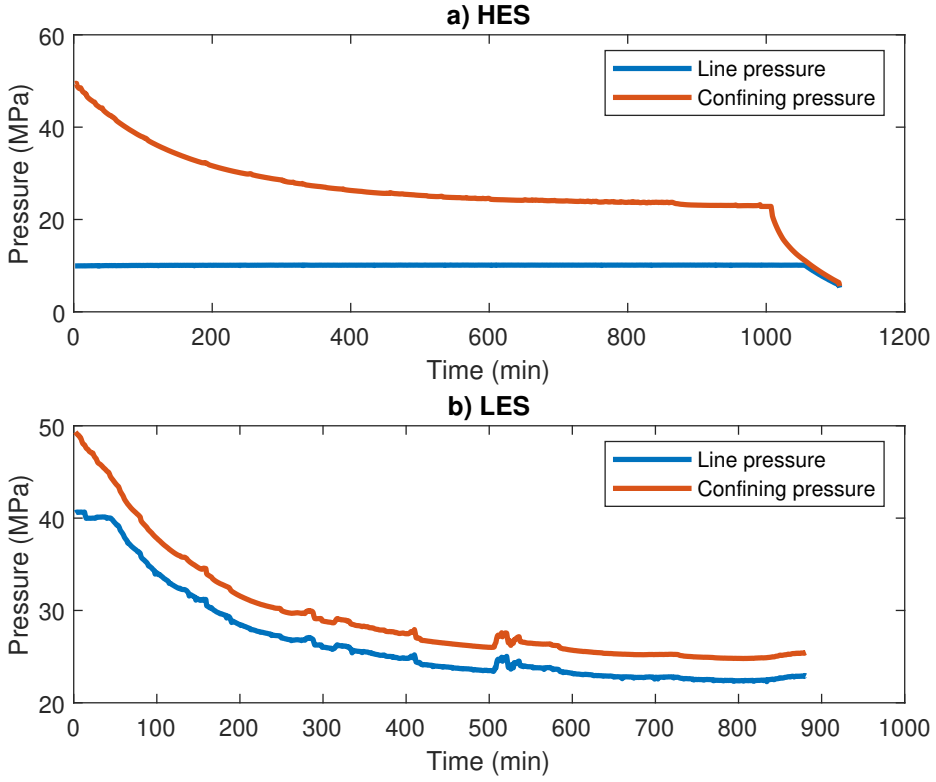

Figure 3.12: Pressure release path for a) a low pore pressure experimental scenario and b) a high pore pressure experimental scenario.

Fluid Sampling function

A last example of useful function concerns the fluid sampling. A 5 ml sampling loop has been installed at the outlet of the Hassler cell (figure 3.2). A flushing procedure of the loop has been set, so that a fluid sample could be taken only after the loop was flushed by, at least, four times its volume, which is equal to a volume of 20 ml running through the loop (figure 3.13).

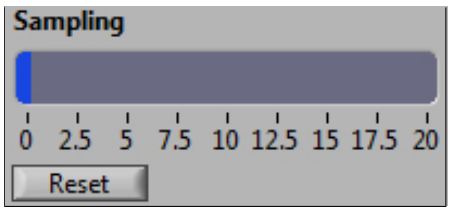

Figure 3.13: Fluid sampling tool interface present on the reading panel. By clicking on the 'sample' button, the user resets the volume to zero.

The fluid sampling frequency is therefore determined by the injection rate. A function has been developed in order to have an indication on how much fluid has passed through the sample loop since the last fluid sampling. After a sampling of the fluid, the user has the option to reset the volume that has been injected (figure 3.14a). If the volume injected has not reached 20 ml, the user should let the tank to refill (figure 3.14b).

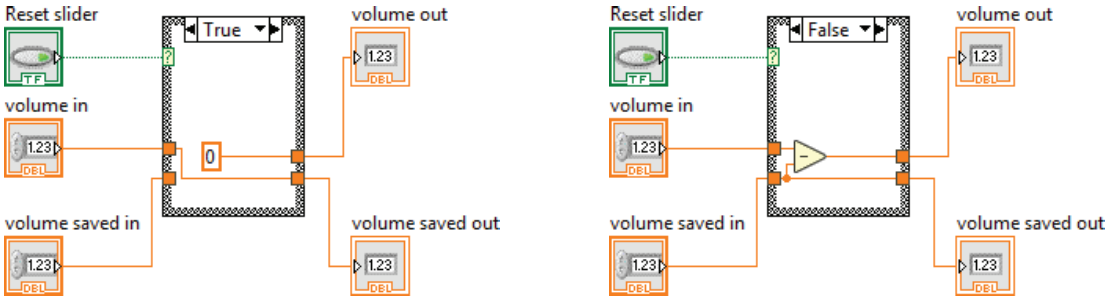

(a) Fluid sampling case. **(b)** No fluid sampling case.

Figure 3.14: Fluid sampling function: a) after a sampling is done, the user should reset the volume of fluid that has flooded the sampling loop; b) the user has not sampled any fluid.

3.3 Numerical development

3.3.1 Introduction

The programs presented in this section have been developed to meet the needs of simplifying and automatize a 2D slice analysis of µCT scans. A significant part of this project is based on the numerical development of solutions capable of analysing 2D images of rock samples as a way to extract the principal geometrical and statistical variables. Several software solutions have been developed through the this project, with the objective of providing input data to assist the understanding of the key processes leading to the rock matrix alteration during rock water flooding. The ICCR-Macropore, has been developed and adapted to perform 2D numerical analyses of µCT images of core sample. The software is able to output several types of file used during Hydro Mechanical and Chemical (HMC) modelling using the OGS software (Kolditz et al. (2012), and chapter 8). This work has been developed in collaboration with Dr. Christopher McDermott of the University of Edinburgh. The second solution, named the Slice Picker, uses the main functions of the ICCR-Macropore, and has been developed as a pre-processor of data for the Artificial Neural Network (ANN) presented in chapter 7. This tool provides a better understanding of the leading processes during heterogeneous rock alteration under constant water flooding.

3.3.2 ICCR-Macropore

3.3.2.1 Presentation

The ICCR-Macropore is an evolving solution developed over the entire course of this study. A version of the ICCR-Macropore is available in appendix F. The ICCR-Macropore can be used in two ways:

- As a processor of macro structures of 2D slices. ICCR-Macropore performs

geometrical calculations based on the images and generates spreadsheets which can be used for further analysis.

- As a data pre-processor of the OGS software. ICCR-Macropore generates 2D mesh files of the slices for further HMC modelling. Figure 3.17 shows an example of input file for OGS.

.

OGS was not used by the author in this thesis. However, preliminary results of an OGS analysis are described in the chapter (8), and were the product of a collaboration with Dr. Andrew Fraser Harris of the University of Edinburgh. The solution uses 2D slices taken from 3D volumes of image stack. The volumes were rendered by the µCT scan of a rock sample while the reconstruction process of the 3D rendering is described in the chapters 4, 5, 6, and 7, and is done using Fiji (Schindelin et al., 2012) and Avizo® 9. ICCR-Macropore has been used at various stages during this study (chapters 5, 6, and 7) and represents the core processor of the Slice Picker (cf. section 3.3.4).

3.3.2.2 Numerical structure of a pore

The interpretation of a SVG file (converted TIFF files) creates instances or objects. Figure 3.15 is a simplified Unified Modelling Language (UML) diagram displaying the relationship between the different classes. At this stage, a pore is interpreted as a polygon; a polygon is comprised of nodes, referred to as points; each pair of point forms a line. These classes belong to a single project. The relationship between classes can be summarized as follow:

- A project contains 1 to n Polygon(s).
- A Polygon belongs to 1 Project only, and is made of n Point(s).
- A Point belongs to 1 Polygon only.
- A Line is made of 2 Points, and can only belong to 1 Polygon.

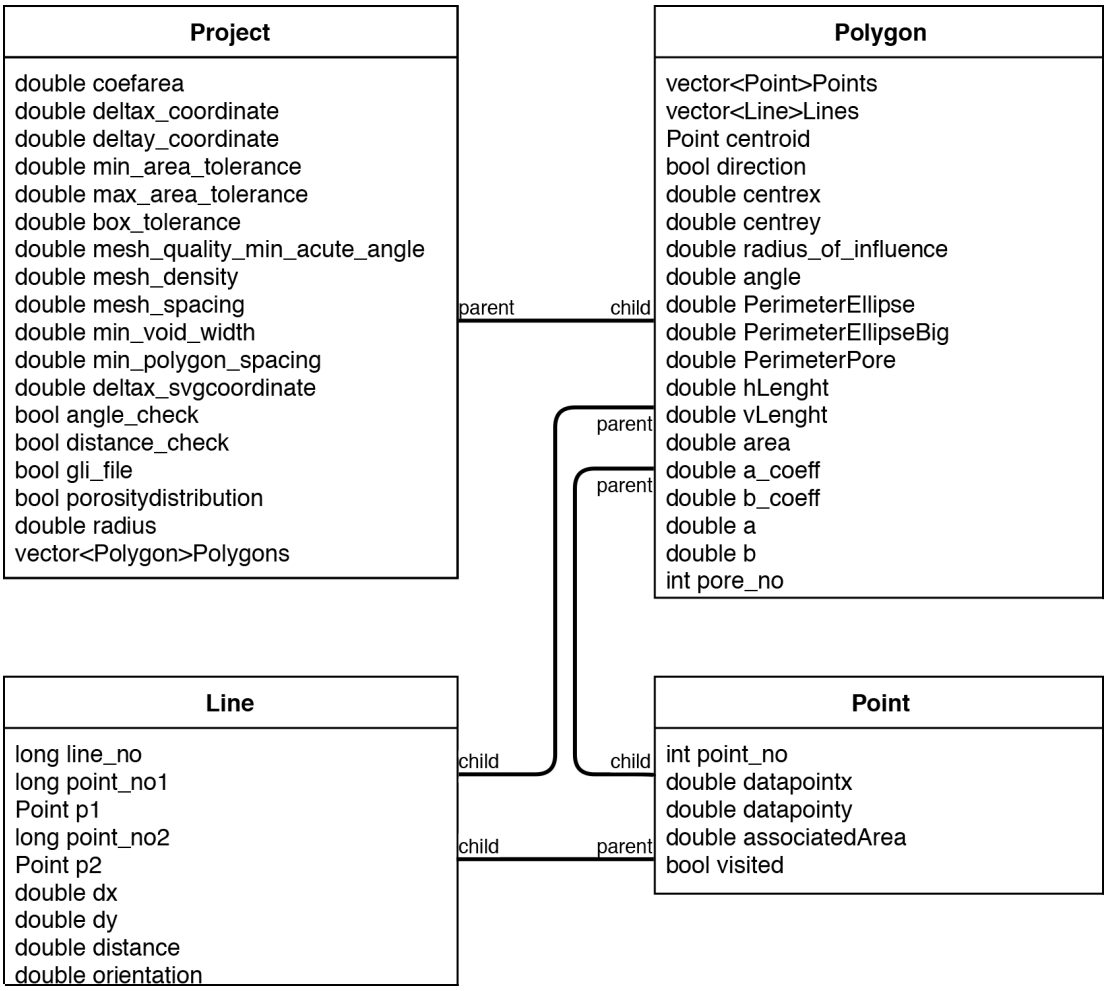

Figure 3.15: Simplified UML diagram presenting the main classes of the ICCR-Macropore, as well as the relationship between them.

3.3.2.3 Workflow

Figure 3.16 presents the general workflow for using the tool. Four types of input file are necessary (further developed in section 3.3.2.4). The tool offers three options: option 1) and 2) process one or more orthogonal slices, while option 3) observes the evolution of porosity and area of the pores of a 2D image stack in the axial direction. Along with the above-mentioned geometrical analysis, the ICCR-Macropore also creates .GEO and .GLI files of the scanned slices, which are inputs for OGS.

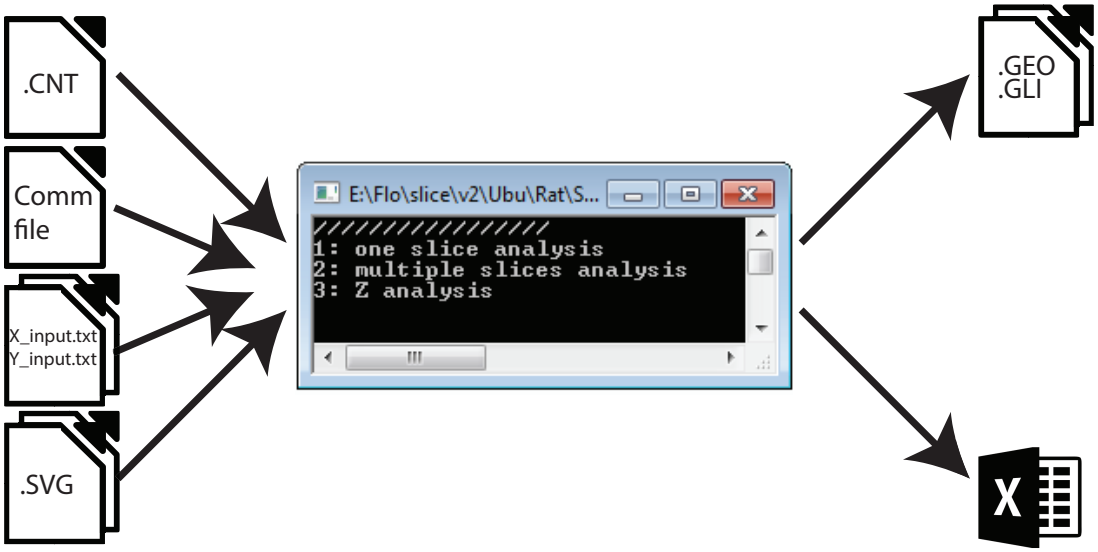

Figure 3.16: General workflow for the ICCR-Macropore. Three input types are necessary (a CNT file, a comm file, a text file, and the SVG pictures). The tool generates three types of output files (mesh file, geo files, and geometrical data).

3.3.2.4 Input files

The input files are described as follow:

- CNT file: this file is the control file. It contains interpretive and boundary variables. This user defined file is read by the executable before analysing any images, and defines how finely the images should be interpreted. The main variables of a CNT file are described in appendix E.

- SVG file(s): an SVG file is an XML-based vectorized image. The well documented encoding system allowed us to create reading functions capable of extracting the geometrical data of a 2D slice such as the contour of the pores, their positions, the size of the picture, and the differentiation between pore and background rock matrix. The input picture can take the form of a picture of a clean cut of a rock or a slice of a 3D volume of a core sample. This picture is further binarized and converted into a SVG file. The binarization and conversion are further described in section 3.3.3.

- Comm file: the comm file is a communication file used by the Slice Picker. The file is further described in section 3.3.4. For a normal use, the variable 'Status' should be set to 2.

- Slice text files: they contain the names of the SVG files that should be processed by the ICCR-Macropore, and take the form of two text files for the two sampled orthogonal direction (X_input.txt and Y_input.text).

3.3.2.5 Output files

The tool is able to extract data from a SVG file format according the user defined settings. It produces the following files:

- data.geo is used for meshing a slice (figure 3.17). A GEO file can be further edited using Gmesh (Geuzaine and Remacle, 2009), before producing the mesh for modelling purposes. The data.geo file is further used as a mechanical mesh (eg. in section 8.17).

- data1D2D.geo is used for meshing the links between pores (figure 3.21). Similar to the 'data.geo' file, the links between pores can be edited and adjusted under Gmesh (Geuzaine and Remacle, 2009) before being meshed. The data1D2D.geo file is further used as a hydraulic mesh (eg. in figures 3.21 and 8.17). The theory behind link generation is described in the section 3.3.2.7.

- svg.gli is used in OGS (Kolditz et al., 2012) to connect the meshes with the desired system of equations that calculates a solution. The .gli file represents the geometry of the mesh (under the form of points and polylines). These geometric objects connect the mesh to the rest of the OGS code, calculating the solution.

- Geometrical attributes: they are the results of mathematical interpretation of the polygons analysed by the ICCR-Macropore functions. Each of the attributes of interest is described in section 3.3.2.6.

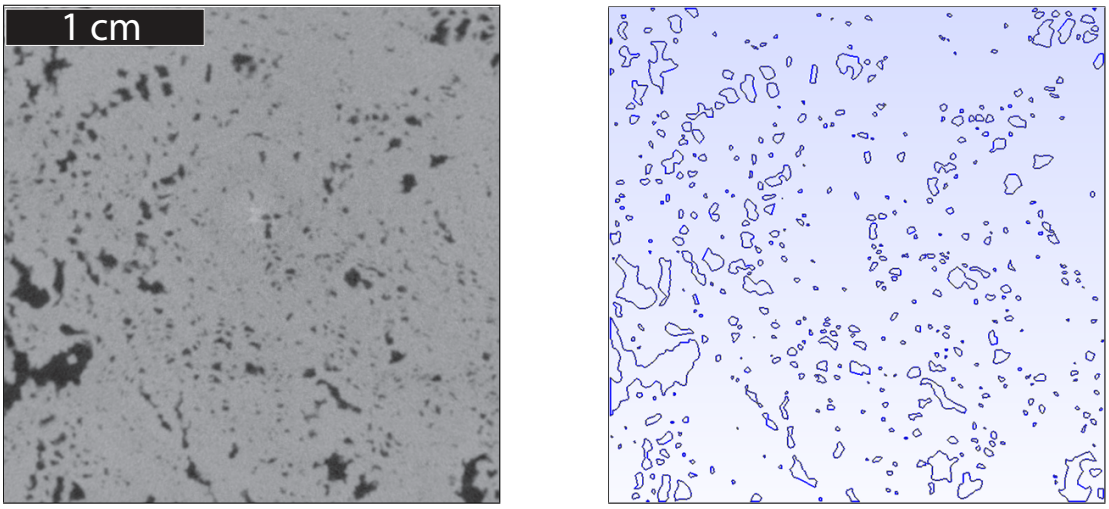

(a) Slice of a travertine sample. **(b)** Isolated porosity for meshing.

Figure 3.17: a) Slice from a travertine sample used in this study ($LFR\ LES$ - cf. chapter 5); b) Isolated porosity after ICCR-Macropore processing.

3.3.2.6 Geometrical attributes

Area of each pore

The area of each pore is calculated from any irregularly shaped polygon. Each polygon's perimeter being formed by points of known coordinates (x, y), we use

the following formula for Area calculation:

$$a = \left| \frac{(x_1\ y_2 - y_1\ x_2) + (x_2\ y_3 - y_2\ x_3) ... + (x_n\ y_1 - y_n\ x_1)}{2} \right| \tag{3.1}$$

Pore perimeter

The perimeter of irregular shaped pores is calculated using the distances between each pair of point (x_1, y_1) and (x_2, y_2), so that:

$$d = \sqrt{(x_1 - x_2)^2 + (y_1 - y_2)^2} \tag{3.2}$$

Coefficient A (major axis)

The coefficient A represents the largest axis of an ellipse shape of a pore (cf. figure 3.19).

Coefficient B (minor axis)

The coefficient B represents the smallest axis of the ellipse shape of a pore, and is perpendicular to the major axis (cf. figure 3.19).

D and l

D and l parameters are the average width and height of each pore, plus the average width and height of the entire porosity of slice.

Distances

This file contains a summary of the distance between each pores. Each pore is defined by a center point of coordinate (x, y), while the distance between two pores is computed using the same function as for the pore perimeter.

Ellipse perimeter

The perimeter of an ellipse is calculated using Ramanujan's approximation (Ramanujan, 1914), and is expressed as follows:

$$\begin{aligned} h &= \frac{(a-b)^2}{(a+b)^2} \\ p &\approx \pi\ (a+b)\ \left(1+\frac{3h}{10+\sqrt{4-3h}}\right) \end{aligned} \tag{3.3}$$

With a and b being the major and minor axis of the ellipse. This formula has been chosen due to its very good approximation of near-circular ellipses, while being very simple to implement. A pre-analysis of the pore shapes of our rocks shows that the aspect ratio for most of the ellipse of the pores in travertines and Pre-salt core rocks is under 5, with a vast majority of the ellipses below 1.5 (figure 3.18).

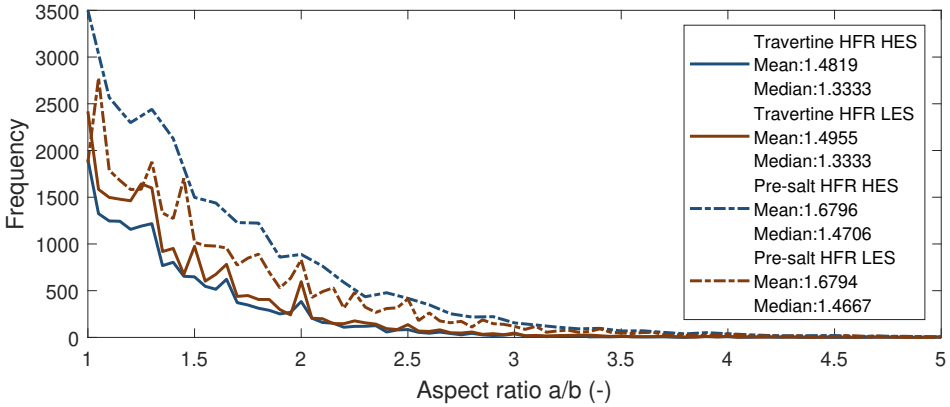

Figure 3.18: Aspect ratio (a/b) of four samples of heterogeneous nature (travertine and Pre-salt).

Ratio

Per 2D slice scanned, the ICCR-Macropore generates an excel file which contains all aspect ratios (a/b) of all ellipses (pores) present on that slice.

3.3.2.7 Ellipse simplification

The ICCR-Macropore has been developed as a 2D interpreter of pore network. This network, generated for each scanned slice and saved under the 'data1D2D.geo' file, relies on the arrangement and overlap state of the 2D porosity: each pore of a 2D slice is virtually replaced by an ellipse of equivalent area, shape, and orientation. Studies have simplified the complex structure of the pores by the ellipse equivalent shape of a pore (Fournier et al., 2011), while Tsukrov and Kachanov (1993) demonstrated that elongated pores could be replaced by their ellipse-equivalent shape for DEM modelling. Although we have not done any DEM modelling, we assume that the ellipse shape has a similar impact on the surrounding pores. The ellipses generated by the ICCR-Macropore are enlarged by a factor controlled by the user and defined as the 'area of influence' (cf. appendix E), and set constant for the entire sample analysis. This factor is a 2D computational way of representing the 3D hydro-geological influence of a pore over its surrounding area. Figure 3.19 presents a simplified workflow for pore connection detection. The overlap-detection function of ICCR-Macropore uses the geometrical attributes of an ellipse: knowing that the sum of the distances between the foci $F_{1,2}$ and any point of the ellipse E_1 is a constant C_1, we assume that if the distance between foci of E_1 and any point of a second ellipse E_2 is less than C_1, then E_2 overlaps E_1, leading to the creation of a link, referred to as 'Line' in figure 3.15, between those two pores. A link is a 2D representation of a potential connection in 3D, while the 2D arrangement of a set of links symbolizes the pore network of a 2D slice (figure 3.21). The ellipse simplification has the advantage of avoiding corner effects that can be encountered by a rectangular simplification against a more resource-consuming processing. Figure 3.20 shows an example of artefact produced during link detection between two pores: we observe that replacing the pores by rectangular shapes (case A) would have developed a connection (represented by a blue area) where case B does not detect

any. In the case of this sketch, the growing coefficient, or 'area of influence' would have been set to 1.

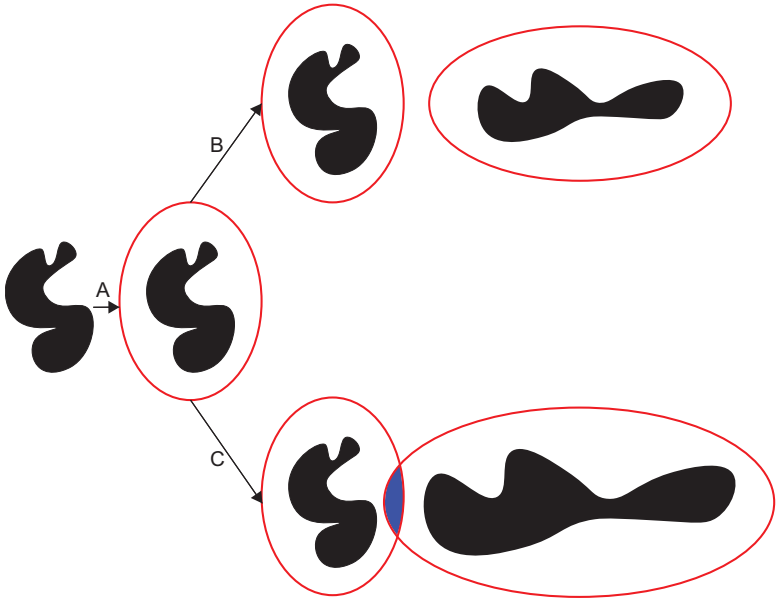

Figure 3.19: Steps for the detection of a link between two pores (black shapes). Step (A) represents the area of influence applied around a pore through a multiplier of the original pore area. The case (B) shows two non-overlapping pores; Case (C) displays a case of overlapping ellipses.

The materialized links are displayed in figure 3.21. For this example, a slice has been analysed three times, using three different 'area of influence'. As observed in case 3.21a, a small factor of 5 only connects the larger pores, which have a large influence on their nearest neighbours. Case 3.21b shows a factor of 10 applied on the same slice. In this case, most of the larger vugs are connected, while the microporosity begins to be part of the global hydraulic network. No connection between top and bottom of the slice is detected yet. With case 3.21c we see that almost all pores are part of a network. Only the ones sitting where the rock matrix is most present are avoided, highlighting the poor influence of rock matrix and microporosity during water flooding. The larger vugs have created a bottom-to-top connection.

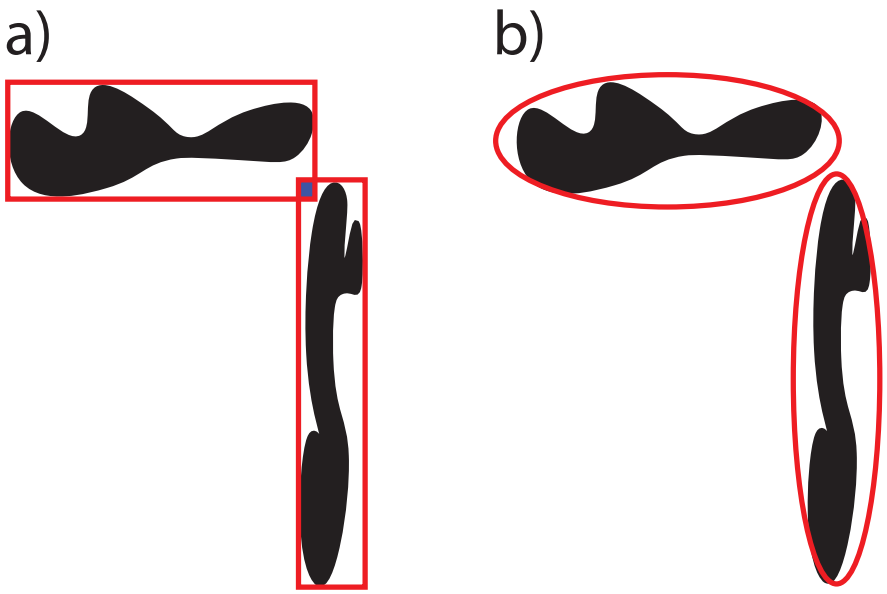

Figure 3.20: Sketch of an overlap detection (blue square) between two pores (black) defined by area equivalent of a) rectangles and b) ellipses. The ellipse simplifications of the pores allow a finer rendering than the rectangles.

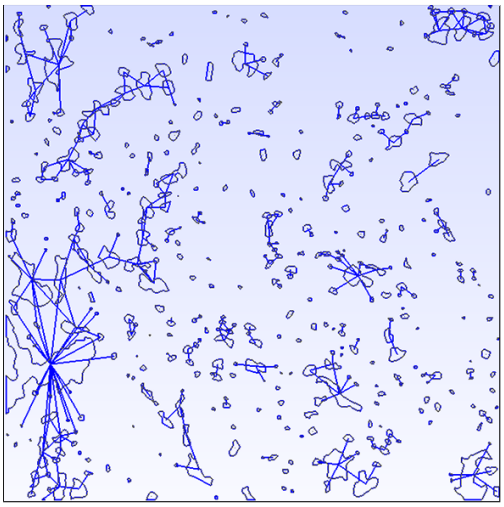

(a) Area of influence: 5

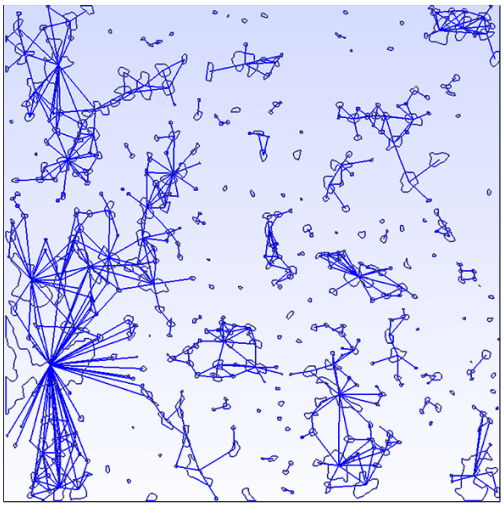

(b) Area of influence: 10

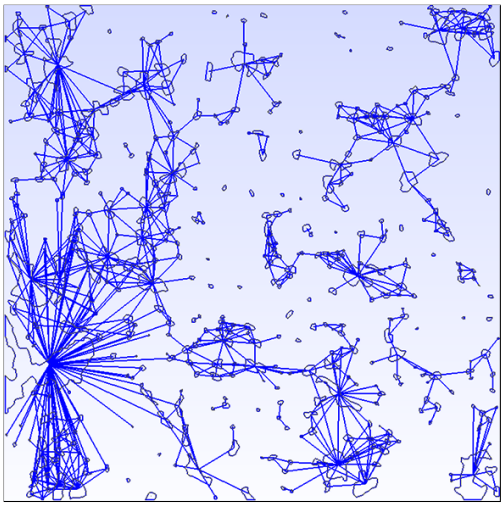

(c) Area of influence: 15

Figure 3.21: Visual rendering of the 2D connections between pores forming a network of interconnected vugs. Three different 'area of influence' have been used: 5, 10, and 15.

3.3.3 SVG Converter

3.3.3.1 Presentation

At the time of writing, the reading function of the ICCR-Macropore is able to read and interpret the SVG format. Section 9.3 describes possible evolution of this software, which would include other vector formats. Amongst other graphic editors, the encoding functions of the Corel® X7 suite give excellent results, and allow us to further use the ICCR-Macropore. Corel® X7 suite is a set of vector graphic editors offering functions similar to the one available using Adobe Photoshop®, for an affordable price.

The creation of a VBA software was motivated by the large amount of 2D slices to process. Figure 3.22 displays the user interface of the SVG Converter, which applies repetitive graphic operations in a short time. The general workflow for image conversion is given in appendix G.

3.3.3.2 Input files

The SVG Converter uses PNG format files as inputs. The PNG format is described as a lossless format type. In reality, PNG format can be compressed.

3.3.3.3 Output files

The SVG converter outputs files under the SVG 1.1 format. It also creates the 'X-Y-Z_input.txt' files file which are input files for the ICCR-Macropore (cf. section 3.3.2.4).

3.3.3.4 Limitations

One limitation of the SVG Converter resides in the non-exportability of an executable. Contrary to the ICCR-Macropore or the Slice Picker, the SVG Converter is a batch software coupled with functions implemented by the Corel®

suite, and thus cannot work if the graphic suite is not installed on the user's computer beforehand.

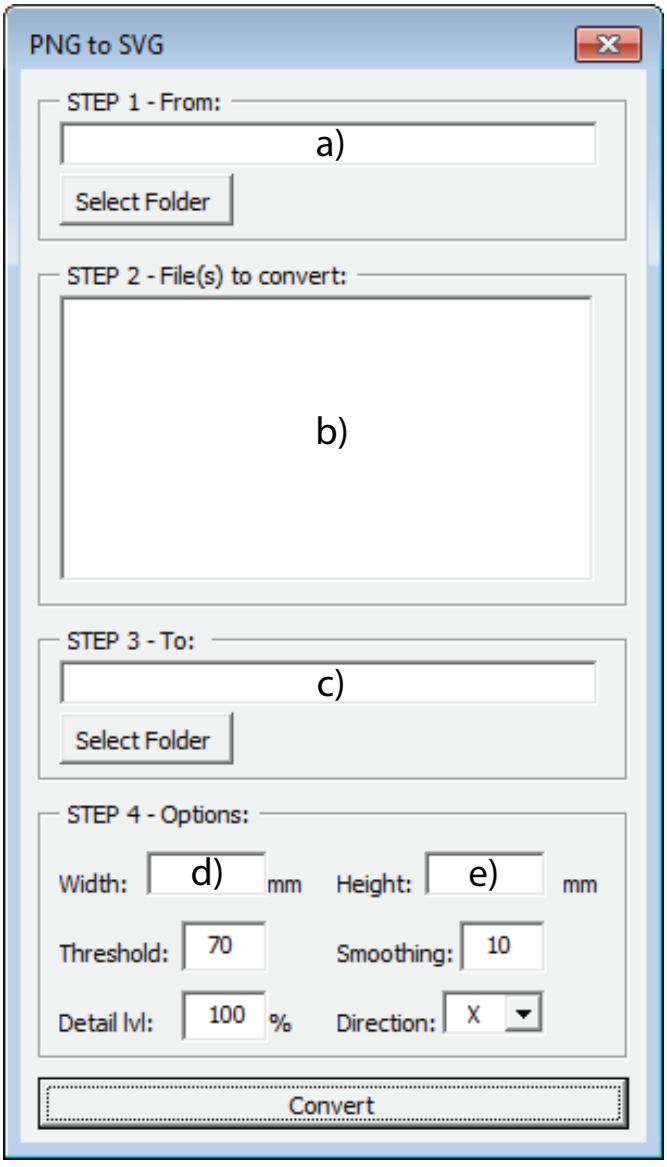

Figure 3.22: SVG Converter user interface: a) selection of the folder containing the PNG pictures; b) the list of pictures to convert is displayed in the box; c) selection of the destination folder; d) & e) original size of the slices for resizing.

3.3.4 Slice Picker

3.3.4.1 Rationale

The Slice Picker is a software written in C++ and specifically developed as a pre-processor for the Artificial Neural Network study (chapter 7). A version of the Slice Picker is available in appendix F. The software is based on the ICCR-Macropore main functions. The variables generated by the Slice Picker and their post-processing use are further discussed in chapter 7. A convergence of factors have motivated the development of this tool:

- The idea of a relationship between the geometry of the porosity within a rock and the subsequent dissolution flow-path.

- The development of hydraulic models based on OGS (Kolditz et al., 2012): the HMC models developed by Dr Christopher McDermott and Dr Andrew Fraser-Harris (presented in the chapter 8) are capable of showing the zones of likely dissolution as a function of the stress state at the edges of the pores of a pre-experimental slice of a rock sample. The coupled solution offered by the Slice Picker and the neural network (chapter 7) is able to provide the end user with a set of comparative 2D slices of pre- and post-dissolution as a way to cross-compare the results of the HMC model against the actual erosion of the post-experimental rock.

- A yet to be resolved resource leak within the ICCR-Macropore drains the computing power after a certain amount of a slices analysed (depending on the porosity present on the slices, the amount of interconnection between pores, and the overall amount of slices). While useful for a limited amount of slices (approximately 200), the Slice Picker becomes more suitable for analysing specific variables over a virtually unlimited number of slices.

3.3.4.2 Input files

The following files are needed in order to run the Slice Picker (figure 3.23):

- The executable of the ICCR-Macropore, along with the input files needed for a correct use of the software.
- The Comm file. The 'Status' variable should be set to 0 before running the Slice Picker.
- The 'Slices' text file, which should contain the names of the files to be analysed. The user can user the 'X-Y-Z_input.txt' previously generated by the SVG Converter (cf. section 3.3.3).

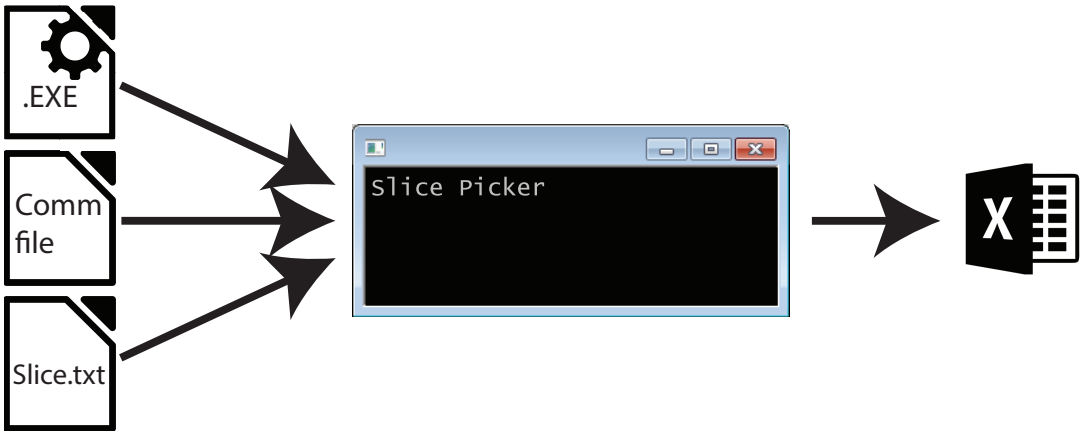

Figure 3.23: Input files of the Slice Picker. The three input units are the ICCR-Macropore, the Slice.txt file, and the Comm file.

3.3.4.3 Output files

The Slice Picker generates a formatted excel spreadsheet containing 18 variables, further used by the neural network solution (cf. chapter 7,) plus 1 variable (In/Out connection). The In/Out connection is a Boolean that offers a rapid and alternative way to control whether a breakthrough might occur on a 2D slice of pre-experimental scan of a rock. The function, compiled within the executable of the ICCR-Macropore, is only triggered through the use of the Slice Picker, and

is based on the recursive analysis of the connected network of pores, based on the 'area of influence'. The variable is set to 1 if at least one route connects the bottom of the slice to the top, and 0 otherwise.

3.3.4.4 Slice Picker - ICCR-Macropore interactions

The 'Status' variable of the Comm file guides both software into splitting tasks (figure 3.24). A Comm status of 0 indicates a running Slice Picker, while a Comm status of 1 puts the Slice Picker in a stand-by mode during which the ICCR-Macropore processes the current 2D slice through a set of available and hidden functions only triggered through the use of the Slice Picker. Once done with the slice processing, the ICCR-Macropore updates the Comm file accordingly and closes itself, while the Slice Picker saves the set of 18 + 1 variables in a vector. The process continues until each slice has been analysed, after what an excel spreadsheet containing all the data gathered by the coupled solution is generated.

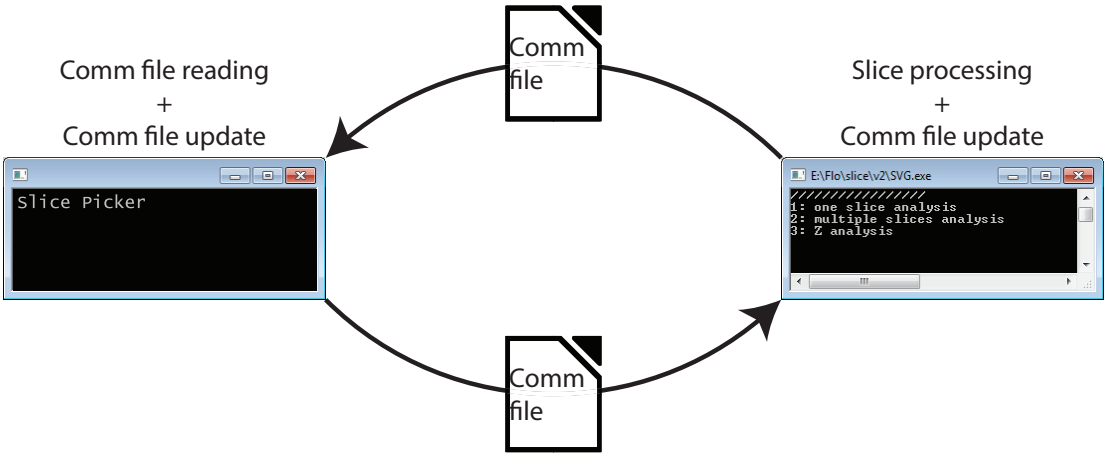

Figure 3.24: Programming logic and communication between the Slice Picker and the ICCR-Macropore. The Comm file is used as an intermediate file.

3.4 µCT imaging acquisition

3.4.1 Introduction

Fluid injected through carbonate rock samples generates dissolution that physically relates to the formation of wormholes. They are preferential flow-paths that increase fluid conductivity and allow the injection fluid to flow more easily from one end of the sample to another (Hoefner and Fogler, 1988; Fredd and Fogler, 1998; Golfier et al., 2002). These changes in the rock matrix can be detected using µCT scanning acquisition and post-processing of the images, by arithmetically comparing the pre- and post-experimental datasets. The µCT facility of the University of Edinburgh has been used for qualitative and quantitative analyses of these post-flooding damages. A reconstructed volume provides us with a 3D map of absorbed light due to the difference in density of the matrix of a rock (Landis and Keane, 2010). For each core, pre- and post-experimental flooding tomographic data were acquired at ∼130 kV, and ∼25 W target power loading, with a copper energy filter. A rotary stage is placed on top of an adjustable screw, which allows the scans of different parts of a sample by adjusting its elevation. The instrument has a conventional cone-beam configuration with a Feinfocus 10-160 kV dual transmission/reflection source, a MICOS UPR-160 air bearing rotary stage and a Perkin Elmer XRD 0822 amorphous silicon 1 MP flat-panel camera with a terbium-doped gadolinium oxysulfide scintillator. The geometry of the cone-beam window is approximately 3 cm wide, which can be less than the length of the cores, therefore each scan of a whole sample was split in two to three sections. Scans consisted of 2,000 projections; each of 2 s duration, during a 360° revolution. They were first recorded as 2D TIFF of projected images, followed by a tomographic reconstruction into a 3D stack. Further details about acquisition and reconstruction processes along with the underlying physics of µCT scanning can be found in various studies (Landis and Keane, 2010; Salvo et al., 2010). For each section, reconstruction by filtered back projection was done by using

Octopus v8.7 software (Dierick et al., 2004), while post-processing data analysis was done through Fiji (Schindelin et al., 2012) and Avizo® 9 functions (https://www.thermofisher.com/uk/en/home/industrial/electron-microscopy/electron-microscopy-instruments-workflow-solutions/3d-visualization-analysis-software.html).

3.4.2 Image processing

The reconstruction stage of the projected images was done using Octopus v8.7 (https://octopusimaging.eu/). Back processing, registration, and analysis was done via Avizo® 9, using the Image Registration Wizard and the Merge tool. Image Registration Wizard assists the user into registering several 3D volumes by mathematically enclosing the overlap between them while the Merge function combines the stacks into one set of data. Our methodology involved a registration of both unaltered (pre-experimental) and altered (post-experimental) datasets into the same 3D space, allowing us to further subtract both stacks in order to account for potential differences. As such, we used several tools in Avizo® 9: the Arithmetic operator, Interactive Thresholding, Label Analysis, and the Analysis Filter function. The Arithmetic operator applies a mathematical condition on the input 16 bit datasets; here we wanted to have the absolute difference between the pre- and post-experimental dataset. The Interactive Thresholding module differentiates the volumes based on the intensity values of the raw images. The thresholding was applied over the entire volume, and a voxel was set to black if its intensity I_{ij} is less than a fixed value T set by the user, so that $I_{ij} \geq T = 1$ and $I_{ij} \leq T = 0$. The Label Analysis function creates a connected network of voxels depending on their 3D arrangement, i.e. whether they are connected by their sides, corners, or faces. Finally, we used the Analysis Filter which applies a user-defined filter over any geometrical parameter of the 3D volume. We filtered our dataset in order to isolate the main parts of the channels by removing 3D volumes smaller than a certain amount of voxels. The drawback of imaging 38

mm diameter large samples lies in acquiring the images at a lower resolution, against the high energy needed to scan through the entire sample. As a result, our volumes displayed a voxel side length of 40 µm, which was enough to resolve most of the features that could be expected in these kind of study, but too large to obtain a detailed picture of the microporosity.

3.4.3 Output data

µCT images have been obtained on dry samples, prior and after each experimental flooding. The core samples have been cleaned for ∼15 min in a sonic bath, after the coring/cutting phases and after the flooding stage, in order to drive the remaining seawater out the sample. These extra steps have allowed us to obtain clearer outputs from the µCT scanning. The reconstruction process produced ∼2.5 GB 16 bit grey scale images which have been used in different ways:

- For assessing the cumulative thickness of the main wormholes of a core sample.
- For displaying the spread and shape of the wormhole formation.

For each experiment, we have calculated the total thickness of the principal wormholes as well as the main branches. While the thickness can be computed in 2D (on a slice-by-slice integration - Teles et al. (2016)), we opted for a 3D calculation based on a filled wormhole volume. A largely branched wormhole can lead to possible error in the thickness assessment due to the resolution limitation of the µCT scan, as well as the averaging and smoothing processes during the surfacing of the volumes, which implies that the smallest branches might be lost in the process. Thickness data and point coordinates were extracted from the volumes using the Auto Skeleton function (Fouard et al., 2006) for Indiana limestones, and the Centerline Tree (Sato et al., 2000) for travertines (both functions run under Avizo® 9).

The shape and spread of a wormhole has been calculated by evaluating the density of nodes per region of ∼0.01 cm^2. A wormhole formation expands and branches as the injection rate is increased (Siddiqui et al., 2006) implying that the thickness of a wormhole should then be primarily linked to the forcing of the fluid. In this work, we have isolated the main wormholes and branches before computing the total thickness of every newly created pore space along the radial axis of the core sample, with the assumption that for homogeneous rocks, and at similar injection rates, the resulting signal should be similar in width and spread.

3.5 Experimental parameters

Six cross-comparable experimental scenarios can be defined by the combination of an effective stress (σ') and a pore volume rate (PV_{rate}), as shown in table 1.1. In this thesis, each experimental scenario was named after:

- The relative PV_{rate} used, and is made of a letter (H for High, M for Medium, or L for Low) followed by FR (standing for Flow Rate).

- The effective stress scenario used during the experimental run. This part is made of a letter (H for High, or L for Low) followed by ES (standing for Effective Stress).

Table 3.2 summarizes the PV_{rate} and effective stress scenarios used for each sample during this project, associated with the injection rates.

The effective stress in this study refers to the work of Terzaghi (1951):

$$\sigma^{'} = P_c - P_p \tag{3.4}$$

While the different pore volume rates PV_{rate} (-) are presented as the amount of

pore volume flooded per minute of experimental work:

$$V = \pi \cdot r^2 \cdot L \tag{3.5}$$

$$V_p = V \cdot (\frac{\phi}{100}) \tag{3.6}$$

$$PV_{rate} = \frac{Q(t)}{V_p} \tag{3.7}$$

With V the volume of the core sample (m^3), r the radius of the core sample (m), L the axial length of the sample (m), V_p the volume of pore (m^3), ϕ the porosity of the rock (-), and $Q(t)$ the amount of fluid injected per minute logged (m^3).

Rock type	Experimental Scenario	PV_{rate}	Q (cm^3/min)
IL	$HFR\ HES$	3	23.97
	$HFR\ LES$	3	24
	$MFR\ HES$	1.5	12.47
	$MFR\ LES$	1.5	11.98
	$LFR\ HES$	0.7	6.56
	$LFR\ LES$	0.7	6.51
Trav	$HFR\ HES$	2.5	14.25
	$HFR\ LES$	2.6	15.58
	$MFR\ HES$	1	6.24
	$LFR\ LES$	0.2	0.99
PS	$HFR\ HES$	2.5	23.12
	$HFR\ LES$	2.5	14.64

Table 3.2: Injection rates used for the twelve experiments (IL: Indiana limestone; Trav: travertine; PS: Pre-salt).

Throughout each experiment, the following variables were controlled:

- The upstream injection rate.
- The confining pressure.
- The pore pressure.

The mechanical and chemical controls on permeability evolution were analysed through the logging of the following variables:

- The confining pressure.
- The differential pressure across the core sample.
- The injection rate.
- The temperature of the system.

The permeability evolution over time ($k(t)$) has been calculated using Darcy law:

$$Q = -A \cdot \frac{k \cdot \triangle P}{\mu \cdot L} \tag{3.8}$$

With Q is injection rate read from the injection pump sensor (m^3/s), μ the viscosity of the fluid (Pa.s) which depended upon the temperature of the system (Isdale et al., 1972), A the area of the core sample (m^2), $\triangle P$ the differential pressure across the sample (Pa) which was directly obtained from the differential pressure transducer, L the length of the sample (m), and k is the intrinsic permeability of the porous media (m^2).

All experiments were terminated when $\triangle P$ was reaching values close to 0 Pa, with the exception of the $HFR\ LES_{Pre-salt}$ experiment, which was kept under constant flooding even at $\triangle P \approx 0$ Pa. Due to the exceptional nature of the rock, and as in the effort of comparing permeability, chemical, and µCT data, the experiment was terminated when a similar amount of pore volume between $HFR\ HES_{Pre-salt}$ and $HFR\ LES_{Pre-salt}$ had been injected.

3.6 Chemical investigations

3.6.1 ICP-MS analysis

The calculation of the amount of calcium and magnesium ions removed from the samples during experimental flooding has been realized through the use of an Inductively Coupled Plasma Mass Spectrometer (ICP-MS) at the University of Edinburgh. Effluent fluid has been sampled at the outlet of the Hassler cell during each flooding experiment, and at regular intervals. Approximately twenty fluid samples were taken throughout each experimental run. Five to six millilitres of each sample were sub-sampled and put in centrifuge tubes. Standards, as well as calcium and magnesium detection from fluid samples have been commissioned by Dr. Laeticia Pichevin of the University of Edinburgh. Results were given in part per million, and per samples.

3.6.2 Sampling process

Each sample was collected in 10 ml centrifuge tubes, allowing us to collect 5 to 6 ml of effluent fluid, which was then filtered using an EMD Millipore™ - Millex™ 33 mm Syringe Filters from Fisher Scientific. The filtered brine was placed into a new centrifuge tube from which we measured the pH using a Hanna instruments model HI 2210, followed by the addition of 2 % of the volume of fluid in nitric acid (HNO_3) to prevent re-precipitation of the dissolved ions. For each experiment, a sample of the injection fluid was also taken and analysed following the steps described above. The Ca and Mg content (if possible) of the injection fluid has been subtracted from every syn-experimental fluid samples, so that $[I(t)] = [i(t)] - [B]$, with $[I]$ the concentration in either ion at time t used as a results in this project, $i(t)$ the non-corrected concentration in either ion at time t, and $[B]$ the concentration in either ion from the injection brine. The error associated with all chemical analyses has been set to a constant value of 2 %.

3.6.3 Theory

The evolution of each ion concentration has been integrated from the following equation:

$$\alpha = \int_{t=n}^{t=n+1} [I(t)] \cdot Q \times 10^6 \; dt \tag{3.9}$$

$$\beta = \int_{t=0}^{t=\tau} \alpha \; dt; \; 0 \leq \tau \leq t_{max} \tag{3.10}$$

$$\gamma = \frac{\beta}{\rho} \tag{3.11}$$

$$\Omega = \frac{\gamma}{V_s} \tag{3.12}$$

With $[I]$ the Ca-Mg concentration at time t and given in ppm, α the mass of Ca-Mg (g), Q the amount of fluid injected per minute (cm^3), β the cumulative mass of calcium (g), γ the volume of calcium (m^3), ρ the density of either ion, and Ω the dimensionless ratio of Ca-Mg removed over the volume of solid V_s of a core sample (m^3). The extra steps represented by equations 3.11 and 3.12 have been introduced as a way to avoid any overprint in calcium and magnesium due to a larger rock sample.

3.6.4 Porosity evolution

Initial porosity measurements have been done using the triple weighing technique, while the porosity evolution throughout an experimental flooding was derived from the Ca and Mg mass balance evolution. We used the equation given by Luquot and Gouze (2009) and Luquot et al. (2016) to obtain a porosity evolution as a function of time (only Calcite and Dolomite were taken into account as they represent most of each sample's composition):

$$\phi(t) = \phi(0) + \frac{V_{\mathrm{CaCO_3}} + V_{\mathrm{CaMg(CO_3)_2}}}{V} \tag{3.13}$$

With $\phi(0)$ the initial porosity value (from the TW method), $\phi(t)$ the porosity at any given time, $V_{\mathrm{CaCO_3}}$ / $V_{\mathrm{CaMg(CO_3)_2}}$ the cumulative volume of calcium and magnesium having been removed from the rock sample, under the form of calcite and dolomite, and V by the volume of solid rock.

Chapter 4

Observation of channel propagation at variable effective stresses and injection rates on Indiana limestone rocks

4.1 External Contributions

Dr. Ian B. Butler has kindly provided the Indiana limestone rocks, as well as valuable help during µCT scanning phases and post-processing scan analyses. Rock coring has been realized by Alex Jackson. ICP-MS fluid sample analyses have been carried out by Dr. Laeticia Pichevin. Finally, Nic Odling assisted with XRD analysis of rock samples.

4.2 Summary of the chapter

4.2.1 Rationale

Chapter 4 has been coupled with chapter 5 to form a comprehensive scientific report (available in appendix J), while parts of this work have been presented at the EAGE 2018 and SEG 2018 (Brondolo et al., 2018a,b). While this PhD project aims to better understand the geomechanical and underlying rock physics of Pre-salt rocks under geo-reservoir conditions of P-T, we soon realized that, to our knowledge, no similar and comparable work had been done on any type of rock. Therefore, it became evident that a baseline set of data was needed in order to further interpret the Pre-salt analogues and Pre-salt results. We opted for the Indiana limestone as the rock is widely documented, and renowned for its homogeneity. Chemically, the Indiana limestone resembles the travertines by displaying a high Ca content, seconded by traces of Mg.

4.2.2 Summary

In flooding experiments, porosity and permeability of carbonate rocks is enhanced through the dissolution of the rock matrix enhancing inter-connection of the pre-existing porosity. This enhanced interconnected porosity is termed 'wormhole' or 'channel'. Several factors can affect the way a wormhole propagates within a carbonate rock, such as the presence of heterogeneities (eg. vugs within the rock matrix), variation of the confining pressure, variable rock composition, and injection rate. While most studies have well constrained the impact of the above mentioned variables on wormhole formation and morphology, very few experiments have been done to look at the effect of variable effective stress ($\sigma' = P_c - P_p$) under steady state condition of P-T. In this work, we have injected seawater into 38 mm diameter Indiana limestone core samples under constant geo-reservoir condition of P-T: $\sigma = 50$ MPa, and $T = 60$ °C. We have also varied the effective stresses and pore volume rates: $\sigma'_{low} = 10$ MPa

/ σ'_{high} = 40 MPa, and PV_{rate} = 0.7/1.5/3. This experimental matrix has been designed to allow cross-comparison between identical PV_{rate} / different σ', and identical σ' / different PV_{rate}. To minimise the well-established influence of acidity and heterogeneity controlling wormhole formation, and to look in detail at flow rate and effective stress, we used a circumneutral pH seawater, and a highly homogeneous carbonate rock. Finally we reduced the influence that confining pressure has on the permeability by keeping this variable constant throughout every experimental scenario, and by changing the pore pressure to control the effective stress. We used several variables as proxies for our analysis, such as the poro-permeability evolution, the Ca-Mg concentration analysis, and µCT scans. While it is agreed that injection rate plays a major role in carbonate alteration of the rock matrix, through a higher dissolution rate corresponding to a high injection rate, and our work confirms this, we also demonstrate that a high effective stress has an important secondary impact on carbonate alteration. We observed that the effective stress, in the case of the homogeneous Indiana limestone, acts as a stimulant, and positively enhanced the poro-permeability, as well as the Ca and Mg recovery. The branching of the dissolution channels also appeared to be increased as we increased the effective stress. The processes involved behind this are not yet clarified by the experimental work, but we believe that they are time or chemistry related, with further study by the authors indicating that our results are energy-dependent.

4.3 Introduction

Acidity of percolating fluids is a known key control in the dissolution of carbonates, resulting in the development of preferential flow-paths referred to as channels or wormholes (Hoefner and Fogler, 1988; Fredd and Fogler, 1998; Golfier et al., 2002). Wormholes are important features of rock flooding as they can initiate an inter-connected pore-network within the carbonate rocks if

the optimal equilibrium between stress and fluid flow is obtained. Along with the optimal equilibrium (Wang et al., 1993; Frick et al., 1994b; Bazin et al., 1995; Fredd and Fogler, 1998; Panga et al., 2005; Siddiqui et al., 2006; McDuff et al., 2010; Maheshwari et al., 2013), single dominant wormholes can bypass the formation entirely, leaving most of the porosity untouched. The opposite scenario involves a complete rock dissolution where pores are mostly interconnected by the newly formed network of fluid. To identify this optimal injection rate/stress state, the processes of wormhole formation can be recreated in the laboratory by injecting acids or water into characterised core samples under controllable flow, temperature, and stress conditions (Frick et al., 1994b; Bazin et al., 1995; Fredd et al., 1996; Fredd and Fogler, 1998; Golfier et al., 2002; Egermann et al., 2006; Luquot and Gouze, 2009; Menke et al., 2015; Ott and Oedai, 2015; Barri et al., 2016; Luquot et al., 2016; Teles et al., 2016; Zhang et al., 2016).

The injection of a low salinity brine through a carbonate reservoir has been described as having a positive impact on mineral dissolution and pore connectivity through a rise in pH induced by calcite dissolution and cation exchange with the injected brine (Soraya et al., 2009). The mechanisms behind the development of flow-paths are important for many subsurface applications such as carbon sequestration, groundwater resource competition, and geo-energy applications, which include geothermal energy, energy storage applications and enhanced oil recovery.

This study has investigated the mechanical and chemical controls on the optimal equilibrium for permeability enhancement and channel formation within homogeneous carbonate samples. We believe that depending on the rock morpho-type, the mechanical effect that the effective stress has on the grain to grain contacts, as well as on the walls of the pores, could alter a sample or, inversely, preserve its matrix integrity during production phases. We used an artificial seawater as the injection fluid during core flood experiments under typical geo-reservoir

conditions of pressure, temperature, and representative geochemistry. Few investigators have assessed the relative contribution of stress changes and kinetic chemical alterations on the dissolution of carbonates and subsequent wormhole formation under the natural temperature, fluid and pressure conditions found at reservoir depths. While most previous studies worked with variable confining pressures and/or acidic injection fluids (Hoefner and Fogler, 1988; Frick et al., 1994b; Bazin et al., 1995; Fredd et al., 1996; Fredd and Fogler, 1998; Golfier et al., 2002; Egermann et al., 2006; Luquot and Gouze, 2009; Menke et al., 2015; Ott and Oedai, 2015; Barri et al., 2016; Luquot et al., 2016; Teles et al., 2016; Zhang et al., 2016), our experimental scenarios used a matrix of constant variables for the six rock samples that have been flooded. The strength of this comparative work relied on rigorously following the same experimental matrix for each experiment in order to isolate the key-controls for permeability and chemistry recovery while running our experiment under in-situ geo-reservoir P-T conditions.

4.4 Material and methods

4.4.1 Samples selection process

Pre-experimental $\triangle P$ have been calculated using Darcy law, and via nitrogen permeability measurements, while the syn-experimental $\triangle P$ were based on the $\triangle P$ at t=0 min. This preliminary task was realized in order to assign each core sample a PV_{rate} and a stress state scenario. Due to the high degree of homogeneity of the rock, the Indiana limestone rock samples have been randomly attributed a PV_{rate} and an effective stress. In figure 4.1 we observe:

- A clear dependence between effective stress and $\triangle P_{t=0}$, with a higher effective stress (low P_p) corresponding to a higher $\triangle P_{t=0}$.
- An obvious link between predicted experimental $\triangle P$ and injection rate.
- A very clear and predictable behaviour, as well as an expected lower

predicted $\triangle P$ due to the use of nitrogen and slippage effect (cf. section 2.4.4).

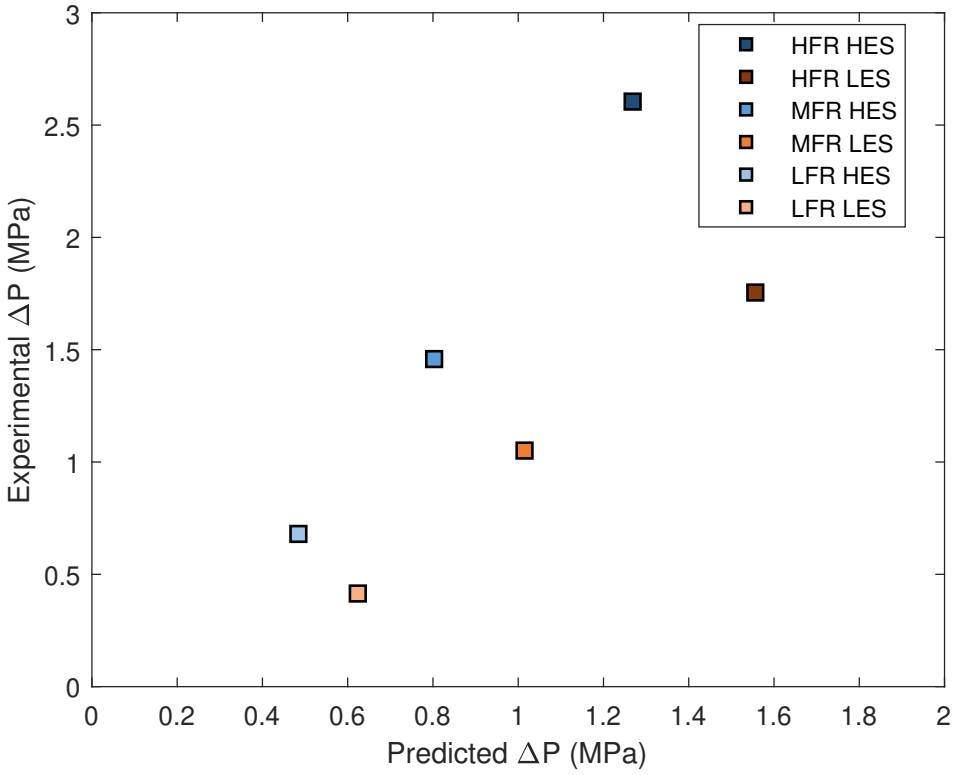

Figure 4.1: Experimentally calculated $\triangle P$ as a function of predicted $\triangle P$ for Indiana limestone rocks. The predicted $\triangle P$ is calculated by solving Darcy equation and using the pre-experimental $k_{nitrogen}$. The experimental $\triangle P$ represents the first log of the differential pressure transducer during a core flooding experiment.

4.4.2 Experimental design

A rig used for various rock flooding studies (Edlmann et al., 2013; McCraw et al., 2013; McCraw, 2016) has been modified in order to meet the requirements of single phase flow through low permeability carbonate rocks under controlled in-situ pressure and temperature conditions, and variable injection rates. The experimental setup is described in section 3.2.2, while logging and controlling

was done remotely using a LabVIEW software (further detailed in chapter 3 and appendices H and I).

4.4.3 Experimental approach

The experimental approach consisted in flooding six cylindrical core samples of 38 mm diameter and similar length (cf. table 4.3). The six rock flooding experiments consisted in injecting an artificially made seawater of known chemistry (30.5 g NaCl per litre of distilled water) and pH (∼7). The six experiments have been carried under geo-reservoir conditions of pressure (50 MPa), temperature (60 °C) and representative chemistry. The temperature is not thought to have a significant impact on the channelling architecture (Frick et al., 1994b; Soraya et al., 2009), while this secondary variable should only affect the viscosity of the injection fluid (Sun et al., 2016; Zhou et al., 2016), as we used a constant temperature of 60 °C during each experimental flooding. The main difference between each experimental scenario resided in using a different pore volume rate and effective stress. The permeability evolution over time ($k(t)$) has been calculated using Darcy law (equation 3.8), while the calculations for the PV_{rate} are explained in section 3.5 of chapter 3. The experimental matrix, displayed in table 4.1, shows the six flooding scenarios. Two conditions of effective stress were set: 10 MPa (referred to as the Low Effective Stress -LES) and 40 MPa (termed the High Effective Stress - HES). The experimental matrix was completed by three different injection rates (High, Medium, and Low, respectively HFR, MFR, and LFR).

		Flow expressed as pore volume		
		Low	Medium	High
σ'	Low	0.7 PV/min 10 MPa	1.5 PV/min 10 MPa	3 PV/min 10 MPa
	High	0.7 PV/min 40 MPa	1.5 PV/min 40 MPa	3 PV/min 40 MPa

Table 4.1: Pore volume rate (PV_{rate}) and effective stress (MPa) values for the six scenarios.

4.4.4 Flow scenarios and dissolution regimes

The chemical imbalance of the fluids injected through the carbonate rocks is the primary cause for dissolution and matrix alteration. Rock alteration is driven by the original porosity arrangement, the chemical interaction at the rock-water interface, the stress state changes, and the temperature of the system (Sippel and Glover, 1964; Wang et al., 1993; Golfier et al., 2002; Menke et al., 2015). Our experimental plan consisted in injecting an artificially made seawater of known chemistry and pH into carbonate rock samples. Six experimental plans have been designed in order to unpick which variable between injection rate (Q) or effective stress ($\sigma^{'}$) has the greatest impact on carbonate alteration. For each experiment, the Damköhler number (Da - cf. equation 2.11), and the Péclet number (Pe - cf. equation 2.14) have been calculated, and the expected dissolution patterns are plotted on the map suggested by Golfier et al. (2002) (figure 4.2). This map gives a good indication of the expected chemical and physical behaviour during matrix flooding. The evolution of the permeability was directly solved from the Darcy flow equation. The equation is applicable if it meets two criteria. The first validity check concerns the ratio between the average pore length l (m) of a flooded sample - later referred to as the characteristic length in this work -

and the length L of the core sample (m), so that l/L should remain largely inferior to 1 (Whitaker (1986) - cf. equation 2.8). The length of the six cores is displayed in table 4.3, while Freire-Gormaly et al. (2016) gave a pore size length of $l = 3 - 5 \times 10^{-5}$ m, resulting in α values comprised between 9.45×10^{-4} and 1.13×10^{-3}. The second condition requires a small Reynold number (Re - Stokes (1851); Fourar et al. (2004), and further described in section 2.3.1). The Reynold number is a dimensionless number that indicates the behaviour of the flow and its pattern in a medium, where a small Re number describes laminar flow behaviour while it characterizes a turbulent regime at higher values. For a homogeneous medium represented by packed spheres, the Re number ranges from 1-10 (Fourar et al., 2004) to more than a hundred (De Marsily, 1986; Seguin et al., 1998). De Marsily (1986) stated that laminar flow is achieved when $Re < 2000$. For our calculation we solved Re for every experimental scenario of this study and our results range from 0.06 to 0.24, which demonstrates that our experiments should remain within a laminar flow regime, confirming that the Darcy equation was valid for interpreting the permeability.

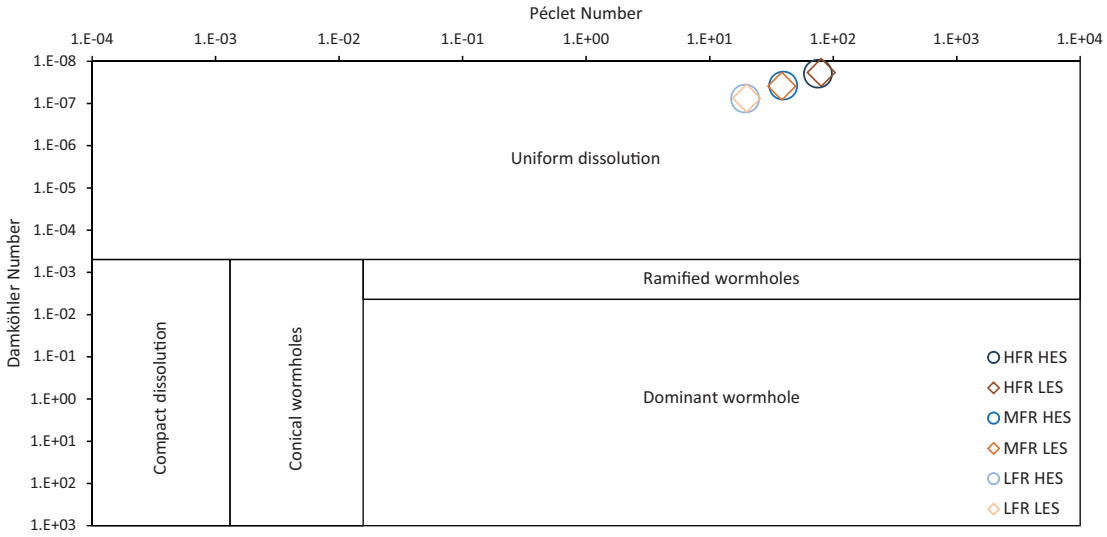

Figure 4.2: $Da - Pe$ map for the six core samples flooded. The boundaries have been suggested by Golfier et al. (2002) for a HCl-calcite system.

4.4.5 Sample characteristics

The samples used in this work have been sourced from a block of grey Indiana limestone. These rocks are widely used in experimental rock physics due to their homogeneity in permeability ($\sim$ 6 mD) and porosity ($\sim$ 15%) (Seminar, 1966; Smith, 1966). Petrophysical values of the six core samples used are shown in table 4.3. Most chemical analyses show a high $CaCO_3$ content ($>$ 97 %) plus $\sim$ 0.4 $-$ $\sim$ 1.2 % $MgCO_3$. Table 4.2 compiles the results of three studies plus in-house XRD analysis of our Indiana limestone samples. Figure 4.3 shows a µCT image taken from the $MFR\ HES$ core sample. The porous media is made of homogeneously distributed pores, whose size and shape appear to be similar. Churcher et al. (1991) describe the Indiana limestone as a calcite cemented grainstone, made up of fossils and oolites, often larger than a 1 mm.

Compound	Atomic weight (%)			
	(1)	(2)	(3)	In-house
Calcite	97.07	98.57	97.3	96.03
Magnesite	1.2	0.56	0.4	/
Quartz	0.8	0.35	1.7	0.99
Al_2O_3	0.68	0.12	0.5	/
Dolomite	/	/	/	0.73
Gypsum	/	/	/	0.41
Illite	/	/	/	0.74
Chlorite	/	/	/	0.83
Ankerite	/	/	/	0.26
Traces	0.25	0.39	0.1	/

Table 4.2: Chemical composition of the Indiana limestone compiled from three different studies plus an in-house XRD analysis. 1) Churcher et al. (1991); 2) Freire-Gormaly et al. (2016); 3) Powell (2004).

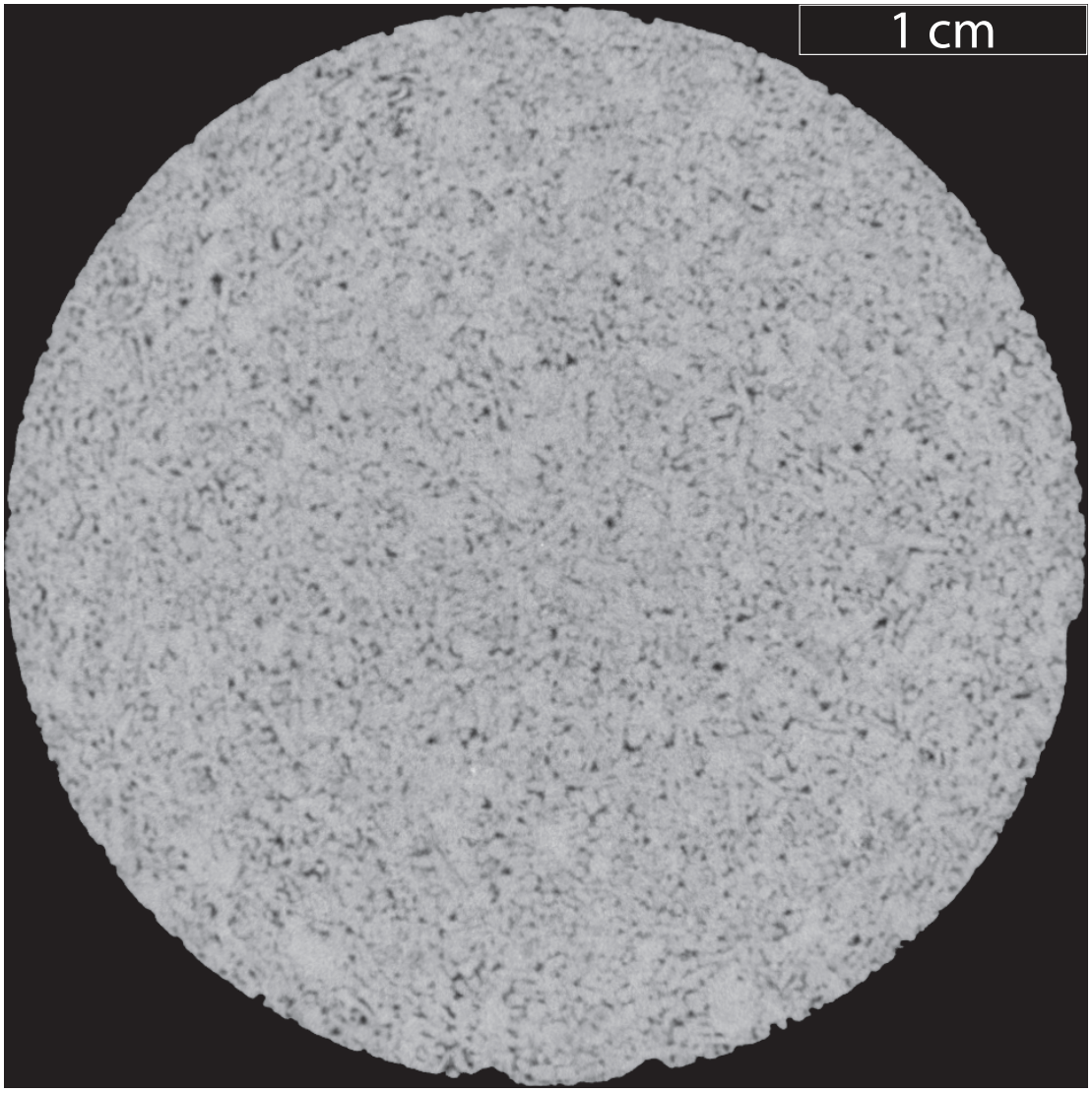

Figure 4.3: µCT slice of the $MFR\ HES$ core sample. Each sample used in this chapter have been cored from the same homogeneous block of Indiana limestone, and present similar petromorphological characteristics. Image size: 3.8 cm by 3.8 cm.

Sample	Length (mm)	Diameter (mm)	ϕ (%)	V_p (cm^3)	V_s (cm^3)
HFR HES	44.06	38	13.55	6.77	43.22
HFR LES	50.29	38	14.46	8.24	48.78
MFR HES	48.77	38	14.32	7.93	47.46
MFR LES	49.83	38	14.21	8.06	48.66
LFR HES	49.82	38	15.32	8.73	48.23
LFR LES	51.20	38	14.80	8.66	49.86

Table 4.3: Petrological characteristics of the samples. The volume of solid is calculated from the difference between the volume of the cylindrical core and the volume of pore: V - V_p.

4.4.6 Sample preparation

Special attention has been given to strictly follow the steps reported in section 3.2.4 (chapter 3) for the preparation of the six core samples. Prior to being loaded into the Hassler cell, each sample has been coated with a layer of heat shrink, to ensure cohesion of the sample, and a protection to potential extrusion of the pressure sleeve into the rock porosity.

4.4.7 Measurements

Physical and chemical data acquisition and subsequent data processing are detailed in chapter 3. The µCT images have been treated using Fiji (Schindelin et al., 2012) and Avizo® 9. The data on the thickness and point coordinates were extracted from the volumes using the Auto Skeleton function (Fouard et al., 2006). Figure 4.4 displays an example of generated surface (a) and the resulting skeleton (b).

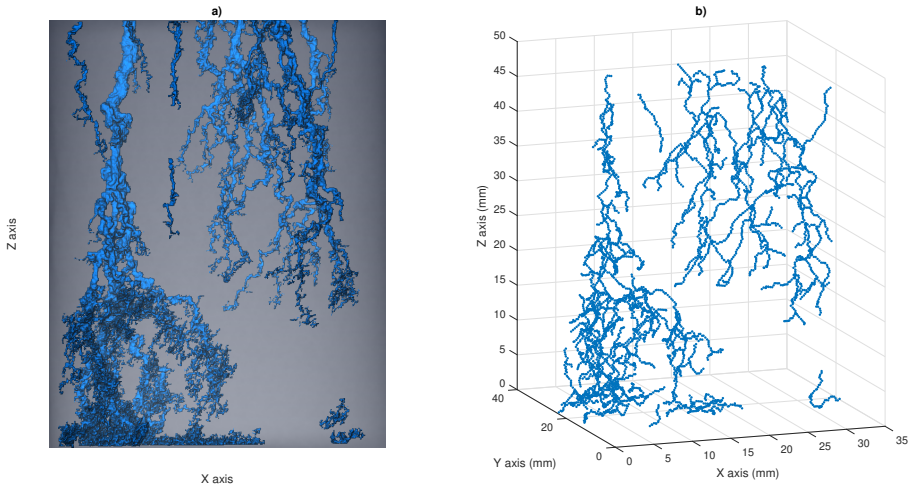

Figure 4.4: Example of skeletonization operation from the $MFR\ LES$ sample (AutoSkeleton function under Avizo® 9): a) 3D rendering of the experimentally generated wormhole; b) Corresponding simplified wormhole's skeleton. In this example, the fluid was injected from top to bottom.

A wormhole formation expands and branches as the injection rate is increased (Siddiqui et al., 2006) implying that the thickness of a wormhole should then be primarily linked to the forcing of the fluid. In this work, we have isolated the main wormholes and branches before computing the total thickness of every newly created pore space along the radial axis of the core sample, with the assumption that for homogeneous rocks, and at similar injection rates, the resulting signal should be similar in width and spread. A largely branched wormhole can lead to possible error in the thickness assessment due to the resolution limitation of the µCT scan as well as the averaging and smoothing process during the surfacing of the volumes, which implies that the smallest branches might be ignored.

4.5 Results and discussion

4.5.1 Laboratory analysis

4.5.1.1 Permeability

In core flooding experiments, we describe a breakthrough as a large increase of the permeability of a rock sample in a short period of time due to the creation of one or more flow channels between the inlet and the outlet of the rock sample. This creates a pressure bypass which leads to an equilibrium throughout the rig (Hoefner and Fogler, 1988; Teles et al., 2016). In this study, the typical S-shaped permeability curves presented in figure 4.5 are a first indications that preferential flow-paths formed in the rocks. The permeability evolution has been obtained after solving for k in equation 2.7. Figure 4.5 shows that despite a very homogeneous base rock, slight petromorphological variations can cause small shifts in k. We observe three distinct families of breakthrough initiation, which appear to cluster according to the pore volume rate set at the beginning of each experiment. Although the breakthrough onset and progression of each curve does not present any ordering, the onset times of each experiment were distributed by family of PV_{rate}, with an onset window at ∼700 min for HFR experiments, followed the MFR at ∼780 min, and the LFR samples broke-through at t>1,100 min.

The variation in $\triangle P$ due to slight heterogeneities within the six samples at $t = 0$ led to imprecision in the relative initiation of each experimental breakthrough, which can be corrected by plotting the relative permeability k/k_0 (figure 4.6; left subplot). The error associated with the differential pressure logging is represented on the right subplot of figure 4.6, where the plain curves are within the margin of error given by the manufacturer (cf. chapter 3). The dashed curves are linear extrapolation of the data gathered between the point marked in figure 4.9 and the last data logged whose reading remain above the margin of error. Due to

the nature of this work, the breakthrough onset time and behavior has been further analysed, hence the subsequent extrapolated evolution are showed for the purpose of scientific accuracy. Here, an interesting observation of the permeability evolution is that it appears to be defined by 1) the initial -rock dependent- pore volume rate and 2) the -rock independent- effective stress. Each family of effective stress driven experiments ($\sigma' = 10$ MPa & 40 MPa) saw its own breakthrough event happening according to the injection rate, so that, for a given effective stress, the first experiment to breakthrough displayed a PV_{rate} value of ∼3, followed by ∼1.5 and finally ∼0.7. While rocks of all type have a natural tendency to see their permeability being reduced as a strong effective stress is applied (Shi and Wang, 1986; Berryman, 1992; Kok et al., 2002; İşcan et al., 2006; Selvadurai and Głowacki, 2008; Ghabezloo et al., 2009; Sun et al., 2016; Zhou et al., 2016), we have observed that a high effective stress applied upon homogeneous limestones enhances the permeability generation.

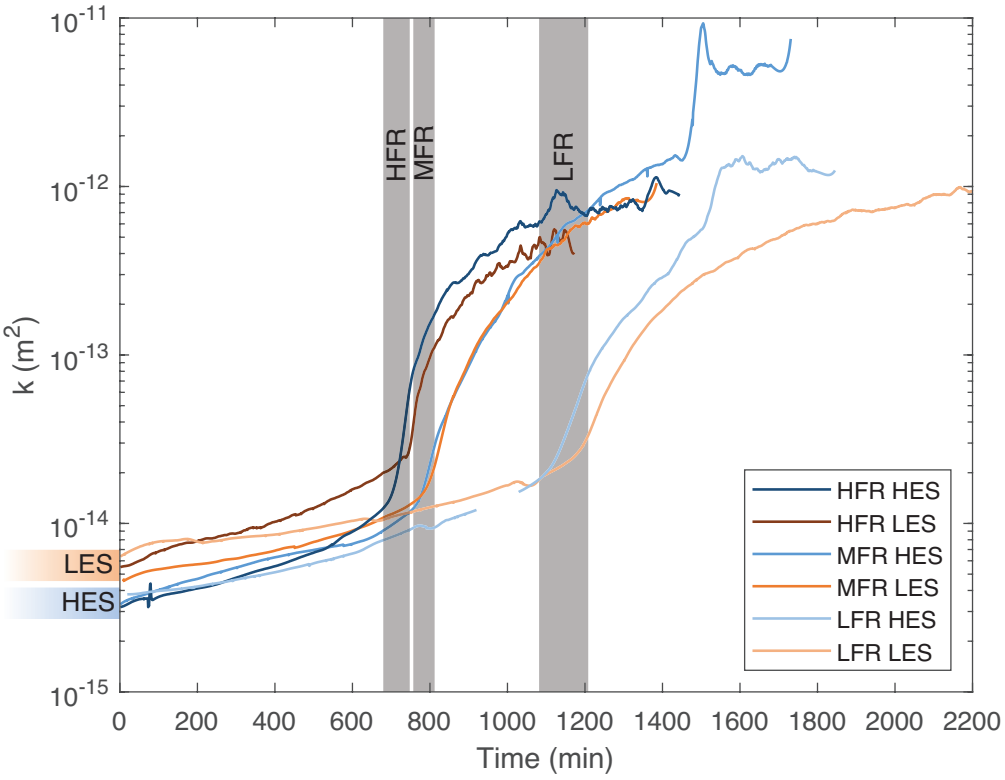

Figure 4.5: Permeability output. The permeability calculation is derived from Darcy law. All randomly selected LES samples ended up displaying a larger $k(0)$ than the HES samples. The breakthrough onset windows are distributed according the PV_{rate}, and as follows: HFR, MFR, and LFR.

The impact of the effective stress on the rocks is also demonstrated by comparing each pair of PV_{rate} driven experiments and their breakthrough: figure 4.7 shows $\frac{\partial log(k)}{\partial t}$, over the experimental time t. Each peak on the figure represents the largest intensity of permeability generation, which should sit at the steepest point within the curves in figures 4.5 and 4.6. Per PV_{rate}, the maximum of permeability was firstly reached by the high effective stress experiments (blue curves), followed by the low effective stress experiments (orange curves). As expected, the intensity of permeability generation, represented by the steepness of the curves, as well as the maximum peak for each curves is PV_{rate} dependent: for a given family of PV_{rate},

the permeability trend remains similar, the main difference being a slight shift in time before observing a peak (characterizing a breakthrough).

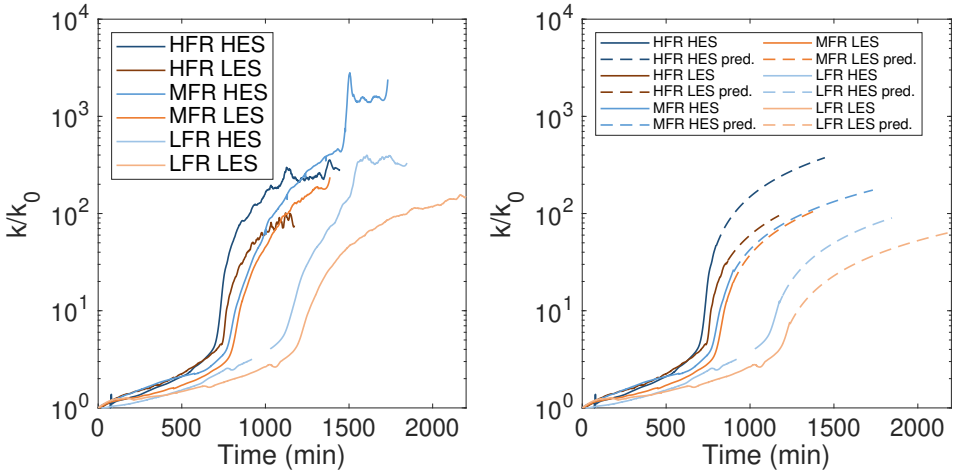

Figure 4.6: Permeability evolution normalized against the permeability value recorded at $t = 0$ min. Left: untreated data; right: the plain curves display the data outside the error region, while the dashed lines are the extrapolated data. The linear extrapolations are based on the recorded data sitting in between the marks of figure 4.9 and the last valid recorded value.

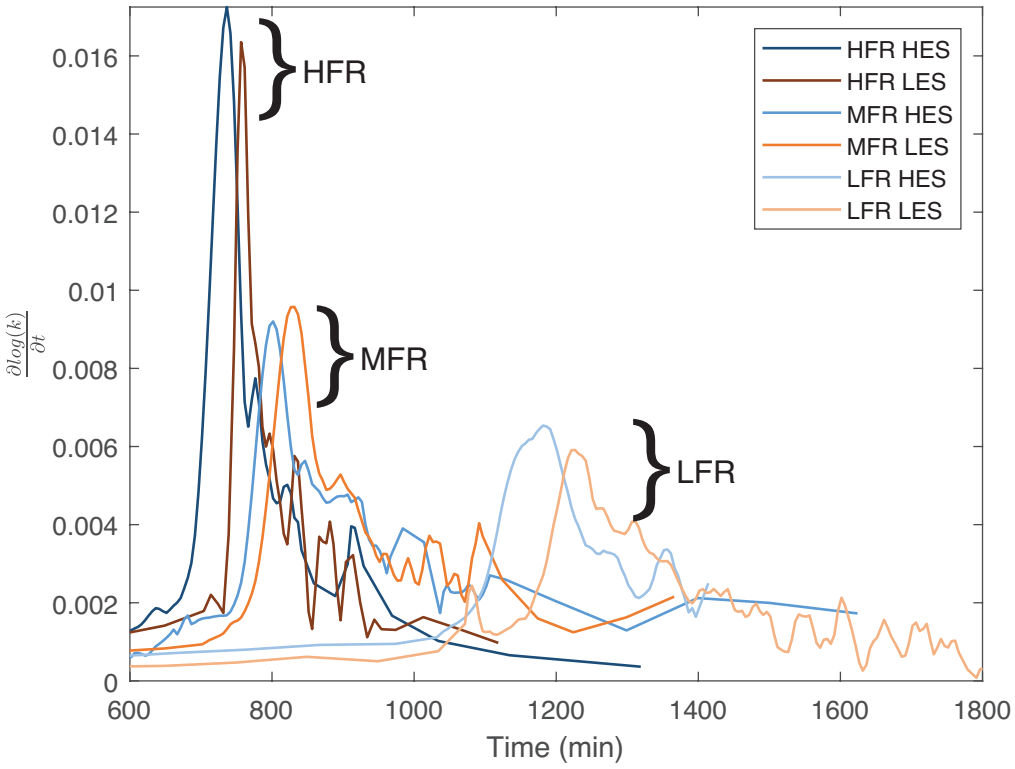

Figure 4.7: Derivative of the permeability with respect to time. Each major peak represents the maximum permeability generation during the breakthrough. Per family of PV_{rate}, the HES experiment has peaked before the LES one. The influence of the PV_{rate} is clear, with the HFR experiments peaking before the MFR ones, themselves peaking before the LFR floodings. Interestingly, the permeability is generated quicker as we increase the PV_{rate}.

By analysing our experimental permeability curves we are confident that the evolution of the relative permeability of each sample was not related to the amount of fluid injected. Figure 4.8 shows k/k_0 as a function of the amount of pore volume injected. Fredd and Fogler (1998) showed that a wormhole becomes ramified at higher injection rates due to the forcing of the fluid into smaller pores, increasing the dissolution over a larger surface area, further resulting in

an increase in pore volume required to breakthrough. We note that all breakthroughs were set at approximately the same k/k_0 value, and seemed relatively independent of the experimental scenario. While ramification, hence porosity evolution, shows signs of correlation with the PV_{rate} and effective stress scenario (cf. sections 4.5.2 and 4.5.3), this window of onset of breakthrough could be an indication of the relatively low influence of the acid front in our experiments, and obviously plays an inverse role to what previous studies have stated (Hoefner and Fogler, 1988; Maheshwari et al., 2013). Here we observed that the amount of fluid required to increase our average permeability neither greatly increased nor decreased with the injection rate or the effective stress scenario, and therefore any breakthrough and/or amount of pore volume to breakthrough could be linked to more complex processes than the chemical interactions between brine and rock.

We consider that a breakthrough could be energy-dependent, and can be exposed by observing the relationship between the actual breakthrough event and the rate at which the fluid is injected. The pore volume to breakthrough (PV_{bt} - Hoefner and Fogler (1988); Fredd and Fogler (1998)) can be accurately resolved for each curve by calculating $\frac{\partial \triangle P}{\partial^2 t}$ (figure 4.9) or $\frac{\partial log(k)}{\partial t}$ (figure 4.8). The breakthrough time can then be related to the amount of pore volume injected. We note that, for each sample, $\frac{\partial \triangle P}{\partial^2 t}$ reached a plateau before the permeability stabilized. This uncoupling between the behaviour of $\triangle P$ and the permeability evolution could be explained by an evolution of the Re number during the experimental flooding, leading to a more unstable fluid flow, slowly switching from a Darcy flow to a less laminar regime.

An analysis of figures 4.8 and 4.9 allows the estimation of PV_{bt} by knowing the time at which a breakthrough happened. Plotting PV_{bt} as a function of PV_{rate} (figure 4.10) shows that the amount of pore volume to breakthrough increased as we increased the PV_{rate}.

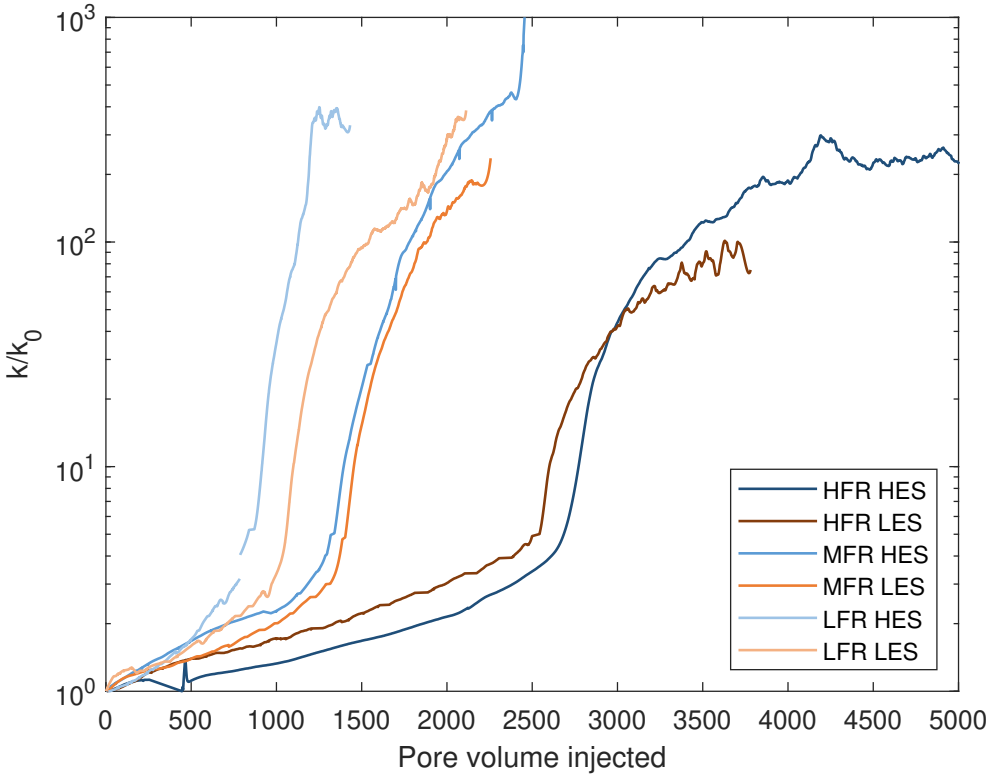

Figure 4.8: Normalized permeability generated as function of pore volume injected. Regardless of the PV_{rate} in use, each experiment have seen its breakthrough onset happening within a k/k_0 window spanning from 3 to 6 times the original permeability of the samples.

By itself, this exponential relationship can be an indication that another process than dissolution was involved in the triggering of breakthroughs: as the PV_{rate} was increased, the PV_{bt} was logically increased too. This could be explained by:

- A strong inverse relationship between porosity evolution and breakthrough event.
- A possible link between the energy input and evolution of $\triangle P$, which could relate to the mechanical action of water over the rock and/or the overall weakening of the sample as the porosity increases, especially near the walls of the wormholes (Egermann et al., 2006; Barri et al., 2016).

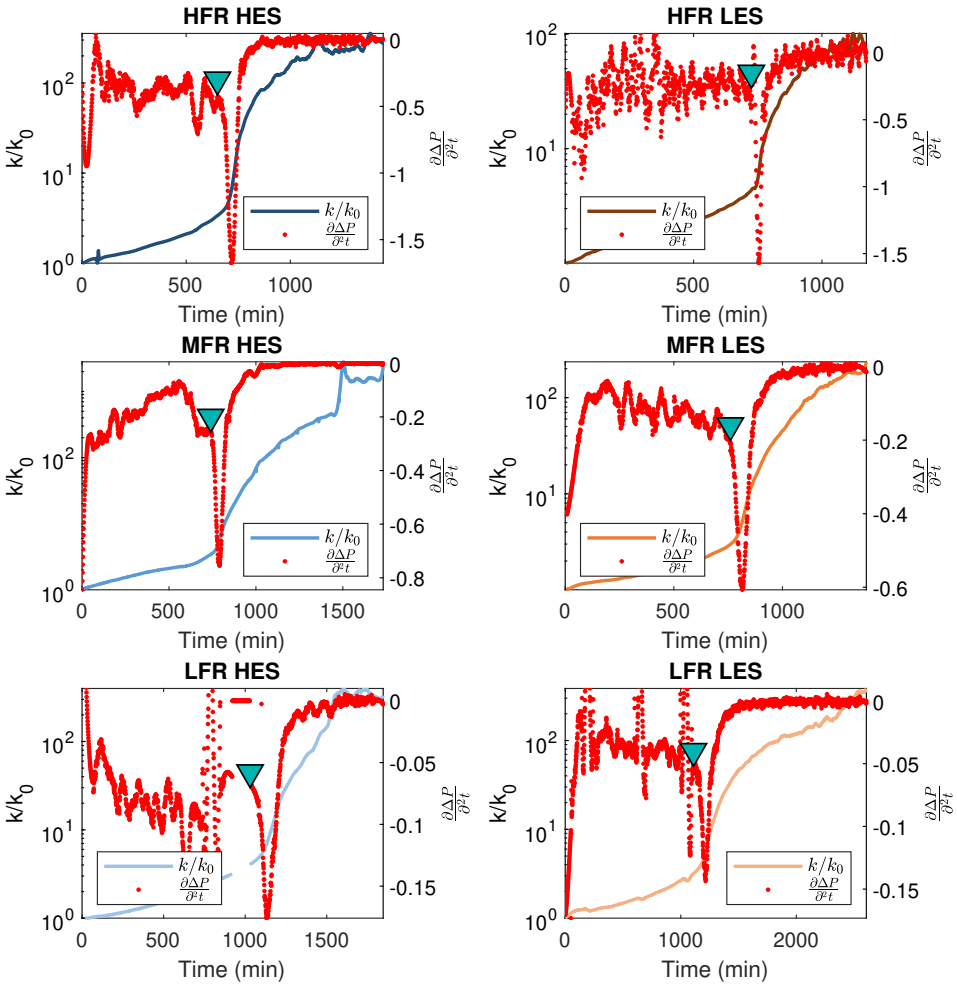

Figure 4.9: Differential pressure analysis and relative permeability evolution for the six experiments. The blue marker indicates the time at which a breakthrough begins. We observe the clear behavior of $\triangle P$ on k.

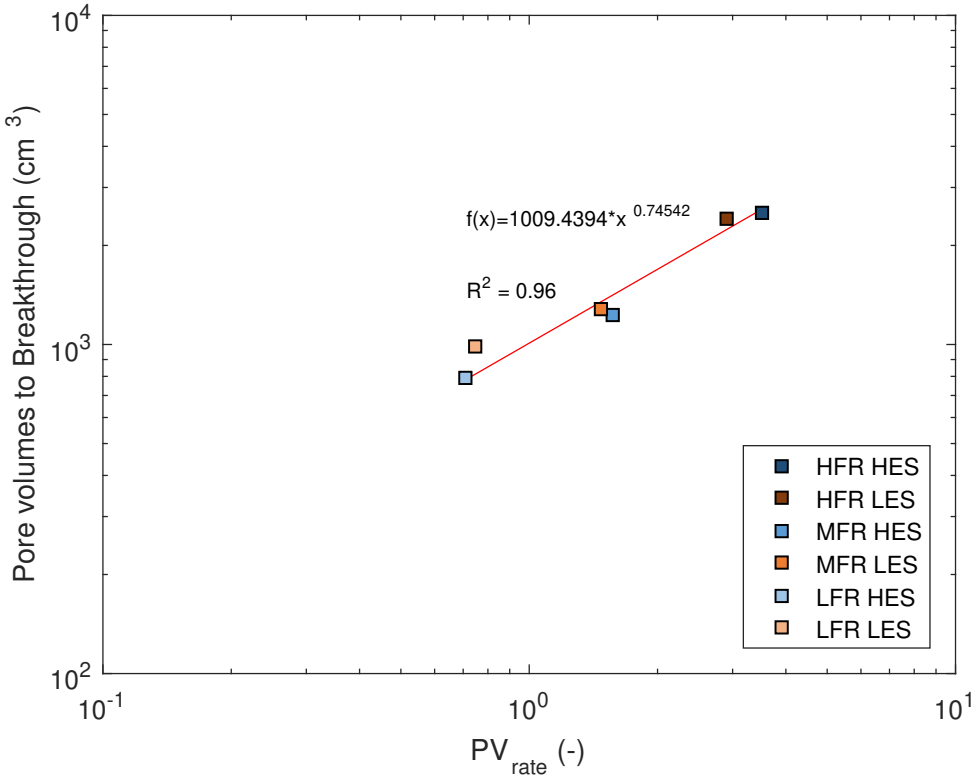

Figure 4.10: Pore volume to breakthrough as a function of constant PV_{rate} used for the six experiments. The values for PV_{bt} have been derived from the markers of figure 4.9, while the PV_{rate} values are given in table 4.1.

4.5.1.2 Calcium and magnesium evolution

In this section we present the concentration of calcium and magnesium, as well as the cumulative volume of both ions present in the effluent fluid, and normalized against the volume of solid of the rock sample (equation 3.12). This extra step aims to discard potential disparities in the sample sizes, either as a result of the cutting of the rock, or due to the petromorphological arrangement of the rock matrix itself.

Our $\triangle C_{Ca}$ displayed positive values throughout each experiment ($\triangle C_{Ca} > 0$),

implying that calcium removal occurred during flooding phases (Luquot et al., 2016). This is also confirmed by the pH measurements whose values were consistently higher than the pH of the injection brine (∼7 - figure 4.11). The pH values displayed a sharp increase at the first stages of the experiments, which is attributed to a flushing phase of the saturation brine (pH ∼7), before slowly stabilizing at pH 9-10.

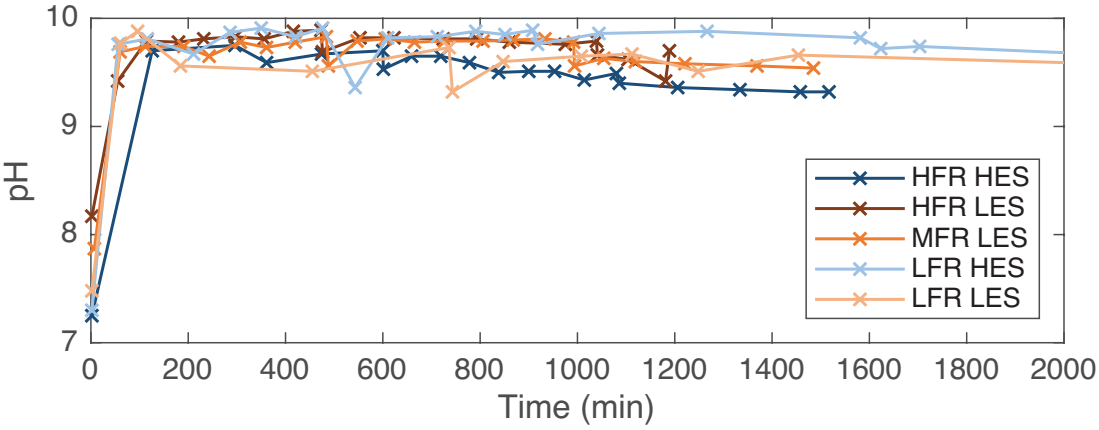

Figure 4.11: pH measurements for 5 of the 6 experiments. All measures have been done on sub-samples of the fluid before ICP analysis.

Ion behaviour

In this section, we have discarded the LFR results for calcium calculations as the values were abnormally high, which could be explained by an external contamination that happened during sample processing or during ICP-MS analysis. Further modelling using web-phreeq (Saini-Eidukat and Yahin, 1999) showed largely supersaturated samples, confirming an external contamination. Figures 4.12 and 4.13 display the Ω ratio (cf. equation 3.12) respectively for calcium and magnesium removal. The general behaviour for calcium seems to follow a similar trend to the permeability (figure 4.6), with most calcium removed from the rock at high PV_{rate} rather than at medium PV_{rate}. A similar trend is identified for

magnesium, which appears to be an excellent proxy for our rock flooding experiments: as expected, the intensity of Ω decreased as we decreased the PV_{rate}. We observe a dichotomy between 1) the flow rate, and 2) the effective stress. Within a family of PV_{rate}, we see that the higher the effective stress, the larger Ω was, which supports a tendency previously noticed with the permeability evolution. If, for calcium concentrations, the alternation between HES and LES experiments starts to demonstrate the influence of the effective stress on carbonate alteration, the clear arrangement between blue and orange curves displayed on figure 4.13 is a robust argument that shows how important the effective stress variable is for magnesium dissolution. Indeed, with a PV_{rate} of 0.7, the $LFR\ HES$ scenario managed to dissolve a similar amount of magnesium than the $MFR\ LES$ scenario, whose rock sample was flooded at twice the PV_{rate} of $LFR\ HES$. A similar description is valid between the $MFR\ HES$ and $HFR\ LES$ experiments.

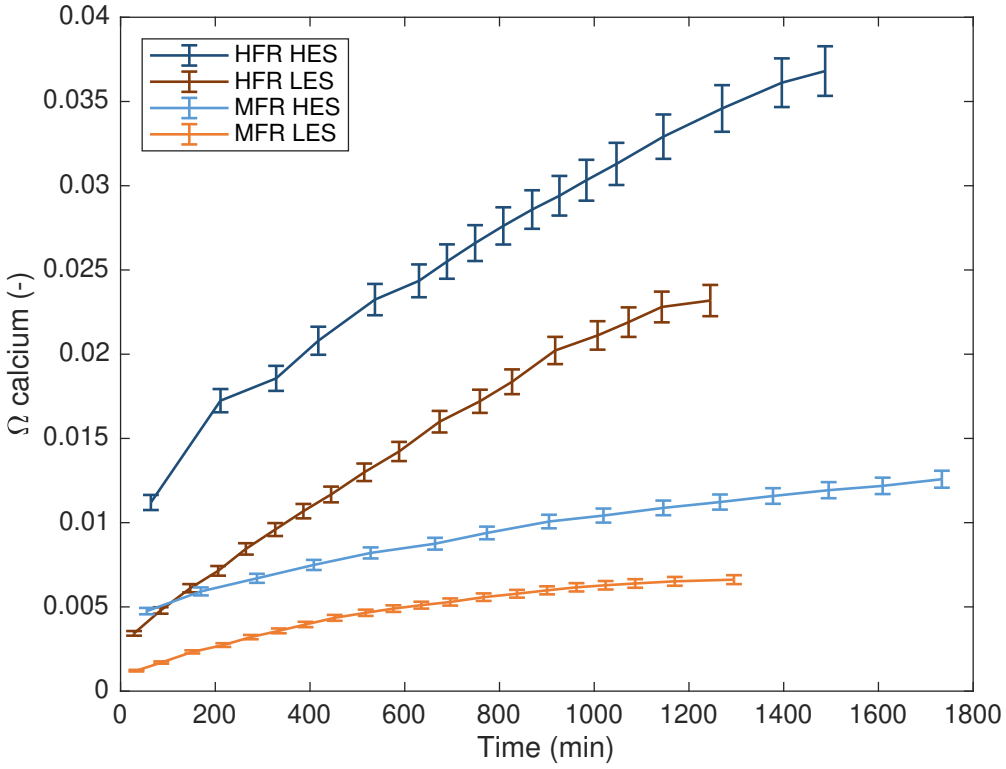

Figure 4.12: Volume of calcium derived from the effluent fluids sampled directly out of the Hassler cell and normalized against the original volume of rock of the core sample (Ω). The low flow rate experiments have been discarded with regards to the abnormally high content values. The curves splits in two families, with the HFR experiments on top of the MFR experiments. Within a family of PV_{rate}, the HES experiment has dissolved more Ca than the MFR one.

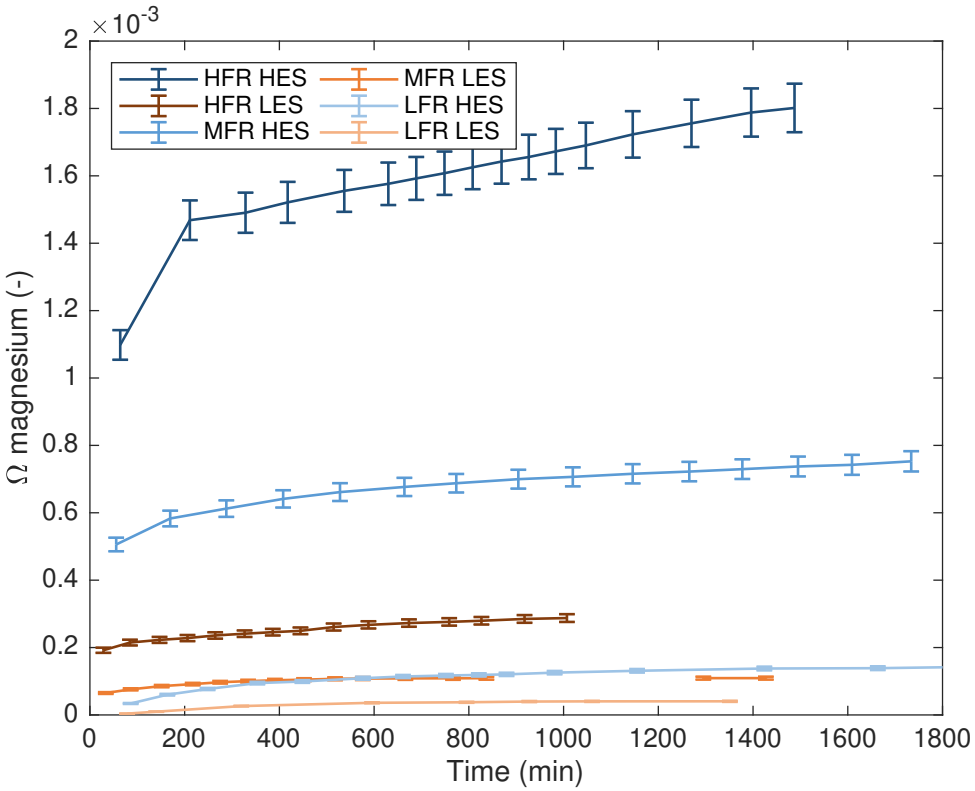

Figure 4.13: Volume of magnesium derived from the effluent fluids sampled directly out of the Hassler cell and normalized against the original volume of rock of the core sample (Ω). It appears that Mg has largely reacted to a larger effective stress with the HES experiments on top of the LES ones.

The concentrations of Ca and Mg ions have been calculated for each minute of flooding and per cubic meter of fluid injected through each sample. As shown in figures 4.14 and 4.15, the concentration of species in our effluent fluid seems to be the results of 1) the effective stress, and 2) the PV_{rate} as we note a clear division of HES curves grouping on top of the LES ones. Here, we observe for the second time the catalytic influence of a high effective stress on rock matrix alteration stimulation. We also observe a clear different mechanical response between the two ions, mainly mobilized under the form of dolomite, chlorite, ankerite and illite.

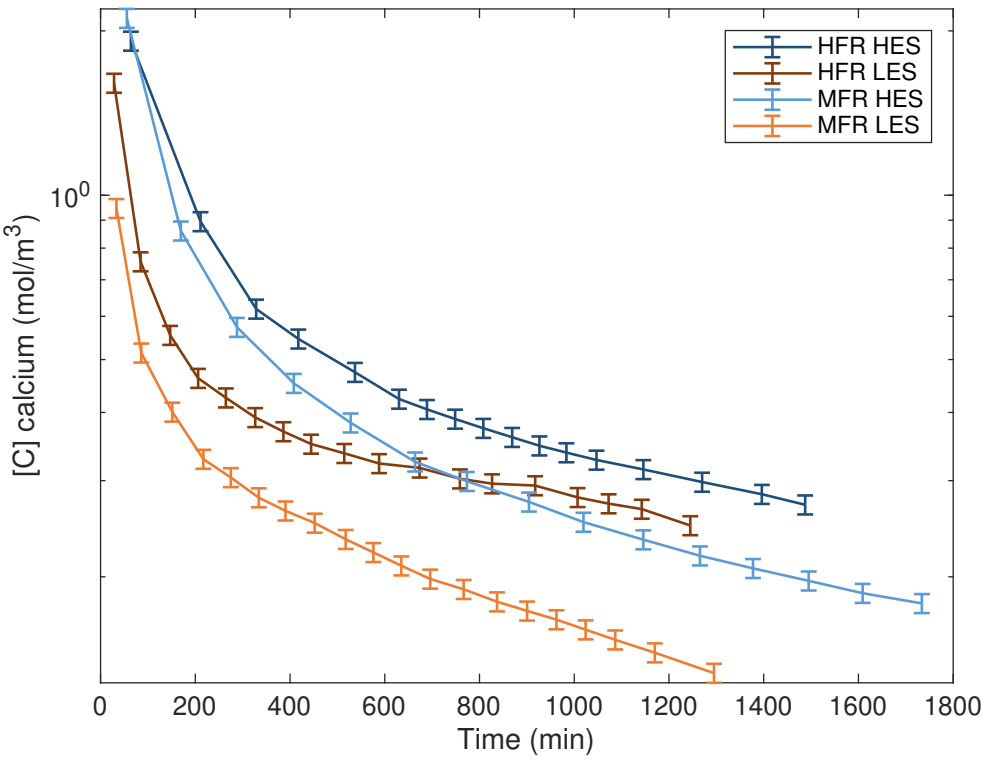

Figure 4.14: Concentration of calcium derived from the effluent fluids. The low flow rate experiments have been discarded with regards to the abnormally high content values. The impact of the effective stress is visible with the HES group gathering on top of the LES one. Within each group, the influence of PV_{rate} is respected, so that a higher flow rate generates more Ca.

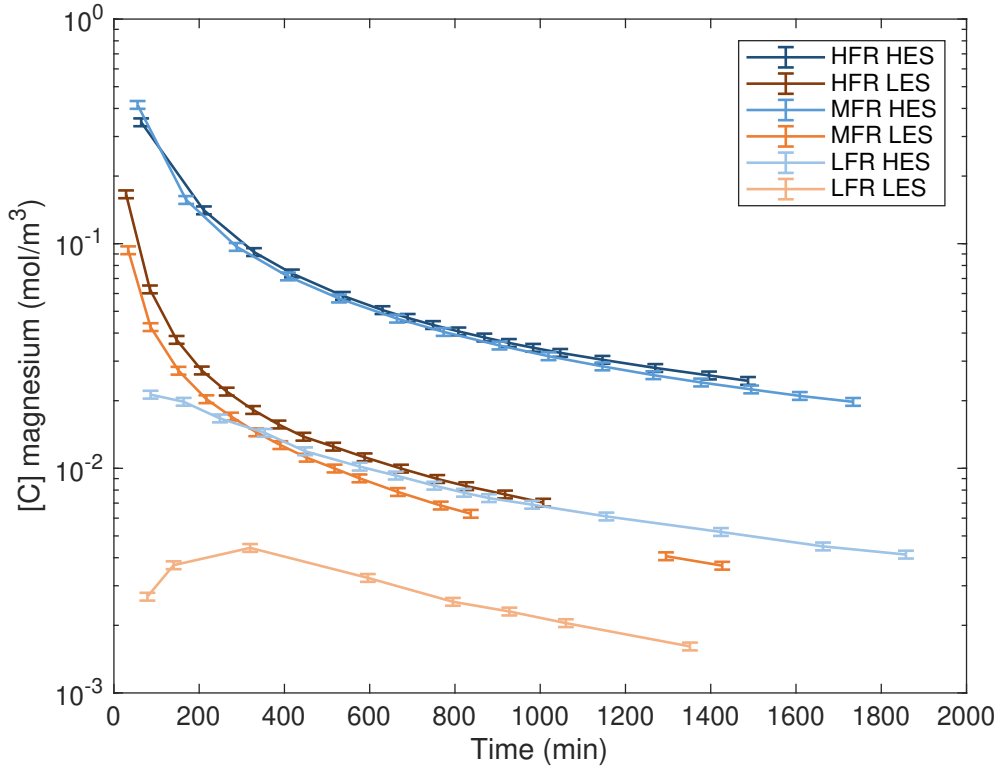

Figure 4.15: Concentration of magnesium derived from the effluent fluids. Mg has largely reacted to a larger effective stress: the HES group is displaying larger [C] in Mg than the LES one. Within each group, the influence of PV_{rate} is respected, so that a higher flow rate generates more Mg.

Normalized ion behaviour

We have normalized the results of equation 3.12 by the PV_{rate} values found in table 4.1 in order to remove the effect of the injection rate while isolating the impact of the effective stress. Figures 4.16 and 4.17 present the results of the above-explained normalization and demonstrate, for a given experimental scenario, the capability stress state has to remove Ca and Mg ions from an Indiana limestone sample. Figure 4.16 shows the alternation of curves for calcium removal. The ordering previously seen in figure 4.12 has changed, now with the HES experiments (blue curves) gathering on top of the LES ones (orange curves). The normalized magnesium values (figure 4.17) display a similar behaviour, this time with a very clear gathering of the HES experiments on top of the LES ones, indicating that for a given PV_{rate}, the capability of removing either ion was greater at high effective stress. As expected, within each group of effective stress, We can observe that the HFR experiments (darker curves) remain on top of MFR and LFR (lighter curves).

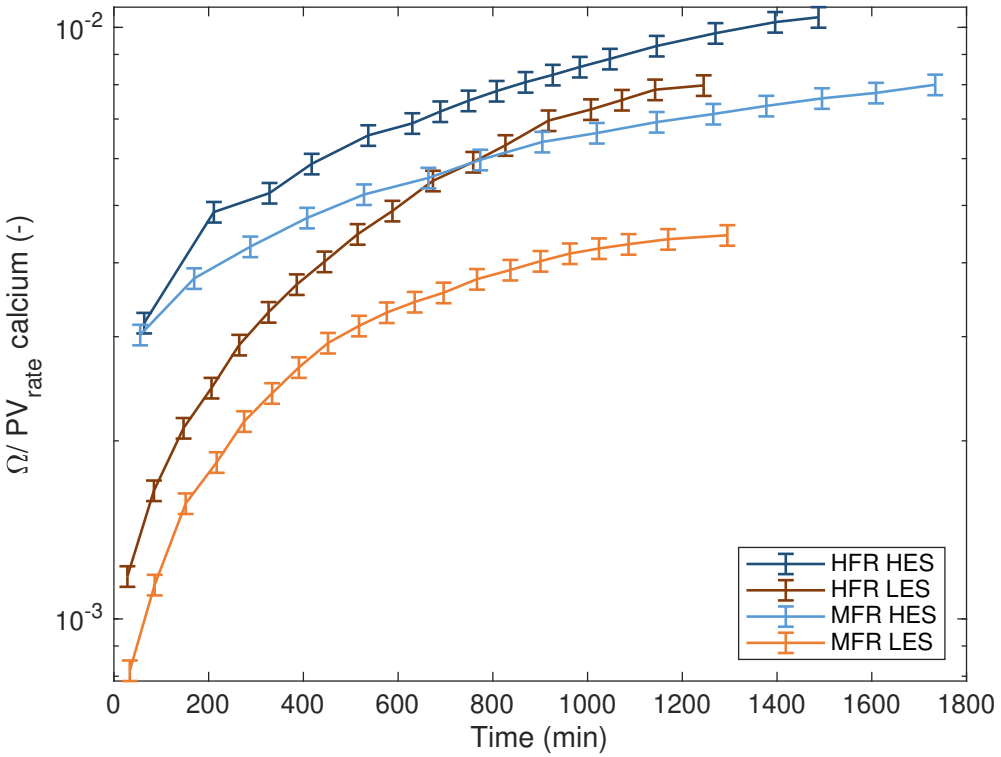

Figure 4.16: Dimensionless capability of calcium to be removed from a carbonate rock during water flooding. The low flow rate experiments have been discarded with regards to the abnormally high content values. A high effective stress (blue curves) appears to be more capable of dissolving calcium, assisting the flow rate which remains the prime variable.

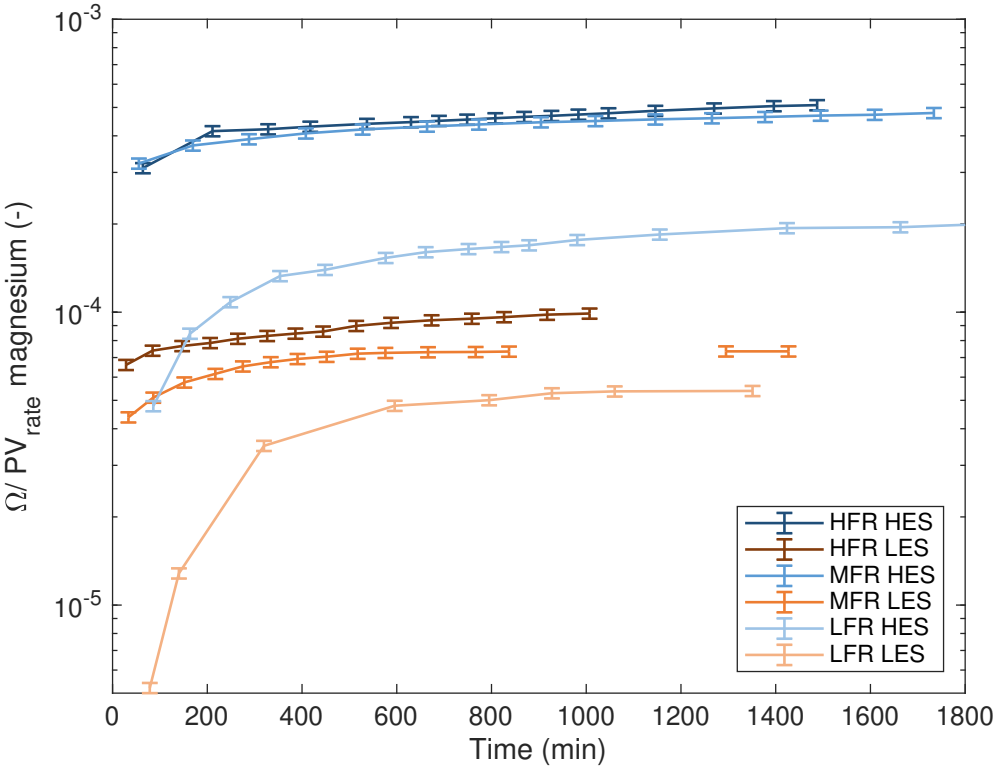

Figure 4.17: Dimensionless capability of magnesium to be removed from a carbonate rock during water flooding, at different PV_{rate} and effective stresses. A high effective stress (blue curves) appears more capable of dissolving magnesium, assisting the flow rate, which remains the prime variable. Mg seems to be very reactive to the effective stress, particularly visible with the $LFR\ HES$ experiment more 'capable' than the $HFR\ LES$ one ($PV_{rate\ HFR\ LES}$ is 3 times larger than $PV_{rate\ LFR\ HES}$).

4.5.2 µCT analysis for rock alteration

Figure 4.18 shows the six experiments through three subplots split into the three different families of pore volume rate. The mean values for channel thickness are shown in table 4.4. We have used a Region Of Interest (ROI) for each calculation of the mean in order to avoid both ends of the sample where the µCT signal was usually more noisy and could lead to over or under interpretations of the images. Moreover, and for unknown reason, we observed abnormally high thicknesses which translate by local peaks. This is attributed to a large amount of nodes clustered at a branching, which could lead to a repetition in the thickness of a same branch. Nevertheless, the general trend displays rather constant curves with local heterogeneities. On average, the total thickness is higher at HES rather than at LES.

Sample	Length (mm)	Mean thickness (mm)	ROI From/to (mm)
$HFR\ HES$	38.6	10.93	5/35
$HFR\ LES$	47.7	9.14	5/35
$MFR\ HES$	45.35	5.21	5/45
$MFR\ LES$	46.63	5.12	5/45
$LFR\ HES$	46.18	6.52	5/45
$LFR\ LES$	49.21	3.64	5/45

Table 4.4: Sample length and total channel thickness for the six experiments.

Figure 4.19 displays the density of the dissolution as seen from the top of a core sample. This density has been calculated from the points coordinates gathered by the Auto Skeleton function in Avizo® 9. At low injection rates, the density of nodes present within a certain area should increase as we observe regular and straight wormholes (i.e. a large amount of points at approximately the same X and Y location), while at higher injection rates, a ramified distribution of the

porosity should involve main branches in addition to less dense areas surrounding the main routes.

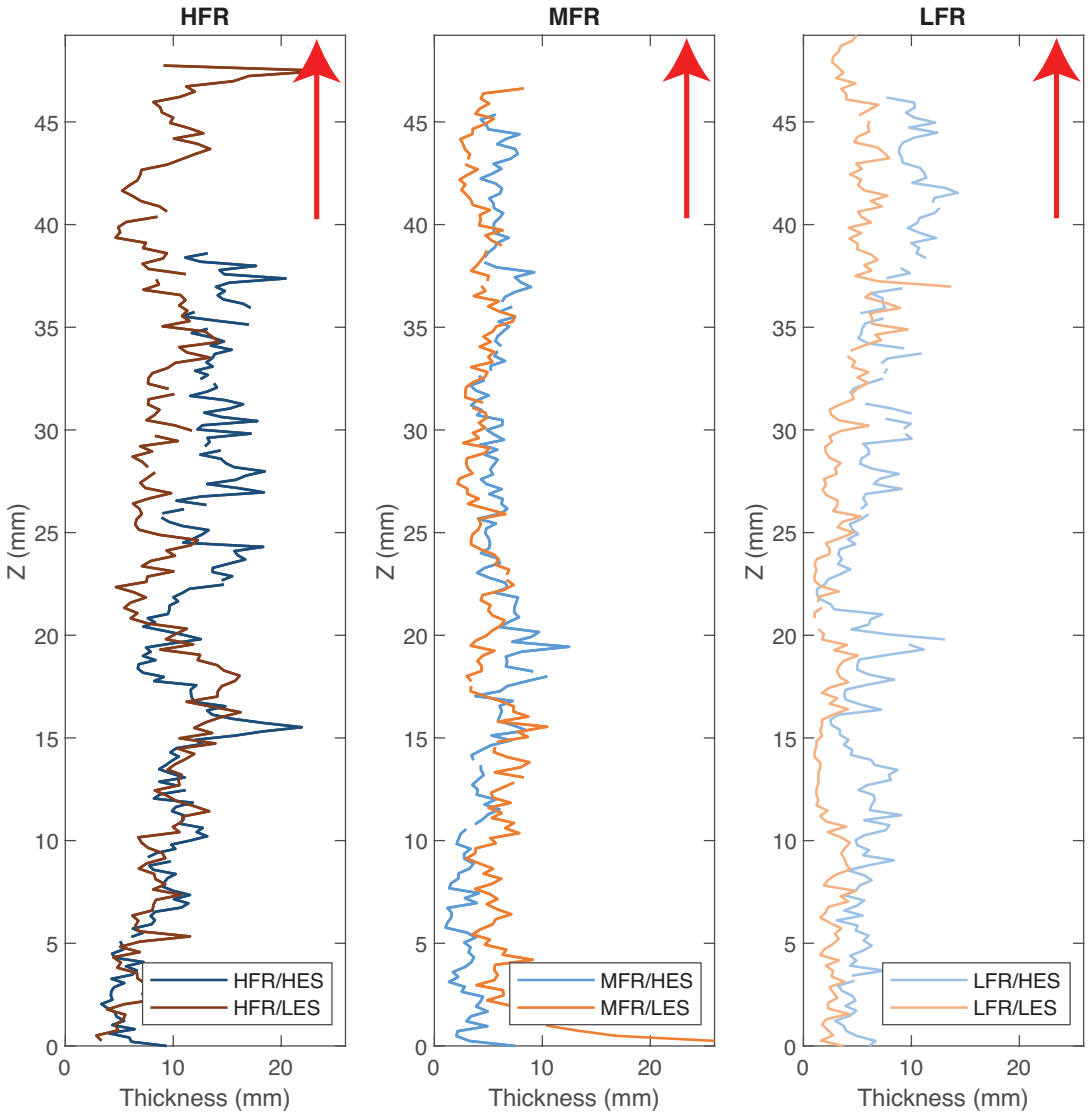

Figure 4.18: Cumulative thickness of the main wormholes and channels. The cumulative thickness has been calculated from the skeletons of the wormholes left after each experimental flooding. The red arrows show the flow direction.

The density subplots can be compared horizontally and vertically. For each family of effective stress (vertical comparison), we note that as the injection rate decreases, the degree of ramification also decreases, which demonstrates that

the ramification of a wormhole in homogeneous carbonates in primarily linked to the injection rate. The amount of dissolution witnessed by the $LFR\ HES$ experiment as well as the thickness of the wormhole (figure 4.18) remained higher than expected. It could be explained by a failure of the experimental setup during the middle stages of the experiment (i.e. missing data on figures 4.5 and 4.6). This failure could have caused more or less important changes in the confining pressure, leading to an unexpected matrix stimulation. Another explanation is linked to the higher porosity of this sample, which could have led to an easier ramification, itself relating to the fact that the permeability of rocks decreases with a decreasing porosity (Bernabe et al., 2010). The right hand subplots of figure 4.19 display a similar trend as the left hand ones, where the alteration increases as the flow rate increases. Horizontally, and for a similar PV_{rate}, the ramification, and apparent dissolution seems higher on the HES side.

In case of local or global homogeneity, the fluid follows the local pressure gradients created by possible heterogeneities (Izgec et al. (2010); Siddiqui et al. (2006); Kalia and Balakotaiah (2009); Teles et al. (2016) and chapter 7). The high homogeneity of the Indiana limestone explains the increased and homogeneous branching of the dissolution channel at high PV_{rate}, while the branching decreases as we lower the PV_{rate}, to end up with a main wormhole likely caused by a front dissolution without any forcing of the fluid, coupled with the amount of energy withstood by the system (appendix L). While a tortuous pattern of a wormhole can be caused by vugs driving the fluid flow (Izgec et al., 2010; Teles et al., 2016), we observe here that tortuous pattern also results in higher PV_{rate}, as previously described in the dissolution map (figure 4.2).

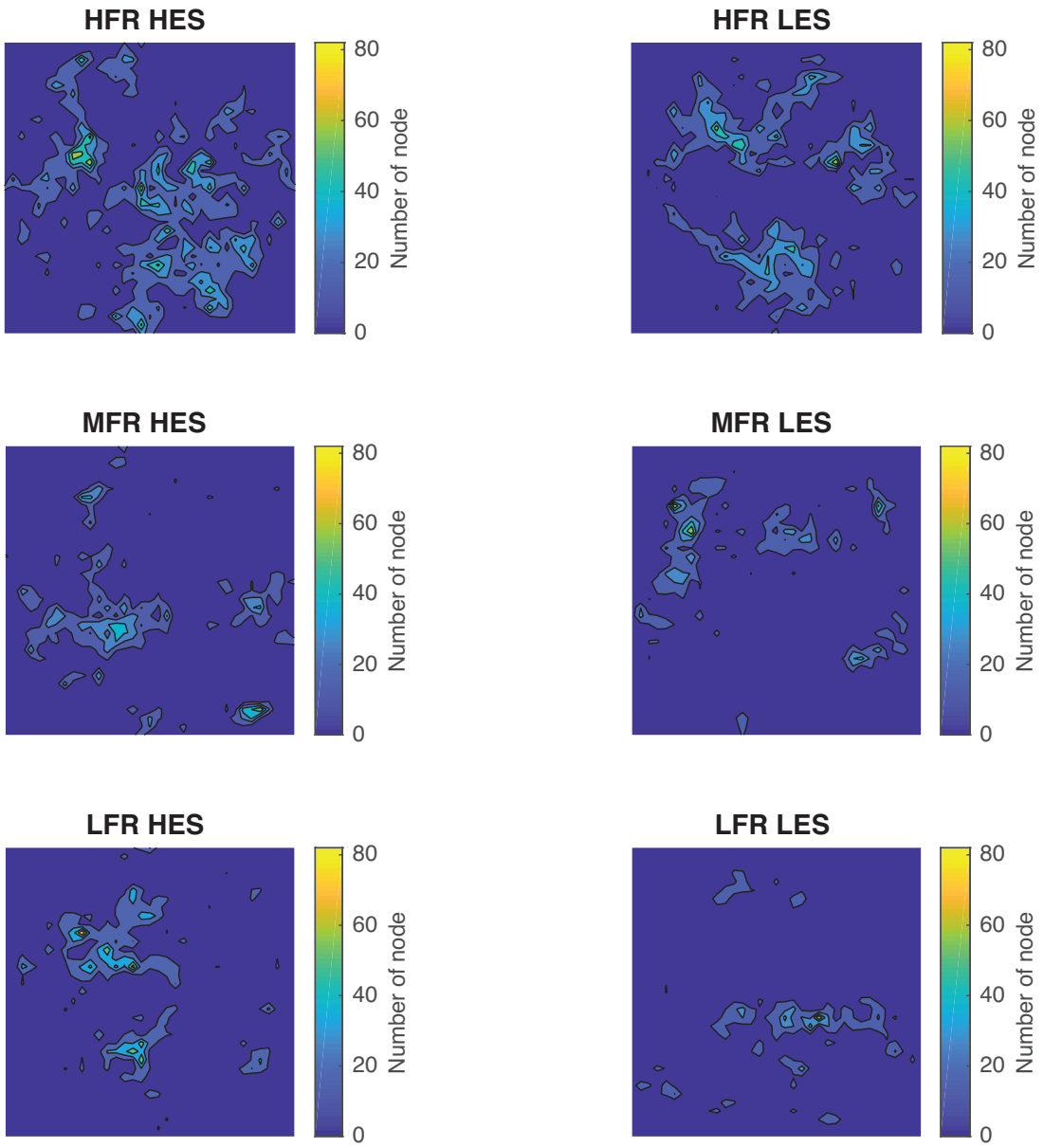

Figure 4.19: Density plot of the dissolution pattern. Each picture displays the nodes forming the skeleton shape of the wormhole left after flowing. Left subplots show the HES experiments; right subplots show the LES experiments. The color-scale displays the amount of nodes in the Z axis. Each square is 3.8 cm by 3.8 cm.

4.5.3 Porosity evolution

The porosity evolution calculations of the Indiana limestone experiments was based on the work of Luquot and Gouze (2009), while we used equation 3.13 in order to derive the porosity evolution from calcium and magnesium dissolution. Our in-house XRD analysis of the bloc of Indiana limestone revealed it to be mainly composed of calcium and magnesium; the main contributors for calcium and magnesium being calcite and dolomite. For simplification purposes, we assumed that all the Mg was provided by the dolomite, while the remaining Ca from the calcite. The remaining ∼3 % were not accounted for this calculation. Figure 4.20 presents the normalized porosity evolution for four experiments calculated using equation 3.13. Two families of flow rate are well defined, while within a family of flow rate, the high effective stress experiments seems to produce more porosity than the low effective stress ones. As stated in section 4.5.1.2, the porosity calculation cannot account for the $LFR\ LES$ and $LFR\ HES$ experiments due to probable calcium contamination during sampling.

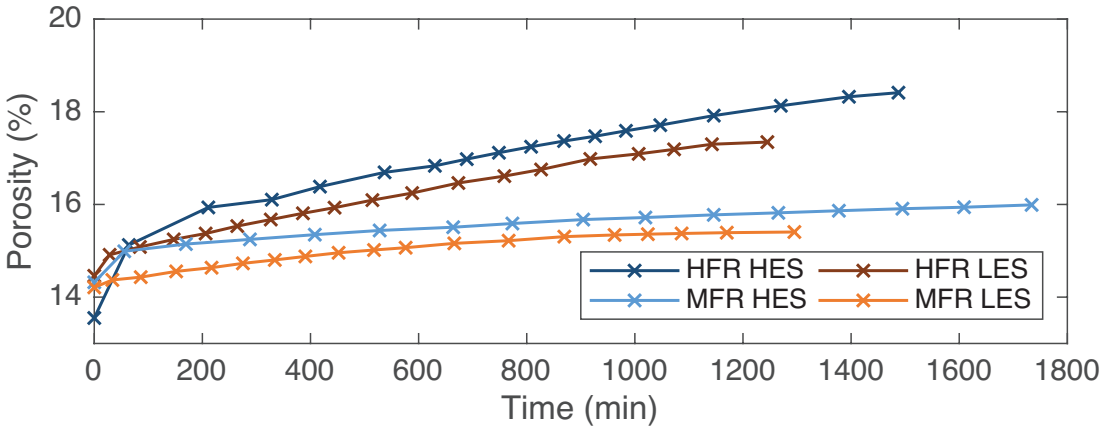

Figure 4.20: Porosity evolution calculated from Ca and Mg mass balance.

Figure 4.2 can be qualitatively updated. Golfier et al. (2002) have set boundaries that are valid for an acid capacity number (Nac) of 4.66×10^{-2}. Due to the neutral pH of our injection fluid, the Nac value for our experiments averages at

1.16×10^{-5} (cf. section 2.3.3). As seen in figure 4.2, the experimental scenarios described in table 4.1 should have generated a uniform type of dissolution within the rock matrix according to the boundaries set by Golfier et al. (2002). Figures 4.21, 4.22, and 4.23 present the physical damages caused by the experimental flooding. We observe that more rock matrix was dissolved as the PV_{rate} was increased, as well as a slight matrix stimulation at higher effective stress for a given PV_{rate} (left hand side). While all the samples withstood changes, we have not noticed any kind of uniform dissolution.

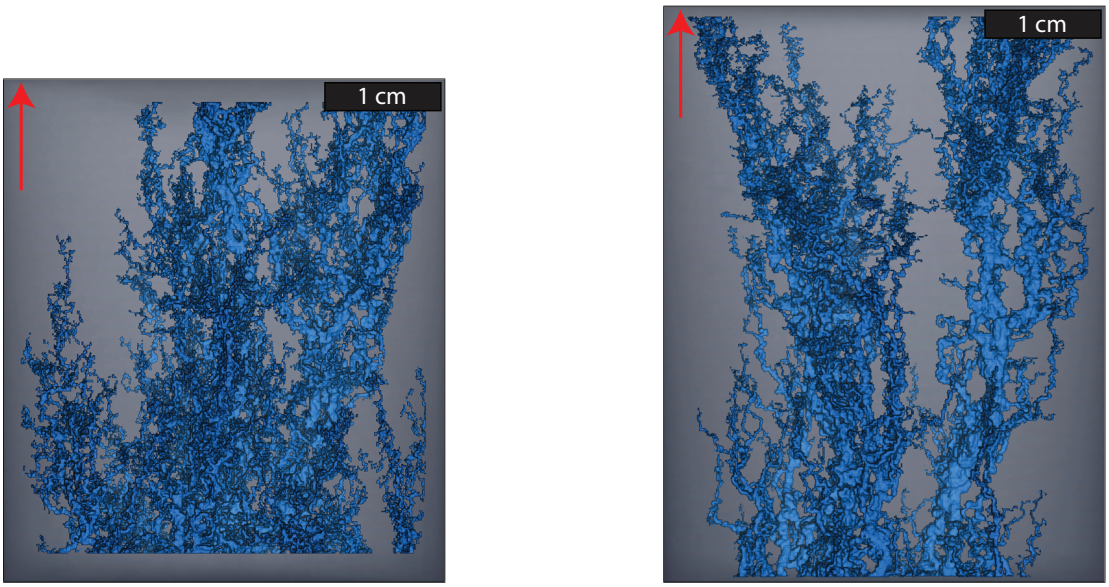

(a) $HFR\ HES$ **(b)** $HFR\ LES$

Figure 4.21: µCT scans of the HFR experiments. The 3D volumes have been computed under Avizo® 9. The fluid was injected from bottom to top (red arrow).

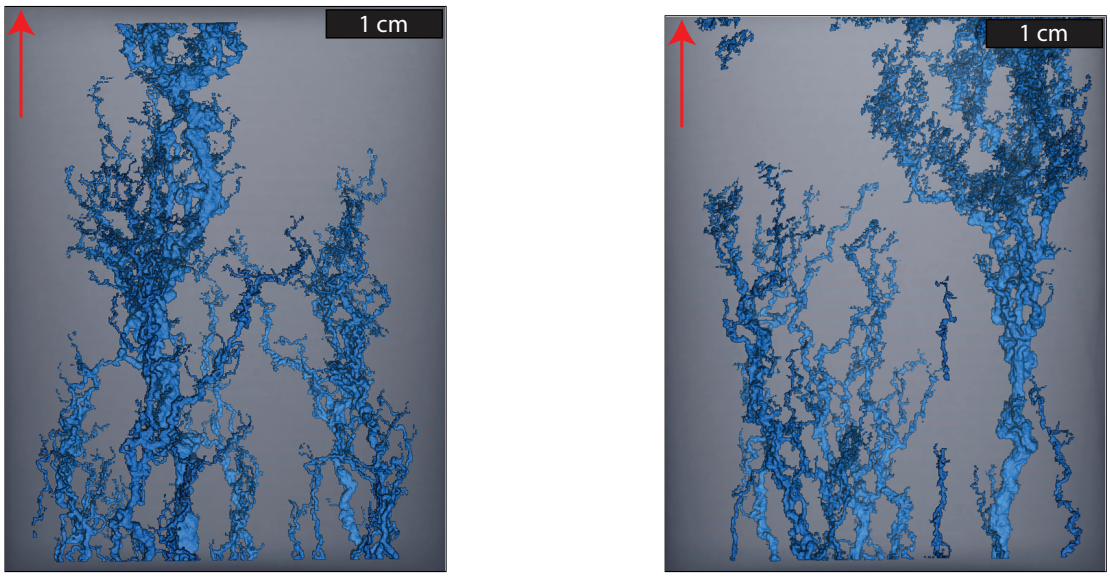

(a) $MFR\ HES$ **(b)** $MFR\ LES$

Figure 4.22: µCT scans of the MFR experiments. The 3D volumes have been computed under Avizo® 9. The fluid was injected from bottom to top (red arrow).

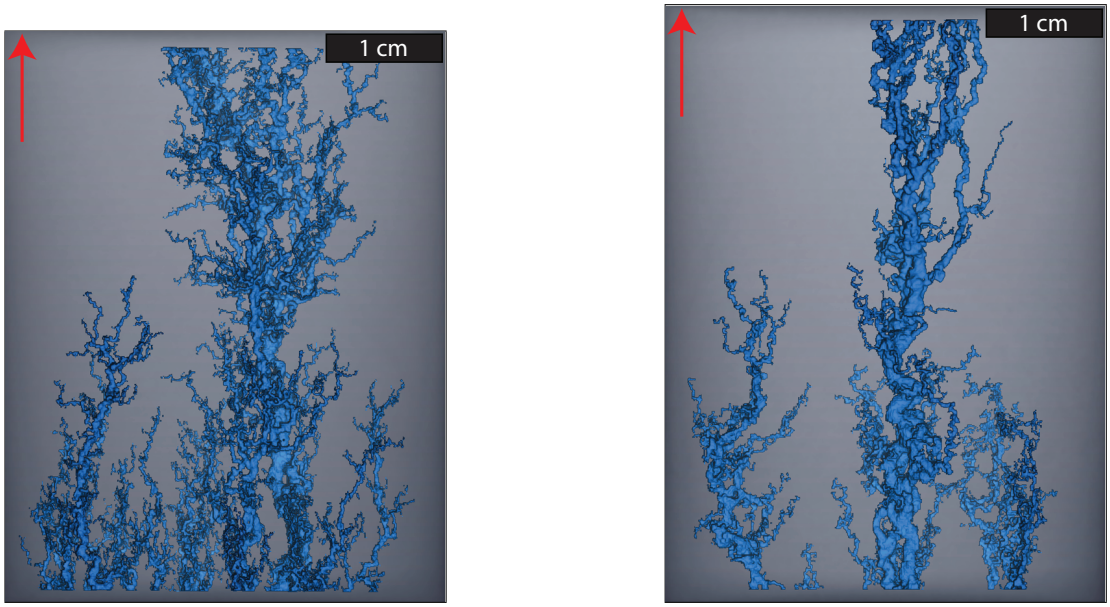

(a) $LFR\ HES$ **(b)** $LFR\ LES$

Figure 4.23: µCT scans of the LFR experiments. The 3D volumes have been computed under Avizo® 9. The fluid was injected from bottom to top (red arrow).

We suggest new boundaries for the dissolution map, and for a seawater-calcite system, based on qualitative assessments of the dissolution patterns. Figure 4.24 shows the new dissolution limits: the red line is supposedly not fixed, and our data suggest that the stress state has positively affected the rock matrix dissolution, and could represent a 3rd dimension on this graph. The red arrow shows the direction of the shift if a high effective stress was applied to this homogeneous type of rock during seawater flooding, suggesting that the experimental response would tend towards a more ramified system at higher effective stress. Conversely, lowering the effective stress would result in dissolution falling in the dominant wormhole regime.

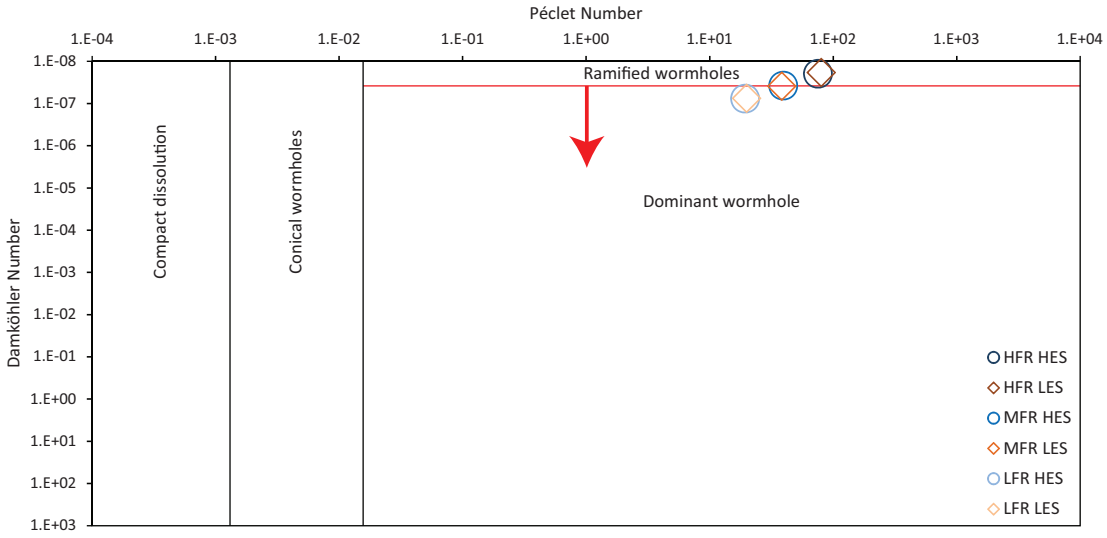

Figure 4.24: Suggested new boundaries for the dissolution map of Golfier et al. (2002). The new boundaries have been shifted after a qualitative assessment of the experiments presented in this chapter, and correspond to a seawater-calcite system. The red line is supposedly affected by the stress state while the arrow indicates the shift direction.

4.5.4 Interpretation

While the influence of the injection rate, here termed PV_{rate} was expected, the influence of the effective stress has been attributed to different processes (mechanical and chemical) taking place at different regions within each porous medium. Figures 4.25 and 4.26 represent the processes thought to be responsible for the largest generation of k/k_0, [C] in Ca-Mg, and porosity increase and spreading for Indiana limestone under a higher effective stress (lower line pressure). The large confining pressure (red arrows) applies a constant pressure over an homogeneously distributed surface contact (red lines). The contacts in figure 4.25 are dissolving first by potential pressure solution. Pressure solution can be considered the dominant mechanism by which both a change in permeability can be achieved and elevated concentrations of species in the effluent could be obtained. Figure 4.26 represents the rock state during experimental flooding: the first zones to be altered are the pore throats, which over time should keep dissolving as the confining pressure largely overcomes the low fluid pressure (blue arrows), and should tend to close/reduce the size of the pore throats. Wall dissolution would occur at later stages, when enough dissolution would form a flow-path, which then should drive the fluid flow.

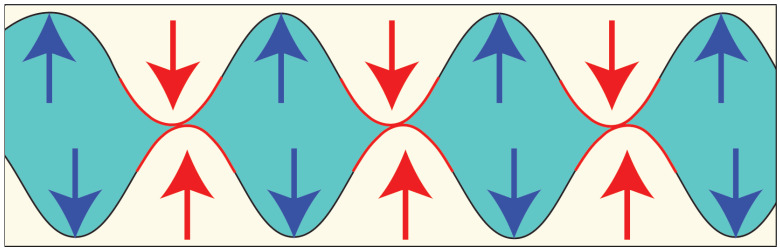

Figure 4.25: 2D sketch of an homogeneous rock before experimental flooding. The blue arrows represent a low fluid pressure, the red arrows a high confining pressure, and the red lines are regions of likely dissolution.

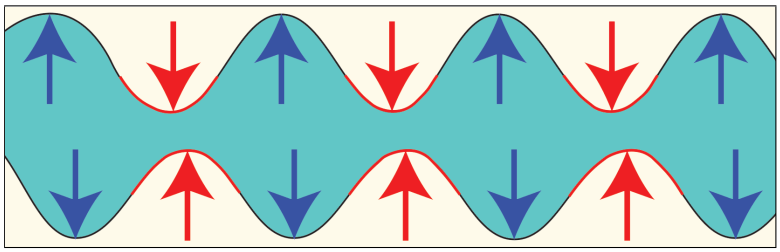

Figure 4.26: 2D sketch of an homogeneous rock during/after experimental flooding. The blue arrows represent a low fluid pressure, the red arrows a high confining pressure, and the red lines are regions of likely dissolution.

Referring to section 2.7.4 in chapter 2, we note that the limit for observing pressure solution is set to 25 MPa. We assume that the large amount of contacts between grains in the homogeneous Indiana limestones, coupled to a high effective stress scenario (40 MPa), has led to a coupled system where chemical dissolution was assisted by some degree of pressure solution. Conversely, the late breakthrough onset, as well as the lower amount of Ca-Mg in the effluent fluid in the case of the *LES* experiments is attributed to an effective stress value lower than the above limit (10 MPa).

4.6 Conclusion

pH neutral seawater has been injected at different rates and pore pressures in order to obtain an experimental matrix that allowed us to isolate the pore volume rate and effective stress variables for independent analysis. We have flooded six rock sample of similar sizes and poro-permeability under reservoir conditions of P-T, and up to 2,500 min, allowing the samples to withstand and react to the forces in play for extended periods of time.

Studies have shown the relationship between carbonate poro-permeability evolution and injection rate, as well as the likely calcite-water interaction using acid based fluids which lowers the pH of the solution (Frick et al., 1994a; Bazin et al.,

1995; Fredd et al., 1996; Fredd and Fogler, 1998; Golfier et al., 2002; Egermann et al., 2006; Luquot and Gouze, 2009; Menke et al., 2015; Ott and Oedai, 2015; Barri et al., 2016; Luquot et al., 2016; Teles et al., 2016; Zhang et al., 2016). The usual consequence being a higher dissolution rate, and a greater wormholing process at high flow rates (Garcia-Rios et al., 2014) which led to shorter experimental time. In his work, Barri et al. (2016) noticed negligible changes in compressional and shear wave velocities leading to the conclusion that the original stiffness of the rock allows it to maintain its elastic properties intact even after flooding. While it is agreed that mechanical effects take place in a dissolving sample, especially near the walls of a wormhole (Walle et al., 2015; Barri et al., 2016), in this study, we noticed a strong coupling between the effective pressures and the permeability generation leading to the following key findings: our results suggest a strong relationship between the rate of injection of the fluid, the experimental stress state, and the dissolution of the rock matrix. Although we acknowledge the impact of the injection rate over the rock matrix (further discussed in section 8.2.1), our experimental outputs indicated that a high effective stress played a large secondary role for permeability recovery, which complements previous studies based on sandstone samples (Zoback and Byerlee, 1975, 1976; Davies et al., 1999), where a stress dependency was found, so that the overall permeability would decrease with an increases stress. Here we observed an opposite trend for Indiana limestone under constant flow rate, where a high effective stress resulted in a stimulated permeability increase.

- Permeability: we have focused our study on the onset time or wormhole development, as well as the rate at which a wormhole forms. Results are two-fold: the prime variable for wormhole formation appeared to be linked to the PV_{rate} (later described as a proxy for total energy in section 8.2.4), followed by a high effective stress which acted as a secondary stimulant. For each experiment, the breakthrough event was influenced by the PV_{rate}

(cf. equation 3.7 in section 3.5), while for a given PV_{rate}, the HES scenario always observes its breakthrough happening before a LES scenario.

- Chemistry: following the permeability results, all chemical outputs converged towards the leading role of PV_{rate} while a high effective stress improved Ca and Mg recovery. The Ω values for both ions showed clear signs of the influence of a high effective stress over the volume of Ca-Mg released. Normalized Ω and concentration values clearly displayed the large influence the HES scenario in the dissolving process.

- µCT imaging: the analysis of pre- and post-µCT volumes and subsequent extrapolated data confirmed the positive relationship between porosity increase and the association between a high PV_{rate} and a high effective stress. We observed an increased porosity as we increased the PV_{rate}. Interestingly, the volume of fluid to be injected into a sample in order to obtain a breakthrough increases as the PV_{rate} is increased, leading to the conclusion that the amount of material removed due to fluid renewal might play a small role compared to other, unidentified, process(es).

Although it is acknowledged that the rate of the injection fluid is the controlling variable for poro-permeability recovery, often referred to as the optimum injection rate (Wang et al., 1993; Frick et al., 1994b; Bazin et al., 1995; Fredd and Fogler, 1998; Panga et al., 2005; Siddiqui et al., 2006; McDuff et al., 2010; Maheshwari et al., 2013), we now believe that effective stress plays a major secondary role in the rate at which this poro-permeability can be enhanced. Therefore, this work contributes to the understanding of the mechanical impact of effective stress on rock matrix alteration, with the prime aspect of using in-situ P-T conditions.

Chapter 5

Observation of wormhole formation at variable effective stress and injection rate on travertine rocks

5.1 External Contributions

Petrobras and Shell have provided us with travertine blocks. Rock coring has been realized by Alex Jackson. Dr. Ian B. Butler has provided help during µCT scanning phases and post-processing scan analyses. ICP-MS fluid sample analyses have been carried out by Dr. Laeticia Pichevin. Finally, Nic Odling assisted with XRD analysis of rock samples.

5.2 Summary of the chapter

5.2.1 Rationale

Chapter 5 has been coupled with chapter 4 to form a comprehensive scientific report (available in appendix J), while parts of this work have been presented at the EAGE 2018 (Brondolo et al., 2018a). Due to the unpredictable and heterogeneous nature of the media, only ∼5-10 % of the core samples have been selected for further experimental work. Only four samples produced consistent experimental dataset (additional work including three samples -not presented in this thesis- is described by Brondolo et al. (2018a)). This work allows to constrain the impact of heterogneities and effective stress over a physically poorly known rock-type.

5.2.2 Summary

The relationship between permeability enhancement and injection rate has been widely studied for the past 30 years. It is agreed that an optimum injection rate exists so that a minimum amount of fluid is required to obtain the best permeability and porosity recovery. Most previous studies were based on acidic injection fluids which induce rapid permeability and porosity changes within the first pore volumes injected. This also results in short duration experiments, with minimal experimental time spent at reservoir P-T conditions. We believe that the effect of effective stress can have on a rock has been neglected. For the first time, we have undertaken experiments designed to better understand the impact of effective stress, through an experimental matrix of four experiments, with the aim of cross-comparing the effects of injection rate and effective stress, during seawater flooding. Key variables have been logged throughout each of the four experiments, as well as the effluent fluid sampled every 1 to 2 hours for chemical analysis. Each sample has been µCT scanned before and after the flooding phases. In chapter 4, we have previously learned that both injection rate and stress state

play a relatively important impact on the creation and spread of pore space, on the development of permeability through time, as well as on the overall dissolution of major ions within homogeneous carbonates. Here we assessed the impact of the same variables on the highly heterogeneous travertine rocks. Our work suggests that injection rate remains the main variable for permeability creation, as well as porosity enhancement. However, the effect of a low effective stress has shown to have a positive influence on calcium and magnesium removal. If we overlook the effect of the PV_{rate}, the most successful scenario in term of permeability recovery per pore volume injected was observed at the lowest injection rate and effective stress. At higher injection rates, the low effective stress experimental scenario showed a greater porosity and permeability enhancement than the high effective stress, confirmed by 3D µCT analysis. This work confirms previous studies in that injection rate is the dominant process, but we noted that the effective stress also played a major secondary role on heterogeneous rock. Our findings suggest that it is not only the PV_{rate} that is important in optimising the enhanced permeability through dissolution wormholes. Managing the pore pressure to ensure a minimum change in effective stress is also crucial for optimising recovery in heterogeneous carbonate reservoirs.

5.3 Introduction

Acid or water flooding through carbonate rocks results in large alteration of the structure of the rock, due to the mobilisation of the calcite followed by its re-precipitation and/or its complete removal from the rock. In most studies, researchers have observed the creation of preferential flow-path referred to as channels or wormholes (Frick et al., 1994a; Fredd and Fogler, 1998; Golfier et al., 2002; Ott and Oedai, 2015). These wormholes can connect the wider pore network within the carbonate rocks if an optimised flow rate is obtained that generates the most advantageous dissolution morphology. The mechanisms

behind the development of the most advantageous flow-paths are important for many subsurface applications such as carbon sequestration, groundwater resource competition, geo-energy applications including geothermal energy, energy storage applications and enhanced oil recovery.

Fluid-rock mass transfer depends upon several physical and chemical factors describing the petromorphology of the rocks (Luquot and Gouze, 2009), and uncoupling the processes leading to the alteration of the rock matrix requires extensive and cross-comparative studies. Single phase flow for rock dissolution has been widely studied (Hoefner and Fogler, 1988; Bazin et al., 1995; Fredd et al., 1996; Golfier et al., 2002; McDuff et al., 2010), and results point toward a relationship between dissolution and injection rate (Buijse et al., 1997), as well as the acidity of the percolating fluid: at high injection rate, a single dominant wormhole can bypass most of the pores while at lower rates we see complete face dissolution of the rock, with intermediate in-between states which involve a more or less branched and ramified dissolution pattern. To identify the processes behind carbonate dissolution, this work recreate the processes of wormhole formation by injecting fluids into core samples within laboratory controlled experiments.

This study complements the work previously described in chapter 4, while focusing on heterogeneous travertines, which is a good and easy-to-source analogue for the Brazilian Pre-salt upper-reservoir due to their similar petromorphological nature (Borghi et al., 2013; Virgone et al., 2013; Boyd et al., 2015; Chitale et al., 2015; Rezende and Pope, 2015; Soete et al., 2015; Schröder et al., 2016; Claes et al., 2017; Erthal et al., 2017). We aimed to investigate the mechanical and chemical controls on the optimum equilibrium for wormhole propagation within Pre-salt carbonate shrub facies using the Saturnia travertine rocks and purified seawater as the injection fluid during core flood experiments under Pre-salt geo-reservoir

conditions of confining pressure (P_c = 50 Mpa), temperature (T = 60°C) and representative geochemistry (saturation and injection brine). To our knowledge, few studies have assessed the relative contribution of effective stress changes and kinetic chemical alterations on the physical changes of heterogeneous carbonates under the natural temperature, fluid, and pressure conditions found at reservoir depths. And for most single-phase flow studies, acidic fluids or low salinity brines are used as an injection fluid. This later type of injection has been described as having a positive impact on enhanced oil recovery (McGuire et al., 2005; Lager et al., 2008) by acting similarly to an alkaline flooding (McGuire et al., 2005; Soraya et al., 2009), by rising the pH of the system through calcite dissolution and cation exchange. Our brine displayed a circumneutral pH as well as a salinity ∼6 times higher than the ones used during low salinity injections. Therefore, any noticeable changes during our experiments could not be attributed to any effect related to the salinity and/or acidity of our fluid. We still observed the development of wormholes of various sizes and shapes, and while we are certain about the relation between their development and the injection rate, we believe that chemistry-related alterations of the rock matrix remained relatively small besides the usual calcite-water interaction (Bemer and Lombard, 2010), and we presupposed that an energy-driven alteration partially linked to the stress state of the rock was a key parameter (appendix L).

5.4 Materials and methods

5.4.1 Samples selection process

Assigning an experimental scenario to a travertine rock was a complex task, mainly due to the high degree of heterogeneity of the rocks. Approximately 40 cores have been measured using a nitrogen permeameter, and only the cores displaying $k_{nitrogen}$ comprised between ∼0.5 and ∼15 mD would be selected for

further experimental testings. This arbitrary window has been set after preliminary experimental flooding were realized using travertine samples. Following this pre-selection, the pre-experimental $\triangle P$ of each core sample has been calculated using Darcy law, which relied on the above nitrogen permeability measurements, while the syn-experimental differential pressure was based on the $\triangle P$ at t=0 min. This preliminary task was realized in order to assign each core sample a PV_{rate} and a stress state scenario. In the case of travertine rocks, no correlation between expected and experimental differential pressures was visible (figure 5.1). This was attributed to the high degree of heterogeneity in porosity and permeability of the rocks. Therefore, the PV_{rate} were assigned with the expectation of obtaining a large enough $\triangle P$ for permeability calculation. In reality, a large number of core samples did not produce any $\triangle P$, where others (grey markers) would end-up collapsing after a few hours of flooding, or would see their differential pressure suddenly drop to nearly 0 Pa after 1-2 min of flooding. Finally, a pre-analyses of the internal structures has been done for each core using µCT imaging techniques, so that any rock displaying large pores or vugs would be assigned a low effective stress (high P_p) in order to avoid any potential collapsing within the Hassler cell.

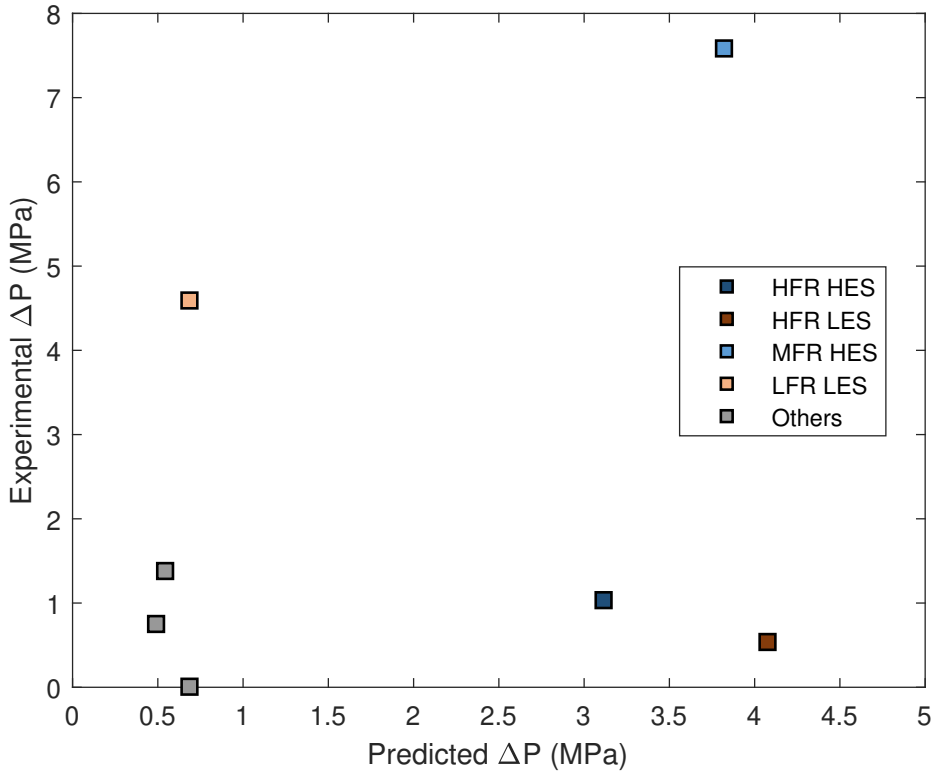

Figure 5.1: Experimentally calculated $\triangle P$ as a function of predicted $\triangle P$ for travertine rocks. The predicted $\triangle P$ is calculated by solving Darcy equation and using the pre-experimental $k_{nitrogen}$. The experimental $\triangle P$ represents the first log of the differential pressure transducer during a core flooding experiment.

5.4.2 Experimental design

We have used a modified version of the rig used by Edlmann et al. (2013) and McCraw (2016) for fractured core sample experiments. Confining pressure P_c and temperature T were constants for each experiments, while the flow rate Q (m^3/s), and the pore pressure P_p (MPa) were kept constant throughout each experiment but were varied over the four experiments. The experimental setup is described in section 3.2.2, while the logging and controlling systems were remotely done

using a bespoke LabVIEW software (further detailed in chapter 3 and appendices H and I).

5.4.3 Experimental approach

The experimental work was similar to the one realized in chapter 4, where six Indiana limestones were flooded under several different effective stresses and injection rates. We have used four cylindrical travertine core samples of 38 mm diameter (D) and 70 to 80 mm axis length (L) which have been flooded with an artificially made seawater (30.5 g NaCl per litre of distilled water) at constant confining pressure (P_c = 50 MPa) and constant cell and injection fluid temperature (T = 60°C). Due to difficulties in obtaining suitable samples for flooding experiments, we have limited the comparative work to four travertine cores. The rationale of the experimental scenario follows the one described in section 3.5, where three different pore volume rate (PV_{rate}) cases and two effective stress (σ') cases were coupled in order to unpick the controlling variables on rock matrix alteration during injection phases in carbonate rocks, through the use of different proxies such as Ca-Mg dissolution, wormhole formation, and porosity/permeability evolution. The experimental matrix in table 5.1 displays the four experiments retained for this study, according to their respective PV_{rate} and σ'. Two conditions of effective stress have been set: Low Effective Stress (LES = 10 MPa) and High Effective Stress (HES = 40 MPa). The PV_{rate} is a dimensionless value that represents the volume of fluid injected over a volume of pore. Section 3.5 (chapter 3) provides expended formulas and further explanations on the PV_{rate}. The effective stress is based on the work of Terzaghi (1951). The PV_{rate} values have been chosen to decrease logarithmically as a way to avoid any possible overprint of the injection rate over the effective stress at high injection rates. The experiments undertaken allowed a cross-comparison by normalizing the experimental results by the PV_{rate} values.

		Flow expressed as pore volume		
		Low	Medium	High
σ'	Low	0.2 PV/min 10 MPa		2.6 PV/min 10 MPa
	High		1 PV/min 40 MPa	2.5 PV/min 40 MPa

Table 5.1: Pore volume rate (PV_{rate}) and effective stress (MPa) values for the four experimental scenarios.

5.4.4 Flow scenarios and dissolution regimes

We have calculated the α number (Whitaker (1986) - cf. equation 2.8) and Re number (Stokes (1851); Fourar et al. (2004) - cf. equation 2.9) to validate the Darcy law applicability in the case of our travertine rock samples. Further information about both numbers are provided in section 2.3 of chapter 2. The characteristic length of a pore l is an important parameter used for the calculation of both α and Re numbers, as well as for the Da and Pe numbers. The variable l has been defined through an analysis of µCT images using the ICCR-Macropore software (cf. section 3.3.2): for each core sample, a pre-experimental 3D stack of images has been re-sliced a hundred times in the radial axis direction. Each slice has been used as an input for the ICCR-Macropore for geometrical analyses of the porosity (cf. figure 3.17 in section 3.3.2 for an example of pre- and post-processed slice). The definition of l has been done by using the mean value of the distribution of the major coefficient of the ellipse shape of the pores, whose implementation is described in chapter 3. For each core sample, the distribution of these values is presented in figure 5.2. As a first observation, it appears that the $LFR\ LES$ sample, while displaying a characteristic length l on average similar to the other samples, had a larger number of pore.

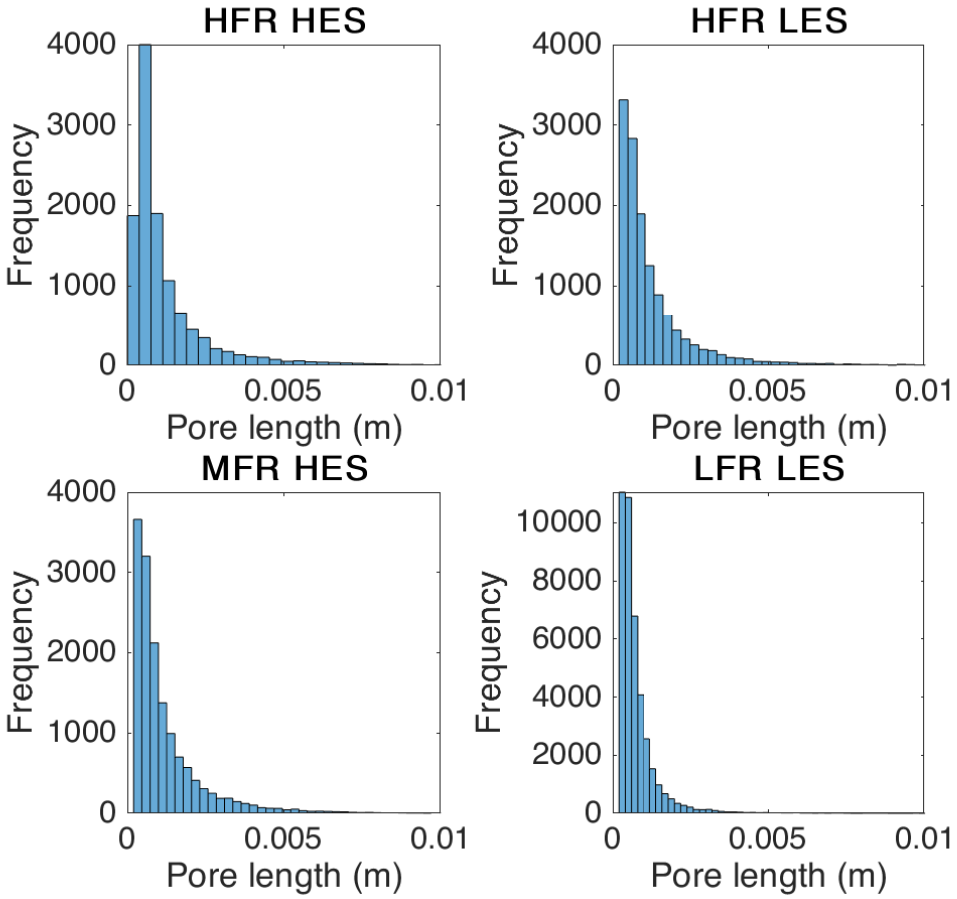

Figure 5.2: Distribution of the major axis lengths of the ellipse shape of the pores after analysis of 100 slices in the Z direction, and using the ICCR-Macropore (bin size = 60).

Table 5.2 presents the α and Re values calculated for the four rock samples. For laminar flow, α should sit below unity, while Re should be comprised in between 1 and 10 (Fourar et al., 2004). Authors have defined larger Re values for laminar flow (De Marsily, 1986; Seguin et al., 1998) for highly homogeneous rocks, while De Marsily (1986) observed laminar flow for Re reaching 2000. In this study, both α and Re indicate that Darcy law was valid for interpreting the permeability change during water flooding.

Sample	α	Re
$HFR\ HES$	1.78×10^{-2}	6.57
$HFR\ LES$	1.88×10^{-2}	7.24
$MFR\ HES$	1.65×10^{-2}	2.92
$LFR\ LES$	9.43×10^{-3}	0.37

Table 5.2: Reynold and alpha numbers calculated for the four core samples.

The dissolution regimes in which the four experiments fall in have been plotted on the dissolution map proposed by Golfier et al. (2002), according to the dimensionless Damköhler (Da - equation 2.11 - Golfier et al. (2002); Menke et al. (2015); Ott and Oedai (2015)) and Péclet numbers (Pe - equation 2.14 - Golfier et al. (2002); Egermann et al. (2006); Luquot and Gouze (2009); Menke et al. (2015); Ott and Oedai (2015)) (figure 5.3). The limits fixed on this map have been set according to empirical measurements done studying HCl-calcite interactions during flooding experiments, while we injected a pH neutral fluid. Although the map remains valid, we should expect variations in the boundary positions.

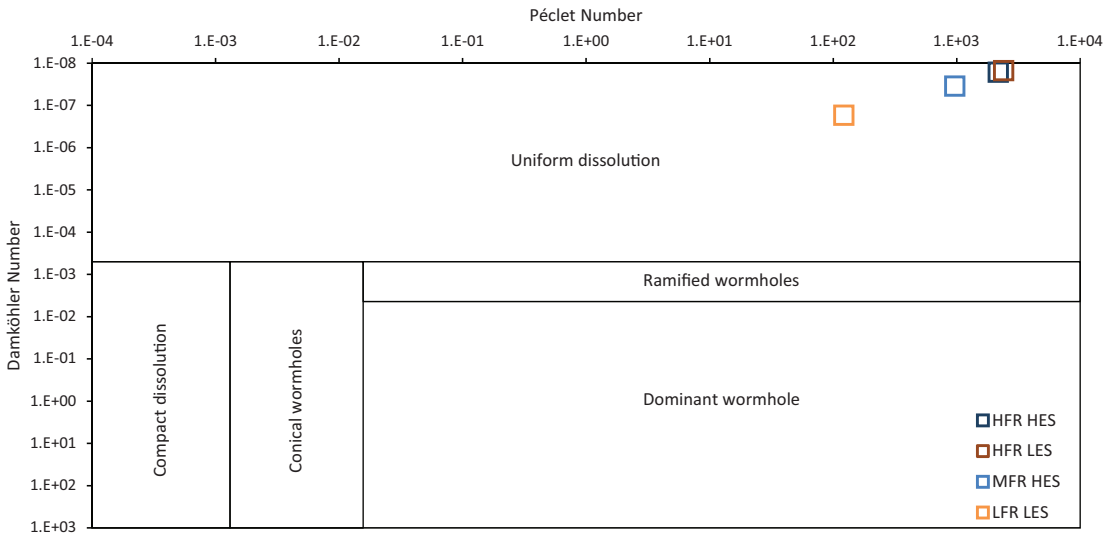

Figure 5.3: $Da - Pe$ map for the four core samples flooded. The boundaries have been suggested by Golfier et al. (2002) for a HCl-calcite system.

5.4.5 Sample characteristics

The rock used in this study is called travertine, whose formation and morphology were described by various authors (Kitano, 1963; Chafetz and Folk, 1984; Pentecost, 1990; Guo and Riding, 1992, 1994, 1998; Chafetz and Guidry, 1999; Fouke et al., 2000; Kele et al., 2008; Yagiz, 2009; Jones and Renaut, 2010; Wright, 2012; Chafetz, 2013; Chitale et al., 2015; Soete et al., 2015; Wright and Barnett, 2015; Claes et al., 2017; Erthal et al., 2017; Marques Erthal, 2018). We used travertine rocks as proxy for the upper Pre-salt reservoir rock, as studies have noticed noticeable petromorphological links between both rocks (Borghi et al., 2013; Virgone et al., 2013; Boyd et al., 2015; Soete et al., 2015; Chitale et al., 2015; Rezende and Pope, 2015; Schröder et al., 2016; Claes et al., 2017; Marques Erthal, 2018). Further information on travertines are available in chapter 3. All four samples' geometrical and physical properties are presented in table 5.3. Figure 5.4 shows µCT slices taken from each core sample used in this chapter. The porous media is made of heterogeneously distributed pores, whose size and shape appear to widely vary along a slice. Ronchi and Cruciani (2015) has finely described the Saturnia travertines, so that: A ($LFR\ LES$ sample) and B ($MFR\ HES$ sample) display a mixture of shrubby porosity coupled with coated bubbles which have been formed due to degassing during the precipitation of the calcite. Both sample evolve toward the shrubby structures seen in C ($HFR\ LES$ sample) and D ($HFR\ HES$ sample), which display elongated pores and dendritic calcite crystals (not seen under µCT imaging).

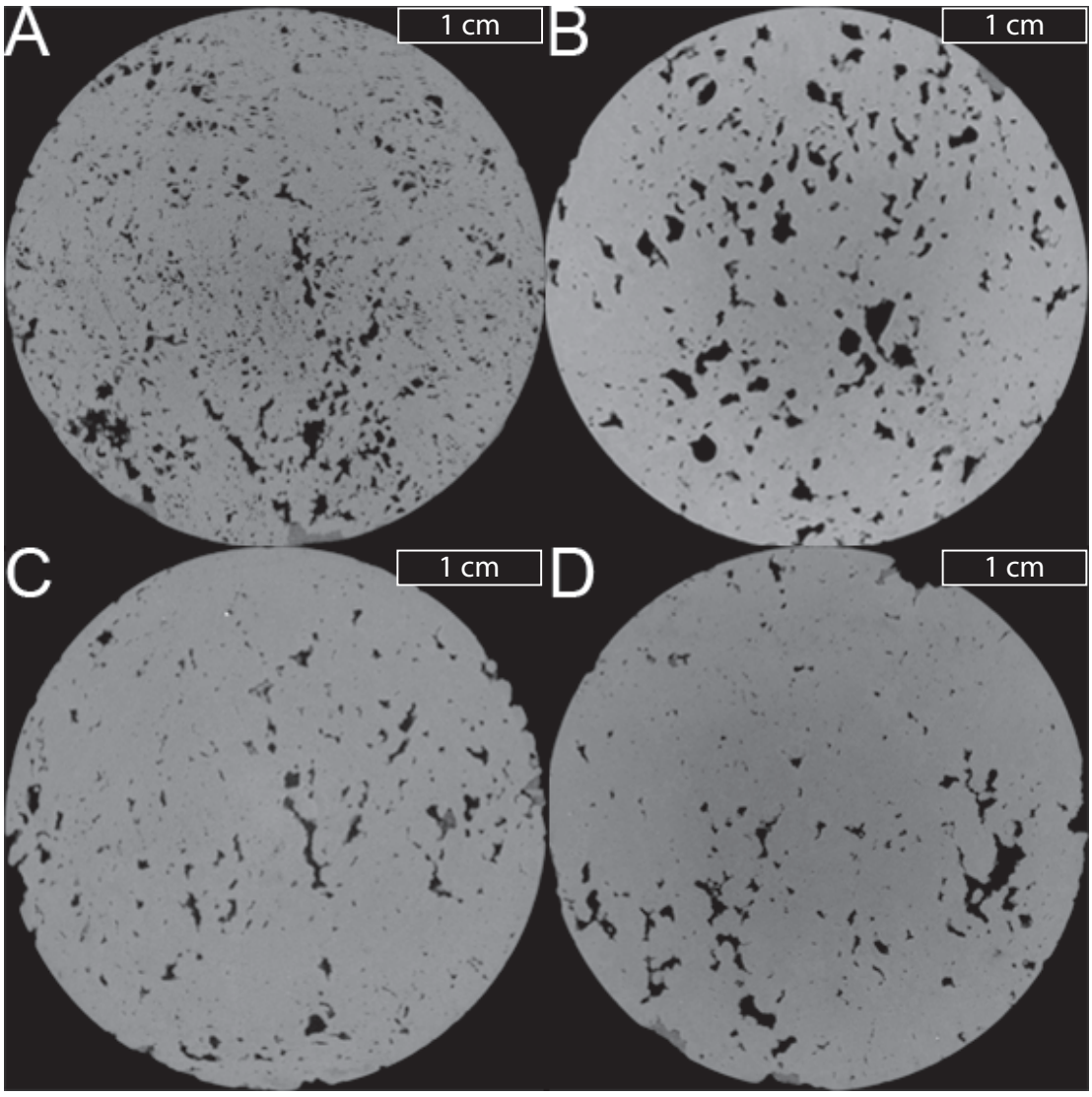

Figure 5.4: μCT slices of each travertine core sample used in this study. A: $LFR\ LES$; B: $MFR\ HES$; C: $HFR\ LES$; D: $HFR\ HES$. Image size: each slice is 3.8 cm by 3.8 cm.

Travertines are mainly made of calcium; usually > 90 % $CaCO_3$ (Pentecost, 2005). The remaining element is primarily magnesium which substitutes Ca and can be found under the form of calcite magnesian and dolomite (Chafetz and Folk, 1984; Pentecost, 2005; Kele et al., 2008; Erthal et al., 2017). The results of an XRD analysis ran on our block of travertines are shown in table 5.4.

Sample	Length (mm)	Diameter (mm)	ϕ (%)	V_p (cm^3)	V_s (cm^3)
HFR HES	71.58	38	7.57	6.20	75.71
HFR LES	68.68	38	7.65	5.96	72.01
MFR HES	73.39	38	7.11	5.89	76.94
LFR LES	81.2	38	5.64	5.2	86.99

Table 5.3: Petrological characteristics of the samples. The volume of solid is calculated from the difference between the volume of the cylindrical core and the volume of pore: V - V_p.

Compound	Sample 1 (%)	Sample 2 (%)
Calcite	95.15	95.02
Calcite magnesian	4.41	4.02
Dolomite	0.24	0.47
Traces	0.2	0.5

Table 5.4: Chemical composition of a block of travertine (Saturnia - Italy) from a in-house XRD analysis.

Figures 5.5 to 5.8 show the pre-experimental structures of each sample obtained after post-µCT treatment of image stacks. For each image, clusters of pores larger than $\sim$6.4 mm^3 have been displayed. We note the presence of an interconnected or near-connected network of pore between the inlet and the outlet each sample.

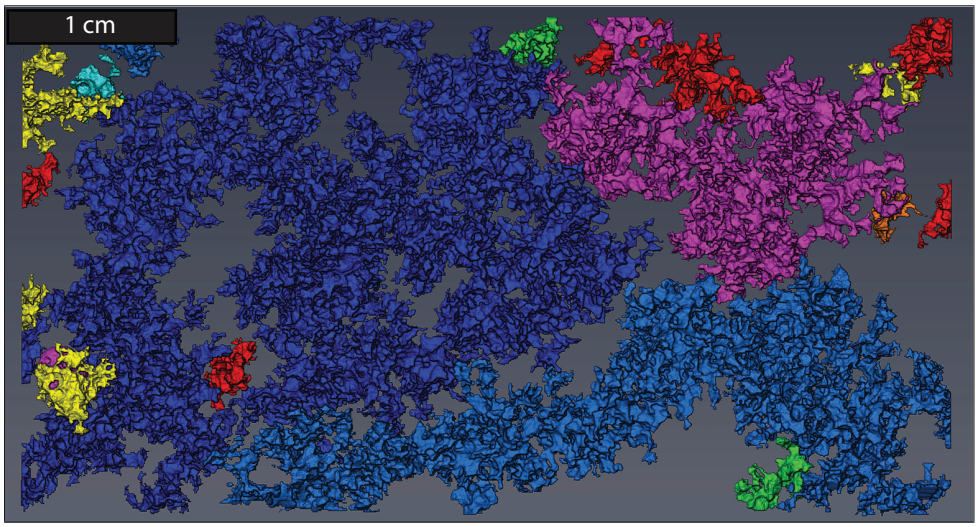

Figure 5.5: Pre-experimental μCT scan analysis of the $HFR\ HES$ experiment. The volumes represent the connected network of pores, while the non-connected cluster have not been displayed. The image respects the initial size ratio of the sample. Image size: 3.8 cm by 7.1 cm.

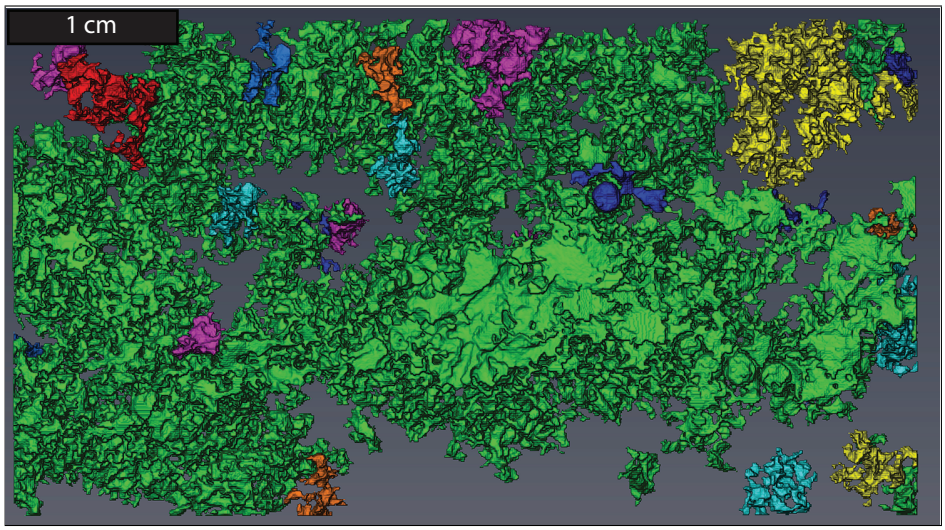

Figure 5.6: Pre-experimental μCT scan analysis of the $HFR\ LES$ experiment. The volumes represent the connected network of pores, while the non-connected cluster have not been displayed. The image respects the initial size ratio of the sample. Image size: 3.8 cm by 6.8 cm.

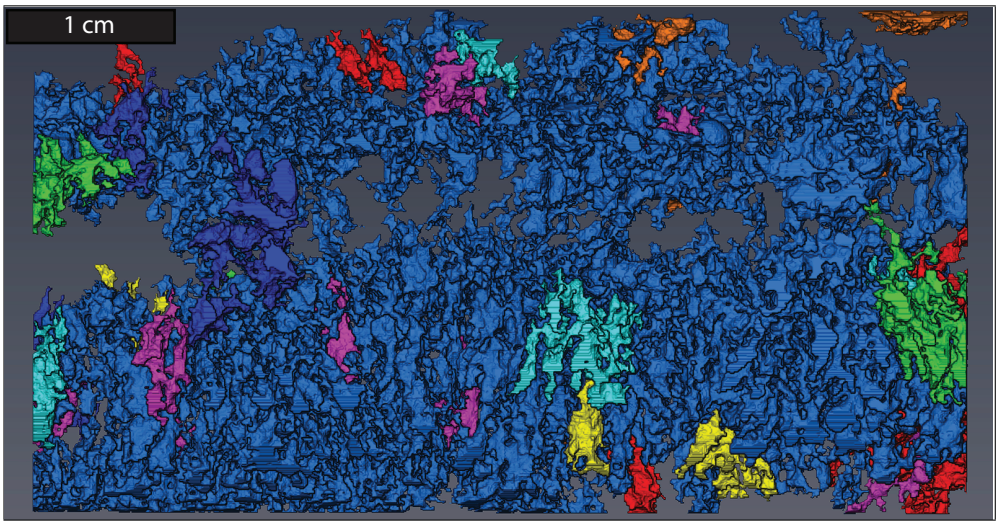

Figure 5.7: Pre-experimental µCT scan analysis of the $MFR\ HES$ experiment. The volumes represent the connected network of pores, while the non-connected cluster have not been displayed. The image respects the initial size ratio of the sample. Image size: 3.8 cm by 7.3 cm.

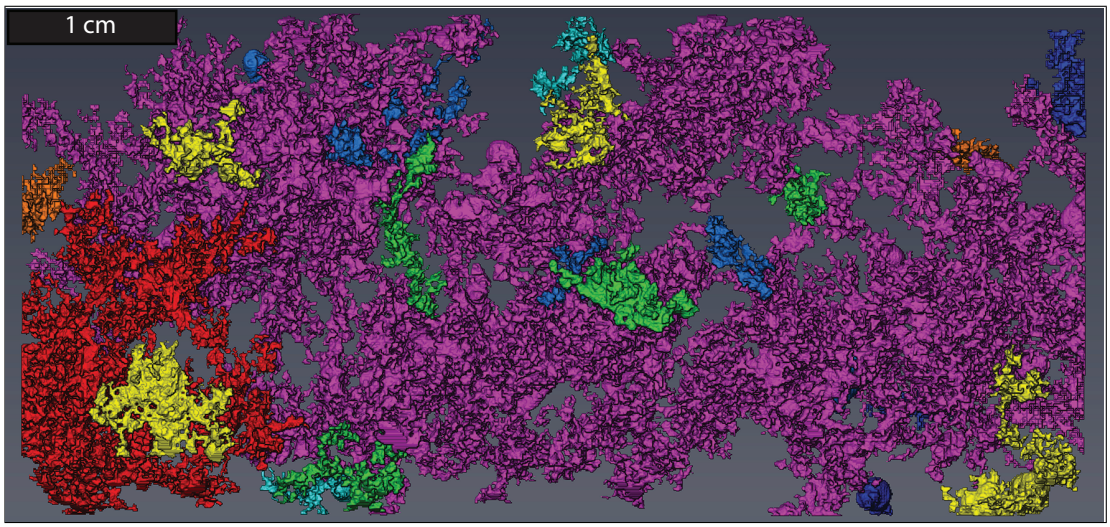

Figure 5.8: Pre-experimental µCT scan analysis of the $LFR\ LES$ experiment. The volumes represent the connected network of pores, while the non-connected cluster have not been displayed. The image respects the initial size ratio of the sample. Image size: 3.8 cm by 8.1 cm.

5.4.6 Sample preparation

The shrub layers within a 25 cm by 25 cm large block of travertine has been cored using a 38 mm diameter diamond impregnated cylindrical core drill. The plugs have then been edge trimmed using a circular saw. Both ends of each sample have been flattened and polished with an abrasive rotating disc. Fines have been removed by thoroughly sonicating each sample with distilled water. A fine layer of cement has been applied around the samples to prevent the confining elastomer sleeve of the Hassler cell to extrude into the largest pores and rupturing. A first layer of thick cement was applied within each larger pore, followed by the application of a more liquid layer which would cover the smaller pores. It is believed that no cement has been part of the Ca analysed in the effluent fluid, as the registered 3D volume did not show any missing plug of cement. The sample was dried and cleaned prior to be loaded into the Hassler cell. The framework of the experimental procedure for sample preparation and conditioning is further described in section 3.2.4 (chapter 3).

5.4.7 Measurements

Physical and chemical data acquisition and subsequent data processing are detailed in chapter 3. The µCT images have been treated using Fiji (Schindelin et al., 2012) and Avizo® 9. The total thickness of the dissolution front in the axial axis of the sample, as well as each $x-y$ coordinate of each node forming the skeleton has been gathered from the Centerline Tree function (Sato et al., 2000) of Avizo® 9. We note that in the case of the travertines, the Centerline Tree function appeared to output better results than the AutoSkeleton function, previously used for skeleton extraction in chapter 4. Figure 5.9 displays an example of generated surface (a) and the resulting skeleton (b). Small structures might have been discounted due to the skeletonization process, which implied a smoothing of the dataset as well as a reduction in the total amount of data.

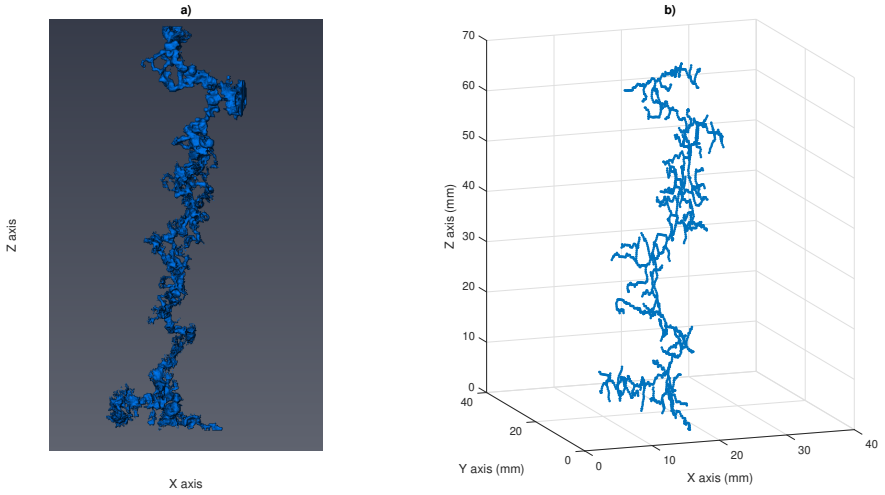

Figure 5.9: Example of skeletonization operation, from the $MFR\ HES$ sample (Centerline Tree function under Avizo® 9): a) 3D rendering of the wormhole experimentally generated; b) Corresponding simplified skeleton. In this example, the fluid was injected from bottom to top.

5.5 Results and discussion

5.5.1 Laboratory analysis

This section presents and discusses the evolution of physically and chemically derived parameters, such as the permeability, the Ca-Mg evolution, or the interplay of either variables. Physical measurements have been logged every half a second during each run from sensors strategically placed on the experimental rig. Each one of the 120 measurements of a minute of log was further averaged to form a minute-log. This process is automated and has been designed as a way to save computational time and space during an experiment. Chemical data were derived from the effluent fluid samples which were used for pH measurements and ICP-MS analysis.

5.5.1.1 Permeability

The usual dissolution result of carbonate core flood experiment is called a wormhole, with the large permeability generation period referred to as breakthrough (Teles et al., 2016). According to several studies, heterogeneities within a rock is a key control for channel propagation (Egermann et al., 2006; Siddiqui et al., 2006; Izgec et al., 2010). Figure 5.10 presents the different permeability evolution trends for the four experiments. While we observe a positive increase in permeability for each of the experiments, it appears that none of the experiment showed sign of breakthrough, which is attributed to the presence of a pre-existing preferential flow-path, related to the high heterogeneity of the pore structure of travertine rocks (Borghi et al., 2013; Alabi et al., 2014) whose porosity is mainly made of macroscopic pores of complex shapes, often referred to as vugs. Studies have shown that in a heterogeneous media, the local pressure gradients generated by larger pores drive the fluid flow (Siddiqui et al. (2006); Izgec et al. (2010), and chapter 7). Here, we presupposed that the larger vugs were already forming a preferential flow-path, which could explain the absence of low and steady evolution of the permeability, which usually precede a breakthrough (as seen in figures 5.5 to 5.8). The four injection rates Q used for each experiment, respectively $Q_{HFR\ HES}$ = 14.25 cm^3/min, $Q_{HFR\ LES}$ = 15.58 cm^3/min, $Q_{MFR\ HES}$ = 6.24 cm^3/min, and $Q_{LFR\ LES}$ = 0.98 cm^3/min, seemed to be the main factors affecting the permeability evolution, without any clear overprint of the effective stress.

We normalized the permeability evolution for each sample by plotting k/k_0 (figure 5.11; left subplot), due to the heterogeneous nature of the rock, partially displayed by $k(t = 0)_{HFR\ LES}$ and $k(t = 0)_{LFR\ LES}$ displaying three orders of magnitude of difference between them. As a consequence of the error associated with the differential pressure transducer (cf. chapter 3), only the beginning of each experiment is scientifically valid, until the $\triangle P$ read enters the error

window of ± 0.5 %. The right subplot of figure 5.11 displays the permeability curves whose corresponding $\triangle P$ values are above the detection limit of the differential pressure transducer (plain), while the dashed curves represent the predicted evolution of the permeabilities. This extrapolation is based on a linear extrapolation of the data recorded between the marks displayed in figure 5.14 and the last $\triangle P$ values whose reading is above the detection limit of the transducer. Interestingly, and once normalized, the curves clearly split in two families of experiment, with the lower injection rates leading to a greater change in k/k_0 than the higher ones. Within each group, the LES scenarios are on top of the HES ones. From this permeability analysis, we note that σ' and PV_{rate} both appear to drive the permeability evolution, with maximum relative generation for a PV_{rate} value of ∼0.2, followed by ∼1, and the HFR experiments at ∼2.5. For a family of injection rate, here broadly split into the lower and higher injection rate families, we observe that a low effective stress seemed to lead to a greater k/k_0 generation. While figure 5.11-left shows these trends, figure 5.11-right further confirm the clear dichotomy between the lower flow rate and higher flow rate experiments, as well as in between the LES and HES scenarios.

Permeability evolution amongst the four rocks can be further analysed by calculating the tendency of the evolution. We have plotted $\frac{\partial k}{\partial t}$ in figure 5.12. As seen in figure 5.11, all experiments, although presenting a positive increase in permeability, did not show any sign of breakthrough. We observe that the permeability generation followed a similar trend at lower injection rates ($MFR\ HES$ and $LFR\ LES$), while at $HFR\ HES$ the increase was moderate for the overall experimental time. $HFR\ LES$ did not show any common feature with the three other experiments as most of its permeability developed within the first 50 min, followed by a positive, although decreasing, trend.

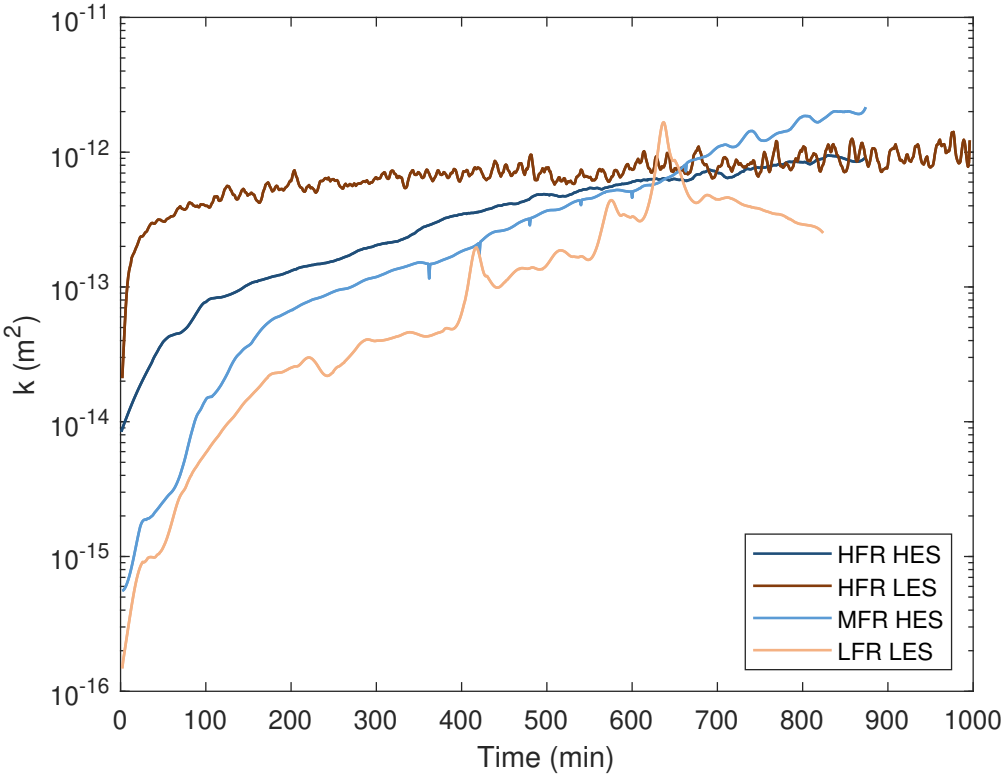

Figure 5.10: Permeability outputs, derived from Darcy law. Although all experiments appear to enter the limit of $\triangle P$ detection at different time, we observe a clear influence of the PV_{rate}.

The reason for this decreasing trend has been attributed to an eased fluid flow through the rock matrix due to a constant high P_p, or due to the original matrix structure and pore arrangement of the core sample which displayed a more established flow-path to start with (cf. figure 5.6). An interesting aspect of these experiments is that, despite having different permeability creation paths, both HFR experiments have seen their relative permeabilities increased by a similar value: ∼80 times for $HFR\ LES$, and ∼100 for $HFR\ HES$, while at lower injection rates, the relative permeability values are two orders of magnitude above the HFR experiments.

Figure 5.13 presents the relative permeability evolution as a function of the pore volume of fluid injected in each sample (a), and $\frac{\partial k}{\partial PV}$ as a function of time (b). We observe that on a) the gain in permeability was not function of the amount of fluid injected into a rock sample. Although, it is commonly accepted that there is a correlation between injection rate and permeability generation (Hoefner and Fogler, 1988; Daccord et al., 1989; Frick et al., 1994a; Bazin et al., 1995; Fredd et al., 1996), we note a complete opposite dynamic with an apparent larger k generation where the injection rates were at their lowest (also seen in figure 5.12 - grey zone). Figure 5.13b supports this idea by showing the relative contribution each pore volume injected has had on the relative permeability evolution, observing that the permeability generation is an inverse function of the amount of the volume injected. The decreasing, yet positive, curve ($HFR\ LES$) is explained by the early plateau reached by the permeability evolution.

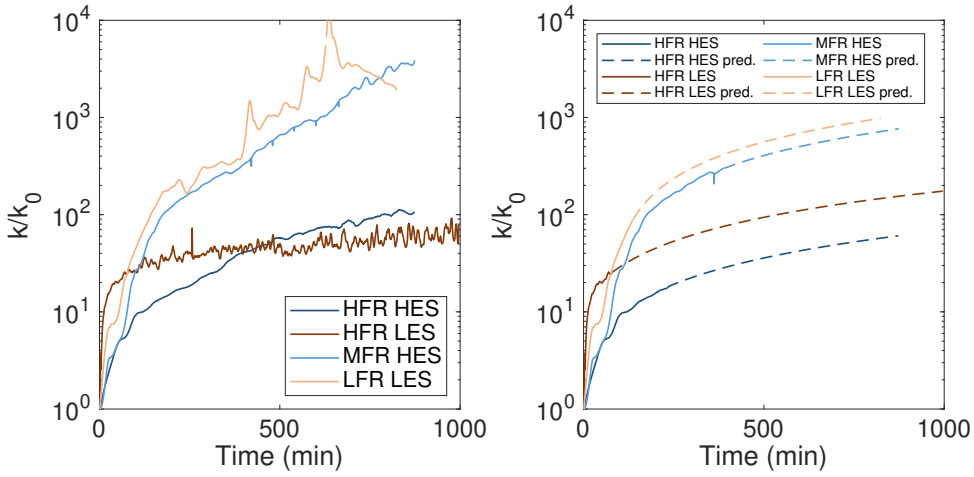

Figure 5.11: Permeability evolution normalized against $k(t = 0)$. Left: untreated data; right: the plain curves display the data outside the error region, while the dashed lines are the extrapolated data. Each linear extrapolation is based on the recorded data logged between the mark of figure 5.14 and the last valid recorded value. Both plots highlight the large influence of a LES on the permeability evolution of travertines.

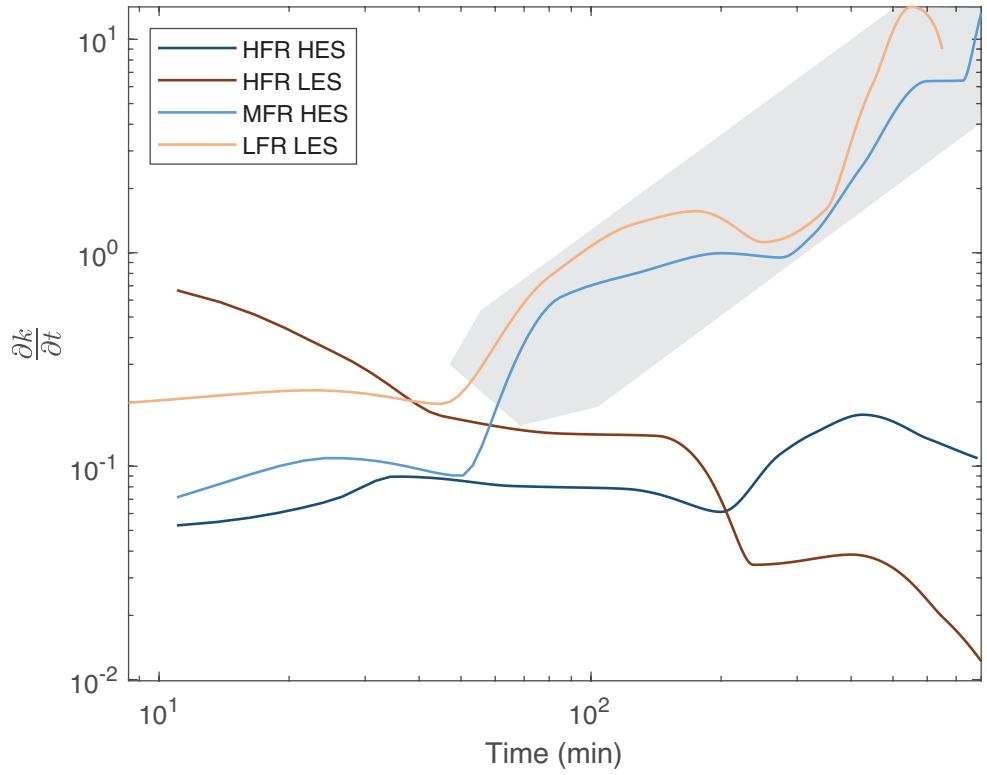

Figure 5.12: Derivative of the permeability with respect to time. The grey area displays a larger k generation for the lower injection rate experiment.

As previously discussed, no breakthrough happened during these four experiments, preventing us from calculating a 'Pore Volume to breakthrough' (PV_{bt}) value (Hoefner and Fogler, 1988). Instead, and as a way to further study the evolution of the permeability amongst travertines, we have analysed the $\triangle P$ behaviour in order to locate a transition zone before which most of the differential pressure has contributed to the permeability generation. The linear relationship between Darcy law and $\triangle P$ (Luquot and Gouze, 2009) for permeability calculation has allowed us to pinpoint the $\frac{\partial \triangle P}{\partial^2 t}$ curves on figure 5.14. For the purpose of this study, we call this threshold value the 'Pore Volume to Maximum Permeability Generation' (PV_{maxK}). A quick reading of the PV_{maxK} values gives access

to the time at which most of the differential pressure has been generated, and therefore to the amount of pore volume injected.

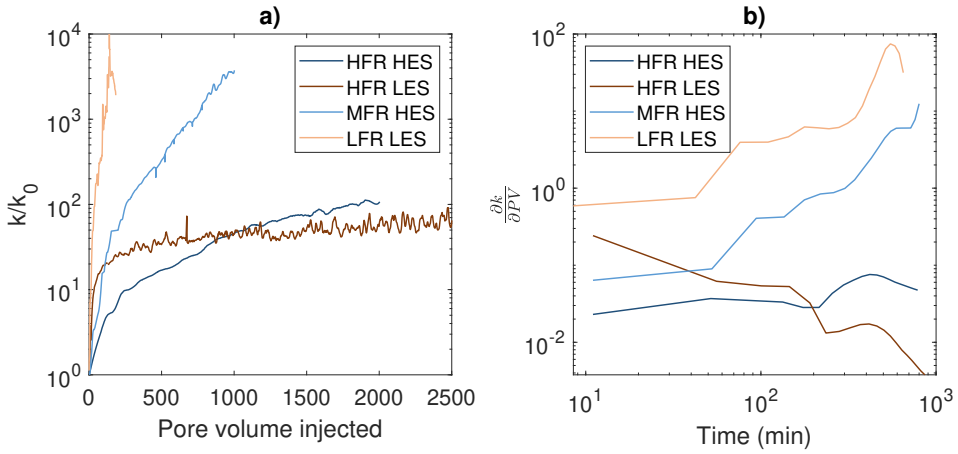

Figure 5.13: a) Normalized permeability generated as function of pore volume of seawater injected. From left to right: most economic to least economic scenario with regard to the injection fluid, and as a mean to generate permeability. b) Relative contribution each pore volume injected has had on the creation of permeability. The lower flow rate experiments have been able to create more permeability per PV injected. Per family of injection rate, the LES experiments might have a secondary positive impact.

Comparing the experimental PV_{rate} and PV_{maxK} shows no clear correlation between permeability generation and the rate at which a rock is flooded (figure 5.15), except if we consider the permeability path of $HFR\ LES$ to be an outlier, and which could highlight a linear relationship of equation $y = 162.6x - 10.15$ between the three remaining experiments ($R^2 = 0.99$). We note that three experiments are not enough to constrain the real relationship between k generation and the injection rate in travertines.

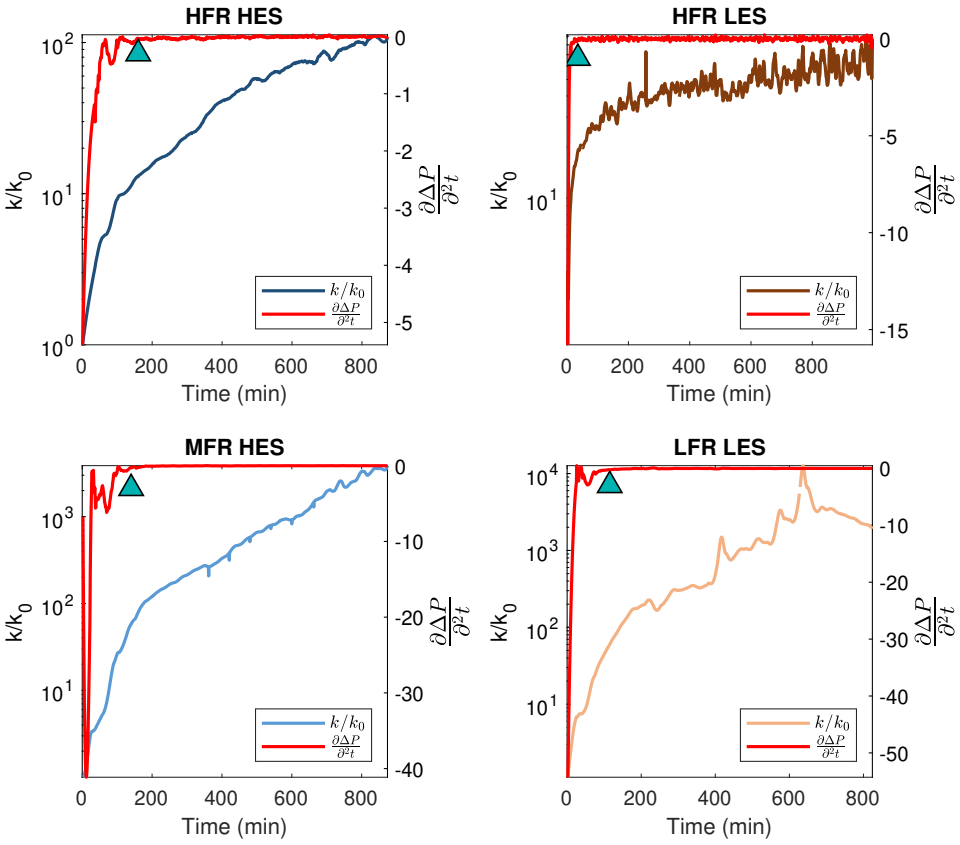

Figure 5.14: Differential pressure analysis and relative permeability evolution for the four experiments. The blue marker indicates the time before which the $\triangle P$ had a maximum impact on the permeability generation.

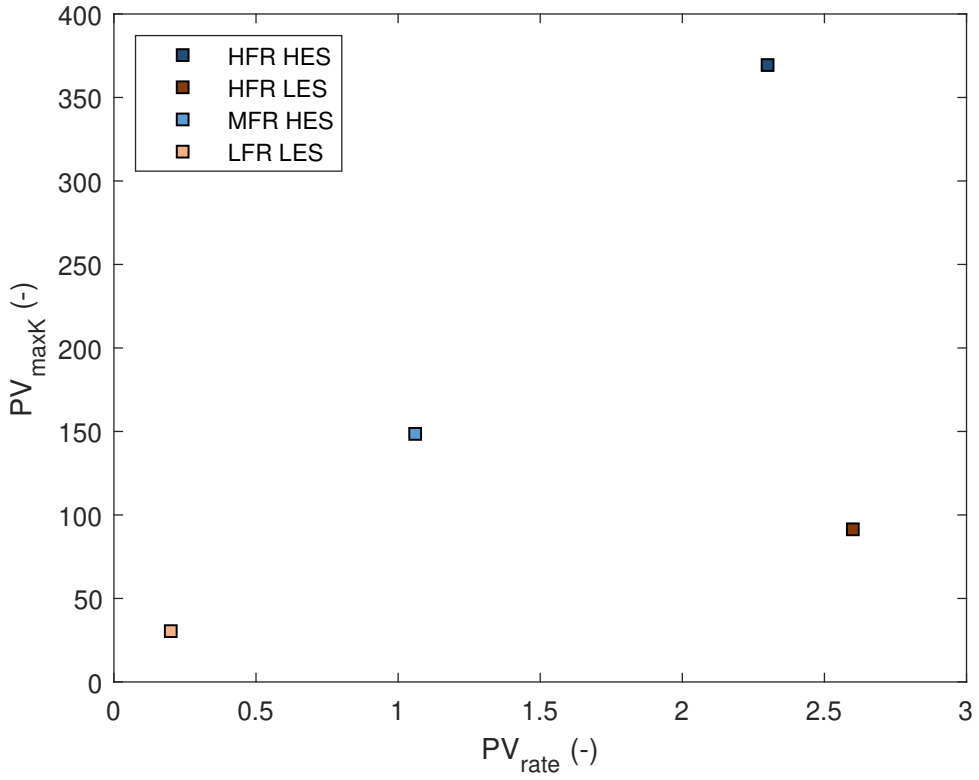

Figure 5.15: PV_{maxK} as a function of constant PV_{rate} used for the four experiments. The values for PV_{bt} have been derived from the markers of figure 5.14, while the PV_{rate} values are given in table 5.1.

5.5.1.2 Calcium and magnesium evolution

The effluent fluid has been sampled at the outlet of the Hassler cell. The rate of sampling differs between experiments due to the use of variable injection rates, which indirectly prevents us from collecting fluid samples if the sampling loop has not been flushed at least four times by the running injection fluid (cf. section 3.2.5.3). Instead of presenting the volume or the mass of Ca and Mg in this section, we display the ratio of volume of either ion in the fluid samples, against the volume of the rock sample (equation 3.12). This normalization is necessary as we used samples of variable lengths. We also unpick the effect of the effective stress σ' from the influence of the injection rate by normalizing Ω with the PV_{rate} values. The four experiments display a $\triangle C_{Ca} > 0$ and $\triangle C_{Mg} > 0$ at all times of the experimental run, which is an indication that dissolution and/or alteration of the rock matrix happened during the experimental flooding (Luquot and Gouze, 2009). This is also confirmed by our pH measurements displaying high values, averaging at pH = 9-10, elevated by the dissolution of calcite (figure 5.16).

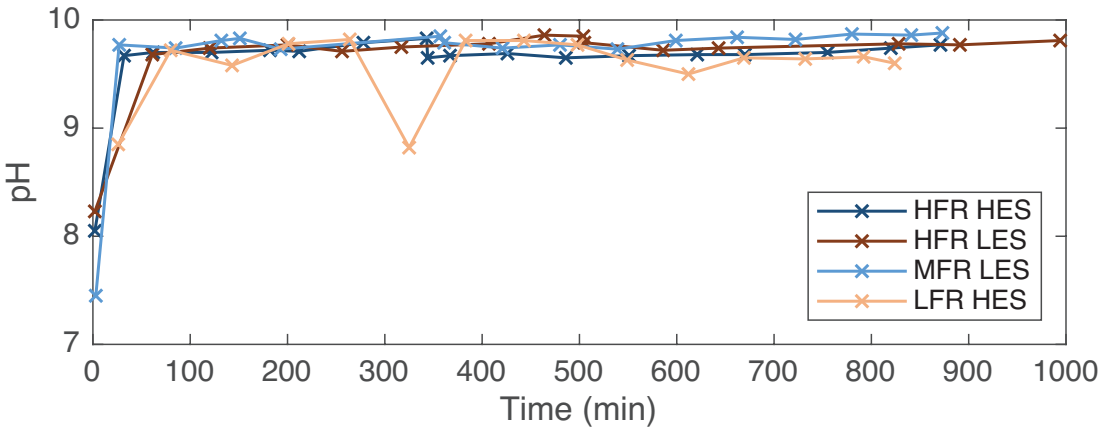

Figure 5.16: pH measurements for the 4 experiments. All measurements have been done on sub-samples of the fluid before ICP analysis.

Ion behaviour

We observed dissolution and/or alteration of the rock samples in each of the four experiment. Figures 5.17 and 5.18 corroborate the permeability analysis of 5.5.1.1. It appears that the driving variable for either ion's removal relates to the injection rate.

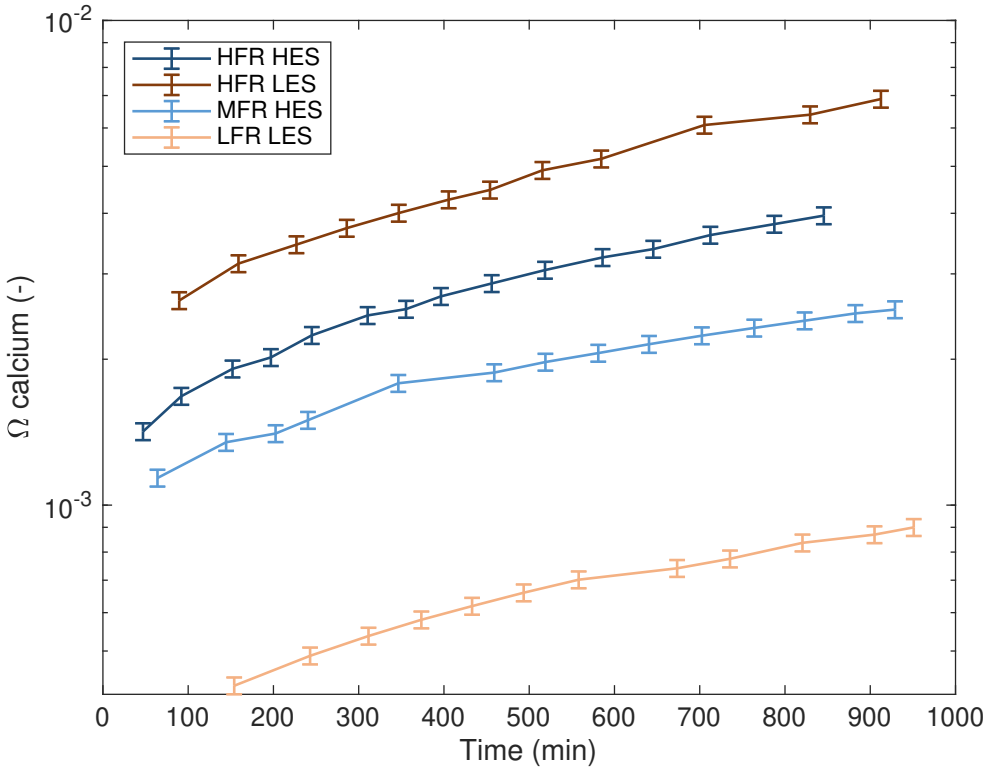

Figure 5.17: Volume of calcium derived from the effluent fluids sampled directly out of the Hassler cell and normalized against the original volume of rock of the core sample (Ω). The influence of the PV_{rate} is apparent, and drives the Ca dissolution for the four experiments.

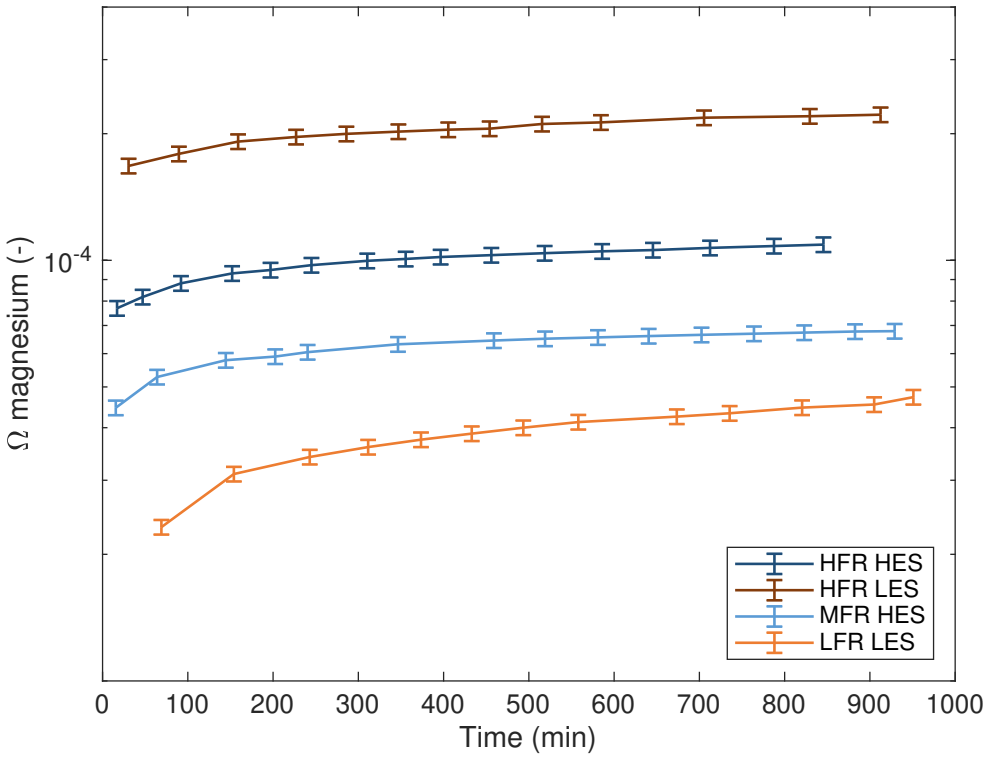

Figure 5.18: Volume of magnesium derived from the effluent fluids sampled directly out of the Hassler cell and normalized against the original volume of rock of the core sample (Ω). The influence of the PV_{rate} is apparent, and drives the Mg dissolution for the four experiments.

The concentration of either ion within the effluent fluid is presented in figures 5.19 and 5.20. We observe that the dissolution of the two ions seemed primarily impacted by 1) the PV_{rate}, and 2) the stress state, which is seen by a splitting of the LES curves grouping on top of the HES ones. In the case of heterogeneous travertines, the stimulant for matrix alteration during water flooding seems to be a lower relative PV_{rate} coupled to a high pore pressure. In this rock, the magnesium ion is mainly mobilized under the form of dolomite and/or calcite magnesian. The bulk modulus of dolomite being larger than the modulus of calcite (table 2.1), we explain the clear definition between low and high effective stress experiments (visible in figures 5.20 and 5.22) by a great mobilization of Mg ions through enhanced dissolution of Montmorillonite, which displays a lower bulk modulus than calcite.

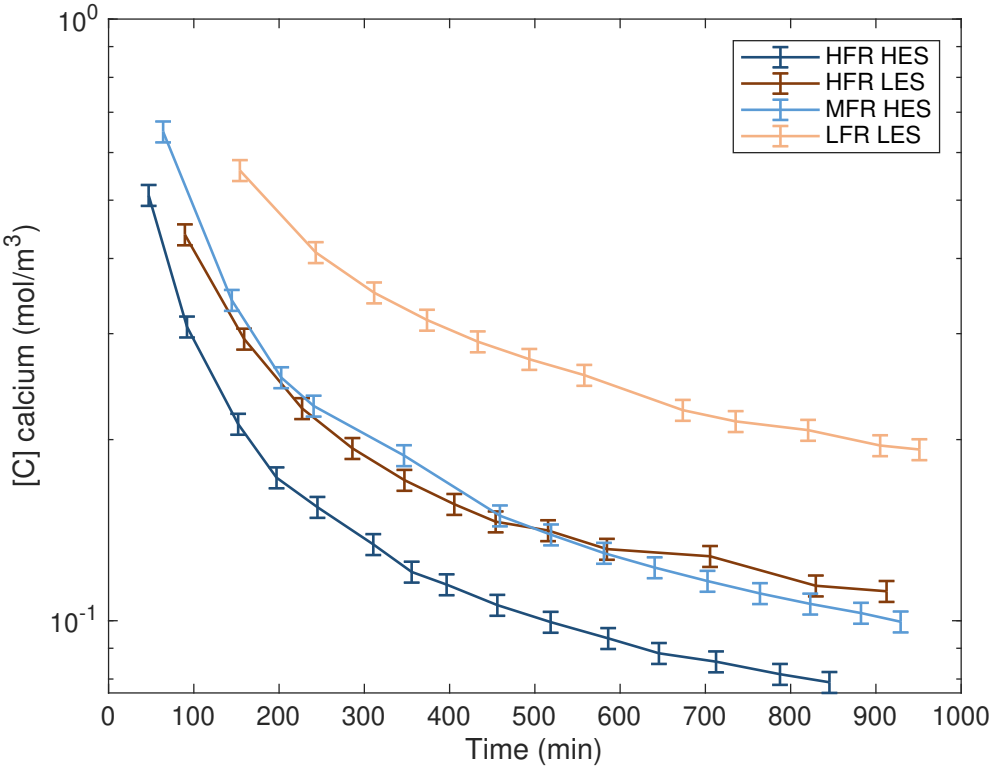

Figure 5.19: Concentration of calcium derived from the effluent fluids. The impact of the PV_{rate} is visible with the lower flow rate group gathering on top of the HFR experiments. Within each group, the influence of the effective is perceptible, with the LES displaying higher Ca concentration than the HES.

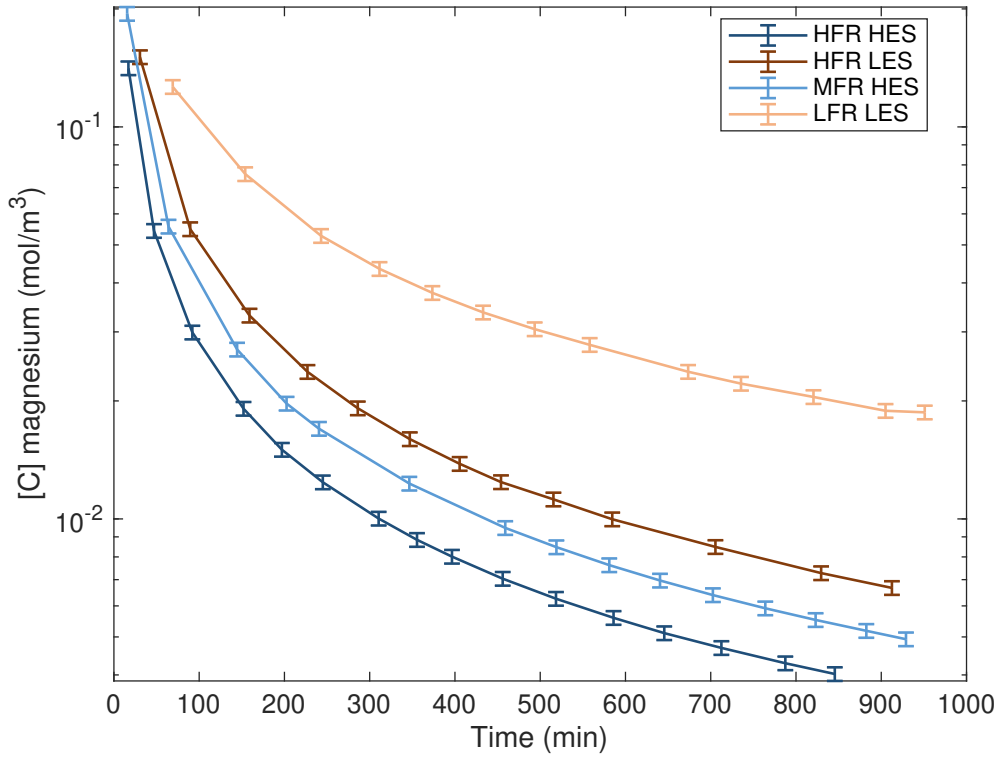

Figure 5.20: Concentration of magnesium derived from the effluent fluids. The impact of the PV_{rate} is visible with the lower flow rate group gathering on top of the HFR experiments. Within each group, the influence of the effective is perceptible, with the LES displaying higher Mg concentration than the HES.

Normalized ion behaviour

A qualitative assessment of the matrix response to effective stress can be achieved by removing the effect of injection rate through the normalization of Ω (equation 3.12) by PV_{rate}. Figures 5.21 and 5.22 present the capability that effective stress had to enhance the dissolution of either ion from the rock by removing the potential effect PV_{rate} can have on the rock matrix. Figure 5.21 shows that for a given effective stress, the lower flow rate scenario appeared more capable of dissolving calcite. Overall, the LES scenarios were the most efficient stress state for Ca dissolution. Figure 5.22 presents the same normalization for magnesium dissolution. It appears that the LES experimental scenario showed a larger capability in removing magnesium as well, with a clear gathering of LES experimental scenario on top of the HES. These observations are in accordance with the permeability curves observed in figure 5.11 which gave an indication of the important of a low effective stress scenario over heterogeneous carbonate rocks.

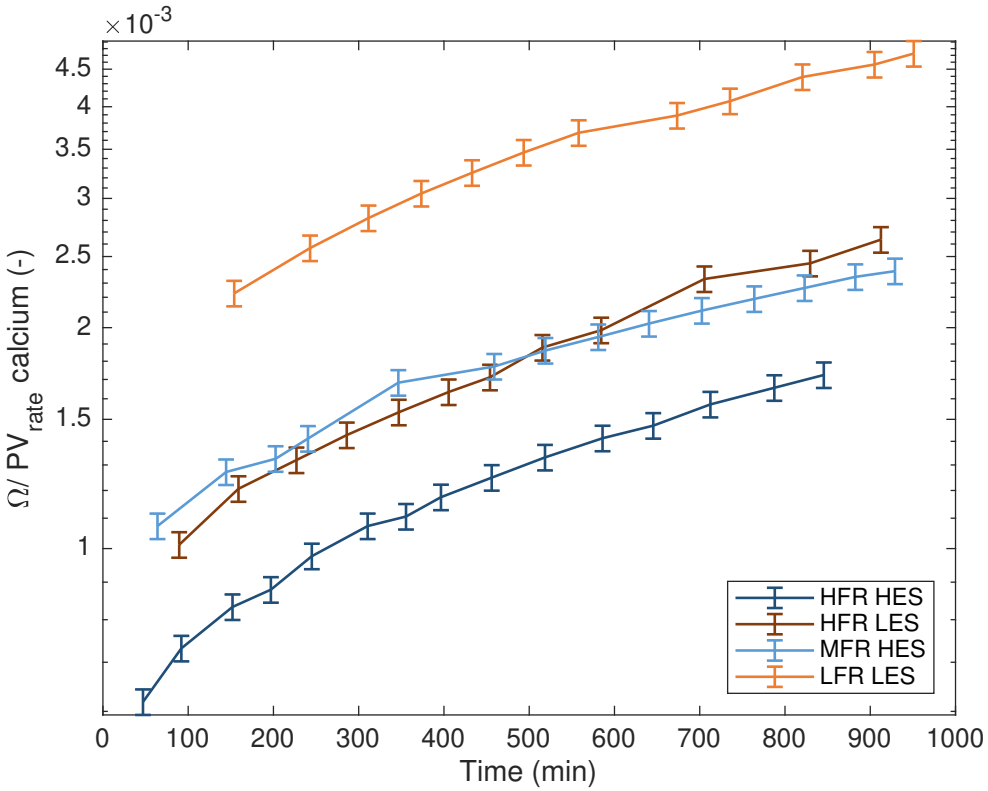

Figure 5.21: Dimensionless capability of the effective stress to remove calcium from a carbonate rock during water flooding. Per family of effective stress, the lower flow rate appears more capable of dissolving calcium. Regardless of the flow rate, a lower effective stress is more capable to dissolve calcium.

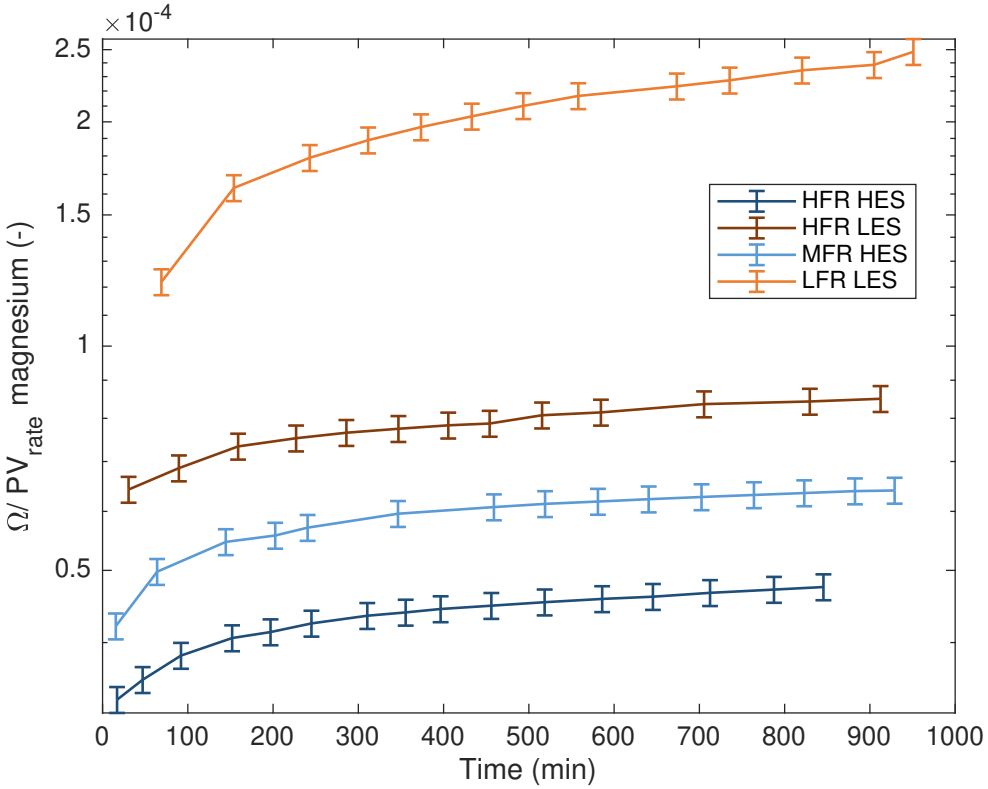

Figure 5.22: Dimensionless capability of the effective stress to remove magnesium from a carbonate rock during water flooding. Per family of effective stress, the lower flow rate appears more capable of dissolving magnesium. Regardless of the flow rate, a lower effective stress is more capable to dissolve magnesium.

5.5.2 µCT analysis for rock alteration

Figure 5.23 shows the total wormhole thickness calculated for the four experiment, and presented as a function of their effective stress. Due to an unknown reason, we observed abnormally high thicknesses which translated by important local peaks. This is attributed to a large amount of clustered nodes, which could lead to a repetition in the thickness of a same branch. Nevertheless, the difference in magnitude is easily explained by a greater injection rate for the HFR experiments, while the MFR and LFR showed smaller wormholes. Only the $LFR\ LES$ experiment did not develop a wormhole connecting inlet to outlet of the sample. The mean thickness of each wormhole is presented in table 5.5.

Sample	Length (mm)	WH length (mm)	Mean thickness (mm)
$HFR\ HES$	71.58	71.58	12.5
$HFR\ LES$	68.68	68.68	13.5
$MFR\ HES$	73.39	73.39	3.5
$LFR\ LES$	81.2	25.42	2.4

Table 5.5: Sample length total channel thickness, and wormhole length for the four experiments.

The $LFR\ LES$ experiment displayed the smallest wormhole in terms of thickness and total length, which showed signs of an early form of face dissolution or early wormhole development, and is directly related to the low injection rate of the experiment (0.2 cm^3/min): the fluid entered the pre-existing porosity and mainly dissolves the entrance and walls of the flow-path (Fredd and Fogler, 1998; Fredd et al., 1999; Golfier et al., 2002; McDuff et al., 2010). Plotting wormhole thickness by family of PV_{rate} (figure 5.24) shows, as expected, that high injection rate experiments have similar and irregular dissolution patterns that affect the entire sample, while at lower flow rates the wormholes developed following a more regular and steady pattern. The $LFR\ LES$ wormhole did not reach the outlet of

the sample, unlike the $MFR\ HES$ one, which, like the high flow rates, reached the outlet. This is due to the weak mechanical action of the fluid over the rock matrix, coupled to a very weakly acidic injection water whose hydrogen ions would be consumed within the first centimetres of the rock.

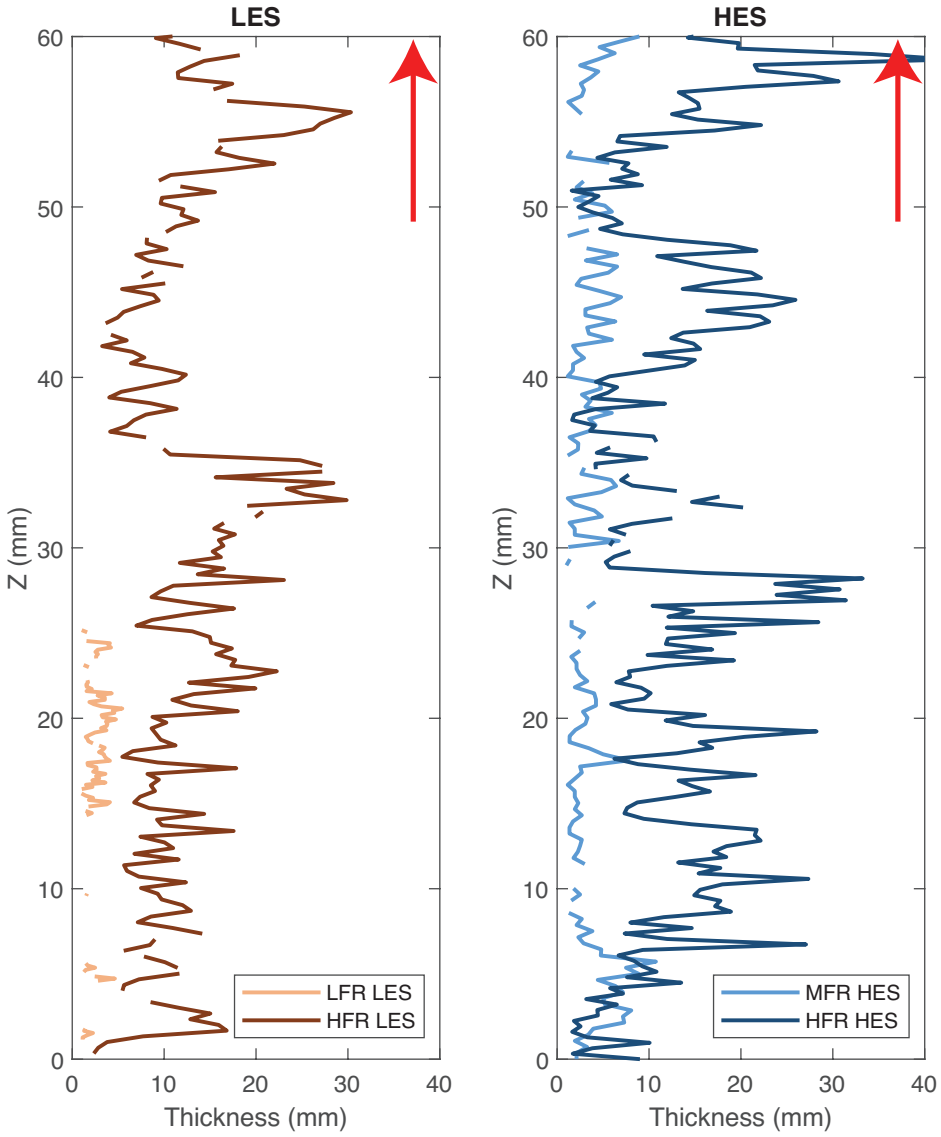

Figure 5.23: Main wormhole thickness displayed by effective stress and computed from the Centerline Tree function of Avizo® 9 (Sato et al., 2000). The red arrows show the flow direction.

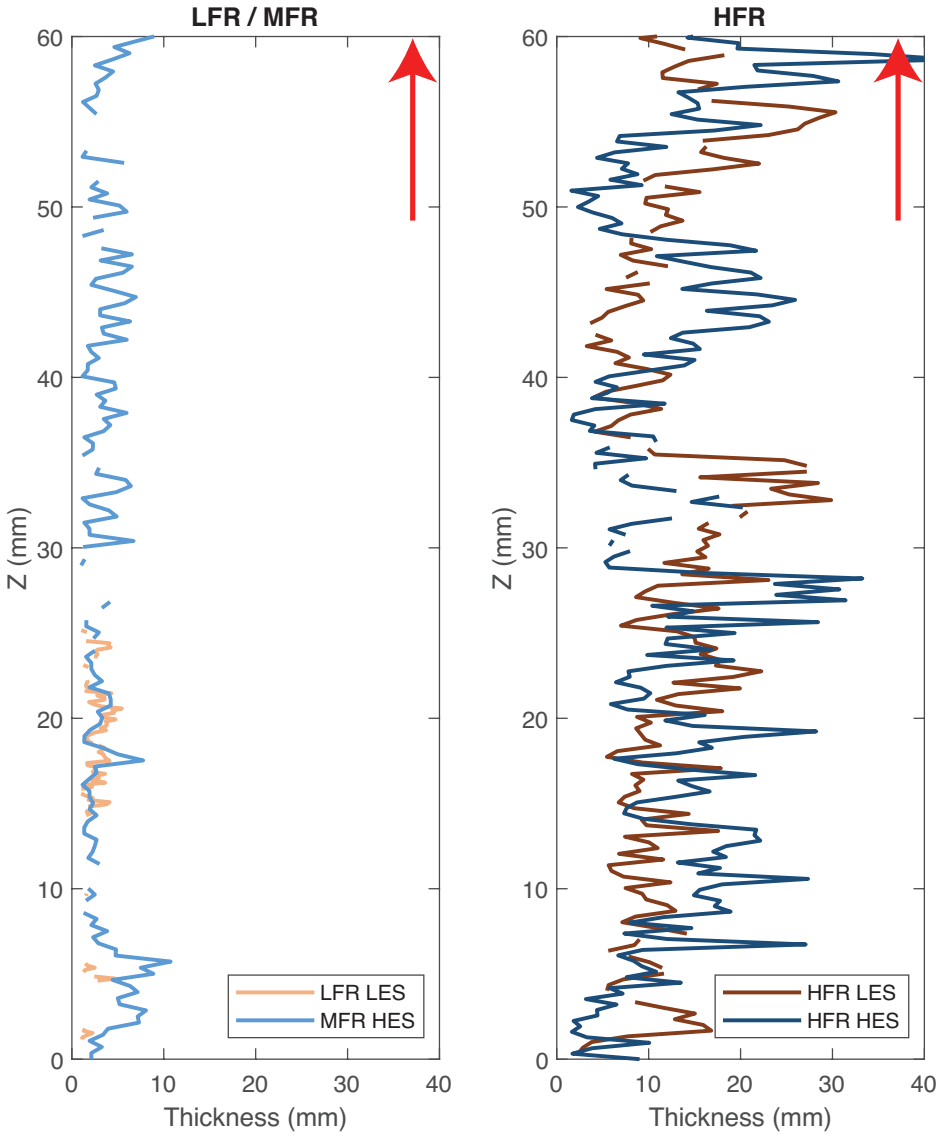

Figure 5.24: Main wormhole thickness displayed by injection rate and computed from the Centerline Tree function of Avizo® 9 (Sato et al., 2000). The red arrows show the flow direction.

The density of dissolution has been calculated from the $x - y$ coordinates of the nodes forming the skeletons (Sato et al., 2000). Although it is relatively simple to assess the effect of the injection rate, the effect of the effective stress was harder to unpick in the case of heterogeneous rocks. This is partially due to an incomplete set of experiments, related to difficulties in obtaining suitable samples. Figure 5.25 presents density plots of the dissolution patterns for each experiment as seen from the top of the sample. We observe that the injection rate drove the wormhole shape and size: The HFR experiments have reached most of the available porosity, while the wormholes are less branched at lower flow rates. The two directly comparable experiments in terms of injection rate and stress sate are $HFR\ HES$ and $HFR\ LES$. For both experiments, we observe that the fluid flow has reached a similar area within each sample, while the intensity of alteration was more pronounced at low effective stress rather than at high effective stress. This is attributed to small collapses or pre-existing flow-paths at high effective stress, disconnecting parts of the samples.

Figures 5.26, 5.27, 5.28, and 5.29 present the pre-existing porosity (blue volumes of the figures) which are now part of the dissolution flow-path (opaque white volumes connecting the pre-existing porosity). The pre-existing porosity has been computed from the differential results of wormhole formation which has been applied as a 8 bits mask over the 16 bits grayscale unaltered volume of rock: in Avizo® 9, we used the Arithmetic function to multiply the mask by the pre-experimental volume. The pictures confirm the importance of the injection rate in the alteration process, while they also show a pre-existing network of more or less connected pores between inlet and outlet of each sample, which explains the absence of breakthrough during the permeability evolution. Figure 5.30 displays a detailed analysis of a slice, taken perpendicular to the axis of the $HFR\ HES$ sample, and confirms that the original porosity has been enhanced, and has driven

the fluid flow throughout the experimental time, while most of the alteration has taken place at the wall of the pores via an increase in size of the existing channels.

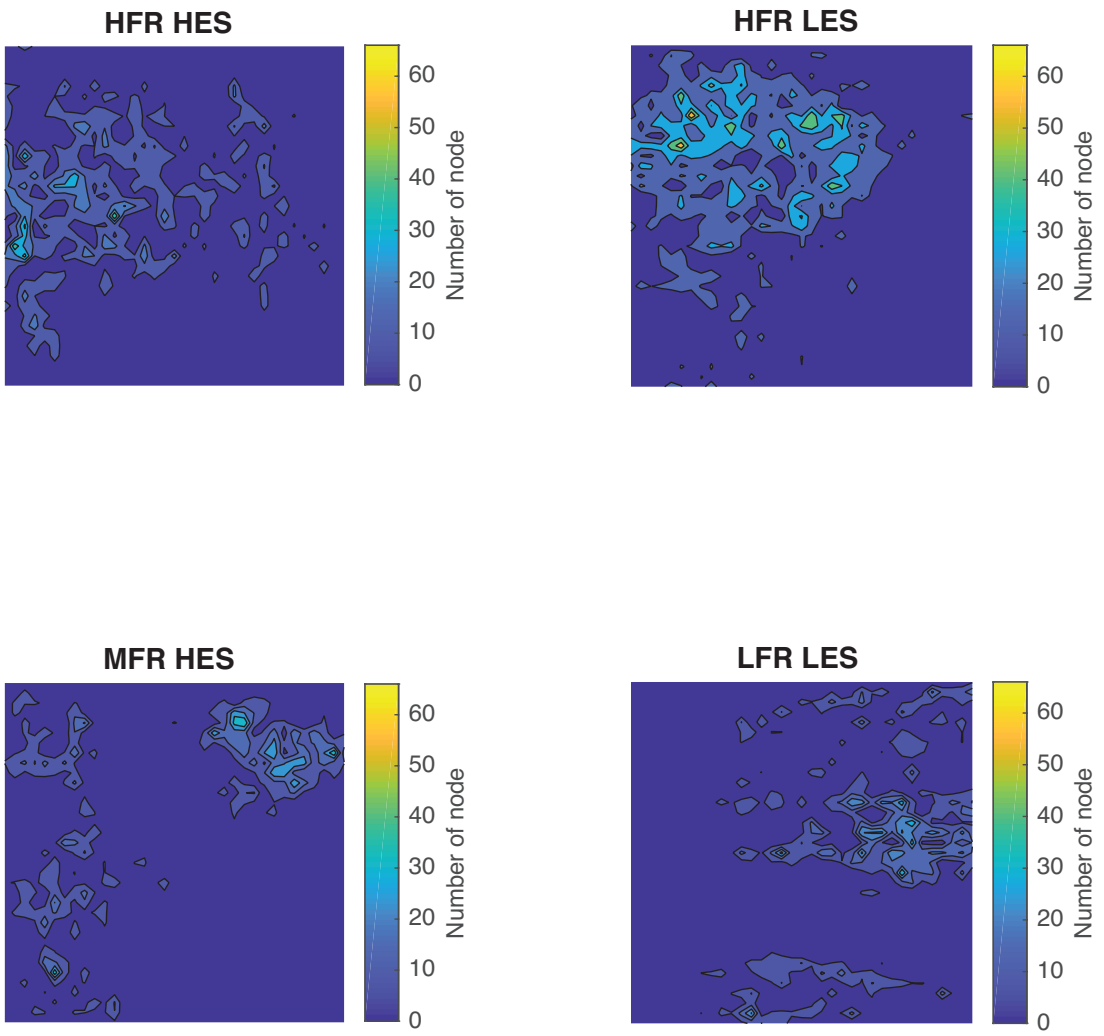

Figure 5.25: Density plot of the dissolution pattern. Each picture displays the nodes forming the skeleton shape of the wormhole left after flowing. The left subplots show the HES experiments; the right subplots show the LES experiments. The color-scale displays the amount of nodes in the Z axis. Each square is ∼2.5 cm by ∼2.5 cm.

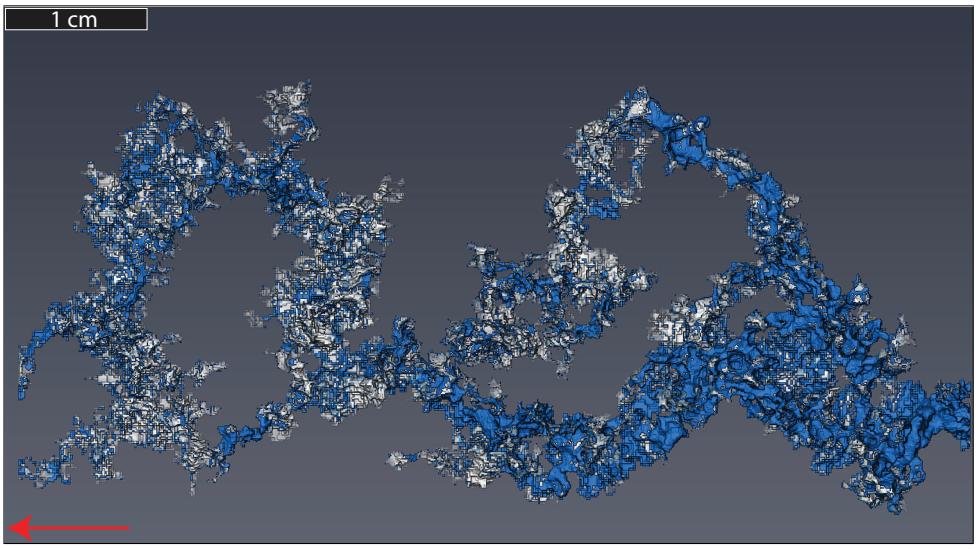

Figure 5.26: Dissolution pattern of the $HFR\ HES$ experiment. Blue = pre-existing porosity amongst the wormhole; white: post-flooding dissolution. The fluid was injected from right to left (red arrow).

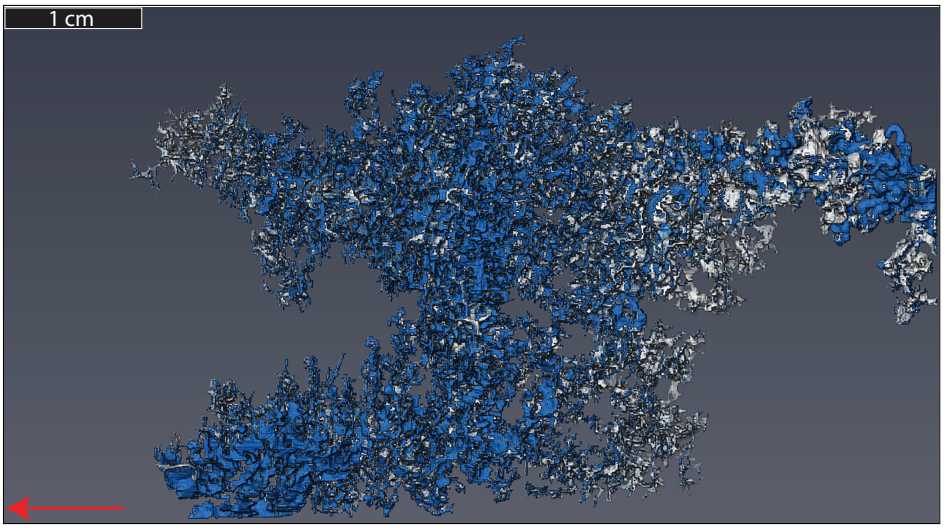

Figure 5.27: Dissolution pattern of the $HFR\ LES$ experiment. Blue: pre-existing porosity amongst the wormhole; white: post-flooding dissolution. The fluid was injected from right to left (red arrow).

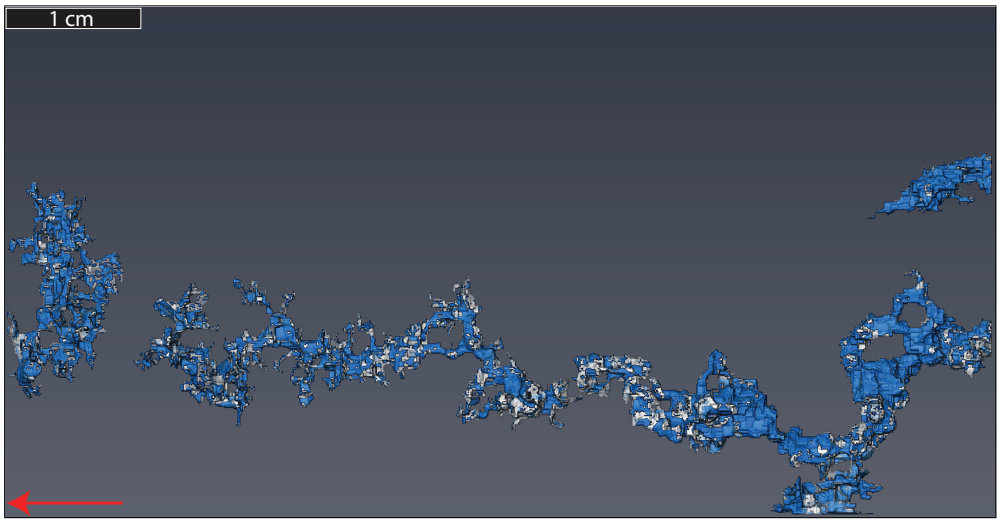

Figure 5.28: Dissolution pattern of the $MFR\ HES$ experiment. Blue: pre-existing porosity amongst the wormhole; white: post-flooding dissolution. The fluid was injected from right to left (red arrow).

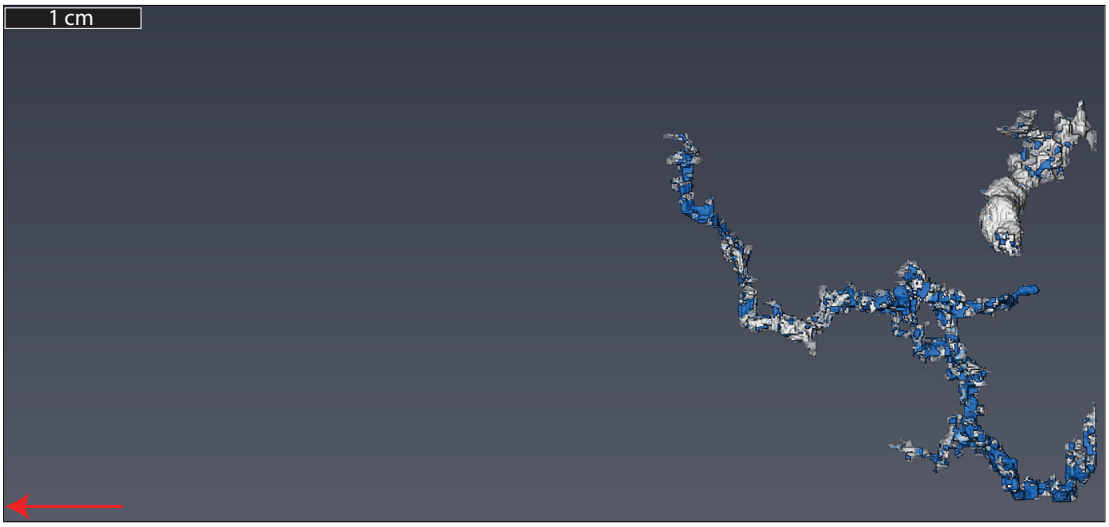

Figure 5.29: Dissolution pattern of the $LFR\ LES$ experiment. Blue: pre-existing porosity amongst the wormhole; white: post-flooding dissolution. The fluid was injected from right to left (red arrow).

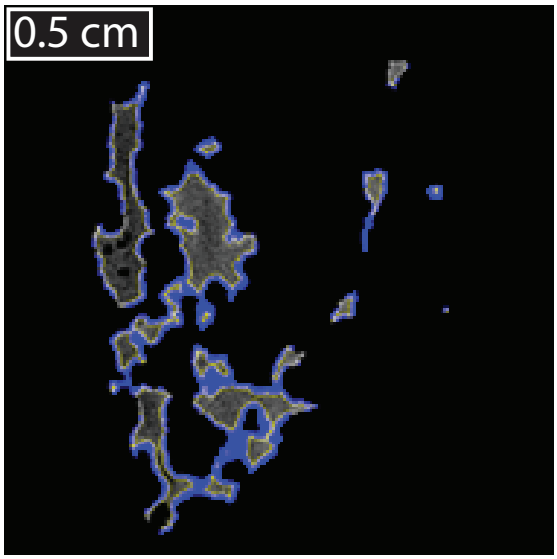

Figure 5.30: Slice (perpendicular to the sample axis) of the $HFR\,HES$ experiment showing the dissolution pattern at the pore scale. The clear zones represent the pre-existing pores; the blue outlines represent the post-experimental porosity enhancement. The image side length is 1.9 cm by 1.9 cm.

5.5.3 Porosity evolution

The experimental process used for this study did not allow the collection of porosity data throughout the flooding phase. Instead, we used the equation given by Luquot and Gouze (2009) and Luquot et al. (2016) as a way to observe the porosity evolution trend from the chemical outputs (equation 3.13 from section 3.6). We assumed that magnesium was provided by the dolomite and the calcite magnesian, while the remaining calcium was provided from the calcite. We did not take into account the left-over material for our calculations. Figure 5.31 presents the porosity evolution. Following k evolution (figure 5.10) and Ca-Mg trends (figures 5.17 and 5.18), the porosity evolution was driven by the injection rate of at the inlet of the sample.

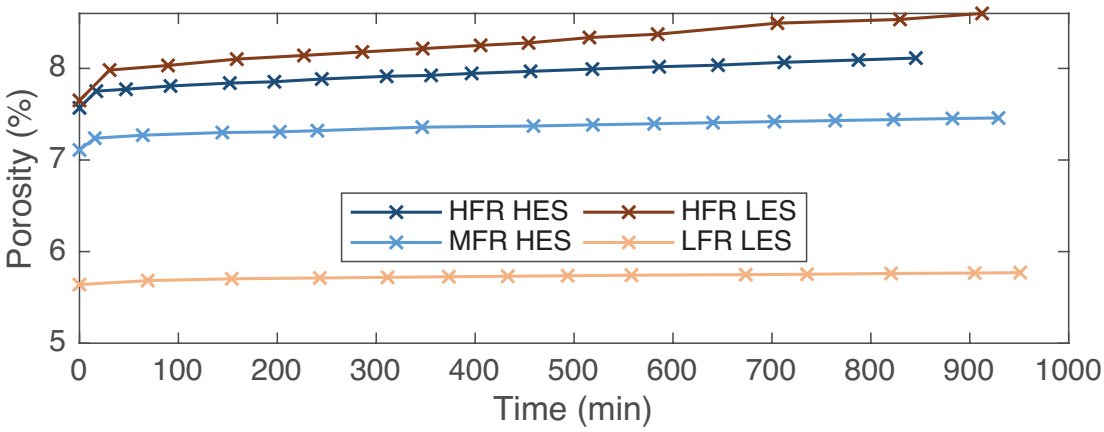

Figure 5.31: Porosity evolution calculated from Ca and Mg mass balance.

A qualitative analysis of figures 5.26, 5.27, 5.28, and 5.29 reveal that no uniform dissolution has occurred during seawater flooding, while previously suggested by figure 5.3. As previously described in chapters 2 and 4, the pH of our injection fluid was too high to observe such degree of dissolution ($Nac_{Golfier} = 4.66 \times 10^{-2}$ - $Nac_{Brondolo} = 1.16 \times 10^{-5}$). We suggest the same boundaries update of the map as the one displayed in chapter 4 (figure 5.32). These new limits have been set by qualitatively describing the experimental damages, and should describe our seawater-calcite system, while the red line should be shifting according to the effective stress in play during the experimental flooding. The red arrow indicates the shift direction of the ramified wormhole limit when a high effective stress is applied to a travertine rock sample, which drives the system towards a less ramified and less stimulated environment.

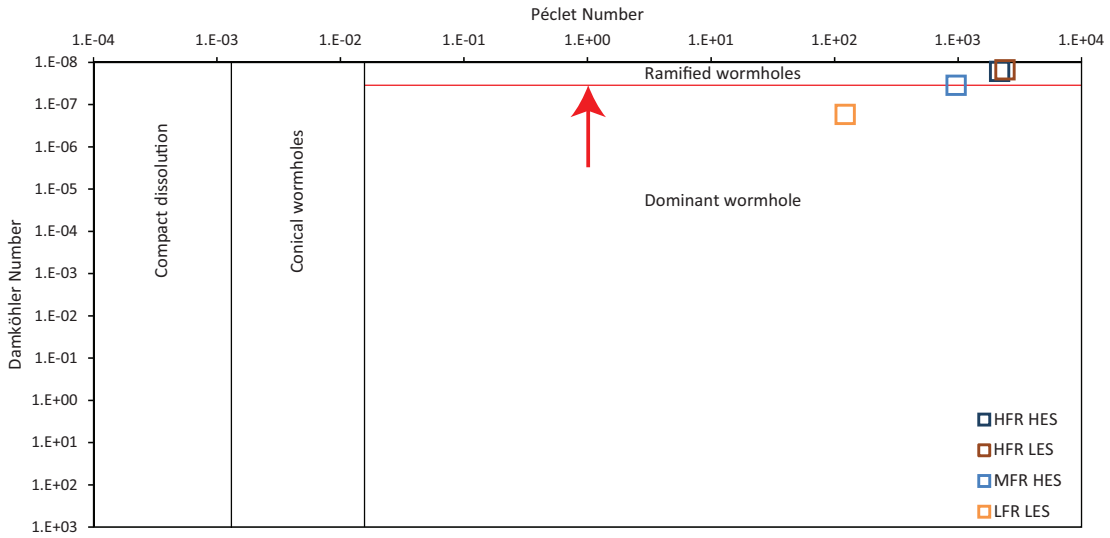

Figure 5.32: Suggested new boundaries for the dissolution map of Golfier et al. (2002). The new boundaries have been shifted after a qualitative assessment of the experiments presented in this chapter, and correspond to a seawater-calcite system. The red line is supposedly affected by the stress state while the arrow indicates the shift direction.

5.5.4 Interpretation

The influence of the injection rate, termed PV_{rate} has been a primary driver for permeability analysis and Ca-Mg dissolution on the heterogeneous travertine rocks. While the above is true, the relative permeability k/k_0, coupled to the analysis of the concentration of the species in the effluent fluid have lead to further findings. We imply here that despite the apparent and obvious influence of the PV_{rate}, a lower flow rate, coupled to a low effective stress, has enhanced k/k_0 generation, and [Ca] and [Mg] evolution. Figures 5.33 and 5.34 represent the processes through which a lower effective stress (higher line pressure) involved a larger increase in k/k_0, a better channelization, and a larger overall [Ca] and [Mg] in the effluent fluids. We believe that the smaller difference in pressure between confining and fluid pressure helps in opening the fewer surface contacts. In the

case of a highly heterogeneous medium, the first parts to dissolve should be the pore throats (red lines in figure 5.33). Once dissolved and/or enhanced, these pathways should be harder to close back as the high pore pressure maintains an overall structural stability. The alteration in heterogeneous carbonates should happen in this newly created or pre-existing flow-path, and at the wall of the pores (red lines in figure 5.34).

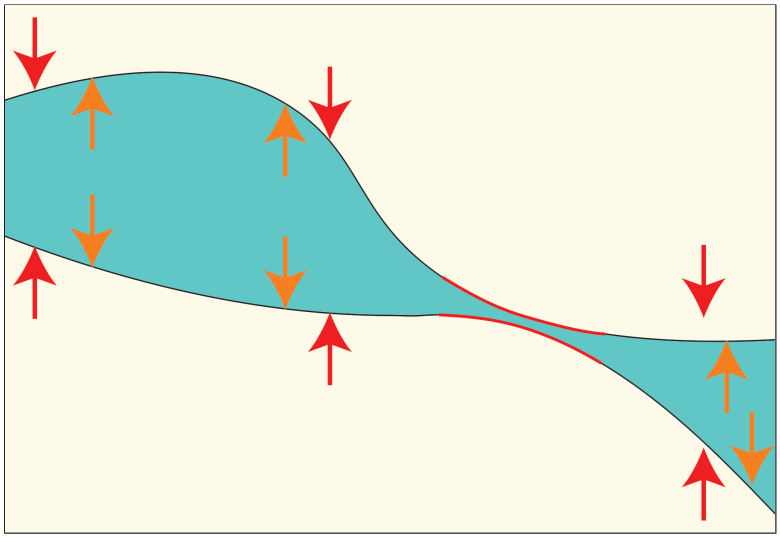

Figure 5.33: 2D sketch of an heterogeneous rock before experimental flooding. The orange arrows represent a high fluid pressure, the red arrows a high confining pressure, and the red lines are regions of likely dissolution.

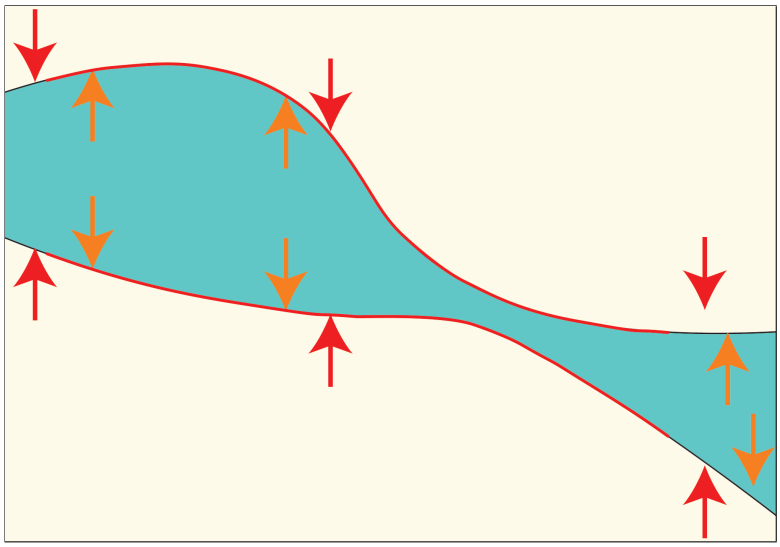

Figure 5.34: 2D sketch of an heterogeneous rock during/after experimental flooding. The orange arrows represent a high fluid pressure, the red arrows a high confining pressure, and the red lines are regions of likely dissolution.

While the same pressure conditions apply in order to obtain some form of pressure-solution between Indiana limestones (chapter 4) and travertines (25 MPa; cf. section 2.7.4 in chapter 2), a less important grain contact area in the travertine samples has limited any pressure solution processes. Considering this heterogeneous type of rock, a low effective stress is thought to have helped in opening small fractures, small pores, as well as keeping opened the pore throats of the macroporosity, hence allowing the fluid to reach most of the porosity. The relative impact of a lower injection rate refers the reactive nature of carbonate rocks, leaving enough time for kinetic reactions to take place.

5.6 Conclusion

We have flooded four travertine core samples with a pH neutral synthetic seawater at geo-reservoir conditions of P-T (P = 50 MPa, T = 60°C) over ~1,000 min. Our experimental matrix has been designed to allow a post-flooding comparative study to isolate the effects of a variable PV_{rate} and variable effective

stress σ'. For each rock, the scenario combined constant P_c, constant P_p, constant T, and constant PV_{rate}. Two samples have been flooded at high PV_{rate}, while the remaining two have been flooded at medium and low PV_{rate}. We also generated two different effective stress scenarios ($\sigma' = 10$ or 40 MPa).

Most studies have worked on the relationship between porosity and permeability enhancement using acidic fluids (Hoefner and Fogler, 1988; Daccord et al., 1989; Frick et al., 1994a; Bazin et al., 1995; Fredd et al., 1996; Fredd and Fogler, 1998; Fredd et al., 1999; Golfier et al., 2002; Siddiqui et al., 2006; Egermann et al., 2006; Bemer and Lombard, 2010; Izgec et al., 2010; McDuff et al., 2010; García-del Cura et al., 2012; Menke et al., 2015; Ott and Oedai, 2015; Walle et al., 2015; Barri et al., 2016; Teles et al., 2016; Zhang et al., 2016; Aman et al., 2018), with the drawback of inducing a surge in permeability and porosity within the first pore volumes injected, due to a small pH of the injection fluid. Acid flooding results in relatively short duration experiments where the effect of other variables such as the effective stress could be missed in the process. While previous work presented the importance of the injection rate (Lasaga, 1984; Hoefner and Fogler, 1988; Steefel and Lasaga, 1990; Frick et al., 1994a; Bazin et al., 1995; Fredd et al., 1996; Fredd and Fogler, 1998; Fredd et al., 1999; Golfier et al., 2002; Kang et al., 2003; Siddiqui et al., 2006; Izgec et al., 2010; McDuff et al., 2010; Garcia-Rios et al., 2014; Walle et al., 2015; Barri et al., 2016), and our results were able to further confirm this, we also observed a coupling with the effective stress, which until now was neglected.

The controlling factor in heterogeneous rock relates to the pore structure and its arrangement (Kalia and Balakotaiah (2009) and chapter 7). Local pressure gradients at the edge of the larger pores drive the fluid flow from one end of the rock sample to the other (Siddiqui et al., 2006; Kalia and Balakotaiah, 2009; Teles et al., 2016; Izgec et al., 2010). The injection rate regulates

how much porosity is bypassed, so that most of the fluid follows the local pressure gradients within the larger pores at low injection rates, and is likely to miss a large portion of the smaller porosity. By increasing the flow rate, one obtains the opposite effect, by counter acting on these pre-existing flow channels, and allowing the fluid flow to reach previously unconnected parts of the rock. This is likely due to an increase in $\triangle P$ leading to open pathways against σ'.

The key findings of this work are as follows: along with the relationship between high effective stress, PV_{rate}, and poro-permeability enhancement witnessed in chapter 4, we observed a similar, although reversed trend during travertine experiments. In the case of highly heterogeneous shrub framestone, the velocity of fluid at the inlet of the sample was linked to an expected increase in volume of Ca and Mg in the effluent fluids, as well as an higher absolute poro-permeability evolution. Further interpretation of the results have led to the discovery of a very specific and reversed behaviour (with respect to the trends observed using Indiana limestone samples).

- Permeability: while it is uncertain that the only driver for permeability recovery is related to the original pre-existing flow-path, our results seemed to present a relationship between a low effective stress (high P_p) and a larger permeability recovery. Moreover, and despite a limited amount of $\triangle P$ data due to the detection limitation of our equipment, our k/k_0 analysis and extrapolated curves also revealed a greater relative influence of a lower flow rate over permeability enhancement. If the stress state influence is almost certain, the effect of injection rate could be related to a pre-existing flow-path, partially or entirely overriding the influence of the PV_{rate}: while the PV_{rate} dominates the absolute creation of pore space and permeability, the effective stress played an important secondary role: the largest increase in relative permeability has been observed at low PV_{rate} and low σ'.
- Chemistry: the volume of Ca and Mg is primarily linked to the velocity of

the fluid flow. However, we observed a reversed tendency compared the one observed in chapter 4. Indeed, we have seen a clear relationship between ions removal and low effective stress by evaluating the concentration of Ca and Mg present in the effluent fluids. The same ordering is witnessed by normalizing the volume of Ca and Mg present in the effluent fluids by the PV_{rate}: the effluent fluid was the highest at low σ' for a given PV_{rate}, which demonstrates the capability a PV_{rate}/σ' association has to remove either ion from a heterogeneous rock sample.

- µCT imaging: 3D volume investigations confirmed the prime influence of injection rates. A second approach also revealed that for a given PV_{rate}, the low effective stress appeared to increase the development of the pre-existing porosity and flow-path. The experimental conditions generating the most permeability per pore volume injected is the low PV_{rate}-σ', while µCT scans analysis showed that the coupling of a high PV_{rate} and low σ' resulted in a better rock matrix flushing, tending towards an enhanced porosity and permeability recovery.

Our findings have gone one step further: for a given stress state, maintaining a relative low injection rate might allow a better permeability, and relative Ca-Mg recovery. For a given injection rate, a low effective stress scenario seemed to enhance the dissolution of calcite, as well as the overall permeability recovery. Our results confirmed previous findings (Fredd et al., 1996), and suggest that for heterogeneous rocks, a low injection rate treatment should be beneficial.

Chapter 6

Observation of wormhole formation at variable effective stress and injection rate on carbonate Pre-salt rocks

6.1 External Contributions

Petrobras and Shell have provided Pre-salt core samples, and allowed to carry out experimental destructive work. Dr. Ian B. Butler has provided help during µCT scanning phases and post-processing scan analyses. ICP-MS fluid sample analyses have been carried out by Dr. Laeticia Pichevin. Finally, Nic Odling assisted with XRD analysis of rock samples.

6.2 Rationale

At the time of writing, this chapter represents the only result section of the PhD that has not be written for future publication. Due to technical and confidentiality limitations, only two core samples have been selected for experimental flooding (described in section 6.4.1). Due to the high initial permeability of the samples, as well as the experimental work previously ran on travertine rocks, the decision has been made reproduce the experimental conditions of PV_{rate} and effective stress of the HFR travertine experiments, as a mean to obtain comparable outputs.

6.3 Introduction

The Lula field, located in the central part of the Santos basin, offshore Rio de Janeiro, has been discovered by Petrobras in early 2000' and was, at this time, the first supergiant Brazilian oil field. To this day, the field is one of the most productive oil fields in the world (Boyd et al., 2015). The upper part of the reservoir is made of an heterogeneous type of carbonate rock, known as travertines, which forms a salt-sealed reservoir lying at 5,000+ m below sea level (Carminatti et al., 2009; Beasley et al., 2010), with evaporitic sequences thicker than 2,000 m (Carminatti et al., 2009). Temperature in the reservoir is relatively low (60 to 80 °C - Alves et al. (2009)). Carbonate reservoirs represent an important part of the world oil reserves (Pizarro et al., 2012), while the Brazilian Pre-salt play, as well as its African counterpart, are two of the largest and most productive oil reservoirs amongst the Atlantic basins (Thompson et al., 2015) and around the world (Carminatti et al., 2009; Nakano et al., 2009). The Brazilian reservoir is termed as non-conventional due to its high heterogenity, and remains poorly understood (Nakano et al., 2009; Beasley et al., 2010; Claes et al., 2017). Although the reservoir is composed of several layers of different nature (Terra et al., 2010), this study focuses on the shrub framestone (Borghi et al., 2013; Alabi et al., 2014), whose depositional process is similar to the one of the modern travertines, and

is related to continental evaporitic deposits. Very few studies have been done on the highly heterogeneous Pre-salt carbonate rocks (Thompson et al., 2015), which can be related to the uncommon setting of the reservoir rock, making its coring complex, and eventually leading to a shortage in available rock samples for destructive works. Following previous work on homogeneous carbonate samples (cf. chapter 4), and heterogeneous Pre-salt analogue rocks (cf. chapter 5), we have realized two experiments on Pre-salt carbonate rocks with the intend of uncoupling the geomechanical processes leading to rock matrix changes. To our knowledge, no study has tried to observe Pre-salt alteration during flooding phases at variable effective stresses. We aim to present a comprehensive analysis over two core samples cored from a non-destructive well of the Santos basin, located offshore Brazil. This work uses the same experimental methodology applied during chapters 4 and 5.

6.4 Material and methods

6.4.1 Samples selection process

The main task consisted in choosing the best rock candidates out of 67 available samples. Several conditions had to be met prior to selecting the samples:

1. Following previous work (cf. chapters 4 and 5), the permeability of a sample should be comprised within a certain range (∼0.5 mD to ∼15 mD).

2. The samples should display a shrub, or shrub-like petromorphology.

3. Ideally, the sample should have been cored perpendicular to the shrub growing pattern (cf. figures D.1 and D.2 in appendix D).

4. The sample should measure no less than 4 cm in length, as this would represent less than half the size of the longest sample used in this PhD project.

5. The sample should not need extensive cuttings and reworking.

Only two samples met the above-mentioned criteria:

- Sample F1012H: described as a reworked shrubby sample. It has been renamed $HFR\ LES$ (High Flow Rate - Low Effective Stress) for the purpose of this study.
- Sample F1494H: described as a reworked shrubby sample. It has been renamed $HFR\ HES$ (High Flow Rate - High Effective Stress) for the purpose of this study.

Figure 6.1 places the predicted and experimental differential pressures amongst the travertine samples of chapter 5. As previously explained in chapters 4 and 5, pre-experimental $\triangle P$ have been calculated using Darcy law, and based on nitrogen permeability measurements, while the syn-experimental differential pressures were based on the $\triangle P$ at t=0 min. We note that the two Pre-salt samples seemed to display similar characteristics with a category of travertine samples (others) which were considered as failed experiments, due to sample breakage or immediate drop in $\triangle P$ after 1-2 min of flooding. Interestingly, and while apparently belonging to this category of unusable samples, the behaviour of the two Pre-salt experiments has allowed us to produce complete sets of data, comparable to the travertine experiments.

The two selected core samples were relatively similar in size and shape, while they showed slight differences in their apparent petromorphology (figures 6.2 and 6.3). Table 6.1 summarizes the information about both samples.

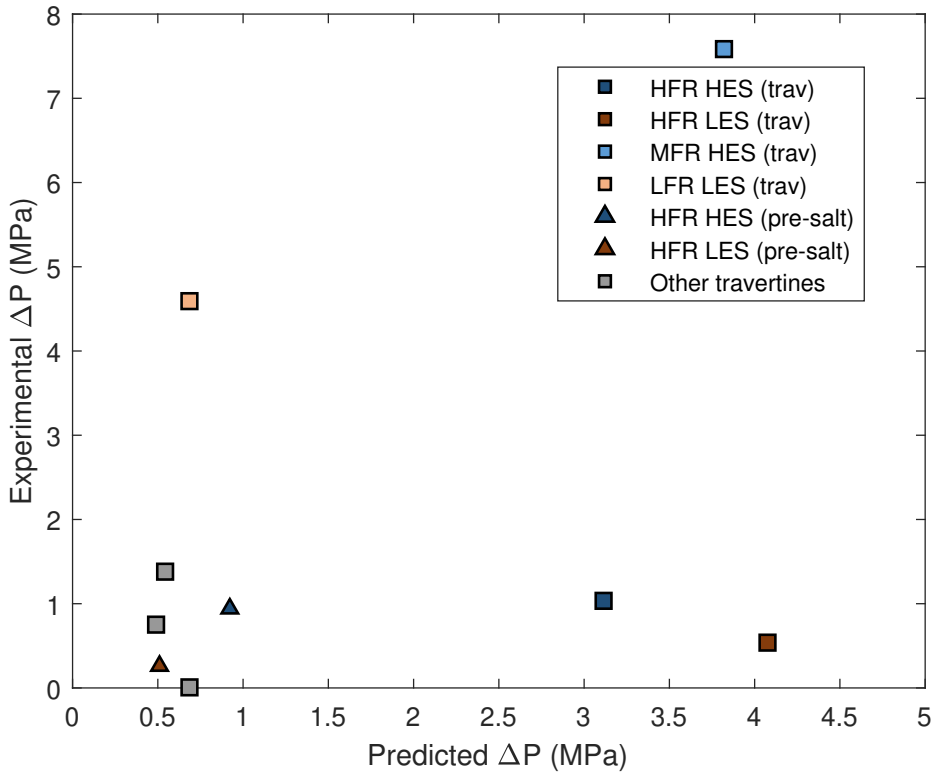

Figure 6.1: Experimentally calculated $\triangle P$ as a function of predicted $\triangle P$ for travertine and Pre-salt rocks. The predicted $\triangle P$ is calculated by solving Darcy equation and using the pre-experimental $k_{nitrogen}$. The experimental $\triangle P$ represents the first log of the differential pressure transducer during a core flooding experiment.

Figure 6.2: Pre-experimental pictures of the $HFR\ HES$ sample. Scale: 1 cm.

Figure 6.3: Pre-experimental pictures of the $HFR\ LES$ sample. Scale: 1 cm.

Details	*HFR LES*	*HFR HES*
Coring depth (m)	4884.7	4971.2
Type	Core	Core
Diameter (mm)	38	38
Length after coring (mm)	66.63	82.07
Length before experiment (mm)	50.18	60
Facies	Reworked Shrub	Reworked Shrub
Petrobras porosity (%)	9.5	13.8
In-house triple weighing porosity (%)	10.29	13.6
Petrobras nitrogen permeability (mD)	11.7	12.2
In-house experimental k_0 (mD)	0.02	0.01
Volume of the sample before exp. (cm^3)	56.9	68.04
Volume of pore (from TW) (cm^3)	5.85	9.24
Volume of solid (from TW) (cm^3)	51.05	58.8

Table 6.1: Petrological characteristics of the Pre-salt samples.

6.4.2 Experimental approach

The experimental scenario followed the experimental plan of chapters 4 and 5: we aimed in obtaining a comparative set of data from which we could uncouple the effect of effective stress from the effect of the injection rate. The first step consisted in allocating the effective stress - low or high - to either sample. As seen on figure 6.3, the F1012H (*HFR LES*) sample displayed large vugs. A pre-experimental µCT analysis ran on both samples confirmed the existence of an interconnected or near-connected network of pore between the inlet and the outlet of the sample (figure 6.4) within *HFR LES*, while a more discrete and less invasive connected porosity has been detected in *HFR HES* (figure 6.5).

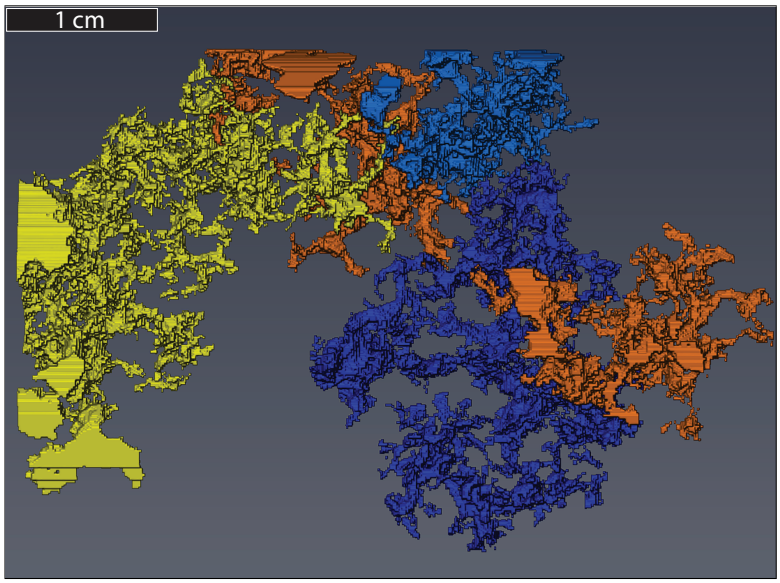

Figure 6.4: Pre-experimental µCT scan analysis of the $HFR\ LES$ sample. The volumes represent the connected network of pores. The image respects the initial size ratio of the sample. Image size: 3.8 cm by 5 cm.

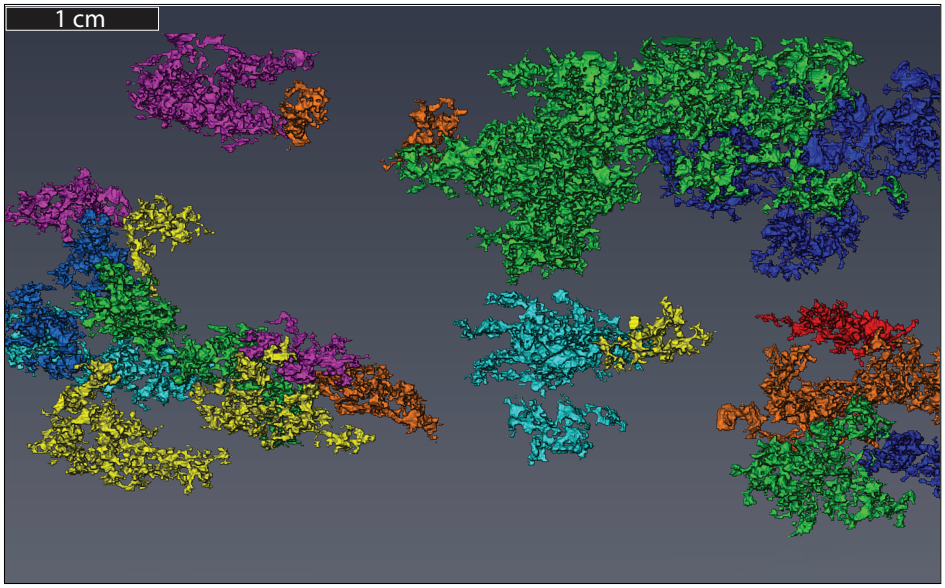

Figure 6.5: Pre-experimental µCT scan analysis of the $HFR\ HES$ sample. The volumes represent the connected network of pores. The image respects the initial size ratio of the sample. Image size: 3.8 cm by 6 cm.

Such differences in the matrix rock structure between the two samples was expected, due to the known heterogeneity of the Pre-salt reservoir (Alabi et al., 2014), which exhibits rapid variation in the diagenetically produced porosity and internal arrangement of the pore structure within short distances (Chitale et al., 2015). It has been decided to apply a low effective stress to the $HFR\ LES$ sample in order to avoid any possible breakage of the rock during pressure loading or during the experiment. The effective stress scenarios remained identical as the one used in chapters 4 and 5: following the work of Terzaghi (1951) we varied the pore pressure P_p while keeping the confining pressure constant (P_c = 50 MPa). The High Effective Stress regime (HES) displayed a constant effective stress of 40 MPa, while the Low Effective Stress one (LES) was set to 10 MPa (summarized in table 6.2).

		Flow expressed as pore volume		
		Low	Medium	High
σ'	Low			2.5 PV/min 10 MPa
	High			2.5 PV/min 40 MPa

Table 6.2: Pore volume rate (PV_{rate}) and effective stress (MPa) values for the four experimental scenarios.

The second step consisted in allocating a PV_{rate} to each experiment. The analysis of the petrophysical and petrographical information provided by Petrobras (summarized in table 6.1) allowed us to solve Darcy law for $\triangle P$:

$$\triangle P = \frac{Q(t) \cdot L \cdot \mu}{A \cdot k} \tag{6.1}$$

Where k (m^2) is the permeability value provided by Petrobras along with the core

sample. The expected $\triangle P$ at t=0 min after solving equation 6.1 for both samples is displayed in table 6.3. We opted for a HES scenario for three reasons:

- A PV_{rate} of 2.5 was within the limits or the injection pump, rated to provide a pulsation-free stream of fluid up to 24 cm^3/min ($Q_{HFR\ HES}$ = 23.11 cm^3/min and $Q_{HFR\ LES}$ = 14.64 cm^3/min).
- The travertine HFR scenarios were the two most comparable experiments (cf. chapter 5).
- The $\triangle P$ generated at PV_{rate} = 2.5 for both samples remained relatively low and far from the limits of the differential pressure transducer (rated to withstand a $\triangle P$ of $\sim$ 8 MPa).

PV_{rate}	$HFR\ HES$	$HFR\ LES$
0.2	0.075	0.04
1	0.37	0.2
2.5	0.92	0.6

Table 6.3: Expected differential pressure values (MPa) for the three scenario of PV_{rate}.

6.4.3 Flow scenarios and dissolution regimes

The experimental matrix has been designed to recreate the physical reservoir conditions of the Brazilian Pre-salt, and thus, both rocks have been flooded with an artificially made seawater displaying 30.5 g NaCl per litre of distilled water, while the temperature of the system was set at 60 °C.

We have used equations 2.8 and 2.9 to verify Darcy law validity in the case of Pre-salt core flooding through the calculation of two dimensionless numbers: α

(Whitaker, 1986) and Re (Stokes, 1851; Fourar et al., 2004). The estimation of α required to know the pore size length l (m), and as such, we used the ICCR-Macropore software (cf. section 3.3.2 of chapter 3) to analyse 100 orthogonally picked slices taken from the pre-experimental µCT 3D image stack of our core samples. Per slice, the ICCR-Macropore analyses the structure of the porosity, and is able to output the characteristic length of the detected pores. As observed in figure 6.6, despite displaying similar modes (Mo $\approx 2.13 \times 10^{-4}$ m) and means ($\bar{x}_{HFR\ HES} = 6.33 \times 10^{-4}$ m, and $\bar{x}_{HFR\ LES} = 8.31 \times 10^{-4}$ m), the distribution of pore sizes largely differs, with $HFR\ HES$ showing smaller pores, which could be interpreted as an absence of vuggy porosity. $HFR\ LES$ has a greater number of pores detected (6,000+ for the largest representative pore length), while the distribution spreads toward larger pores, indicating the presence of vugs. In this work, we have used the mean value of both rocks for the characteristic length. The limits of validity for laminar flows are presented in chapter 2, where α should display a value largely inferior to one (Whitaker, 1986), and Re should be sit between 1 and 100 (Seguin et al., 1998; Fourar et al., 2004). The values of α and Re (table 6.4) indicate that Darcy law was valid for interpreting the relationship between porosity and permeability for the two Pre-salt cores, and considering the two experimental scenarios. The mean values for l for both Pre-salt cores appears closer to the travertine $LFR\ LES$ rock sample, and is one order of magnitude smaller than the three other travertine samples. The distribution remains left skewed, and the density of pore per sample is similar to the travertine rocks.

Sample	α	Re
$HFR\ HES$	1.06×10^{-1}	2.99
$HFR\ LES$	1.61×10^{-1}	3.26

Table 6.4: Reynold and alpha numbers calculated for the Pre-salt core samples

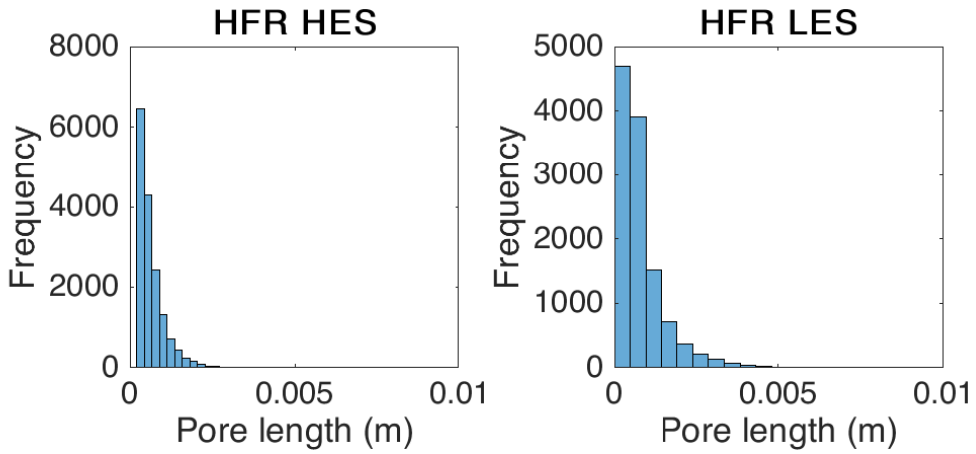

Figure 6.6: Distribution of the major axis lengths of the ellipse shape of the pores after analysis of 100 slices in the Z direction, and using the ICCR-Macropore (bin size = 20).

Using equations 2.11 and 2.14, we have plotted the expected dissolution pattern of both rock samples on a map (figure 6.7) suggested by Golfier et al. (2002).

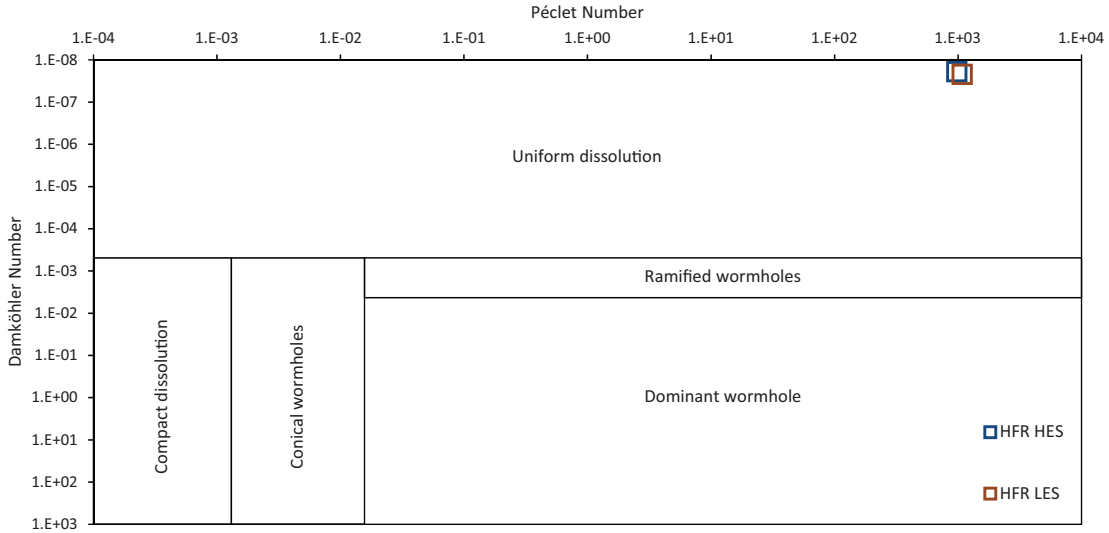

Figure 6.7: $Da - Pe$ map for the Pre-salt core samples. The boundaries have been suggested by Golfier et al. (2002) for a HCl-calcite system.

6.4.4 Reservoir-scale presentation

The Pre-salt reservoir offshore Brazil and offshore African continent have been formed between 123 and 113 Ma (Versfelt et al., 2009; Beglinger et al., 2012; Boyd et al., 2015; Thompson et al., 2015). The breakup of Gondwana initiated the creation of depositional settings which were characterized by fan, deltaic, and lacustrine deposits (Rezende and Pope, 2015). Latest depositional systems were set in a restricted and highly saline system (Rezende and Pope, 2015) that allowed the formation of travertine-like rocks whose most common facies is represented by a shrub-like texture (Kitano, 1963; Chafetz and Folk, 1984; Borghi et al., 2013; Chitale et al., 2015). A more detailed presentation of the Pre-salt reservoir is given in section 2.5.1.6.

6.4.5 Core-scale presentation

The core samples used in this section were Pre-salt carbonate rocks sourced from a non-destructive well. The Pre-salt reservoir displays several main layers of different petromorphology, witness of radical geo-dynamic changes during the reservoir formation. In this study focused on the shrub framestone formation which belongs mainly to the upper part of the Pre-salt section (Aptian), also referred as sag (Nakano et al., 2009; Chitale et al., 2015; Erthal et al., 2017). Similar to the Saturnia travertines, the Brazilian Pre-salt shrub formed in small ponds to lake-sized depositional environments (Chafetz and Folk, 1984; Borghi et al., 2013; Boyd et al., 2015; Claes et al., 2017), where they consist in mm- to cm-scale upward-branching structures (Saller et al., 2016; Tutolo and Tosca, 2018) growing perpendicular to the surface of deposition (Chafetz and Folk, 1984). Saller et al. (2016) describes the rocks as shrubby boundstones whose porosity is made of macro pores, described as vugs.

6.4.5.1 Sample characteristics

This section succinctly presents the rocks, as well as the preparation process. Two cores have been allowed to be destructively tested by the ICCR, Shell, and Petrobras. The expensive nature of the rock as well as the unique nature of the petromorphology of the matrix forced us to adapt our preparation methods.

Petromorphologically, and despite intense burial processes, the shrub growing structures seem to have been preserved (Rochelle-Bates et al., 2018). Chemically, the Pre-salt shrub framestone resembles the modern travertines, and is dominated by calcium carbonate (Tutolo and Tosca, 2018), with variable amount of dolomite and silica, and traces of magnesian clay content (Boyd et al., 2015; Rochelle-Bates et al., 2018), possibly due to diagenetic removal. One main difference we found during chemical analyses concerned the large amount of quartz present within the Pre-salt samples, which was not detected in our travertines. Dolomitization also played a large role during the sag diagenesis (Chitale et al., 2015). Table 6.5 presents the composition of the rocks within the upper sag. Figure 6.8 shows a µCT slice of each sample used in this chapter. While the lighting is independent from the lithology in this case, the porosity arragement, pore sizes, and pore shapes widely differ between the slice A ($HFR\ LES$) and B ($HFR\ HES$). $HFR\ LES$ displays a large amount of apparently poorly connected macropores, while $HFR\ HES$ is made of smaller and more connected pores, which sizes are, for the most part, below the resolution of our µCT facilities.

Compound	Atomic weight (%)		
	Saller et al. (2016)	*HFR HES*	*HFR LES*
Quartz	/	19.2	15.07
Calcite	65	66.7	65.03
Dolomite	30	14.2	19.9
Traces	5	/	/

Table 6.5: Average proportion of mineral forming the upper sag part of the Pre-salt reservoir from Saller et al. (2016) and our in-house XRD analysis. The remaining minerals represented by 'Others' include clay, chert, sand, silts and other trace elements.

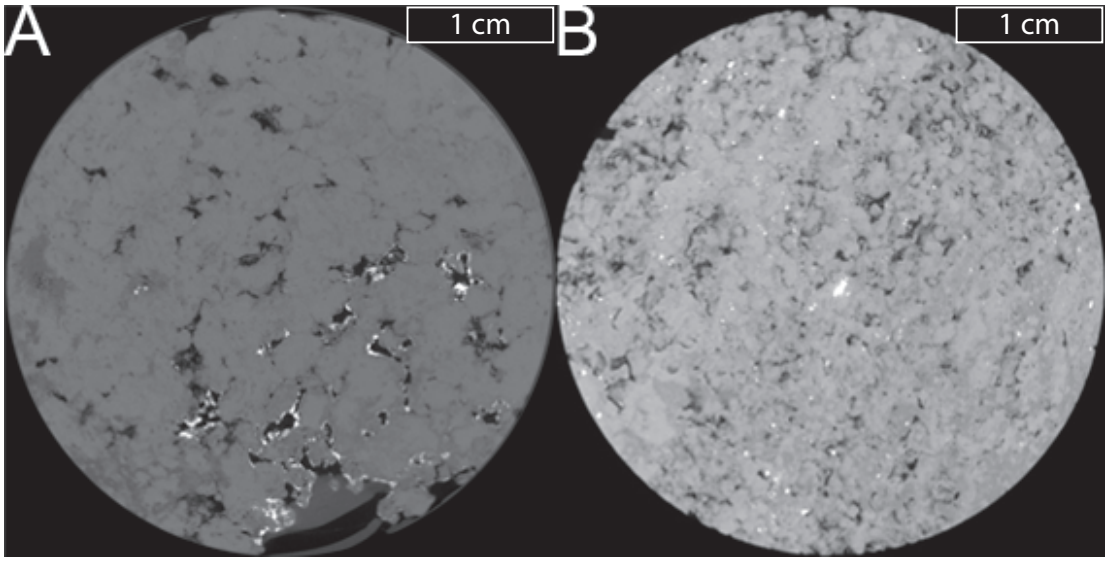

Figure 6.8: µCT slices of the two core sample used in this study. A: $HFR\ LES$; B: $HFR\ HES$. Image size: each slice is 3.8 cm by 3.8 cm.

6.4.5.2 Sample presentation

Most of the sample preparation process followed the steps reported in previous sections (3.2.4, 4.4.6, and 5.4.6). For similar reasons to those edited in section 5.4.6, the $HFR\ LES$ sample preparation process has been adapted in order to avoid damaging the sample and/or the Hassler cell during the confining pressure loading. It has been decided not to alter the sample with cement due to the unique nature of the rock. A non-invasive solution consisted in inserting Teflon-tape in each major vug (figure 6.9-left), before wrapping the sample in water-proof duct tape (figure 6.9-right), ensuring the non-invasion of the elastomer pressure sleeve of the Hassler cell into the larger pores. No particular preparation adjustment was necessary for the $HFR\ HES$ sample, beside the application of a layer of heat shrink.

Figure 6.9: Preparation of the $HFR\ LES$ sample; left: Teflon-tape wrapped sample + Teflon-tape inserted within the major vugs (non-visible on the picture). Right: sample wrapped in duct tape in order to keep the Teflon-tape in place during the experiment. Scale: 1 cm.

6.4.6 Measurements

Physical and chemical data acquisition and subsequent data processing are detailed in chapter 3. The effluent fluid has been sample every 140 min (±121 min) during *HFR LES*, and every 117 min (±48 min) during *HFR HES* The µCT images have been treated using Fiji Schindelin et al. (2012) and Avizo® 9. Following the reconstruction steps edited for the travertine rock samples (chapter 5), the differential results have been gathered using Avizo® 9 with the Generate Surface, Point Cloud Density, and Centerline Tree functions (Sato et al., 2000) on the thresholded subtracted wormhole volumes.

6.5 Results and discussion

6.5.1 Laboratory analysis

6.5.1.1 Permeability

The permeability curves of the the two Pre-salt experiments presents evolution trends similar to the one witnessed during the travertines experiments, with the notable difference of the amount of pore volume flooded to achieve each experiment (∼18 times the amount needed to achieve the longest travertine experiment). This is attributed to a more indurated rock type, which could have been acquired during the burial of the Pre-salt shrub layer, while modern Saturnia travertines never experienced any intense burial or diagenesis. To a lower extent, this has also been witnessed with the Indiana limestones (chapter 4) which have been flooded by ∼3,000 PV on average, while an average amount of ∼1,400 PV have been necessary for achieving the travertine experiments. Figure 6.10 presents the two permeability curves. We did not witness any breakthrough while flooding the *HFR LES*, while *HFR HES* presented signs of it (low and steady increase in k, followed by a relatively sharp increase (Hoefner and Fogler, 1988; Teles et al., 2016). As previously mentioned in chapters 4 and 5, the calculation

of the permeability in associated with a certain margin of error, which itself relates directly to the logging of the differential pressure. Figure 6.11 present the normalized permeability (left) and the predicted evolution of both permeability curves. We note that the two experiments have displayed behavior similar to the travertines' homologous experiments. Most of the permeability of the $HFR\ LES$ experiment has been generated within the first hour of flooding, while it took almost 8 hours to observe the first raise in k under $HFR\ HES$. As previously stated in chapter 3, $HFR\ LES$ has been kept under constant flooding as a way to compare permeability, chemical, and µCT data between both experiments. Several factors could have influenced such differences between both rocks:

- The nature of the rocks, which have not been sampled at similar depths, and therefore are not perfectly identical in terms of diagenetic processes and in-situ stress conditions.
- Considering that local and global heterogneities are governing the flow-path (Egermann et al., 2006; Siddiqui et al., 2006; Kalia and Balakotaiah, 2009; Izgec et al., 2010; Teles et al., 2016), one could argue that the difference in the original nature of the rocks could have impacted the k generation.
- The low effective stress regime might have facilitated the fluid flow through the pore network of the rock.

While the reasons above could account for the large difference in permeability generation, we also observed that the HFR scenarios under travertine rocks have witnessed the exact same permeability increase. Although, we are not drawing any conclusion, it is possible that a low effective stress scenario could increase the chances of permeability recovery over a shorter period of time, providing the heterogeneous nature of the rock.

In total, the $HFR\ HES$ experiment has witnessed a permeability increase of ∼60 times, and $HFR\ LES$ has observed an increase of ∼20 times its original

permeability. Figure 6.12 presents $\frac{\partial k}{\partial t}$, which shows the rate of permeability generation over time. While it appears clear on figure 6.10 that $HFR\ HES$ seemed to be the most effective scenario in terms of k recovery, we observe here that $HFR\ LES$ was the most productive scenario until ~2,000 min, followed by a takeover of $HFR\ HES$ which then became the dominant scenario during the later stages of the experiment.

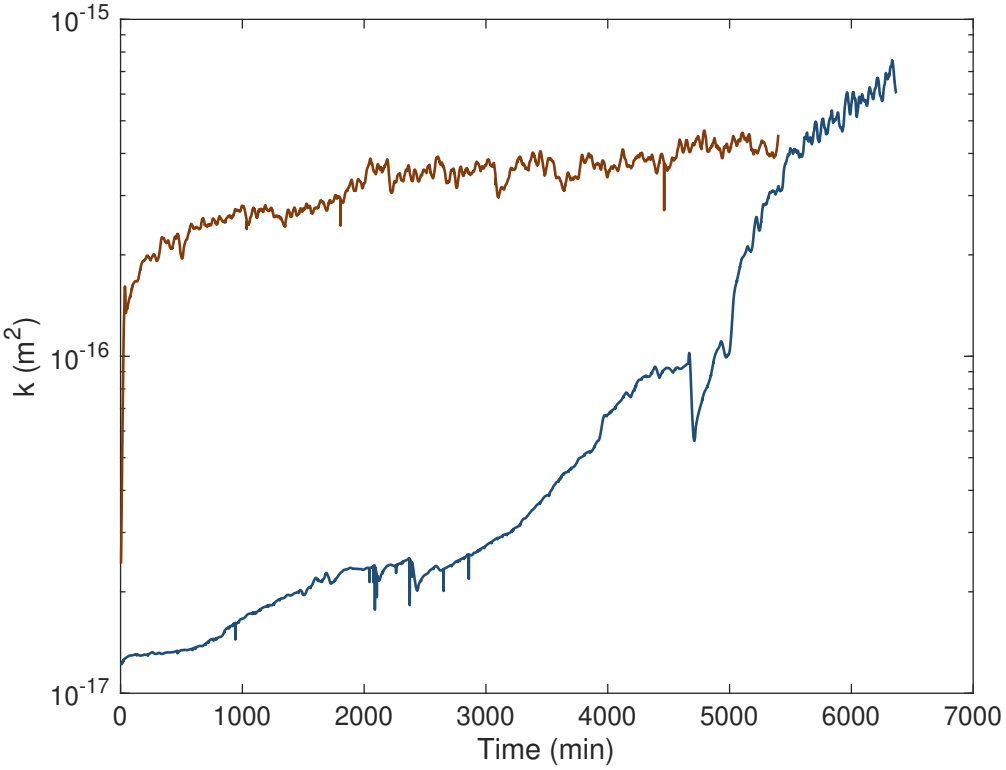

Figure 6.10: Permeability (m^2) of the $HFR\ HES$ (blue) and $HFR\ LES$ (orange) experiments. The large decrease in k during the $HFR\ HES$ experiment (~5,000 min) is due to a pausing of the experiment after a technical issue with the back-pressure regulators.

Injection rate is a prime variable for permeability generation (Hoefner and Fogler, 1988; Daccord et al., 1989; Bazin et al., 1995; Fredd et al., 1996). We used $Q_{HFR\ HES} = 23.11$ cm^3/min, and $Q_{HFR\ LES} = 14.24$ cm^3/min. Converting

the above values using the equation 2.4 results in a similar Darcy velocity of $\sim 2 \times 10^{-3}$ m/s. By using similar injection velocities we intended to observe the relative impact of the stress state over the rock matrix alteration. We infer that the interdependence between pore volume injected and permeability recovery can be largely linked to the stress regime applied. Figure 6.13a shows the relative permeability generated as a function of the amount of pore volume injected into each sample.

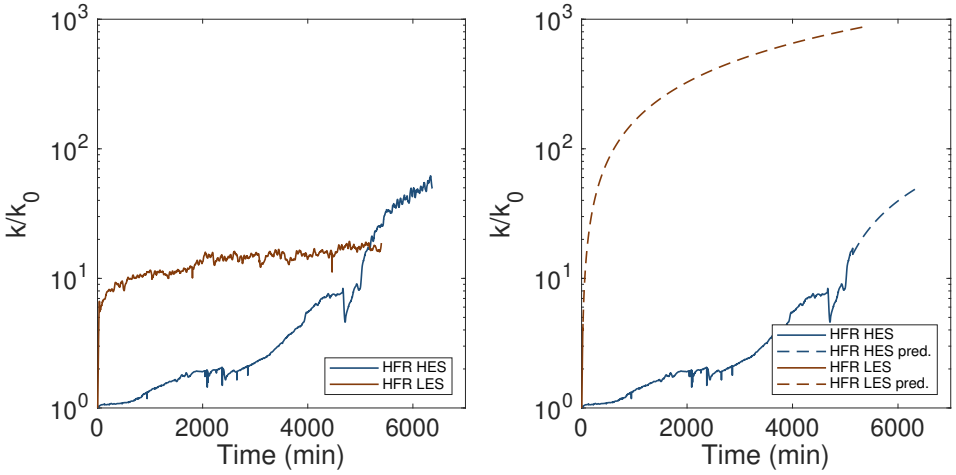

Figure 6.11: Permeability evolution normalized against the permeability value recorded at $t = 0$ min. Left: untreated data; right: the plain curves display the data outside the error region, while the dashed lines are the extrapolated data. The linear extrapolations are based on the recorded data sitting in between the marks of figure 6.14 and the last valid recorded value. By assuming a linear increase of the permeability for both scenarios, $HFR\ LES$ should have generated a larger k/k_0 than $HFR\ HES$.

Most permeability in $HFR\ LES$ has been generated within the very first pore volumes, while the trend developed at a more gradual pace for $HFR\ HES$. While the curve was steeper for $HFR\ HES$, at any given pore volume injected, the $HFR\ LES$ experiment was displaying a higher k/k_0. Figure 6.13b expresses the amount of permeability gained per pore volume injected, over time. Following

the previous conclusions from the permeability reading, this subplot supports the $HFR\ LES$ scenario by showing that it generated more permeability per pore volume injected for a large part of the experimental run. Both samples have witnessed different rock matrix alteration: we observed a breakthrough-like behaviour during the $HFR\ HES$ run, while a near-existing flow-path prevented any breakthrough to happen during the $HFR\ LES$ experiment.

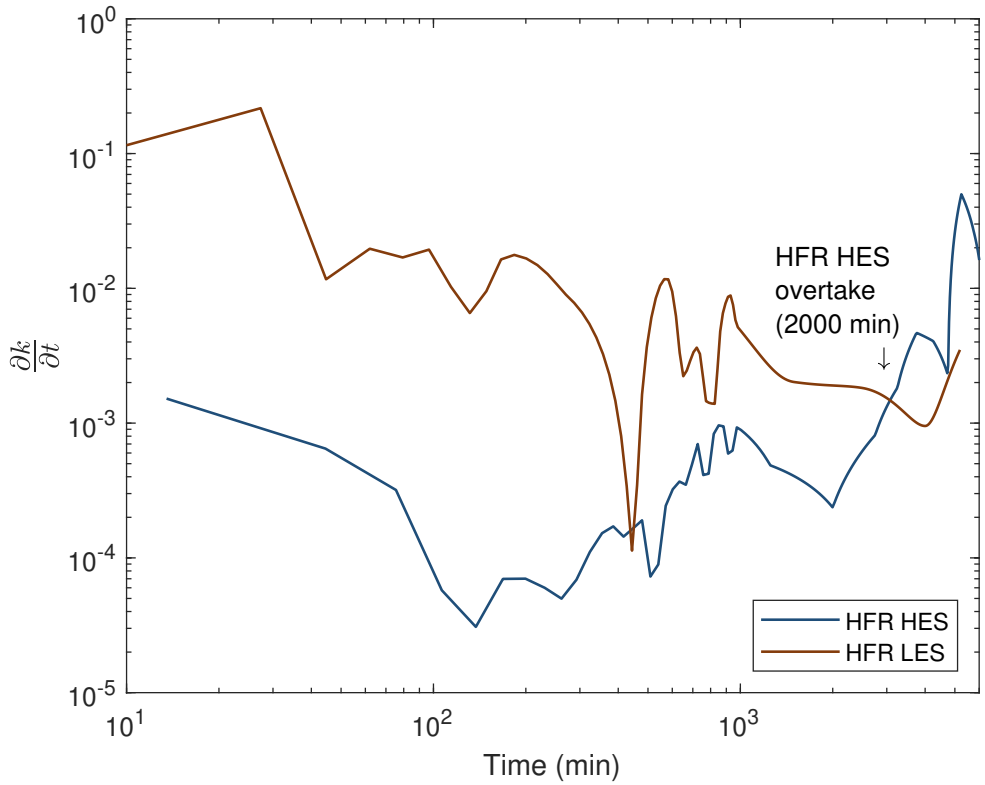

Figure 6.12: Derivative of the permeability with respect to time.

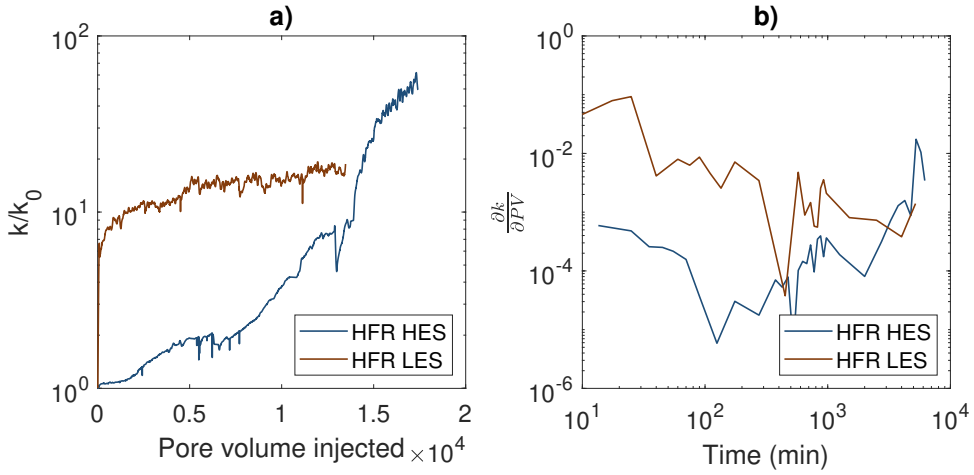

Figure 6.13: a) Normalized permeability generated as a function of pore volume of seawater injected; b) Relative contribution each pore volume injected had on the permeability generation.

Although different, the Pore Volume to Breakthrough (PV_{bt}) (Hoefner and Fogler, 1988) and the Pore Volume to maximum permeability (introduced in section 5.5.1.1, and labelled PV_{maxK}) are a good way of marking a change in dynamic during an experimental flooding: assuming a linear relationship between $\triangle P$ and k (Luquot and Gouze, 2009), we can pinpoint $PV_{bt\ /\ maxK}$ (figure 6.14). By knowing the time at which the $PV_{bt\ /\ maxK}$ happened, we have obtained the amount of pore volume that have been injected before stabilization ($HFR\ LES$) or destabilisation ($HFR\ HES$) of the system. Displaying the PV_{maxK} and PV_{bt} as a function of time (figure 6.15) shows no correlation between the two experiments, and the effect of PV_{rate} on permeability generation: $HFR\ HES$ has seen its permeability being greatly influenced by the differential pressure after ~400 pore volumes injected, while only ~100 where sufficient for $HFR\ LES$.

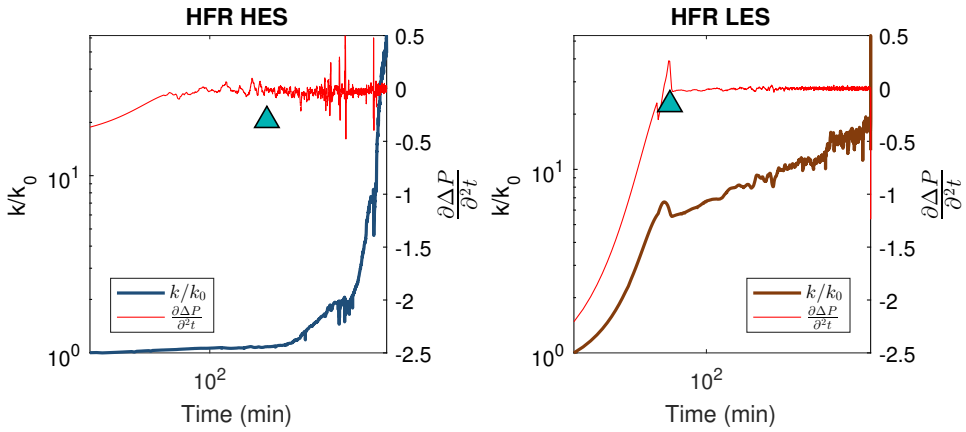

Figure 6.14: Differential pressure analysis and k/k_0 evolution. The blue marker indicates the time before which the $\triangle P$ has had a maximum impact on the permeability generation or at which a breakthrough was initiated.

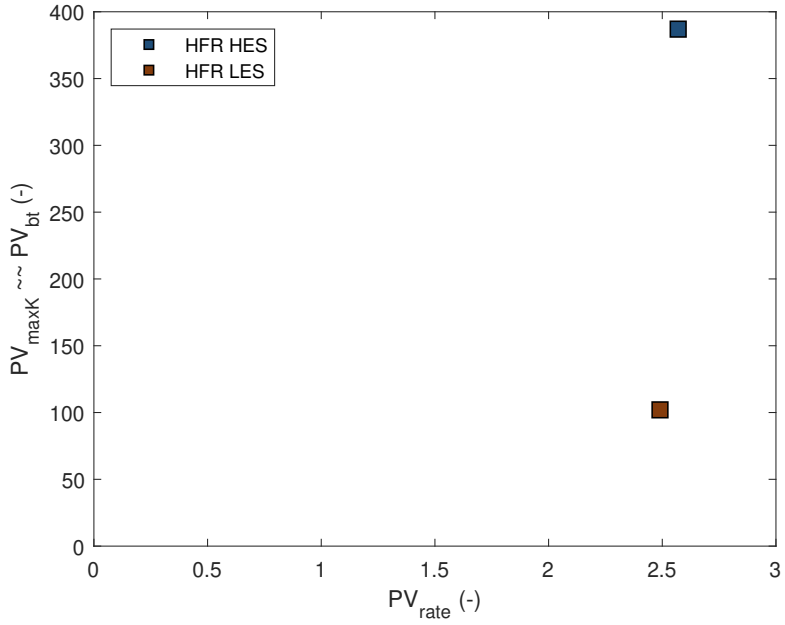

Figure 6.15: PV_{maxK} and PV_{bt} as a function of constant PV_{rate}. The values for PV_{maxK} and PV_{bt} have been derived from the markers of figure 6.14, while the PV_{rate} values are given in table 6.2.

6.5.1.2 Calcium and magnesium evolution

The pH measurements (figure 6.16) support the general permeability analysis: as expected, the pH values increased from ∼7 at the inlet of the sample to 9-10, indicating that calcite dissolution has happened throughout the experiments (Den Ouden et al., 2015). Both samples showed a high pH all over the experimental run. Effluent fluids from the $HFR\ LES$ experiment displayed, on average, a pH of 9.38 (±0.13), while $HFR\ HES$ averaged at 10.2 (±0.22). Although this difference in pH cannot be explained by a more acidic injection fluid resulting in a higher calcite dissolution rate during $HFR\ HES$, it demonstrates that different processes happened during both experiments, and could be explained by a more reactive rock composition, or a more stimulant experimental scenario for $HFR\ HES$ leading to an advanced hydrolysis of the carbonate ion which produced more alkalinity than at $HFR\ LES$. Physically, this can be explained by a tighter matrix for the $HFR\ HES$ sample, leading to mechanical and chemical alteration of the rock at the walls of the pores and/or wormholing (discussed later in this chapter - cf. figures 6.23 and 6.25b), while the pre-existing flow-path of $HFR\ LES$ led to superficial wall dissolution in a flow dominated system, i.e. enhancement of the current preferential pathway.

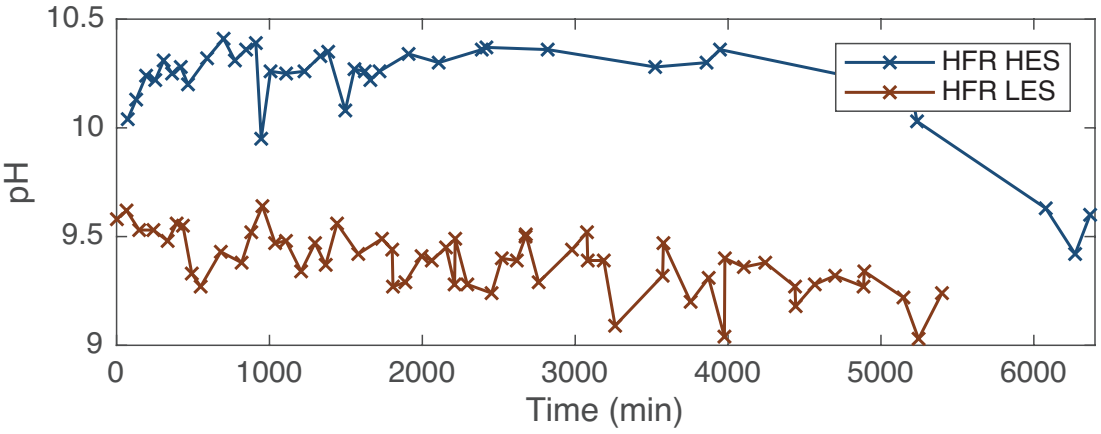

Figure 6.16: pH measurements for the Pre-salt experiments. All measures have been done on sub-samples of the fluid before ICP-MS analyses.

The concentration of Ca and Mg ions is displayed in figure 6.17. Interestingly, the decrease in concentration in both ions is only witnessed for the $HFR\ LES$ experimental scenario, while $HFR\ HES$ showed a constant - never decreasing - concentration in Ca and Mg. This could be explained by a different rock petromorphology, which led to an intense rock dissolution along the entire experiment. Coupled to a mechanically stimulant scenario, the rock sample has withstood a constant dissolution of its matrix throughout the entire experiment. At this stage, we are not able to confirm the reason behind such an intense dissolution, except for a slow and steady collapsing of the rock due to the larger effective stress (cf. section 6.5.2). The ordering of the curves is similar to the experimental flooding of section 4.

Figure 6.18 shows the normalized volume of Ca-Mg in the fluid samples (Ω (-); cf. equations 3.9 to 3.12). Figure 6.16 distinctly shows that more dissolution is expected for the $HFR\ HES$ experiment. Indeed, Ca and Mg are found in higher relative amount within $HFR\ HES$, which reinforces the idea that a wormhole formed through the $HFR\ HES$ sample instead of a more matrix-stimulated process for $HFR\ LES$.

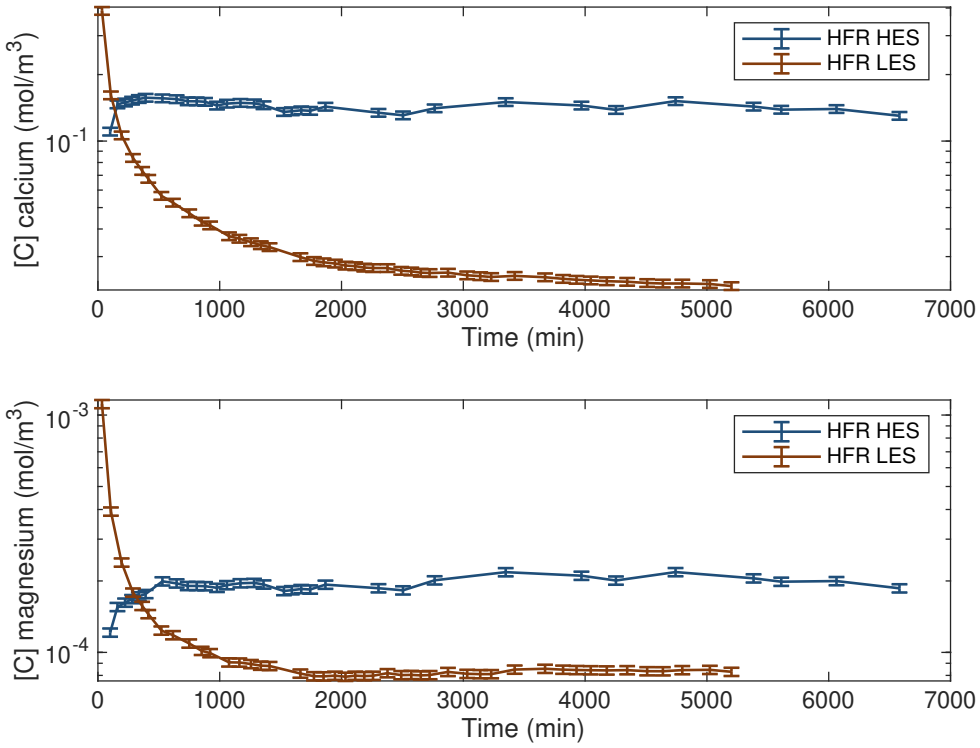

Figure 6.17: Concentration of calcium and magnesium derived from the effluent fluids. For both ions, the $HFR\ HES$ scenario has generated more Ca and Mg. The shapes of the curves largely differ, which might be due to two different processes taking place during each experiment.

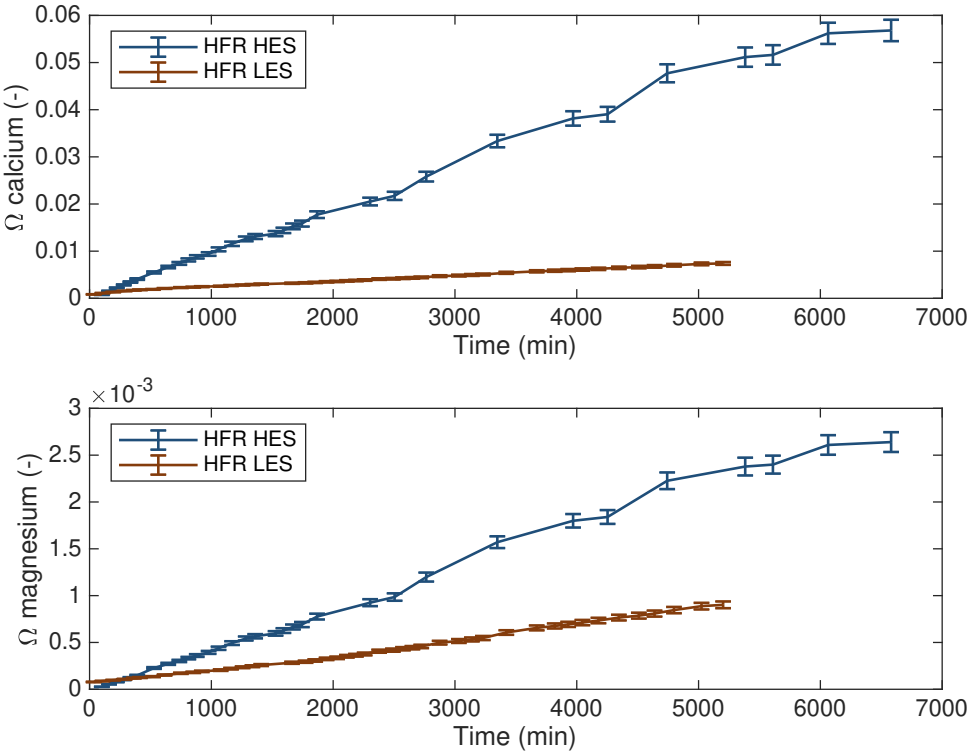

Figure 6.18: Volume of calcium and magnesium derived from the effluent fluids sampled directly out of the Hassler cell and normalized against the original volume of rock of the core sample (Ω). $HFR\ HES$ has dissolved ~6 times more Ca and ~5 times more Mg than the $HFR\ LES$ scenario.

6.5.2 µCT analysis for rock alteration

While both rocks have been flooded for a similar amount of time (~90 hours for $HFR\ LES$ and ~100 hours for $HFR\ HES$), the samples did not behave similarly (cf. section 6.5.1.1). As a result, $HFR\ HES$ broke during the unloading of the Hassler cell and came out in four main pieces (figure 6.19), where $HFR\ LES$ remained unbroken. Unfortunately, no comparative work can be done between the samples: due to heterogeneous nature of the samples, we cannot use a ROI as we could be missing the main wormhole within $HFR\ HES$, which could have

developed in a broken part of the core, or even could have developed in the weakened and missing parts or the sample.

Figure 6.19: Post-experimental $HFR\ HES$ sample. The three smallest pieces of rock (right part) have been cleaned out and kept as displayed on the figure, while the largest bloc has been cast in epoxy resin for further µCT scanning.

The broken sample has been reconstructed using Avizo® 9 (figures 6.20 and 6.21). While we have been able to register the four pieces of rock together, we were not able to resolve enough difference between pre- and post-experimental scans to account for the rock alteration. The only comparative information we obtained was based on the shape of the dissolution flow-path. Figures 6.22 and 6.23 display the pre-existing porosity (blue volumes) contained within the newly formed dissolution flow-path (white volumes). The process for obtaining these volumes is presented in section 5.5.2.

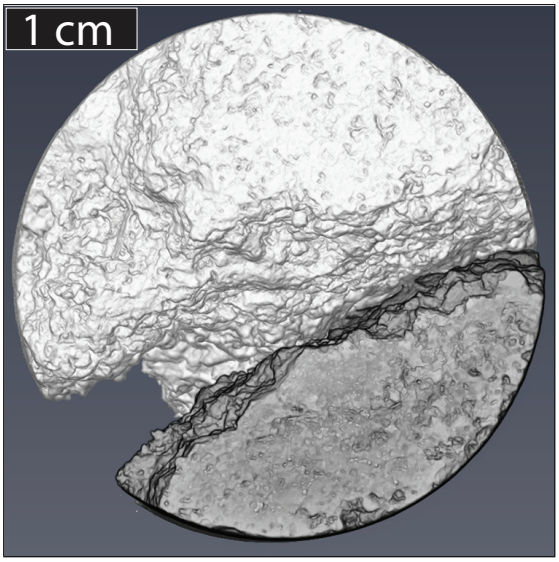

Figure 6.20: Top view of the post-experimental μCT scan reconstruction of the $HFR\ HES$ sample. Side length: 3.8 cm by 3.8 cm.

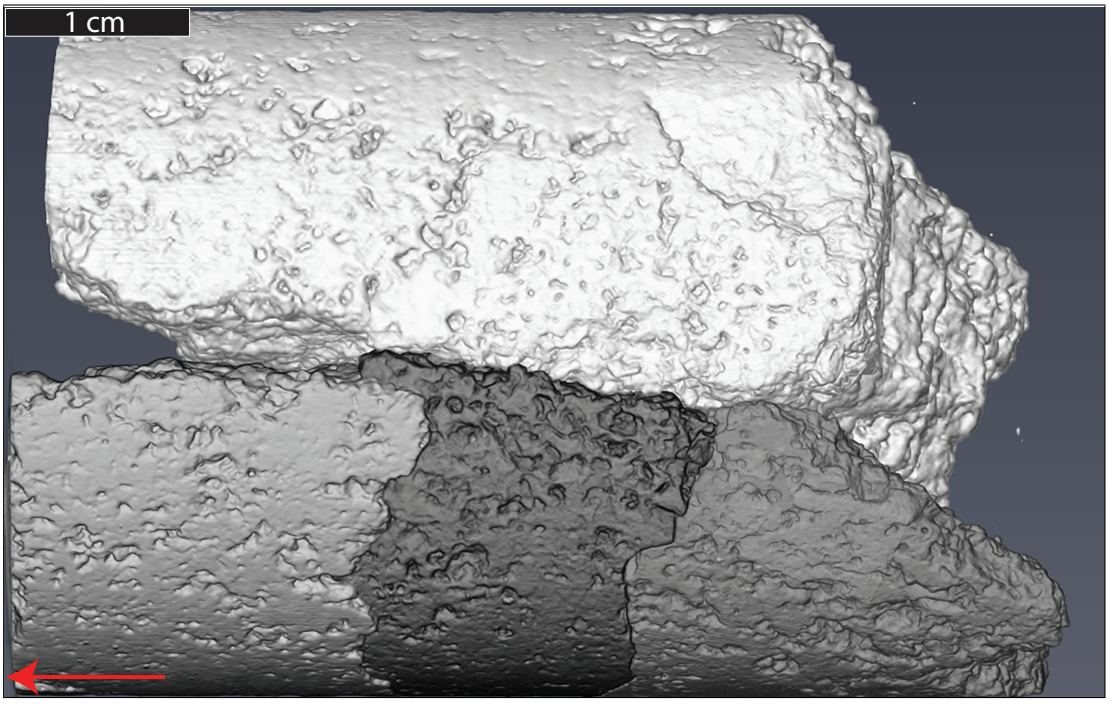

Figure 6.21: Side view of the post-experimental μCT scan reconstruction of the $HFR\ HES$ sample. Side length: 6 cm by 3.8 cm. The fluid was injected from right to left (red arrow).

As seen in figure 6.4, $HFR\ LES$ already featured a pre-existing or nearly existing flow-path between inlet and outlet of the sample, while $HFR\ HES$ (figure 6.5) showed no obvious link between both ends of the sample. $HFR\ LES$ showed a clear dissolution on one side of the sample (figure 6.22), likely related to similar erosion processed witnessed during the travertine experiments (chapter 5 and figure 6.25a), where the pre-existing porosity was enlarged by the fluid flow. It is more complex to extrapolate the dissolution pattern of $HFR\ HES$ based on a reconstructed broken sample, but parts of what appeared to be a channel have been imaged and shown in figure 6.23. We can see that the wormhole has reached a ramified and/or fractal aspect, and was spreading across the porosity. It is impossible to confirm that the entire wormhole would have further developed this ramified pattern or if this output was only controlled by the local pre-existing porosity. An alternative way of confirming the multi-branched nature of the dissolution during the $HFR\ HES$ experiment relies on the modelling work presented in chapter 7. Figure 6.24 presents the 2D prediction of the rock matrix alteration: the X-axis represents the slices of the µCT images which are used for the prediction, while the Y-axis represents the predicted intensity of dissolution. Although these results are not established yet, the outputs presented in chapter 7 and appendix K represent a strong base that can be used in this case. Contrary to figures 7.8 and 7.9, which displayed non-branched wormholes, figure 6.24 shows features comparable to those found in figures 7.10 and 7.11, which were associated to branched and ramified dissolution patterns. The similarities in alteration intensity and spread of this alteration across the sample is a strong indication that branching and ramification likely occurred during seawater flooding at high effective stress and high flow rate.

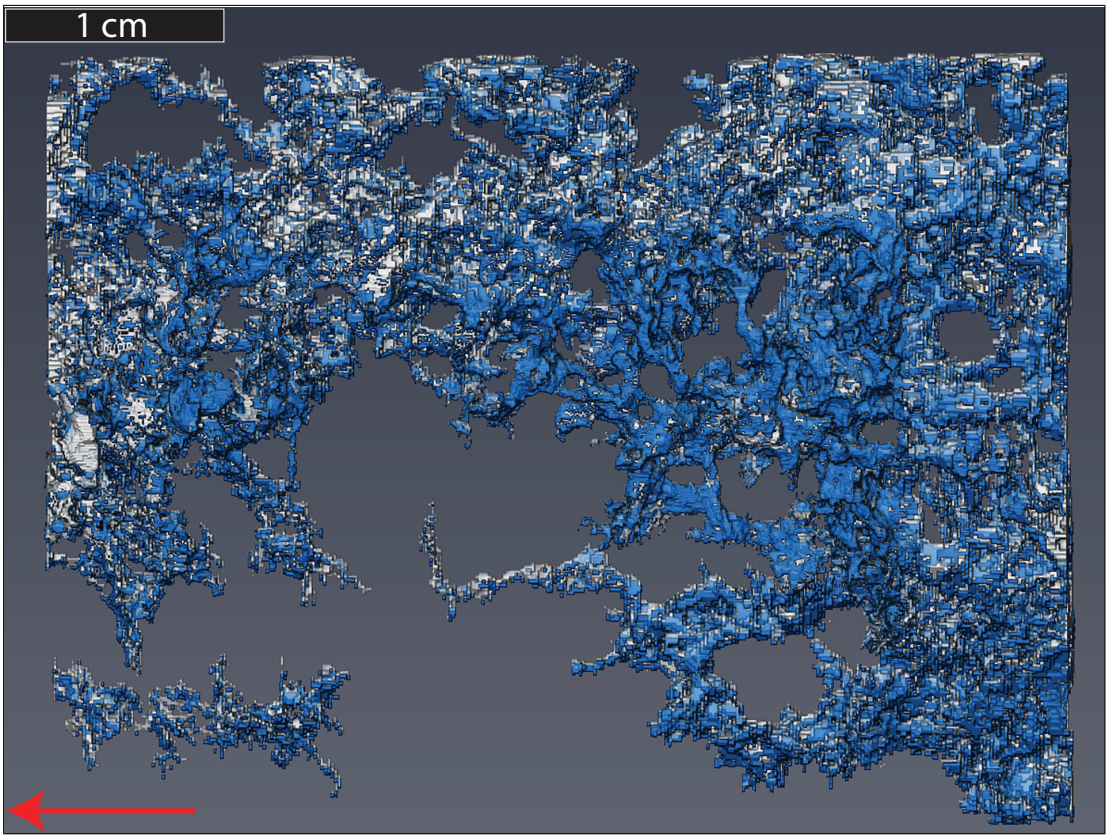

Figure 6.22: Dissolution pattern of the $HFR\ LES$ experiment. Blue: pre-existing porosity amongst the wormhole; White: post-flooding dissolution. Image size: 3.8 cm by 5 cm. The fluid was injected from right to left (red arrow).

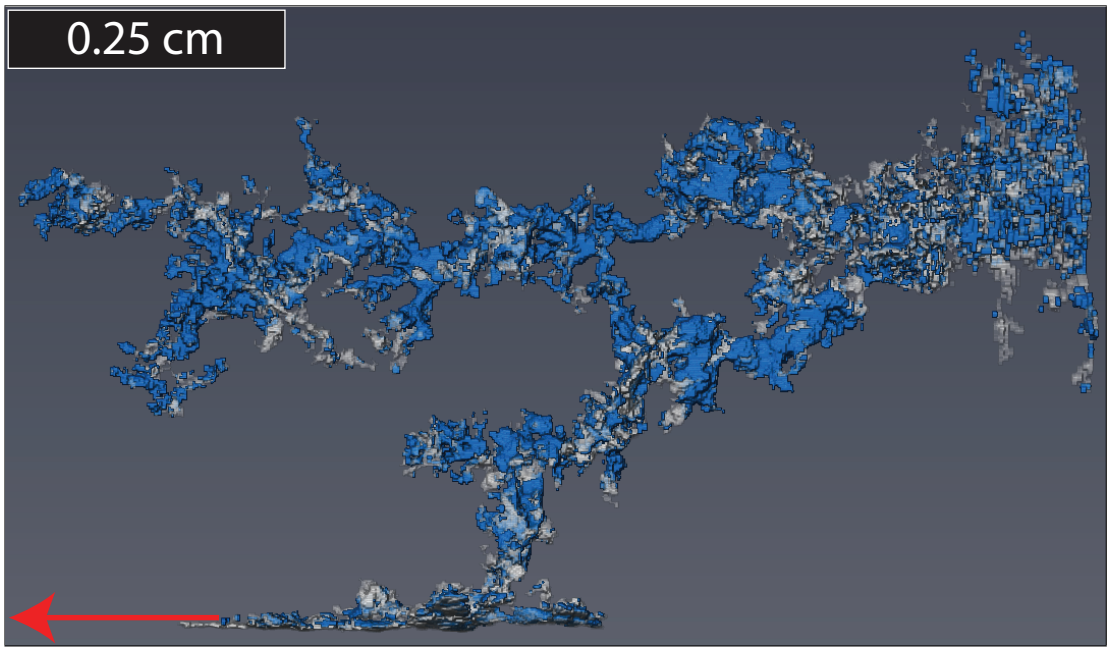

Figure 6.23: Dissolution pattern of the $HFR\ HES$ experiment. Blue: pre-existing porosity amongst the wormhole; White: post-flooding dissolution. Image size: ∼1 cm by ∼0.6 cm. The fluid was injected from right to left (red arrow).

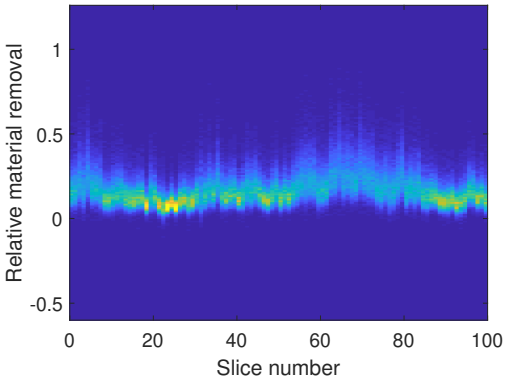

(a) Pre-salt: HFR HES - YZ direction.

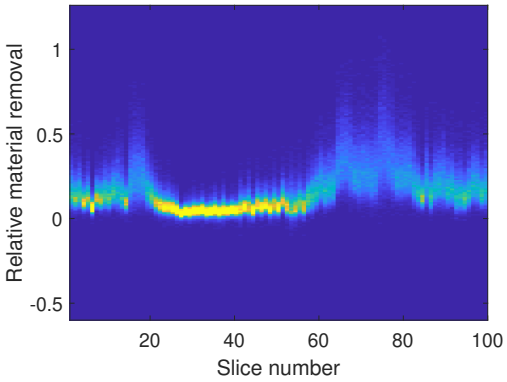

(b) Pre-salt: HFR HES - XZ direction.

Figure 6.24: Prediction of dissolution based on µCT images and geometrical features ($HFR\ HES$ experiment). The features present on both pictures are likely signs of a branched dissolution pattern.

While the porosity structure and shape of the Pre-salt samples resemble what has been described by previous work (Alabi et al., 2014; Chitale et al., 2015), we noted some differences between both samples (figure 6.25) with $HFR\ HES$ (figure 6.25b) displaying smaller pores than $HFR\ LES$ (figure 6.25a). Although in both samples the porosity has been enhanced in a similar way, we noted that the porosity of $HFR\ HES$ displayed smaller pores and could have led to the creation of smaller and more numerous ramified channels amongst the sample; similar to what has been described in chapter 4. The reasons behind the weakening of the sample are not clear, but might involve regions of the sample of variable stiffness which were undetectable via µCT imaging. These regions could have been preferential parts for the development of wormholes, which, coupled with a high PV_{rate} and high effective stress, might have further weakened the entire sample.

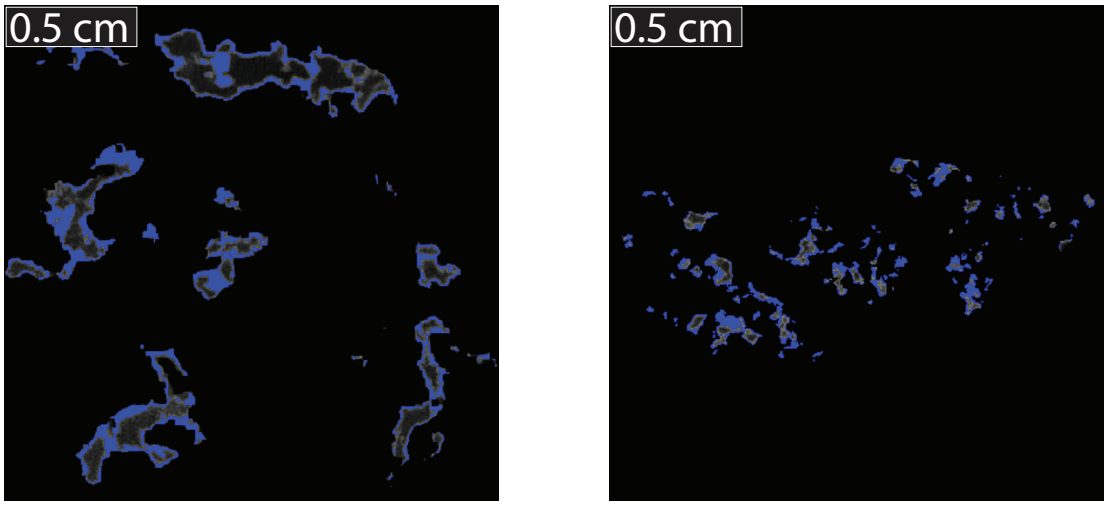

(a) Slice of the $HFR\ LES$.

(b) Slice of the $HFR\ HES$.

Figure 6.25: Slices from the µCT volumes showing the dissolution pattern at the pore scale. The clear zones represent the pre-existing pores; the blue outlines represent the post-experimental porosity enhancement. Images side length: 1.9 cm by 1.9 cm.

6.5.3 Porosity evolution

We have plotted the porosity evolution based on the initial porosity, and the Ca and Mg mass balance evolution over time. Results presented in figure 6.26 have been derived based on equation 3.13 (Luquot and Gouze, 2009; Luquot et al., 2016).

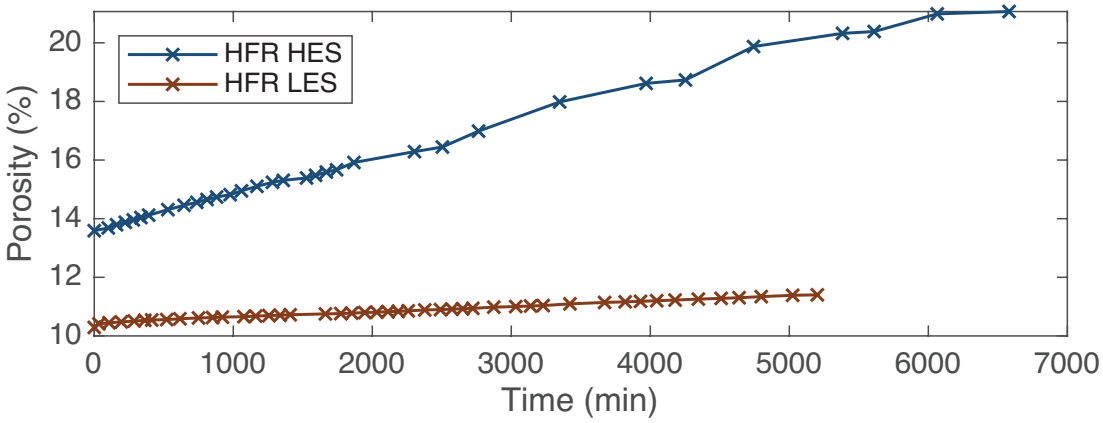

Figure 6.26: Porosity evolution calculated from Ca and Mg mass balance.

As expected, the porosity of $HFR\ HES$ has been greatly increased. We attribute this creation of porosity to the absence of pre-exiting flow-path, which have not been observed at the pixel resolution under µCT analysis. The dissolution of the rock matrix, and the creation of a preferential flow-path was linked to large porosity increased.

By using the same updated map as the one previously used in chapters 4 and 5, we have updated the boundaries of the Pre-salt experiments (figure 6.27). We observe that $HFR\ LES$ falls in the ramified dissolution regime (confirmed by figure 6.22). Without any qualitative control of the dissolution regime undergone by $HFR\ HES$, we cannot confirm that the sample has experienced a ramified dissolution regime, although suggested by figure 6.23. The intensity of dissolution of $HFR\ HES$, displayed by the large amount of Ca and Mg dissolved, coupled to a large increase in porosity and permeability, as well as a collapsed sample,

could be signs that the sample has showed early signs of uniformly distributed dissolution.

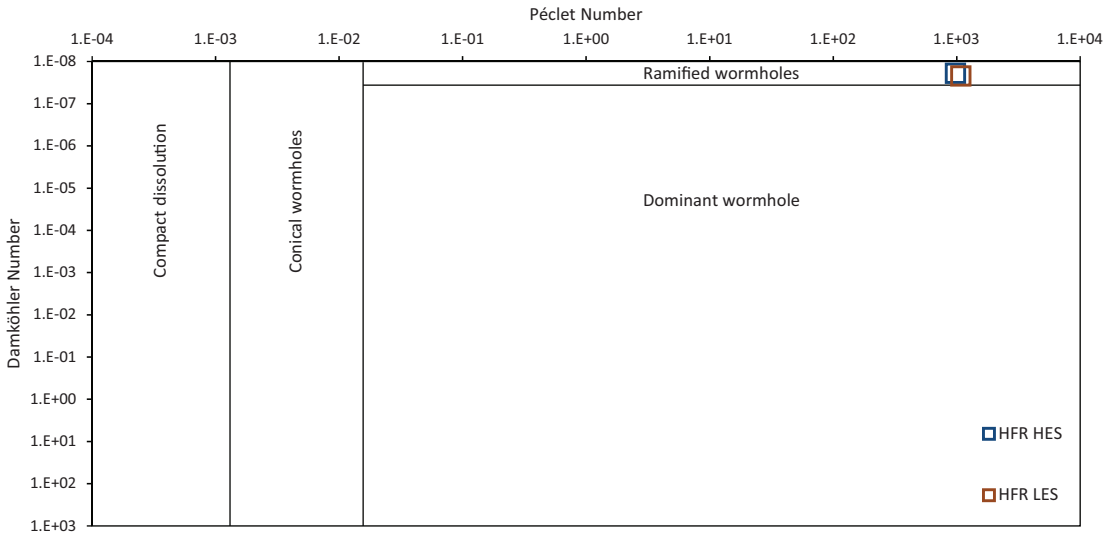

Figure 6.27: Suggested new boundaries for the dissolution map of Golfier et al. (2002). The new boundaries have been shifted after a qualitative assessment of the experiments presented in this chapter, and correspond to a seawater-calcite system.

6.5.4 Interpretation

The Pre-salt core samples have shown a mixed system behavior, where the evolution of k/k_0, although unreliable due to the detection limit of our differential pressure transducer, showed similarities with the travertine HFR experiments, implying that a LES scenario helped in increasing the permeability during the $HFR\ LES$ experimental flooding. Conversely, the chemical analysis give way to a different system type, whose behavior matches with the observations made during the Indiana limestone experiments. The larger dissolution of Ca and Mg at HES, coupled with a sample displaying a porosity composed of micropores mainly, likely lead the $HFR\ HES$ rock to experience some degree of pressure-solution. The nature of the rock, the experimental matrix, and the very large flooding time have driven $HFR\ HES$ to collapse. Interestingly, and despite displaying a porosity

composed of macropores, $HFR\ LES$ remained in one piece after a similar amount of pore volume injected. We believe that no clear conclusion can be drawn due to the variabilities between both rocks, nevertheless, a HES could be the cause of the early collapse of the $HFR\ HES$ sample.

6.6 Conclusion

Two Pre-salt core samples have been flooded with a synthetic seawater at constant Pre-salt reservoir conditions of pressure ($P_c = 50$ MPa) and temperature ($T = 60$ °C) for ∼90 and ∼100 hours. We have reproduced the experimental matrix of previous experimental investigations (cf. chapters 4 and 5), with rocks displaying different petromorphologic natures. We have recreated the HFR experimental conditions, previously described in chapter 5, as a way to expand the cross-comparison to travertine-like rocks (cf. chapter 8). Each sample has been flooded at a PV_{rate} of 2.5, and at different effective stresses ($\sigma' = 10$ and 40 MPa). Regular petrographical and numerical analyses of the samples have revealed similar porosities, permeabilities, volumes of pore, and volumes of solid. Our pre-experimental 3D analysis of the rocks has revealed a pre-existing flow-path in one sample, as well as large differences in pore shapes, numbers, and sizes between both samples. Although rocks presenting similar porosity values can display a large range of permeability results (Garing et al., 2014), which is to be related to the pore structure and its internal organization (Kalia and Balakotaiah, 2009), we confirm that the distinct rock matrix arrangement of both sample have driven the permeability evolution during seawater flooding. The differences between the samples can be attributed to important layer scale variations amongst the Pre-salt reservoir that can result in totally different laboratory interpretation (Alabi et al., 2014). Our findings are as follows:

- Permeability: the main difference between both samples was the absence of clear breakthrough for the $HFR\ LES$ experiment, while $HFR\ HES$

observed a breakthrough-like permeability evolution. This indicated the presence of a preferential flow-path in one sample at least. The permeability of $HFR\ HES$ took longer to increase to a stable level, indicating a tighter rock matrix. We cannot rule out that the stress state of the rock during the experiments could explain the large difference in the permeability evolution. The k/k_0 permeability analysis showed a similar permeability evolution to the one observed during travertine flooding, so that a low effective stress seemed to better stimulate the permeability during the early stages of flooding, while a high effective stress could prevent the fluid to flow more easily, even in the case of a pre-existing flow-path. Again, and as explained in the chapter 5, the high heterogeneity of the rock could have driven the permeability evolution throughout the entire experiment, and while clusters of connected pores were present in both rocks, such randomly distributed poro-permeability could have prevented, and/or partially, or entirely overridden the permeability prediction/evolution.

- Although the permeability evolution seemed more important for the $HFR\ HES$ scenario at the end of the experimental run, the amount of permeability generated per pore volume of seawater injected was greater for the $HFR\ LES$ run.

- The permeability generation appeared more effective for the $HFR\ LES$ scenario during half of the experimental run, despite a more moderate rate of generation. While the sample displayed a pre-existing or near-existing flow-path, the permeability response of the sample is better or equal during the first half of the experiment. While we were limited by the detection limit of our differential pressure transducer, the extrapolated curves clearly advantage the $HFR\ LES$ scenario, which again opens on the advantages of a lower effective stress for permeability gains.

- Chemistry: the larger concentration and volume of Ca and Mg dissolved

during the $HFR\ HES$ run is explained by the creation of one or more dissolution channels within a more compact rock matrix, which could have involved a larger portion of the microporosity, coupled to a higher reactive surface area. One interpretation of such a difference in concentration between the two samples could be linked to the distribution of the fluid flow in $HFR\ LES$. Indeed, the larger vugs present in this sample could have reduced the velocity of the interstitial fluid flow, while the fluid flow could have remained higher into a rock displaying smaller pores (figures 6.6 and 6.25b). The $HFR\ LES$ scenario has shown a different dynamic, and has observed wall dissolution mainly (figure 6.25a). This is corroborated by the lower pH values of the effluent fluids of the $HFR\ LES$ run (figure 6.16), indicating a more moderate dissolution. This correlates with the findings of Menke et al. (2015) whose detailed analysis of the flow fields revealed that, as the fluid/solid reaction progresses, the flow becomes more focused in fast regions due to the driving nature of the local heterogeneity, which leads a large fraction of the pore space to experience lower flow velocities. As a second interpretation, we noted that the permeability curves observed a similar ordering as the one seen during travertine flooding, we could relate the chemical signals to the Indiana limestone one. Indeed, the Pre-salt rocks have witnessed intense burial and diagenesis, comparable to the one observed in Indiana limestone. A last option could relate to small initial chemical composition differences leading to large difference in output signals, which could be interpreted by the large differences in pH values of the effluent fluids (figure 6.16).

- µCT imaging: a breakage of one of the rock sample during water flooding did not allow us to further investigate the extent of the dissolution. While comparative work can be done in this section, we observed a largely stimulated rock matrix in one sample ($HFR\ LES$), and partial indication of a ramified system in the broken one ($HFR\ HES$).

Due to the breakage of the $HFR\ HES$ sample, we have not been able to fully reconstruct the post-experimental 3D volume, as well as the rendering of the dissolution channels. Therefore, we were unable to provide a comparative study of the µCT images, although parts of the sample showed signs of channelling. This would correlate with the fluid flow analysis realized in section 6.4.2 where we expected a dominant to ramified wormhole pattern. The limited amount of 3D data did not allow us to draw conclusions, but a branched channel would be the expected form of dissolution pattern in this sample.

While both samples have witnessed very specific permeability and porosity enhancement, we believe that the main driver is linked to the pre-existing porosity network (Kalia and Balakotaiah, 2009). Nevertheless, while complex to unpick, the effective stress apparently had a conservative role for the $HFR\ LES$ scenario. Indeed, by keeping a high P_p we could have prevented the sample from collapsing. The intense channelling and dissolution witnessed by the $HFR\ HES$ sample has created a new porosity, which coupled with the low P_p could explain the collapsed sample, whose bulk structure has not been preserved.

These results provide an interesting preliminary investigation of the effect of stress state on rocks displaying large pores, while these two experimental flooding did not permit to draw firm conclusions due to the limitation of available data. More work is obviously needed in order to refine the results, by filling the experimental matrix (through different injection rates) or by re-investigating the effect of stress state using larger/smaller effective stresses.

Chapter 7

Prediction of location and magnitude of wormhole formation prediction in heterogeneous travertine rocks using μCT imaging and machine learning

7.1 External Contributions

This work has been developed after Dr. Andrew Fraser-Harris, Dr. Christopher McDermott and I noticed that we needed a pre-processor to OGS which would allow the user to select a 2D slice of digital rock where dissolution was likely to occur. This coupling between OGS and this work has been thought as a step forward for investigating the proposal that dissolution can be linked to HMC processes. Dr. Satyan Singh and Dr. Giorgos Papageorgiou were the first to suggest the use of machine learning. Throughout this project, they gave valuable

advice which led to the actual results presented in this chapter. Phil Cilli (ICCR - University of Edinburgh) is the second author of a paper based on this work (in review - cf. annex K), and has provided codes and plotting algorithms based on the Deep Learning toolbox of Matlab, and helped by writing the section 7.5.3 of this chapter.

7.2 Summary of the chapter

7.2.1 Rationale

Chapter 7 is the final result chapter of this project. A paper version is attached in appendix K, while parts of this work have been presented at the AGU 2018 (Cilli et al., 2018). This part of the PhD project used the coupled solution offered by the ICCR-Macropore and the dataset produced in chapter 5. We aimed to predict the fluid flow-induced matrix alteration within heterogeneous rocks. It is assumed that the velocity of flow at the inlet of a core sample is the main factor for rock erosion (Wang et al., 1993; Frick et al., 1994b; Bazin et al., 1995), but no work has ever used the geometrical features of the porosity of a rock as key variables for fluid flow-induced damage prediction. The prime aspect of this work resided in using an Artificial Neural Network (ANN) with simple computable attributes as input data for porosity change detection.

7.2.2 Abstract

Understanding the mechanisms behind the development of preferential flow-paths in carbonate rocks is important as they are related to several subsurface societal issues, e.g. hydrocarbon production, carbon sequestration, groundwater resource competition, geo-energy including geothermal energy and energy storage applications. The dissolution processes during water/acid flooding cause channelization which leads to the formation of flow-paths called channels. Over the past 50 years,

several studies, performed in a variety of fluid-mineral systems, have managed to describe the effect of rock-water flooding by focusing on the general shape of the channels through an estimation of chemical and physical parameters, but few studies have been able to predict their locations. Here we propose a new method to approximate the spatial distribution and magnitude of channels by linking experimental and numerical work through image pre-processing and machine learning. The experimental work aims to investigate the mechanical and chemical controls on the optimum equilibrium for channel formation within carbonate travertine rocks using purified seawater as the injection fluid during core flood experiments under typical reservoir conditions. Each sample was µCT scanned before and after the experiment. The numerical simulation included a pre-processing of the pre-experimental µCT scans followed by a training of the neural network on channel data, formed as a result of the dissolution and erosion of carbonates during the experimental flooding. The main interest of this study is to provide a predictive tool which can operate independently of the need to determine specific chemical and physical parameters, while demonstrating the strengths of machine learning applied within the sphere of Geosciences. Early simulations show that, for heterogeneous rocks, we can accurately detect the location, the degree, and the spread of the dissolution pathway. Our findings confirm that the neural network has been able to highlight the key variables related to geometrical properties through image analysis. These processes are seconded by flow rate and effective stress. The neural network approach has enabled us to rank the most important features and facilitate the determination of the most likely location for the formation of a preferential flow-path, and its magnitude.

7.3 Introduction

Artificial Neural Networks (ANNs) can be described as a brain-like processing tool which mimic 'qualitative reasoning' (Lapedes and Farber, 1987; Haykin,

1994). They are increasingly used in a variety of problem solving situations (Medecine, Bio-Informatics, Geosciences, etc.). The appealing characteristics of ANNs come from the non-linear aspect of the solving algorithms coupled with its learning capacities (Basheer and Hajmeer, 2000). Few studies have coupled µCT imaging and machine learning as a segmentation tool of 3D volumes (Cortina-Januchs et al., 2011; Chauhan et al., 2016) or for rock modulus estimations (Sonmez et al., 2006). In this study, we investigated the likelihood of channel propagation through carbonate samples of heterogeneous nature by comparing the ANN computed solutions to the experimental results.

Much work has been done on channel and karstification development and classification on variety of fluid-mineral systems, and acidity of percolating water is identified as a key control for carbonate dissolution resulting in the development of preferential flow-paths. Scientists try to recreate these effects by injecting fluids into core samples - often referred to as core flooding. The dissolution processes during rock water/acid flooding lead to the formation of preferential flow-path(s) referred to as channels or wormholes (Golfier et al., 2002). Several authors have characterized wormhole propagation through carbonate samples as a function of the experimental injection rate and the fluid properties (Hoefner and Fogler, 1988; Steefel and Lasaga, 1990; Frick et al., 1994b,a; Bazin et al., 1995; Fredd et al., 1996; Fredd and Fogler, 1998; Golfier et al., 2002; McDuff et al., 2010; Walle et al., 2015). For most experimental setups, the expected/generated channel(s) can be split into five main families: Compact dissolution, conical dissolution, dominant channel, ramified wormholes, and uniform dissolution. Numerical modelling studies have attempted to recreate these wormholes by including variables impacting the general shape and spread of the dissolution footprint, such as capillary pressure, permeability, velocity of the fluid, and kinetic transfer from the walls. Different numerical approaches have been assessed, from a very simplistic approach that considered a pre-existing

cylindrical wormhole (Hung et al., 1989; Wang et al., 1993; Buijse et al., 1997; Huang et al., 1997, 1999), to more complex models which focused on the grain scale (Hoefner and Fogler, 1988; Daccord et al., 1989), on the fluid mechanics (Daccord et al., 1993a,b; Frick et al., 1994b), or on the continuum equations of mass and flow transfer (Liu et al., 1997; Chen et al., 1997). Most of these approaches displayed good qualitative results of channel geometry, and are partially backed by experimental outputs, but none of them works as a predictive tool of channel spatial distribution, spread and magnitude.

Our experimental work aimed to investigate the mechanical and chemical controls on the optimum equilibrium for channel formation within carbonate travertine rocks using purified seawater as the injection fluid during core flood experiments under typical reservoir conditions. We opted for the numerical study of the travertine rocks due to the availability of 3D imaging dataset from our previous work displaying a good resolution of their macroporosity (cf. chapter 5), coupled with the non-confidential nature of the rocks. Each core sample was µCT scanned prior and after the experimental flooding. The numerical work included a pre-processing of the pre-experimental µCT data, followed by a training of the ANN against the post-experimental channels data. By doing so, we aimed to understand and predict the occurrence, shape, and magnitude of wormhole formation in heterogeneous carbonate rocks using attributes extracted from µCT images prior to flooding.

7.4 Materials and methods

The dataset used in this section were the result sets of the four travertine core samples flooded in chapter 5. A set of four experiments have been conducted on highly heterogeneous travertine rocks using 3.8 cm diameter cores of variable

lengths which have been flooded with a 30.5 g/l NaCl artificially made seawater. Several reasons led us to limit our study to the travertine µCT images:

- Several datasets were needed in order for the neural network to couple training and prediction.
- We used a high energy / low resolution source which resulted in the acquisition of full 3.8 cm core sample image stacks, against a lower final resolution of the porosity. Indeed our resolution of $\sim$ 40 microns was too small to resolve the porosity of Indiana limestones, while sufficient for resolving the macroporosity of travertine samples.
- We believe that the heterogeneous nature of a rock is a primary driver for fluid dynamics. This might also be true for homogeneous rocks, in which case the investigation should be done over a smaller - high resolution - ROI.

7.4.1 Rock sample

In this study, we focused our work on the shrub layers of travertine rocks, presented in chapters 2 and 5 and described by various authors (Chafetz and Folk, 1984; Pentecost, 1990; Guo and Riding, 1992, 1994, 1998; Chafetz and Guidry, 1999; Kele et al., 2008; Jones and Renaut, 2010; Wright, 2012; Chafetz, 2013; Chitale et al., 2015; Rezende and Pope, 2015; Wright and Barnett, 2015; Claes et al., 2017; Erthal et al., 2017). The shrub layers from a 25 cm cube of travertine were recovered as 38 mm diameter core plugs by diamond drill coring parallel to layering in the rock.

7.4.2 Rock preparation

The experimental procedure for sample preparation and conditioning is described in chapter 5.

7.4.3 Experimental procedure

The experimental rig used has been built and conceived for fracture flow study (Edlmann et al., 2013; McCraw, 2016), and further modified for our needs (cf. chapter 3). The reduced framework of the pre- and post-experimental procedure is described in the steps below:

- Pre-experimental procedure:
    1. Preparation and conditioning of the rock sample.
    2. Pre-experimental µCT scan of the core sample.
- Experimental procedure: the core was placed into a Hassler cell and connected into the flow rig, followed by a flooding until the permeability evolution reaches stability (i.e. ∼0 Pa $\triangle P$).
- Post-experimental procedure:
    1. Sonic bath of the sample using distilled water.
    2. The core was dried at least one week in an oven at 65 °C.
    3. Post-experimental µCT scan of core sample.

7.4.4 Experimental matrix and dissolution regimes

We injected an artificially made seawater of known chemistry and pH through travertine core samples of 3.8 cm diameter (D) and variable length (L). The four experiments are described in chapter 5.

7.4.5 µCT imaging acquisition

This work focuses on the macroporosity of the travertine rocks, therefore, a voxel side length of the reconstructed stack of ∼40 µm is sufficient to resolve essential macro petrographic structures. Details on the tomographic data acquisition and equipment are given in chapters 3 and 5.

7.4.5.1 Channel processing

The influence of rock water flooding creates damages into the rock matrix which can be detected through image processing by arithmetically comparing the pre- and post-experimental µCT volumes. The registration of the unaltered and altered dataset of each rock, followed by the processing of the differences between both stacks have been done using Avizo® 9. Two types of data have been gathered after each experiment:

- 3D volumes of pre-experimental scan - referred to as input data. This dataset was used for training the ANN and/or predicting the channel(s) location and magnitude.
- 3D volumes of dissolution channels - referred to as signature data. This dataset was the true solution of channel(s) formation, and was used for training the ANN.

As a way to account for difference in samples sizes, we sub-sampled the 3D stacks into cuboids of variable side lengths (550 px to 650 px large) and constant axial length of 710 slices. Both input and signature volumes of a same core sample were sub-sampled at the same location. In order to save further computational time, the 3D sub-sampled volumes were re-sliced a hundred times using the 'Z re-slice' function in Fiji (Schindelin et al., 2012), in two orthogonal directions with respect to the axial axis and the original orientation of the sample within the quarried bloc. Figure 7.1 presents the workflow for µCT data acquisitions. In total, we have scanned four samples, or eight datasets, which were later split in ANN training (six datasets) and ANN prediction (two datasets).

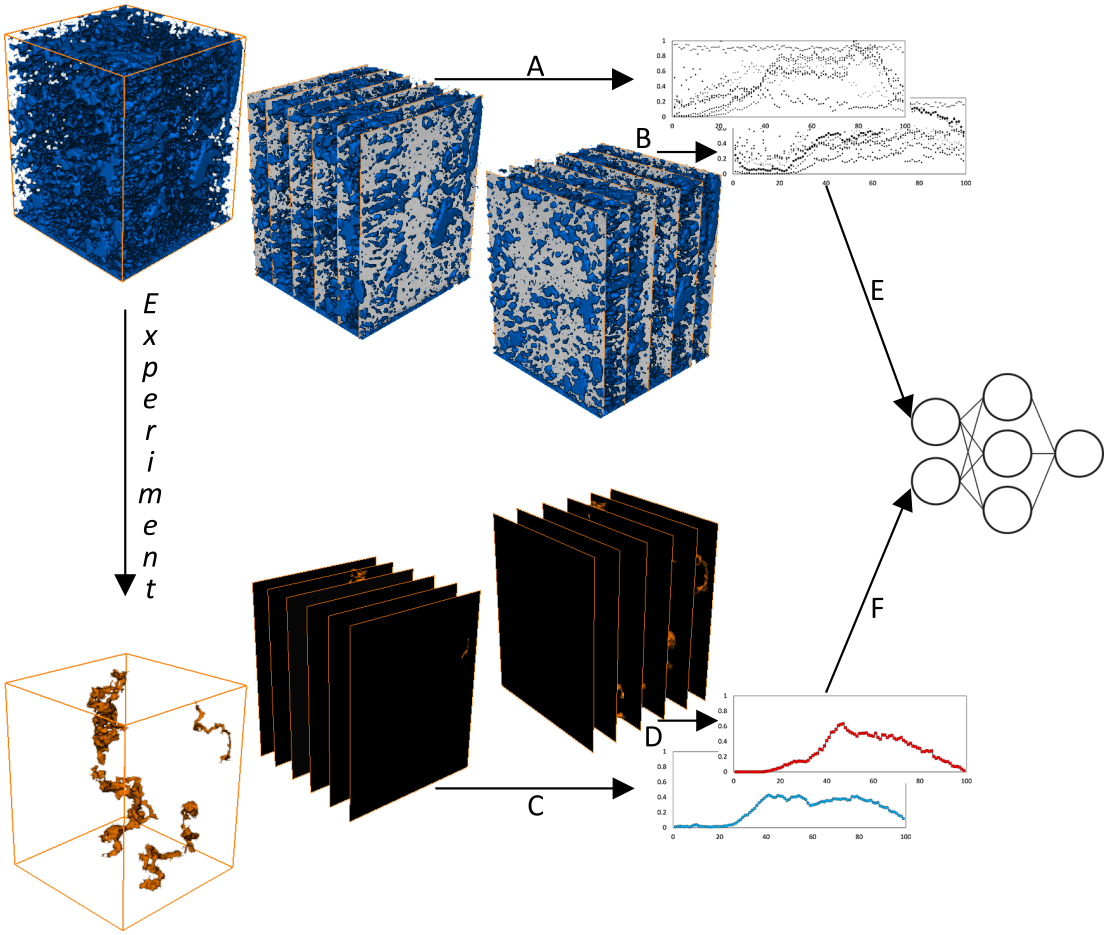

Figure 7.1: Data acquisition workflow. The two sub-sampled cuboids are of the same size. Both stacks have been re-sliced a hundred times in two orthogonal directions. A & B: input data acquisition; C & D: signature data acquisition; E & F: input and signature data are attributes for the ANN.

7.5 Modelling work

7.5.1 Input data pre-processing

The input data are geometric, physical, and simple statistical variables used as a structure for predicting material loss during experimental flooding. Extraction of the information involved a conversion from the 16 bits gray scale 2D slices of

pre-experimental scan to normalized 1D variables that can be evaluated by the ANN.

7.5.1.1 Formatting

A VBA batch coupled with Corel® X7 suite (cf. chapter 3 - section 3.3.3) was used as a quick way to apply the same formatting to each 2D slice. The batch automatically and sequentially thresholds, smooths, vectorizes, and resizes each image to its original size. Finally, it saved the new set of 2D binary slices under the SVG format.

7.5.1.2 Analysis

The analysis of the formatted 2D slices of input data was performed by a coupled solution between the ICCR-Macropore (section 3.3.2) and the Slice Picker (section 3.3.4). For each formatted 2D slice, a set of nineteen relevant variables was collected through an in-depth image analysis:

1. Total pore area
2. Area of connected pores
3. Total length connection
4. Median length connection
5. Mean length connection
6. Median pore area
7. Mean pore area
8. Ratio of pore area
9. Number of pores
10. Mean pore perimeter
11. Small ellipse perimeter
12. Large ellipse perimeter
13. Porosity
14. Number of pore larger than the mean size
15. Number of pore larger than the median size
16. Mean ellipse aspect ratio
17. Mean distance between pores
18. Pore Volume rate
19. I/O connection

Most variables can be easily explained through image interpretation and basic mathematics (1, 6, 7, 9, 10, 13, 14, 15, 17), as well as variable 18 (PV_{rate}) which was calculated from equation 3.7. The remaining variables (2, 3, 4, 5, 8, 11, 12, 16, 19) have been calculated through the use of functions developed for the ICCR-Macropore and using the ellipse shapes of each pore and the pore network (section 3.3.2.6 and figure 3.19).

Pore network analysis (variables 2, 3, 4, 5, 19)

Variables 2, 3, 4, 5, and 18 are determined as follows:

- Area of connected pores is the sum of the 2D area of the pores which are part of a connected network.
- Total/ median/ mean length connection are basic mathematical calculations using the absolute length of every link from a 2D slice.
- I/O connection is a variable which was not used by the ANN, and further helps in determining the potential breakthrough locations. A recursive function analyses the 2D network of links, and sets a Boolean to 'true' if at least one path between bottom to top of the image is found; the Boolean is otherwise set to 'false'.

Ellipse analysis (variables 8, 11, 12, 16)

The ellipse shape of a pore can resolve the following variables:

- Ratio of pore area represents the ratio between the area of the largest pore over the mean pore area of a 2D slice. This variable is used for excluding outliers.
- Small/ Large ellipse perimeter is a simple calculation of both the ellipse shape of a pore and its enlarged version.

- The mean aspect ratio is represented by the ratio of the minor axis b over the major axis a of an ellipse. All the ratios gathered per slice were averaged.

7.5.2 Signature data pre-processing

The signature data refers to the solution of wormhole magnitude and location. This signal was computed from the differential result between the pre- and post-experimental scans.

7.5.2.1 Formatting

The dissolution paths were isolated and sub-sampled using Avizo ® 9. The cuboids were re-sliced and thresholded using the 'Default' method of the thresholding tool of Fiji (Schindelin et al., 2012). The percentage of black and white area was calculated for each 2D slice using a batch based on the measure function under Fiji (Schindelin et al., 2012), and was used as the true solution of the wormhole shape and size for each direction sampled. The signature data were finally normalized so that the maximum percentage area of white equals 1 (presence of dissolution channel) while the minimum is equal or close to 0 (no dissolution detected).

7.5.3 Regression and neural network modelling

Neural networks are effective at fitting complex behaviours in data but their typical, inherent non-linearity makes the physical interpretation of their weights difficult or intractable in many cases. In this work we trained both a linear regression and multiple hidden layer neural network on eight datasets, corresponding to the four experimental regimes as explained in section 7.4.4. With this network trained, we then used it to predict the remaining two, blind datasets' spatial wormhole signatures, which correspond to the remaining experimental regime. For the four combinations of three training experimental regimes (6 datasets) and one blind test experimental regime (2 datasets), we performed a linear

regression where eighteen normalized features were input and fitted to minimize the misfit when compared to the measured spatial wormhole signature extracted from before and after μCT scans, as described in section 7.5. We did not perform any regression or model training using the I/O feature, which was held aside for comparison, as seen in section 7.5.1.2. The I/O features have not been used as an input data as these values have been pre-treated by a separate function and could have biased the results. Instead, they were used as an alternative tool for wormhole detection and validation. After linear regression was parametrised, we performed modelling by artificial neural network. We designed a neural network using Matlab's Deep Learning Toolbox, with three hidden layers, consisting of 11, 8, and 5 neurons in each layer between input and output (Hudson Beale et al., 2018). All eighteen features were normalized, as discussed in section 7.5.1, before input into the network. All transfer functions between the input and all hidden layers were hyperbolic tangent functions. The transfer function between the last hidden layer and the output layer was a linear function. Our experimental aim was to train our models on three experimental regimes (6 datasets), and predict wormhole formation on a fourth experimental regime (2 datasets). The blind test data we held aside in our neural network development was simply the two datasets out of 8 to be predicted. We used Matlab's implementation of the Levenberg-Marquardt algorithm (Moré, 1978) to train our networks.

We randomly partitioned the data and features from six training datasets into 74 % training data and 26 % validation data. We trained a neural network given this random partitioning of training and validation data, and forward-modelled the spatial wormhole signature on the remaining two blind datasets, given this trained network. This workflow has been repeated 3,000 times independently, each time training a new network given a different random partitioning of training and validation data from the same six datasets, and produced 3,000 predictions of the two blind datasets' spatial wormhole signatures. These 3,000 predictions

have been made into a density plot which shows the most likely spatial wormhole signature, as well as the sensitivity of the network to different parametrisation conditions. We performed this workflow for all four combinations of three training experimental regimes (six datasets) and one prediction experimental regime (two datasets), allowing us to simulate four, independent experiments.

7.6 Results

7.6.1 Permeability and calcium evolution

This work focuses on the main controls behind each experimental result with regard to the evolution of the pore system's size, connectivity, and spread. The details of the results and conclusion of the four experiments covered by this study are described in chapter 5. As observed in the dedicated chapter, a detailed temporal evolution of the rock matrix was assessed through chemical analysis and permeability logging. Our $\triangle C_{Ca}$ displayed positive values throughout each experiment ($\triangle C_{Ca} > 0$), implying that calcium removal occurred during flooding phases (Luquot et al., 2016). This idea is reinforced by the pH measurements whose outlet values were consistently higher than the inlet ones.

7.6.2 µCT outputs

7.6.2.1 Post-experimental results

Due to technical limitation, we were not able to acquire a temporal evolution of the core samples. Instead we obtained the absolute difference in 3D volume of missing material by comparing the pre- and post-µCT volumes. No porosity value has been calculated from µCT image analysis as we focused this numerical study on the detection and prediction of volume creation from flow through. The post-experimental networks, extracted through Avizo® 9 and using a label analysis parameter of 24 connections detection between voxels, was able to capture most of

the connected voxels. The shapes of the channels are in accordance with the Da-Pe analysis (figure 5.32): as we increased the injection rate, we also increased the ramification of the system, while at lower injection rates we remained relatively far from a conical channel or face dissolution system, probably due to the weak acidity of our injection brine. Figures 7.2, 7.3, 7.4, and 7.5 present the signal data (blue curve at the bottom of each figure - cf. step C and D in figure 7.1) plotted under their corresponding wormhole, for each of the eight datasets (two datasets per rock sample). The cross-plotting of the thresholded percentage area of black to white of a channel offered a good insight to the location, the spread, and the magnitude of the created pore space. The values of the signature data have been cross-normalized between dataset.

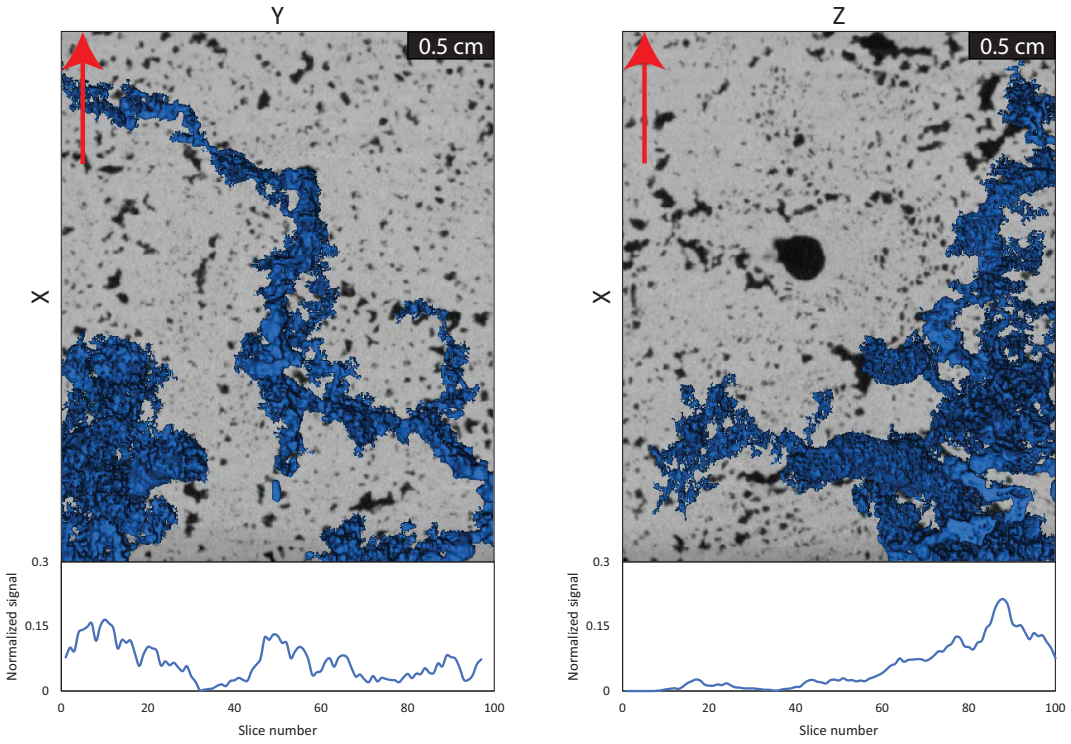

(a) LFR LES - YX direction.

(b) LFR LES - ZX direction.

Figure 7.2: Signal data and their respective post-experimental cross-sectional direction ($LFR\ LES$). The fluid was injected from bottom to top (red arrow).

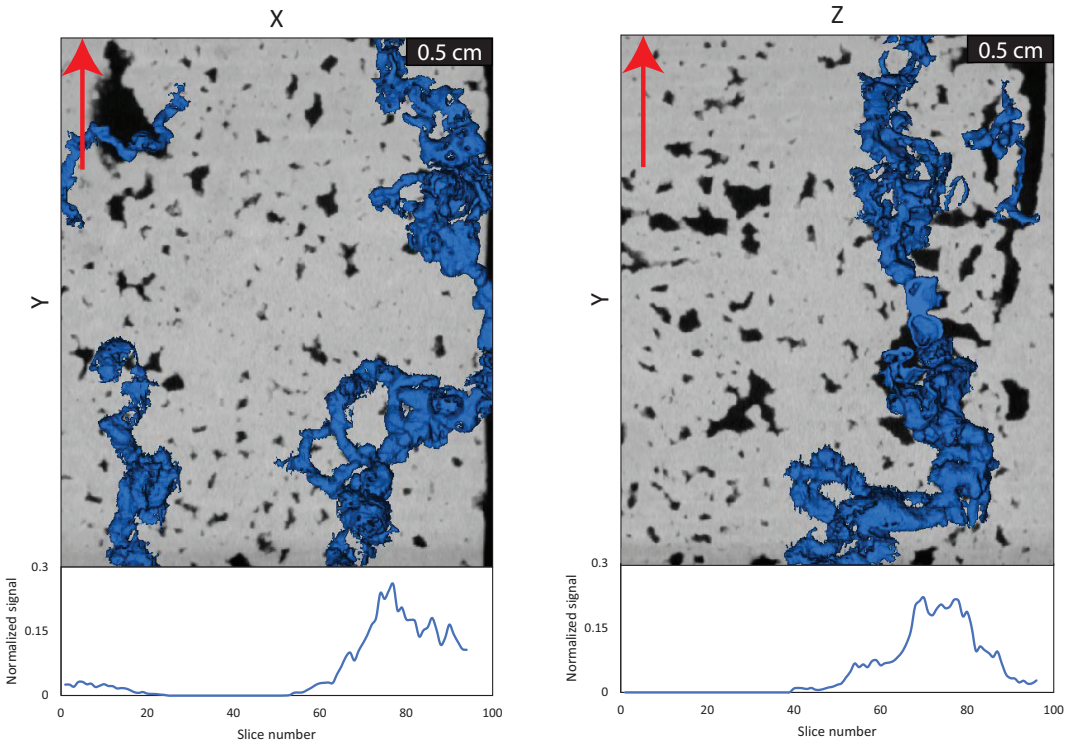

(a) MFR HES - XY direction.

(b) MFR HES - ZY direction.

Figure 7.3: Signal data and their respective post-experimental cross-sectional direction ($MFR\ HES$) The fluid was injected from bottom to top (red arrow).

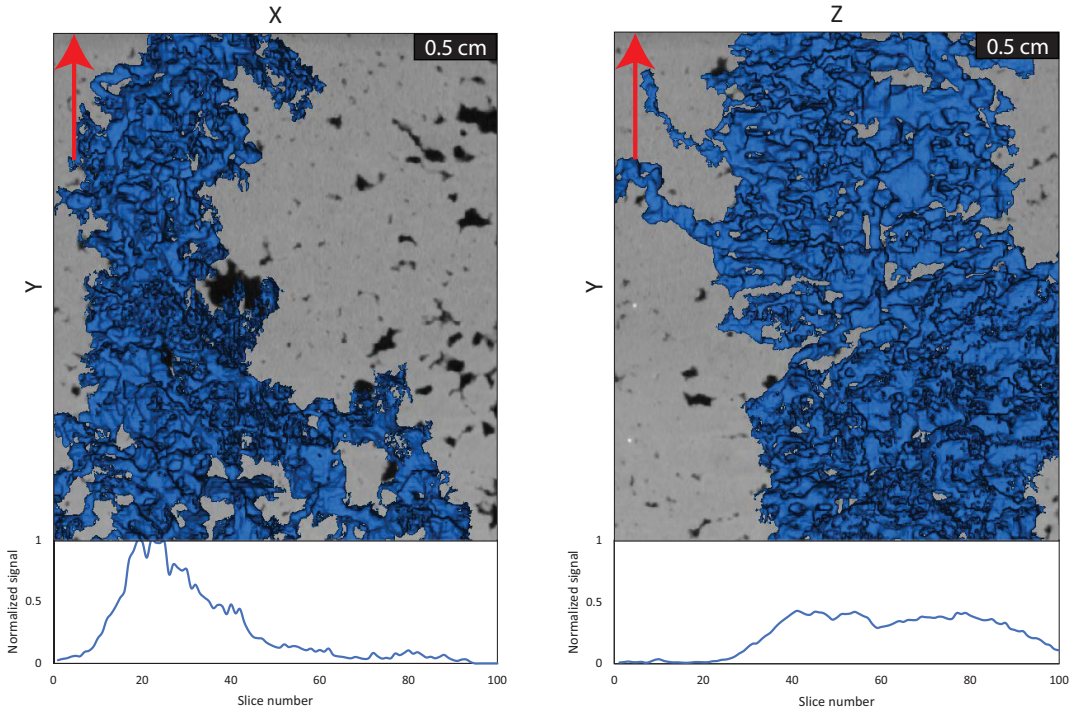

(a) HFR LES - XY direction.

(b) HFR LES - ZY direction.

Figure 7.4: Signal data and their respective post-experimental cross-sectional direction ($HFR\ LES$) The fluid was injected from bottom to top (red arrow).

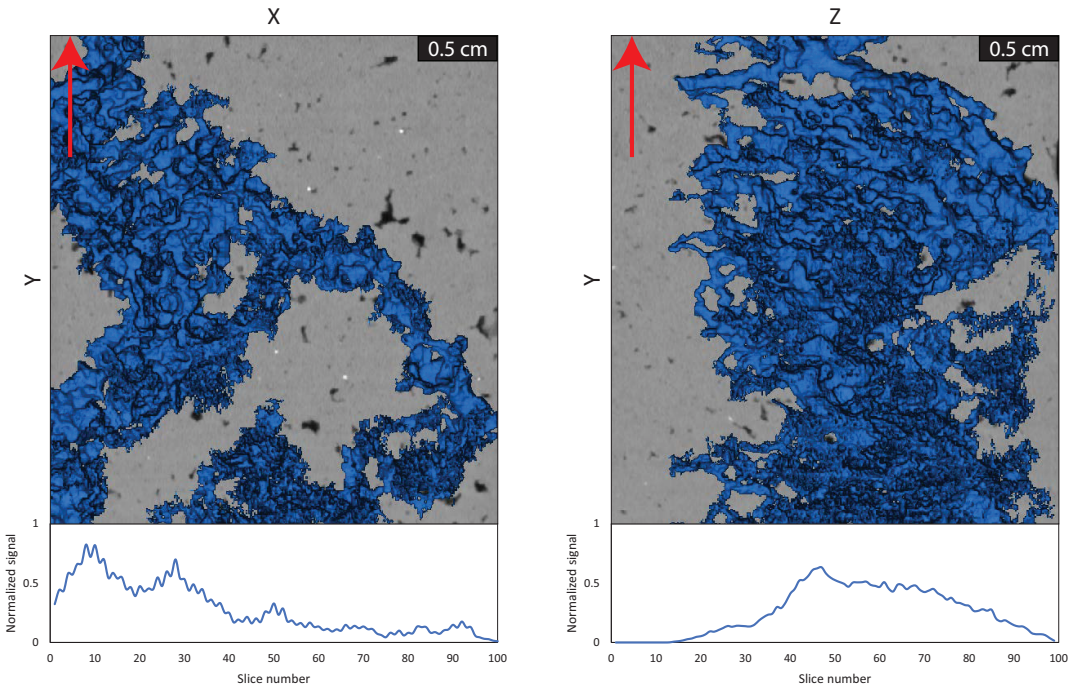

(a) HFR HES - XY direction.

(b) HFR HES - ZY direction.

Figure 7.5: Signal data and their respective post-experimental cross-sectional direction ($HFR\ HES$) The fluid was injected from bottom to top (red arrow).

7.6.3 ANN outputs

The predicted spatial wormhole signatures from the fitted linear regression models, as seen in figures 7.8, 7.9, 7.10, and 7.11, are displayed as white curves, with the signatures measured from µCT scans displayed as red curves. It is clear that the linear regression model is generally ineffective at predicting spatial wormhole signatures. In figure 7.6, we show the linear regression weights for all features, as numbered in section 7.5, over all four training scenarios. The last feature shown (feature 19), is the size of the constant term or bias in the linear regression. As all features were normalized before performing linear regression, we propose that features with small magnitude weights are related to physical attributes which have little effect on rock's wormhole formation. By

this reasoning, we interpret that features 2, 4, 6, 8, 16, and 18 all correspond to physical properties which had little influence on a rock's wormhole formation. These features are the area of connected pores, median length of connections, the median pore area, ratio of pore area, the mean ellipse aspect ratio, and the mean distance between pores repetitively. By the same reasoning as above, we interpreted features with larger weights as proxies for the rocks' physical attributes which exerted a stronger influence on wormhole formation, to first order. These features include numbers 9 to 12, which correspond to number of pores, mean pore perimeter, small ellipse perimeter, and large ellipse perimeter respectively (summarized in table 7.1). Of course, this reasoning of inferring feature influence on enhanced permeability of pre-existing pathway from linear regression weights is flawed as normalized features with large outliers may require large scaling to minimize their fitting residuals. Also, as we see in many cases, linear regression is in fact not a good predictor of wormhole formation on blind test data. Nevertheless, this analysis gives a crude, qualitative first estimate of which features may or may not be important in wormhole formation prediction processes within heterogeneous rocks featuring macropores.

The background density plots in figures 7.8, 7.9, 7.10, and 7.11 show the distribution of blind predictions generated by the 3,000 neural network simulations, given each combination of three training experimental regimes (six datasets) and one blind test experimental regime (two datasets). Intensity ranges from blue (very low confidence) to yellow (very high confidence), and the 'true' solutions (signal data) have been plotted in red on top of each result. We see a generally effective prediction of wormhole location and magnitude by our neural network modelling approach for all four training and prediction experiments. There is a notable improvement on prediction accuracy over the linear regression modelling. The spread in the density plot at locations of high spatial wormhole signature

indicates the sensitivity of neural network training to the particular, random segmentation of validation and training data. In fact, we designed our statistical approach of training and predicting networks multiple times to allow both the prediction of data and to obtain an understanding of modelling sensitivity in locations of interest. The red diamonds on figures 7.8 to 7.11 indicate where the I/O feature is 'true', which marks whether there was an existing pore space connection from bottom to top of the pre-flooded 2D slice. This single feature is an effective predictor for breakthrough location. This implies wormholes were likely to occur where there was a pre-existing input-output connection in the rock before flooding. We note this feature only predicts the location, rather than the magnitude. For this reason, the use of our neural network method was justified.

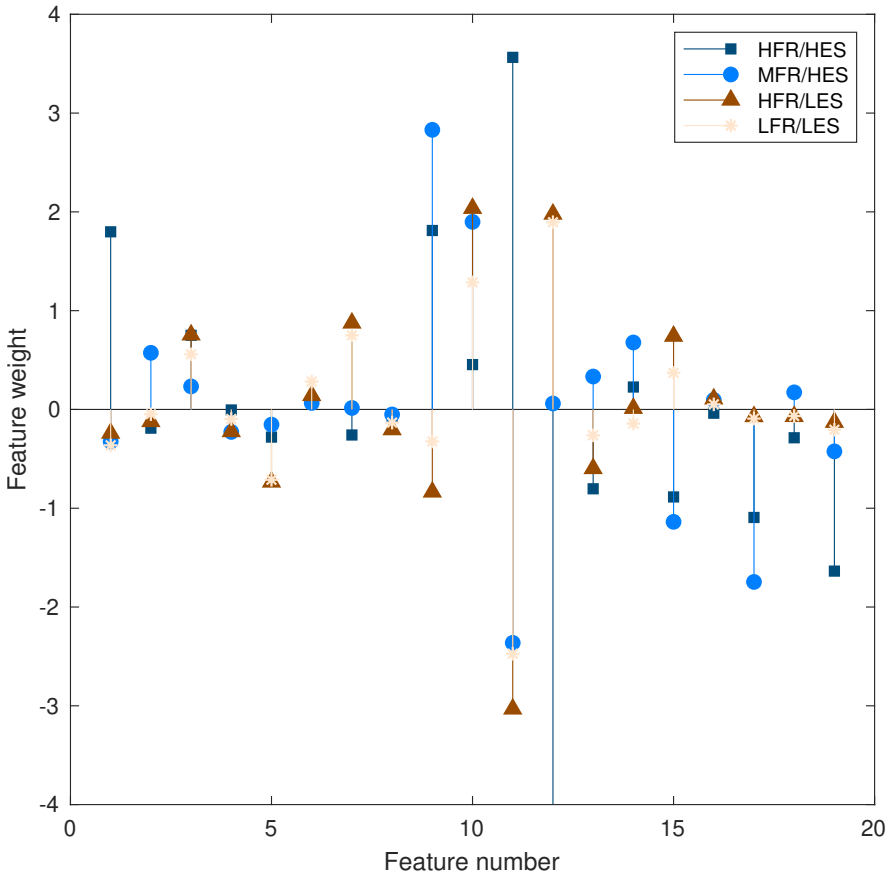

Figure 7.6: Linear regression weights for all features. The outlying weight on feature 12 is -6.22.

Figure 7.7 is a sketch that helps in understanding the spatial reasoning behind this study.

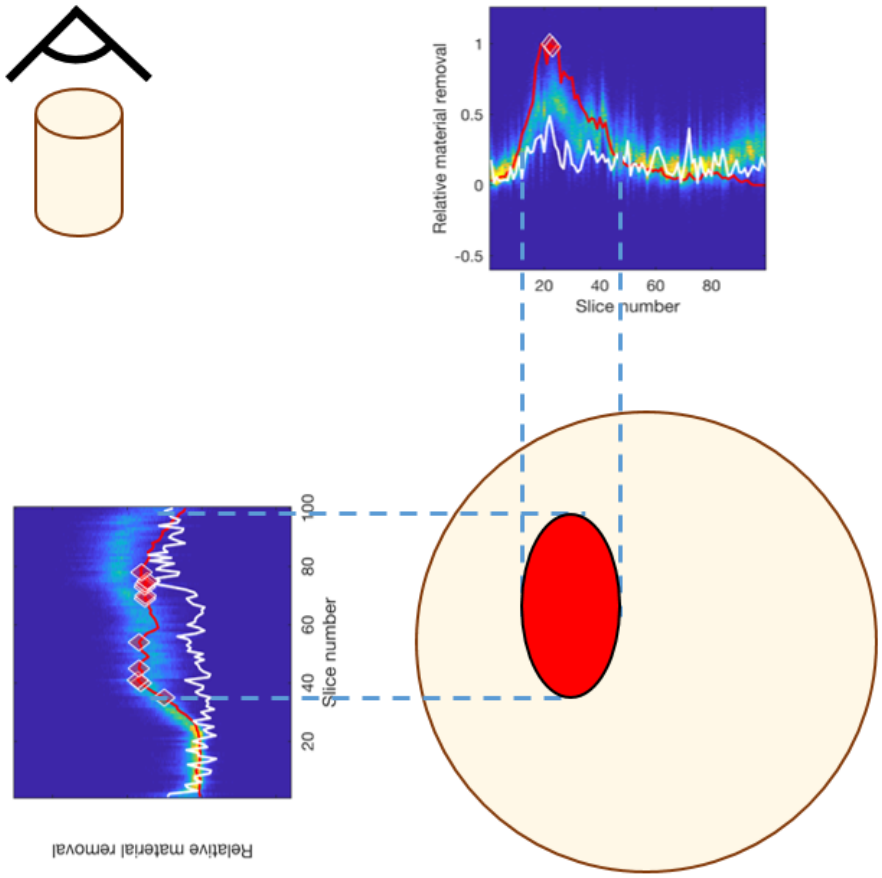

Figure 7.7: Visual representation of the capacity of the ANN solution to predict the location of the forthcoming dissolution in a rock sample. Color scale: yellow = high confidence; pale blue = low confidence.

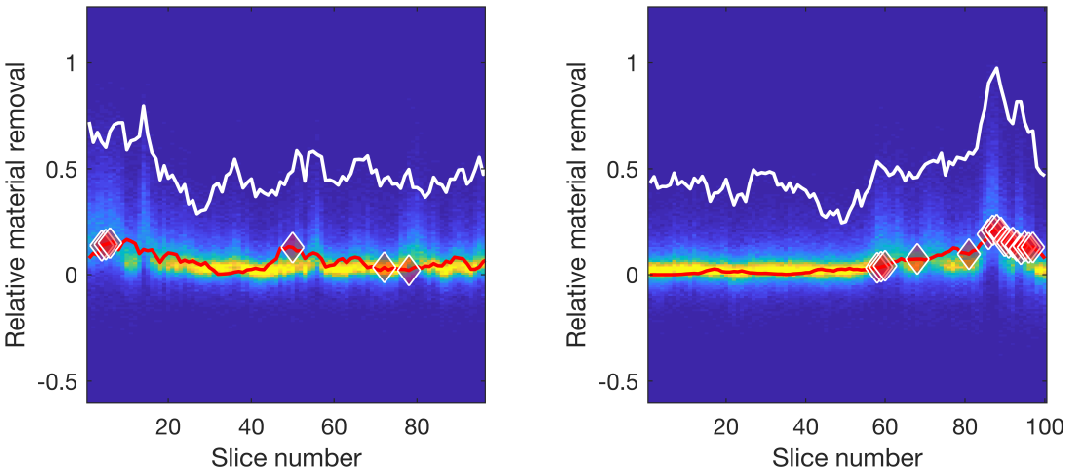

(a) LFR LES - YX direction.

(b) LFR LES - ZX direction.

Figure 7.8: Measured data (red) overlain on density plot of 3,000 trained neural networks' blind test predictions for the $LFR\ LES$ experiment. The white curve represents a linear regression applied to the same dataset, and which comparatively shows the better fit of the neural network solution. Color scale: yellow = high confidence; pale blue = low confidence.

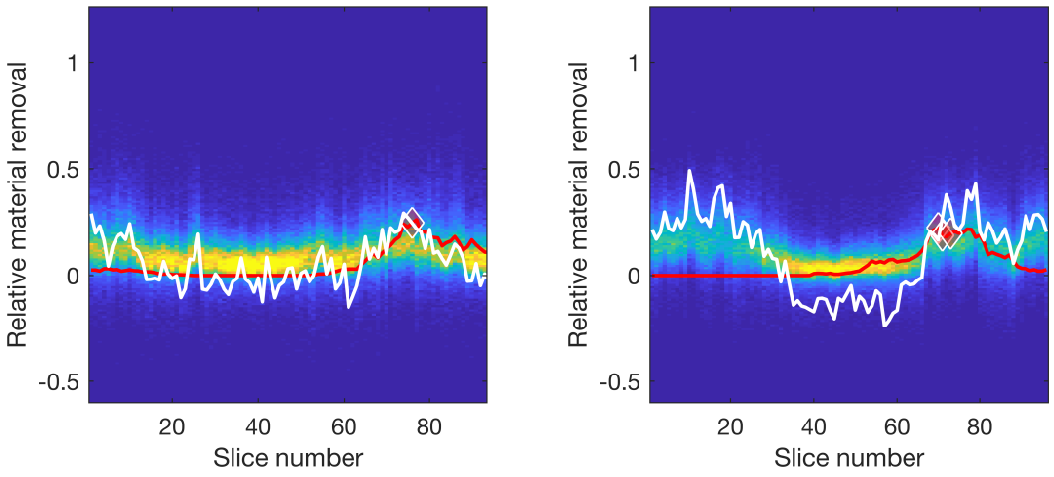

(a) MFR HES - XY direction.

(b) MFR HES - ZY direction.

Figure 7.9: Measured data (red) overlain on density plot of 3,000 trained neural networks' blind test predictions for the $MFR\ HES$ experiment. The white curve represents a linear regression applied to the same dataset. Here the linear regression still fails to find the right magnitude of material removal but appears to relatively accurately shows the zone of material removal. Color scale: yellow = high confidence; pale blue = low confidence.

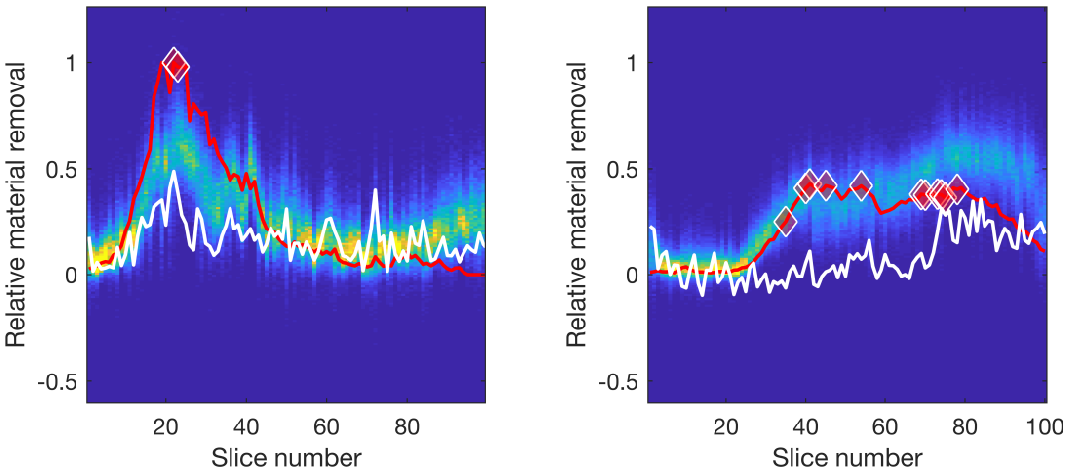

(a) HFR LES - XY direction.

(b) HFR LES - ZY direction.

Figure 7.10: Measured data (red) overlain on density plot of 3,000 trained neural networks' blind test predictions for the $HFR\ LES$ experiment. The white curve represents a linear regression applied to the same dataset, and which comparatively shows the better fit of the neural network solution. Color scale: yellow = high confidence; pale blue = low confidence.

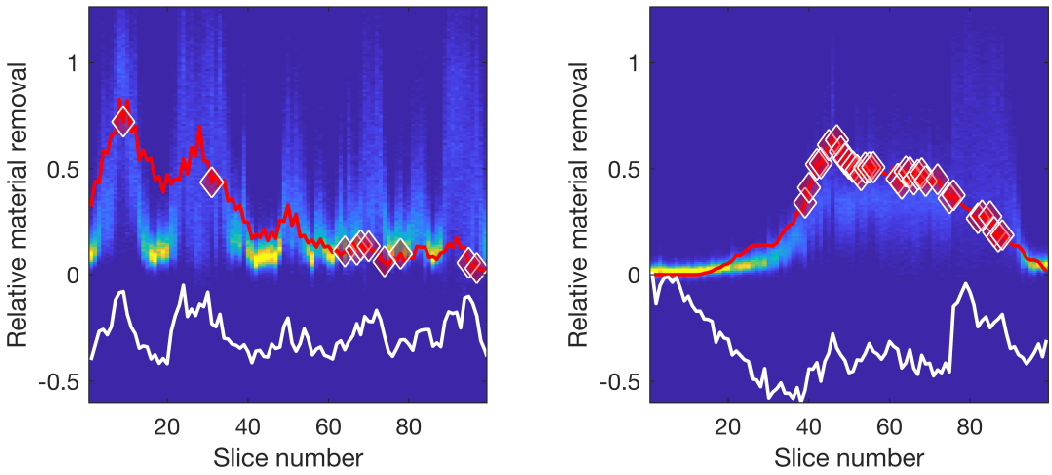

(a) HFR HES - XY direction.

(b) HFR HES - ZY direction.

Figure 7.11: Measured data (red) overlain on density plot of 3,000 trained neural networks' blind test predictions for the $HFR\ HES$ experiment. The white curve represents a linear regression applied to the same dataset, and which comparatively shows the better fit of the neural network solution. Color scale: yellow = high confidence; pale blue = low confidence.

Number	Key parameters	Influence
1	Total pore area	Medium
2	Area of connected pores	Low
3	Total length connection	Medium
4	Median length connection	Low
5	Mean length connection	Medium
6	Median pore area	Low
7	Mean pore area	Medium
8	Ratio pore area	Low
9	Number of pores	High
10	Mean pore perimeter	High
11	Small ellipse perimeter	High
12	Large ellipse perimeter	High
13	Porosity	Medium
14	Number of pore > than mean size	Medium
15	Number of pore > than median size	Medium
16	Mean ellipse aspect ratio	Low
17	Mean distance between pores	Medium
18	Pore volume rate	Low
19	I/O connection	/

Table 7.1: Summary of the key parameters used in this study and their apparent relative influence on preferential flow-path formation.

The parameters ranked as 'High' are believed to be important as they reflect how physical (e.g. fluid dynamic) and chemical variables (such as reactive transport, acidity of the fluid, chemical interaction, etc.) can be influenced by the surface of the pores, so that the larger a pore perimeter is, the more important the wall surface in contact with the flooding fluid should be. These effects were positively impacted by the amount of pore present. This also validates the ellipse shape of pore as a correct simplification of the general shape of a pore (Tsukrov and Kachanov, 1993; Fournier et al., 2011). We note that the variables linked to the area of the pores were not ranked higher than 'Medium' (and most often 'Low'). We explain this by the relatively small importance of the area of the pores. While large pores should drive more fluid, the combination of a large perimeter (likely associated with a large area), guarantee more wall/fluid interaction, and could be associated with a higher degree of alteration. We also believe that the ANN has made a clear distinction between porosity and number of pores, for reasons similar to what has been explained above: a large effective porosity could be associated with large pore areas, while the number of pores remained mathematically disconnected to the area of the pores.

Overall, the neural network method detects the location and extent of material removal under different flow rates, which we summarize as follows:

- *LFR LES*:
  - Figure 7.8a: The main features were detected. The ANN has generated few peaks which were not featured by the solution, but it successfully showed them with a lower confidence.
  - Figure 7.8b: The main area of interest (right) appeared as one peak in this direction, and was clearly detected by the ANN. While the magnitude seemed slightly uncertain, the location was precisely determined.

- *MFR HES*
  - Figure 7.9a: The small amount of missing material shown by the red curve (left side, low magnitude) was resolved with a perceptible offset in the output magnitude. With high confidence, the main channel was detected on the right side. Its magnitude, even if close to the magnitude of the signal data, remained marginally lower.
  - Figure 7.9b: The two main pore networks are easily identifiable (left and right sides). The dissolution channel (red curve, right side) was detected. The ANN showed quality in decision making, as it also offered the left side as a potential site for channel formation, but seems to display a lower - nonetheless still rather high - confidence.
- *HFR LES*
  - Figure 7.10a: Overall, the main shape of the signal data was well resolved. The inaccuracy likely came from the magnitude of the main channel which is not perfectly detected.
  - Figure 7.10b: This cross sectional analysis displays the same issues as the cross-section 7.11b: the spread and magnitude of the signal data are accurately resolved. Although the ANN does not properly determine the exact magnitude of the signal, it mainly expected a large amount of alteration.
- *HFR HES*
  - Figure 7.11a: Input data for this cross-section are scattered. Here the ANN remained careful across the sample. Nevertheless, and despite solving with highly distributed data, the ANN managed to find the two main peaks successfully (left side), as well as the general trend of the signal data, which presents a decrease from left to right.

– Figure 7.11b: The spread of the main flow-path was clearly found (X-axis) while the confidence of the ANN decreased as the intensity of missing rock increased. This is attributed to the fact that, even if the ANN caught the location and spread of the channel, the exact magnitude might be a challenge to resolve as the exact magnitude of a larger and more ramified channel might be linked to variables not yet accounted for by our ANN solution.

7.7 Conclusion

This study offers a new way of coupling Artificial Neural Network and µCT scanning techniques. A limited number of studies have already successfully linked these two tools as a segmentation method (Cortina-Januchs et al., 2011; Chauhan et al., 2016), and for rock modulus estimation (Sonmez et al., 2006), but none used the non linear solving aspect for dissolution prediction. Through this study, we have experimentally flooded four rock core samples and our results showed that we have positively enhanced the pore connectivity, the porosity, and the permeability recovery through brine injection (figures 5.10 and 5.17). While it is commonly stated that the velocity of flow at the inlet of a core sample is the main factor for rock erosion (Wang et al., 1993; Frick et al., 1994b; Bazin et al., 1995), and our results do confirm this, this is only part of the story. We believe that the findings of our work show that spatial distribution of the permeability and porosity evolution can be predicted from the pore network information held by the rock sample; where the micro or macro heterogeneities of the porous medium drives the flow instabilities to direct flow and, as such, chemical removal, erosion towards zones of highest permeability (Hoefner and Fogler, 1988; Fredd and Fogler, 1998; Siddiqui et al., 2006; Kalia and Balakotaiah, 2009; Izgec et al., 2010) eventually leading to material loss. Our early results showed that specific variables (figure 7.6) stood out of the ANN analysis, validating that geometric factors linked to

the porosity and pore shape of a rock contain, most of the time, the necessary data for predicting material loss during rock-water flooding (figures 7.8, 7.9, 7.10, and 7.11 - red lines). Moreover, and by using an iterative function based on the connectivity network between pores, we managed to accurately predict the potential zones where breakthrough could happen. If a linear combination of these µCT extracted attributes can successfully predict a rock's spatial wormhole signature, the weights from the linear regression could be considered indicators of the influence of µCT extracted feature in wormhole formation. Moreover, if a misfitted linear regression is unsuccessful in predicting wormhole signatures on a blind dataset, a more complex modelling tool, such as neural networks, is required in order predict wormhole formation behaviour (figures 7.8, 7.9, 7.10, and 7.11 - white lines). While this statement is valid in heterogeneous travertine rocks, we remain careful with other types of carbonate, or even other types of lithology which have not been tested in this study.

Chapter 8

Synthesis and discussion

8.1 Introduction

This chapter aims in offering a comprehensive comparison of the results and an evaluation of the similarities and differences between the rocks. The experimental and numerical work conducted in this study has been focusing on the effect of injection rate coupled to the effect of the stress state during seawater flooding. The comparative nature of this work has allowed us to draw conclusions for each type of rock and rock texture having been analysed:

1. Homogeneous Indiana limestone (underwent diagenesis).
2. Heterogeneous travertine rock (surface or near surface deposition).
3. Heterogeneous Pre-salt rock (underwent diagenesis).

8.2 Comparative work

Each milestone of this PhD project has been done with the idea of forming a standalone scientific report, along with chapter 6 which cannot be published due to the confidential nature of the work as well as the limited amount of data gathered. While methodologies and datasets are similar, this work also allows for comparisons of results across chapters, where the influence of the prime variables addressed throughout this project are contrasted in the following sections.

8.2.1 Influence of the Injection rate

It is known that the velocity of the fluid has an impact on the erosion of the rock (Wang et al., 1993; Frick et al., 1994b; Bazin et al., 1995). The process was well described by the dissolution map of Golfier et al. (2002), which displayed a ramified to uniform dissolution systems as the Da number was lowered (flow dominated system in the case of this work).

The injection rate has largely dominated the altering processes in place during each experimental run of this project. Using a pore volume rate (PV_{rate}) was relevant in terms of Darcy velocity and residence time, but two similar PV_{rate} could result in different injection rates Q. The influence of Q is particularly clear when observing the permeability (k). Figure 8.1 shows the permeability evolution of all the samples presented in this study. It appears that breakthrough initiation and permeability evolution were primarily driven by the injection rate at the inlet of the sample (table 3.2), however, each rock type has a characteristic behaviour:

- Indiana limestone: the permeability curves gathered in groups formed by two experimental scenarios of similar PV_{rate} (figure 8.1a). For any given effective stress scenario, the earliest breakthroughs happened at the highest PV_{rate} (of value 3), followed by PV_{rate} of 1.5, and finally, the samples to breakthrough last displayed a PV_{rate} of 0.7.

- Travertine: while no breakthrough was noticed (due to the presence of pre-existing flow-paths in each sample), the permeability curves got distributed according to the relevant dominant flow-rate (figure 8.1b). Indeed, due to the heterogeneous nature of the rocks, the PV_{rate} values had less impact than the actual flow rate Q.

- Pre-salt: the experiments seemed to follow a characteristic path which features permeability elements found amongst travertines (an overall larger permeability increase at slower injection rate ($HFR\ LES$) followed by a late takeover by the larger injection rate ($HFR\ HES$)), while the kinetic response of the rocks showed signs observed during the Indiana limestone experiments. The chemical data can be explained by an initial larger pre-existing flow-path within the $HFR\ LES$ sample. In this sample, most of the permeability was generated within the first hour of flooding, while the remaining permeability increase can be linked to chemical kinetic processes. Despite interesting results, we only ran two experiments due to technical limitations, and more results are needed in order to confirm, nuance, or invalidate the above.

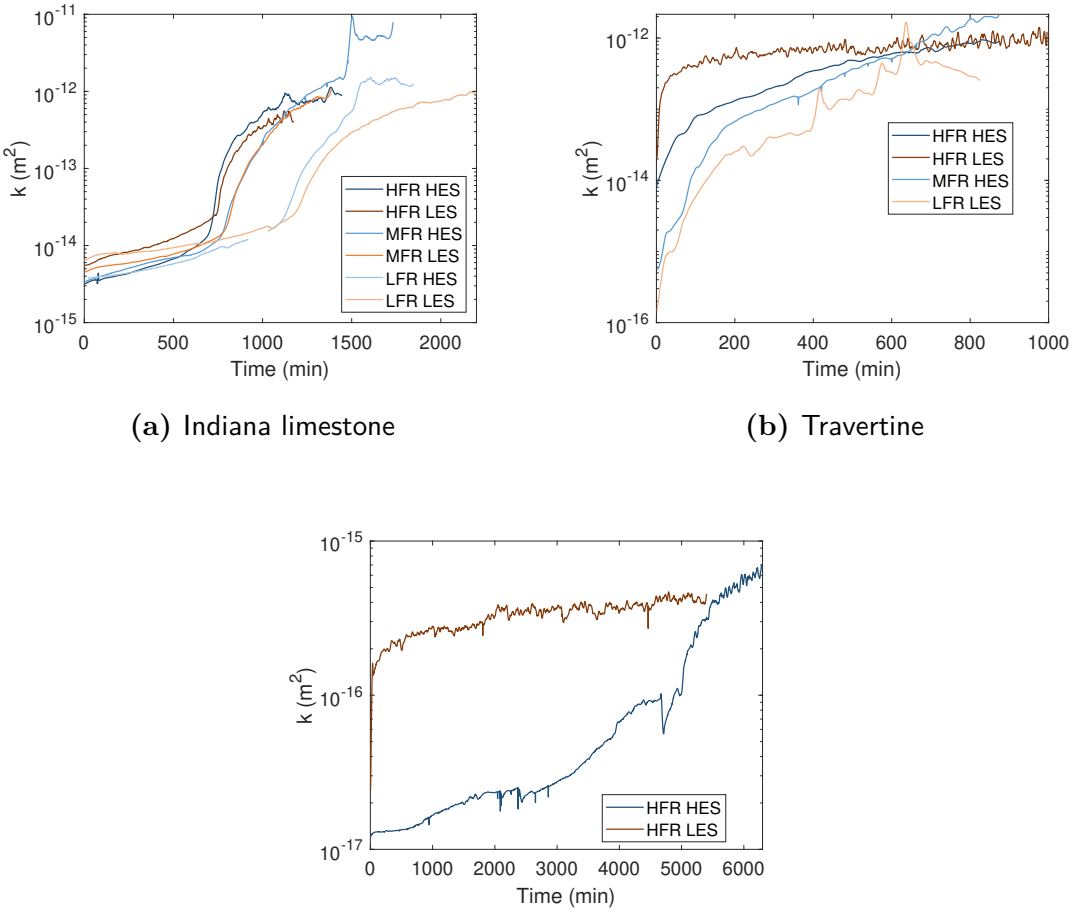

(a) Indiana limestone

(b) Travertine

(c) Pre-salt

Figure 8.1: Absolute permeability generation for the three rock-types experimentally tested, and showing similar trends: the flow rate is the dominating variable for k generation.

The influence of the injection rate is also perceptible by plotting the Ca and Mg removal rates (figures 8.2 and 8.3). The Ω value expresses the ratio between the volume of Ca-Mg in the effluent fluids over the volume of solid rock forming the sample. For each rock sample flooded, and for any given effective stress scenario, we observed a correlation between the largest Q at the inlet of the sample, and the normalized volume of either Ca and Mg found in the effluent fluids, confirming the large influence of the injection rate on carbonate rocks alteration.

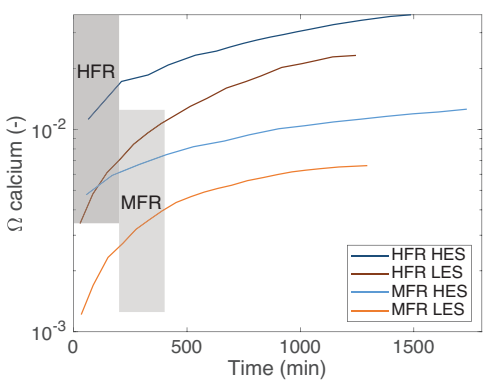

(a) Indiana limestone

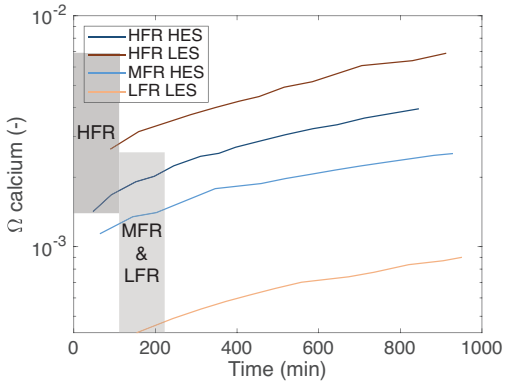

(b) Travertine

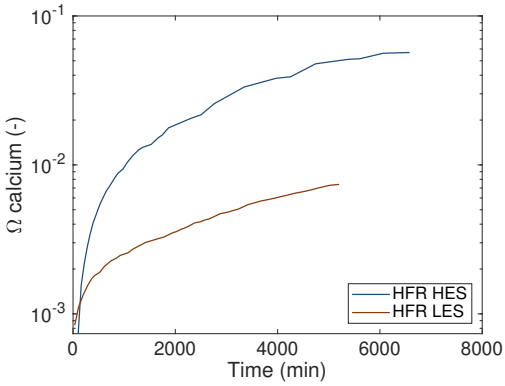

(c) Pre-salt

Figure 8.2: Normalized volume of Ca per volume of solid rock (Ω) for the three rock-types experimentally tested. A trend seems to appear for the Indiana limestone experiments, where an uncoupling between experiment sharing the same PV_{rate} appears. Calcium dissolution within Travertines and Pre-salt rocks is controlled by the injection rate and the sample petromorphology.

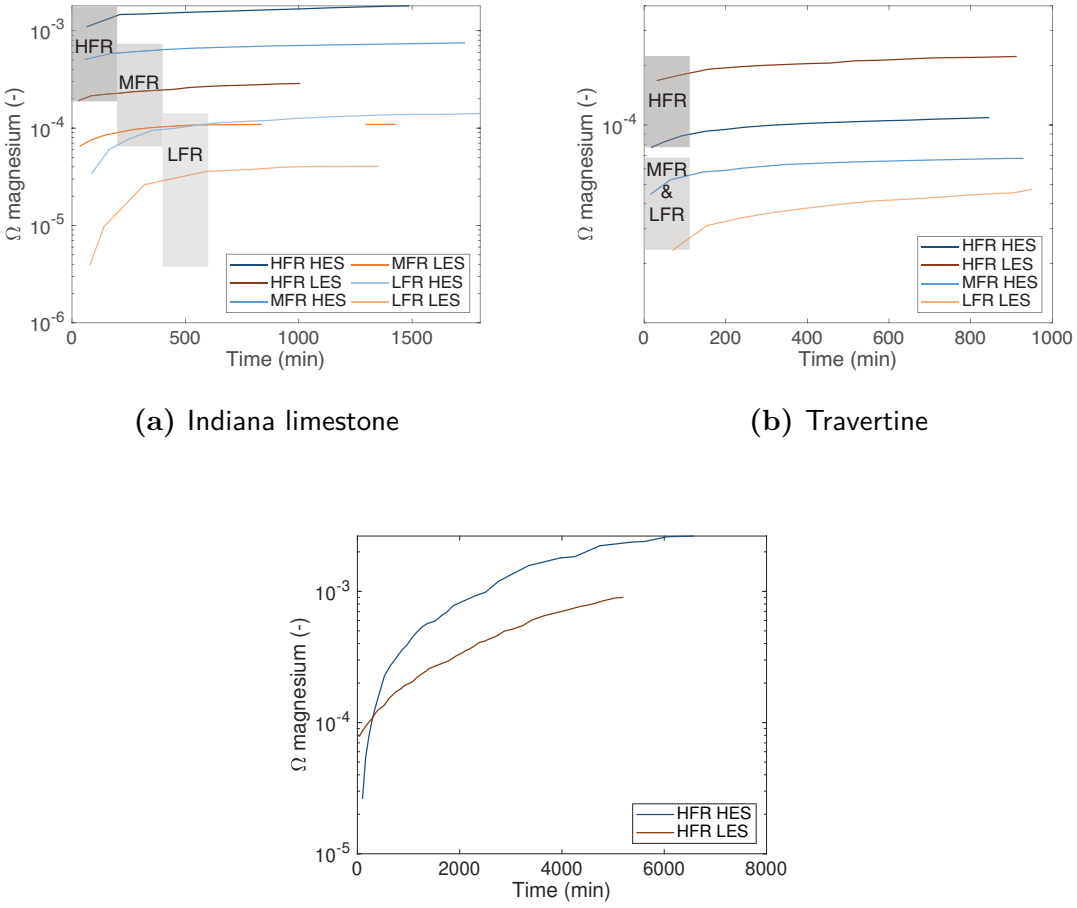

(a) Indiana limestone

(b) Travertine

(c) Pre-salt

Figure 8.3: Normalized volume of Mg per volume of solid rock (Ω) for the three rocks experimentally tested. A trend is clearly visible for the Indiana limestone experiments, where an uncoupling between experiment sharing the same PV_{rate} seems to show the large effect of the HES on Mg dissolution. Magnesium dissolution within Travertines and Pre-salt rocks is controlled by the injection rate and the sample petromorphology

8.2.2 Influence of effective stress

The current state of knowledge validates the influence of confining pressure and effective stress on permeability variation. While the stress state is known for playing a role over petrophysical properties of rocks (Zoback and Byerlee, 1975; Gobran et al., 1987; Berryman, 1992; Kok et al., 2002; İşcan et al., 2006; Ghabezloo et al., 2009), effective stress has been described as a non-influencing variable over permeability during fluid flow (Selvadurai and Głowacki, 2008), while some expressed the negative impact of a high effective stress over hydraulic conductivity and porosity of rocks (Vairogs et al., 1971; Shi and Wang, 1986; Wright et al., 2002; Zhou et al., 2016). Most studies have focused on the relative effect of stress state over permeability by varying the effective stress through a flooding experiment. Although this PhD project has confirmed the already well known effect of injection rate on carbonate rocks through permeability, chemistry, and µCT images analyses, our experimental design allows cross-comparisons of the results via the use of similar Darcy velocities during water flooding. Therefore, we can isolate the effect of injection rate (or PV_{rate}) while focusing on the absolute effect of the stress state on the rocks.

8.2.2.1 Permeability

We have calculated the permeability evolution for each sample flooded (k/k_0) (figure 8.4). k/k_0 allows us to accommodate the differences in the initial rock matrix, as the permeability at t=0 min can vary widely from one sample of same rock-type to another. The normalized permeabilities were interpreted as followed:

- Indiana limestone: in this section we were focusing on the breakthrough initiation times, as well as the breakthrough development rate. On figure 8.4a we observe a clear ordering of blue and orange curves, which respectively represent high effective stress and low effective stress experiments.

The PV_{rate} remained the driving variable for permeability development, now clearly seconded by a high effective stress.

- Travertine: pre-existing flow-paths dominated the development of the preferential channels, and influenced the permeability evolution. These permeability developments can be related to the second half of the Indiana limestone permeability curves, where the pre-existing flow-path has been enhanced, instead of being created. In the case of travertine rocks, both PV_{rate} and stress state seemed to have an impact on the rock: the ordering of the experimental signals appeared to be in a reversed order compared to the one observed for the Indiana limestone. Indeed, the maximum permeability generation was at the lowest PV_{rate} and lowest effective stress, while the most stimulating scenario for the Indiana limestones was the preserving one for travertine rocks.

- The Pre-salt and travertine rocks are thought to share similar petrographical characteristics which makes the latter an analogue for the former (Borghi et al., 2013; Virgone et al., 2013; Boyd et al., 2015; Chitale et al., 2015; Rezende and Pope, 2015; Soete et al., 2015; Schröder et al., 2016; Claes et al., 2017; Erthal et al., 2017). We observed a similar relative permeability evolution between Pre-salt and travertine rocks. $HFR\ HES$ showed signs of what could be interpreted as a slow and steady permeability evolution (breakthrough-like behaviour), where $HFR\ LES$ has seen its likely pre-existing flow-path(s) largely enhanced within the first minutes of flooding. We suppose that, while the pre-existing fabric and heterogeneities of each sample were important drivers, the stress scenarios have probably helped in 1) compressing the rock matrix of $HFR\ HES$, leading to a slower increase in permeability, and 2) further opening the pre-existing flow-path(s) of $HFR\ LES$, easing the fluid flow (cf. section 5.5.4). Although, we are

only basing this assumption on two experiments, this could be an early indication that both rock-type are physical analogues.

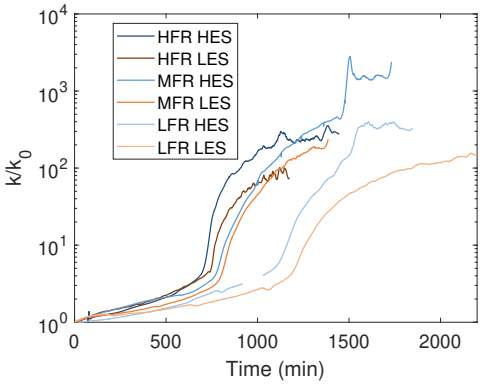

(a) Indiana limestone.

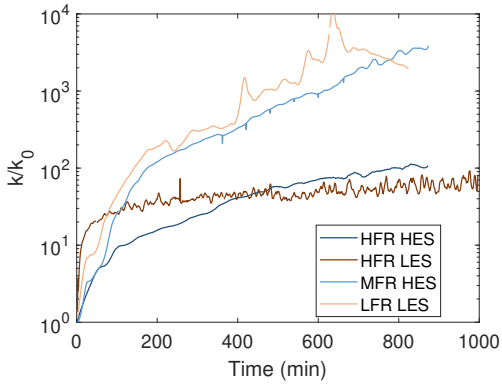

(b) Travertine.

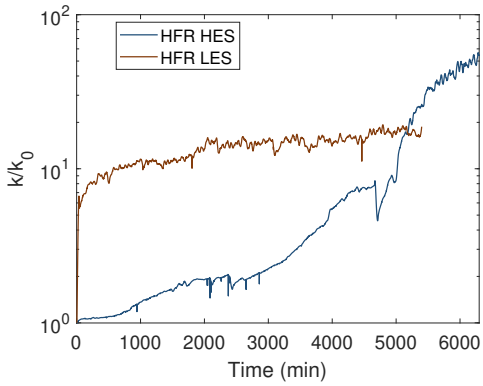

(c) Pre-salt.

Figure 8.4: Normalized permeability evolution for the three rocks experimentally tested. The Indiana limestone curves show a clear arrangement which depends upon the PV_{rate} and the effective stress. The travertine and Pre-salt cores seems to have been affected by the low effective stress scenario. An interesting uncoupling of the processes is visible within the set of travertine experiments, were the lower flow rates appear to have generated larger k/k_0.

A first comparison between the heterogeneous Pre-salt rocks and the travertine analogues can be achieved by the analysis of the PV_{bt} and/or PV_{maxK} done in chapters 5 and 6 (figures 6.15 and 5.15). Four experiments are directly comparable:

- Travertine $HFR\ HES$.
- Travertine $HFR\ LES$.
- Pre-salt $HFR\ HES$.
- Pre-salt $HFR\ LES$.

By plotting the PV_{bt} and/or PV_{maxK} against the PV_{rate} for these four experiments (figure 8.5), we clearly see a stress-driven grouping of the experiments which could be attributed to the stimulation effect of a low effective stress during seawater flooding on heterogeneous rocks.

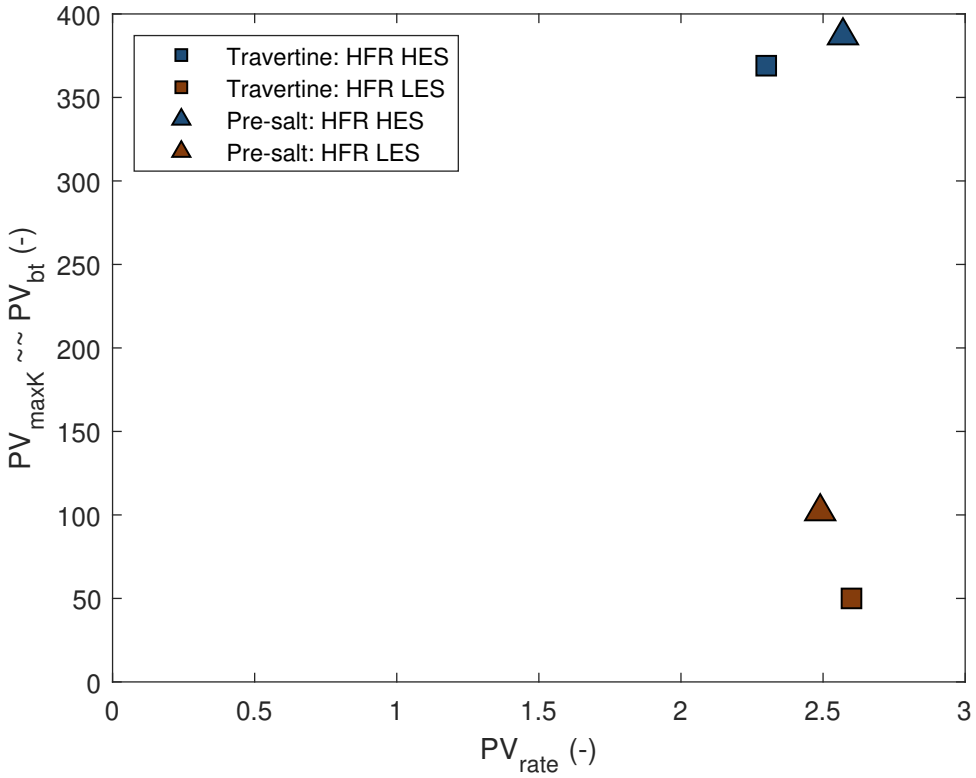

Figure 8.5: PV_{maxK} and PV_{bt} as a function of constant PV_{rate} for HFR experiments of travertine and Pre-salt rocks. The values for PV_{maxK} and PV_{bt} have been derived from the markers of figures 5.14 and 6.14, while the PV_{rate} values are given in tables 5.1 and 6.2. We observe that similar processes took place during the four experiments, which could have been influence by the effective stress in place.

8.2.2.2 Chemistry

The chemical data have been further interpreted in order to:

- Isolate the effect of the injection rate from those of the stress state (figures 8.6 and 8.7).

- Observe the concentration of Ca and Mg within the effluent fluids (figures 8.8 and 8.9).

By doing so we observe significant differences in the trends previously seen in figures 8.2 and 8.3. Figures 8.6 and 8.7 display Ω normalized by the PV_{rate}. This normalization has been done in order to remove the large influence of the velocity of the fluid over the chemical signal. We observe the following:

- Indiana limestone: following previous findings from the relative permeability analysis, we see a gathering of high effective stress experiments (blue curves) on top of the low effective stress ones (orange curves): it appears that a high effective stress seemed to stimulate the dissolution of Ca and Mg during seawater flooding. Along with the stress state, a high PV_{rate} remained a dominant factor for dissolution.

- Travertine: normalizing Ω by the PV_{rate} appears to bring the low effective stress experiments (orange curves) on top of the graph, indicating that a high effective stress seemed to preserve the sample from dissolution. Within a family of effective stress, a high PV_{rate} relatively reduced the overall dissolution.

- Pre-salt: this set of experiments display a tendency observed with Indiana limestone rocks as for the relationship between the stress state and ions removal, with the high effective stress experiment on top of the low effective stress one. While the PV_{rate} values were identical for both experiments, the trends for calcium and magnesium removal were one order of magnitude higher at high effective stress. Here again, this could be due to differences in the samples rock nature: the $HFR\ HES$ sample displayed a smaller and less connected porosity. While still behaving like an heterogeneous rock (see permeability), the sample could represent a mixed environment where processes encountered within both homogeneous and heterogeneous rock might have taken place during fluid flow as explained in sections 4.5.4 and 5.5.4: indeed, while $HFR\ LES$ has mainly seen its pre-existing flow-path enhanced via wall dissolution, $HFR\ LES$ has probably witnessed both

contact dissolution between grains, as well as wall dissolution within the pre-existing (shorter) channels.

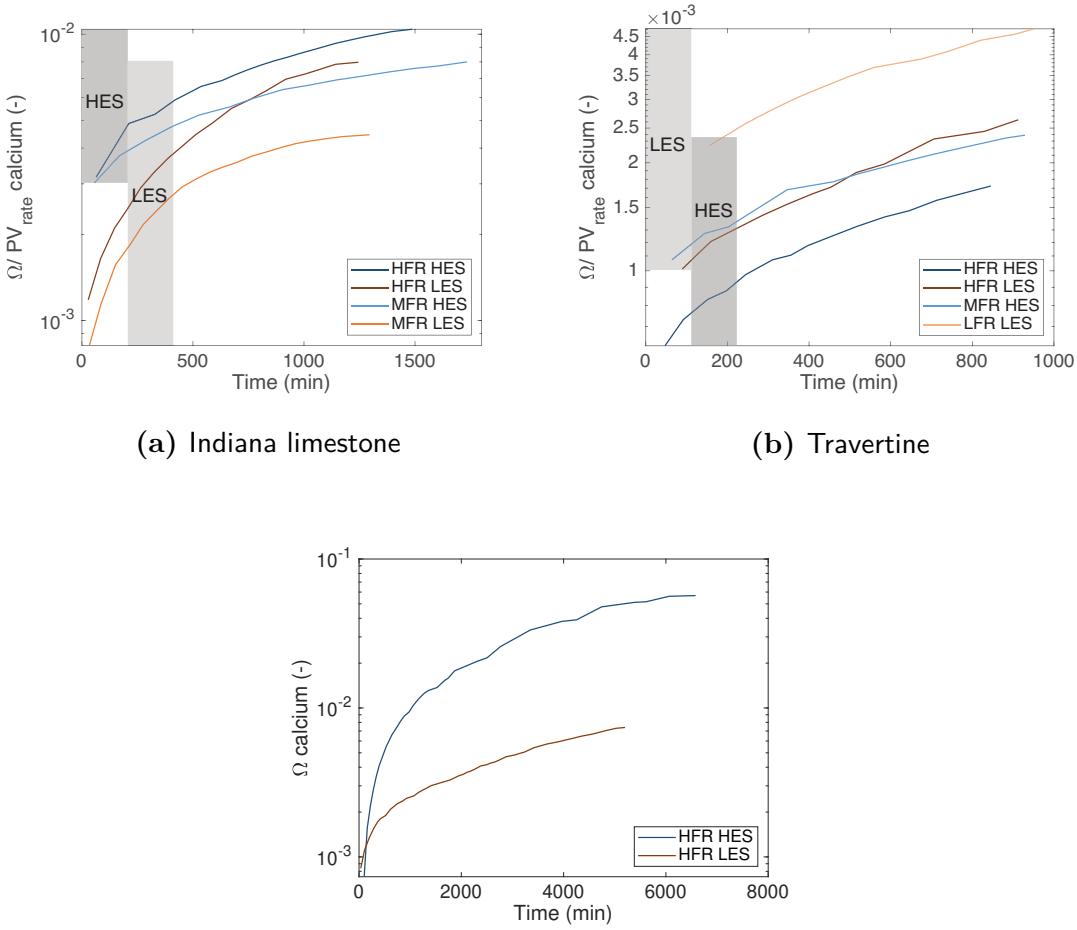

(a) Indiana limestone

(b) Travertine

(c) Pre-salt

Figure 8.6: Ca normalized Ω values for Indiana limestone and travertine rocks. No normalization is needed for the Pre-salt samples due to a similar PV_{rate}. The effect of the stress state is clearly visible: HES had a positive impact on the Indiana limestone and Pre-salt rocks, while a LES had one on travertine samples.

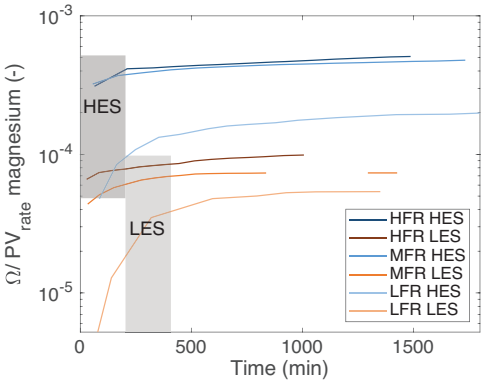

(a) Indiana limestone

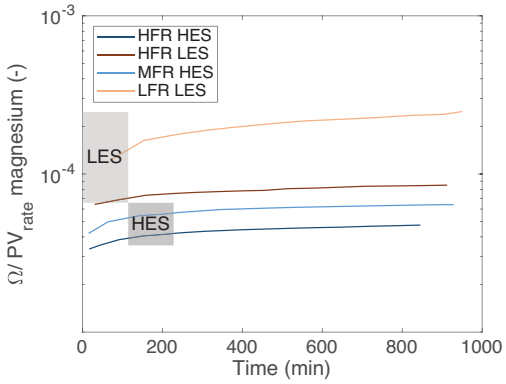

(b) Travertine

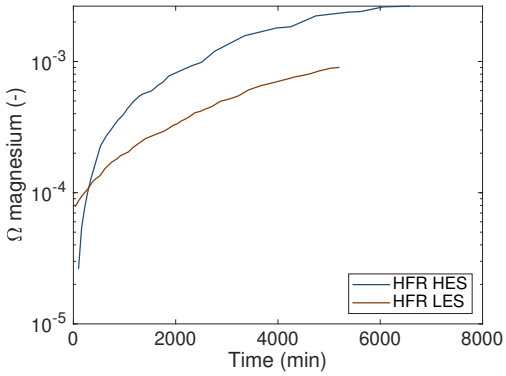

(c) Pre-salt

Figure 8.7: Mg normalized Ω values for Indiana limestone and travertine rocks. No normalization is needed for the Pre-salt samples due to a similar PV_{rate}. The effect of the stress state is clearly visible: HES had a large positive impact on the Indiana limestone and Pre-salt rocks, while a LES had a large one on travertine samples.

Plotting the concentrations of either ions for each experiments (figures 8.8 and 8.9) confirms the tendencies observed on figures 8.6 and 8.7). Indeed, we notice the large influence of the effective stress which appears to complete the action of fluid velocity. While the effective stress can be described as a stimulant for calcium and magnesium dissolution, its impact suggests a rock-dependency, so that a high effective stress is described as:

- A catalyst of Ca and Mg dissolution for homogeneous Indiana limestone.
- An inhibitor for Ca and Mg dissolution for heterogeneous travertine.
- A catalyst for Ca and Mg dissolution for Pre-salt rock. These results should be taken with care as they are based on two samples which displayed slight initial petrographical variations.

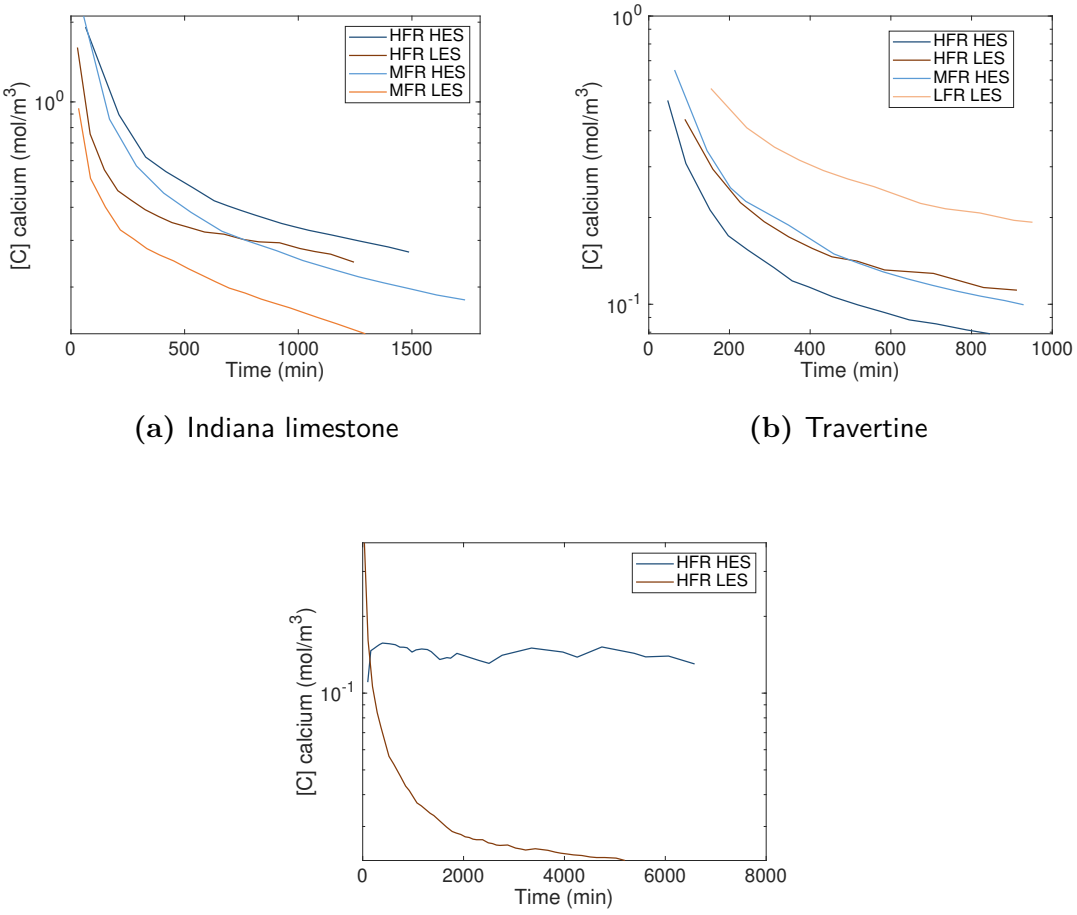

(a) Indiana limestone

(b) Travertine

(c) Pre-salt

Figure 8.8: Ca concentration values for Indiana limestone, travertines, and Pre-salt rocks. From the standpoint of a high Ca dissolution, scenarios tending towards a $HFR\ HES$ were preferable for Indiana limestone and a Pre-salt rocks, whereas scenarios tending towards a $LFR\ LES$ were preferable for a travertine rock.

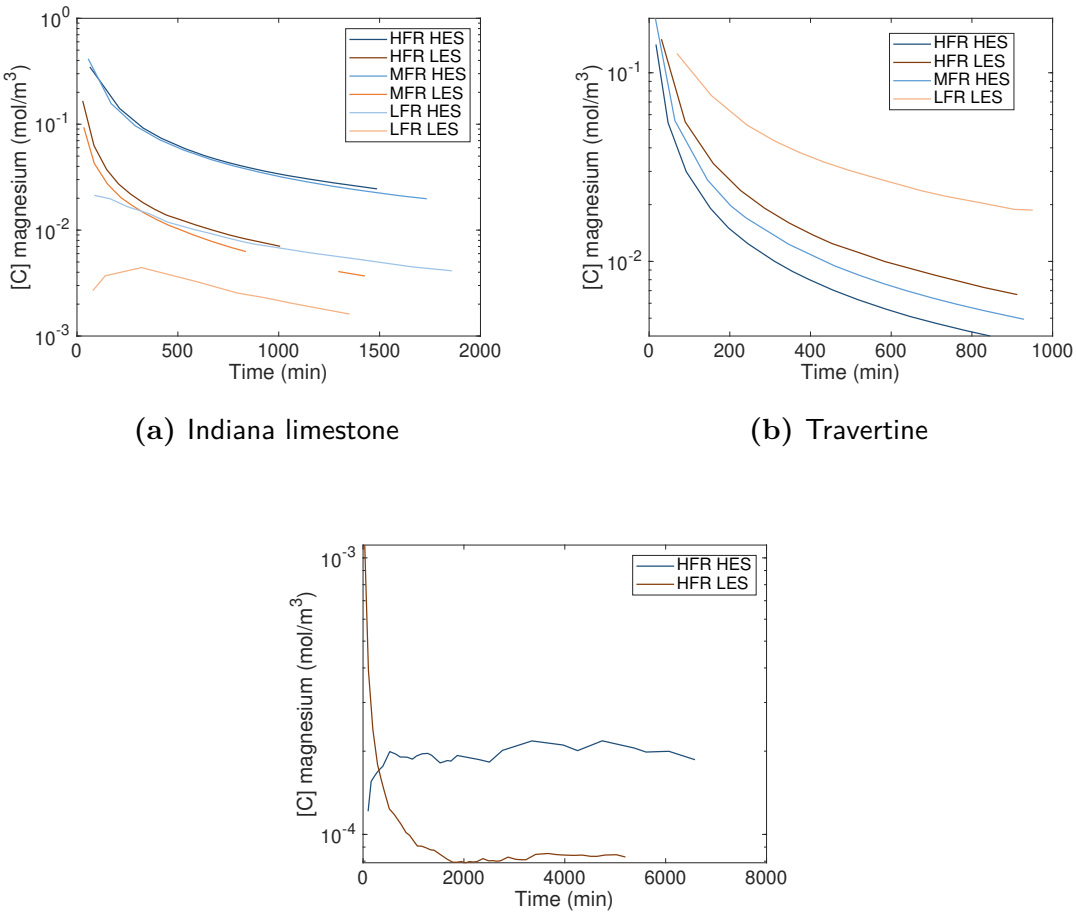

(a) Indiana limestone

(b) Travertine

(c) Pre-salt

Figure 8.9: Mg concentration values for Indiana limestone, travertines, and Pre-salt rocks. From the standpoint of a high Mg dissolution, scenarios tending towards a $HFR\ HES$ were preferable for Indiana limestone and a Pre-salt rocks, whereas scenarios tending towards a $LFR\ LES$ were preferable for a travertine rock.

8.2.2.3 µCT imaging

While in-depth µCT analysis has been done in each result chapter (4, 5, and 6), we are unable to cross-compare all rocks due to differences in PV_{rate} and rock nature. The analysis previously realized on Indiana limestone rocks confirmed the permeability and chemical trends by showing a greater alteration at high effective

stress, for any given PV_{rate}, which is partially confirmed by the µCT analysis available in chapter 4. Amongst heterogeneous samples, three experiments are comparatively relevant:

- Travertine $HFR\ HES$.
- Travertine $HFR\ LES$.
- Pre-salt $HFR\ LES$.

Figures 8.10 and 8.11 respectively show the density of ramification of the post-experimental dissolution, and the wormhole thickness for the three experiments. The thicknesses have been computed from the Centerline Tree function of Avizo® 9 (Sato et al., 2000).

The shrub framestone is complex to compare due to the chemical and physical variations between Italian travertines and Brazilian Pre-salt. Moreover, the Pre-salt broken sample ($HFR\ HES$) limits the quality of the comparative work. Nevertheless, and while the chemical response of a Pre-salt rock appeared similar in trend to the Indiana limestone, the physical outputs of $HFR\ LES_{Pre-salt}$ resembled the homologous travertine ones, by showing a strong and spread dissolution (figures 8.11b and 8.11c). Figure 8.10 presents the wormholes thicknesses of the travertines' HFR experiments, as well as the Pre-salt $HFR\ LES$ experiment. We note that the Pre-salt post-experimental wormhole is slightly above the average value of its travertine high effective stress experimental counterpart:

- Travertine $HFR\ HES$: 12.48 mm.
- Travertine $HFR\ LES$: 13.56 mm.
- Pre-salt $HFR\ LES$: 12.55 mm.

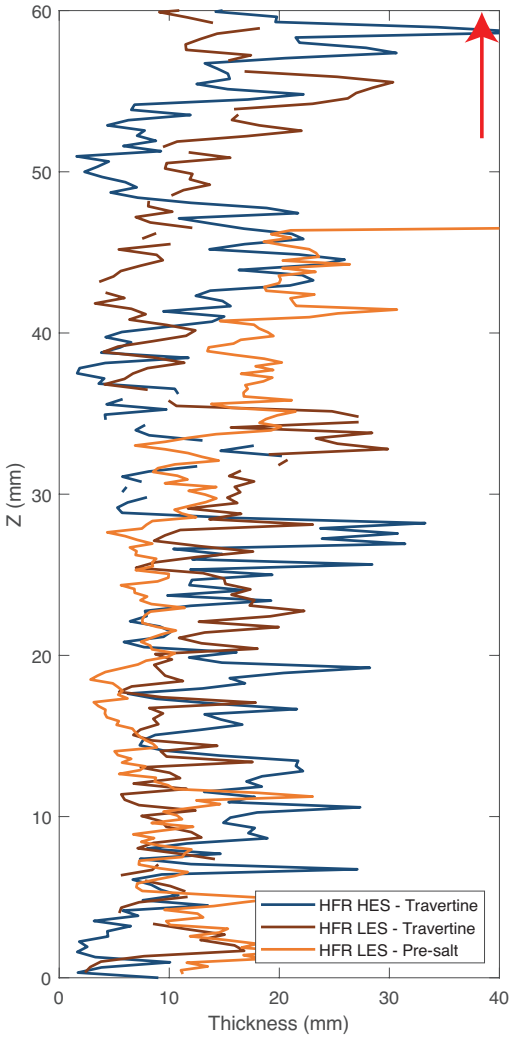

Figure 8.10: Main wormholes thicknesses for the travertine HFR experiments and Pre-salt $HFR\ LES$ experiment. The red arrows show the flow direction.

Figure 8.11 shows the density of ramification of the wormholes left after experimental flooding, which relates to the intensity of dissolution. Although the three samples have witnessed an important dissolution, whose limited spreading indicates a large influence of the initial poro-permeability driving the fluid flow, we observe that both LES experiments seem to have experienced a slightly more

important alteration of their rock matrix. This leads to the conclusion that a low effective stress applied to an heterogeneous shrub framestone could be an important secondary driver for rock alteration during seawater-flooding.

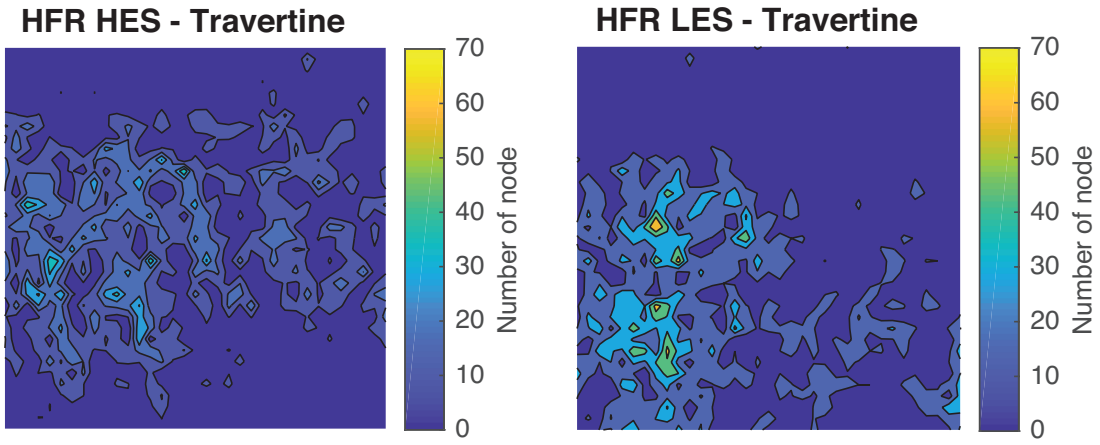

(a) Travertine $HFR\ HES$ **(b)** Travertine $HFR\ LES$

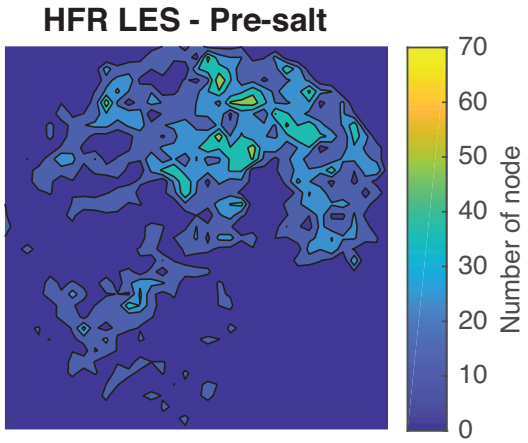

(c) Pre-salt $HFR\ LES$

Figure 8.11: Density plot of the dissolution pattern. Comparison case for the HFR experiments involving a shrub framestone. The color-scale displays the amount of nodes in the Z axis. From three comparable rock samples, the LES experiments have undergone more damage than the HES one.

8.2.3 Influence of the heterogeneity

Heterogeneity within the porous medium is a key factor controlling the development or enhancement of flow-paths. Several studies have addressed the impact of the poro-permeability drains (Hoefner and Fogler, 1988; Egermann et al., 2006; Kalia and Balakotaiah, 2009). While previous sections 8.2.1 and 8.2.2 focused on the importance of PV_{rate} and effective stress, the local and global heterogeneities of a core sample appear to be a key variable for porosity and permeability generation. We are founding our assumption on two numerical works based on the analyses of µCT images:

- The ANN work (undergone with Phil Cilli - University of Edinburgh).
- The OGS work (realized by Dr. Andrew Fraser-Harris - University of Edinburgh).

Both works have highlighted the influence of the rock porous structures on the fluid flow and the resulting calcite dissolution.

8.2.3.1 Artificial Neural Network (chapter 7)

Chapter 7 presents the findings of the relationship between macropores and likelihood of dissolution channel development. We have seen that using several key geometrical variables relating to the porous medium we could forecast the dissolution shape and spread within an heterogeneous rock. figures 8.12, 8.13, 8.14, 8.15, and 8.16 present our ANN solution including the datasets gathered from the Pre-salt experiments of chapter 6. The figures are a way to observe, from a 2D perspective, the potential intensity and spread of the alteration of a rock sample, based on the analysis of the pre-experimental µCT volumes. Not only the method appears to be working for the heterogeneous travertine rocks, but adding the $HFR\ LES$ Pre-salt experiment dataset for ANN solving leads to the following conclusions:

- Including the Pre-salt dataset neither dramatically increase nor decreased the quality of wormhole prediction of the travertine rock samples.
- The main features of the $HFR\ LES$ Pre-salt experiment were detected by our bespoke ANN solution: the trend of the background plots (predictions) followed the general trends of the red lines (solutions). We conclude that the digital pore network of both Pre-salt and travertines are interpreted as a similar rock-type based on the variables used by our solution.
- We believe that, for shrub framestone, heterogeneities present in the matrix represent the principle driver for flow-path determination. The key geometrical variables behind this are summarized in table 7.1.

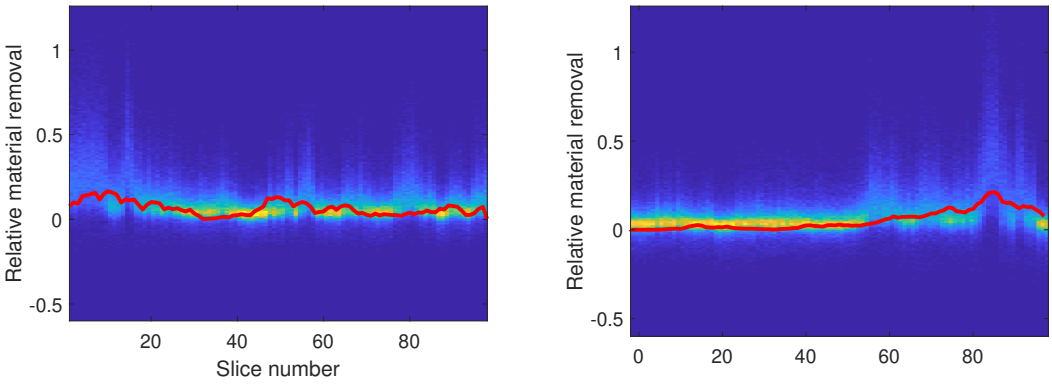

(a) Trav.: LFR LES - YX direction. **(b)** Trav.: LFR LES - ZX direction.

Figure 8.12: Signal data plotted under their respective cross-sectional direction for the travertine $LFR\ LES$ experiment.

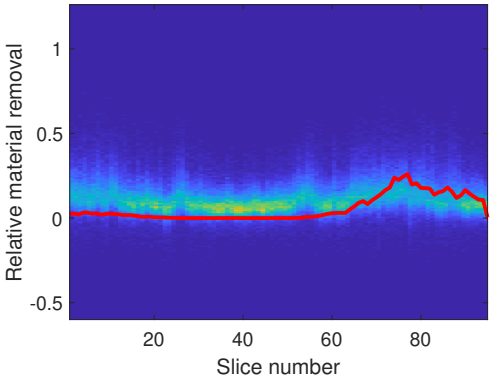

(a) Trav.: MFR HES - XY direction.

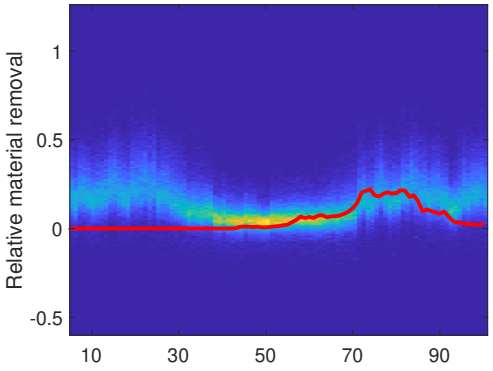

(b) Trav.: MFR HES - ZY direction.

Figure 8.13: Signal data plotted under their respective cross-sectional direction for the travertine $MFR\ HES$ experiment.

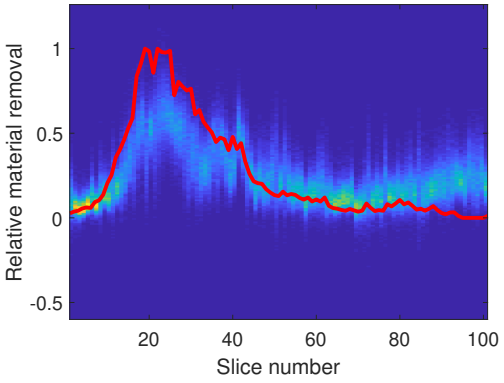

(a) Trav.: HFR LES - XY direction.

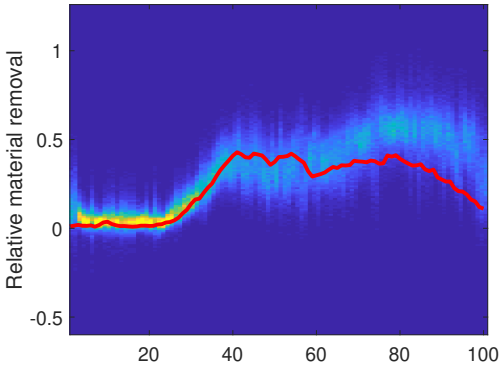

(b) Trav.: HFR LES - ZY direction.

Figure 8.14: Signal data plotted under their respective cross-sectional direction for the travertine $HFR\ LES$ experiment.

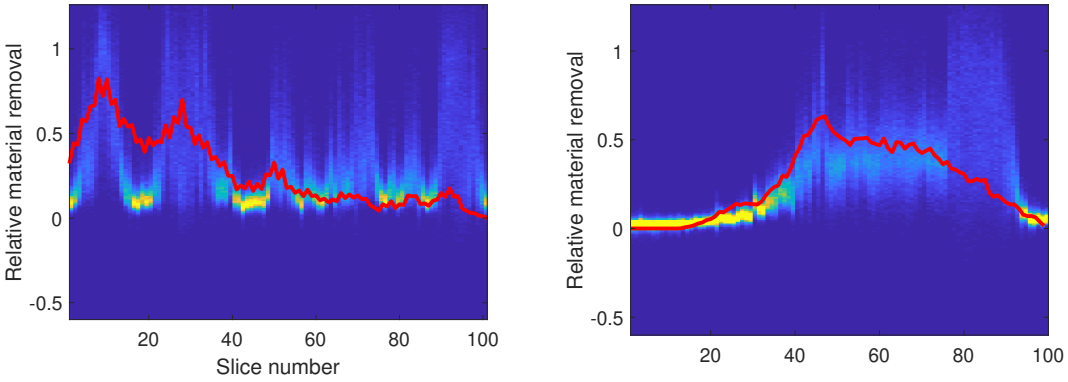

(a) Trav.: HFR HES - XY direction. **(b)** Trav.: HFR HES - ZY direction.

Figure 8.15: Signal data plotted under their respective cross-sectional direction for the travertine $HFR\ HES$ experiment.

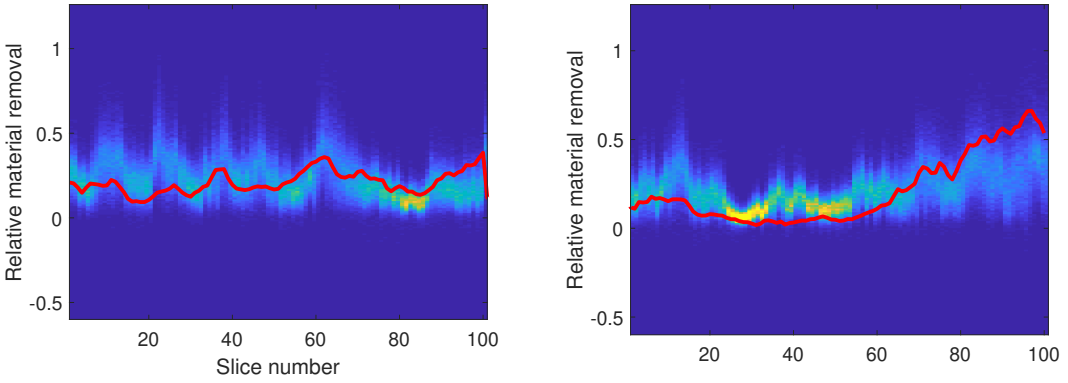

(a) Pre-salt: HFR LES - XZ direction. **(b)** Pre-salt: HFR LES - ZY direction.

Figure 8.16: Signal data plotted under their respective cross-sectional direction for the Pre-salt $HFR\ LES$ experiment.

8.2.3.2 OpenGeoSys simulation

OpenGeoSys (OGS) is an open source software for solving Thermal-Hydro-Mechanical-Chemical applications (Kolditz et al., 2012). The coupled solution offered by the ICCR-Macropore and the evolution brought to the OGS code by Dr. Andrew Fraser-Harris can be used for studying the influence of the heterogeneity of a medium on rock dissolution and wormhole formation. This PhD project being part of a larger group, the work presented in this section has not been realized by myself, while based on the data produced by the experimental work done during this study.

The relationship between the connectivity of the pore in 2D and the post-experimental dissolution has been investigated. A pre-experimental 2D slice of a travertine sample has been analysed using OGS. The principle of this analysis is based on the coupling between the 2D pore network defined by the ICCR-Macropore (cf. section 3.3.2), and the Hydro-Mechanical solver of OGS. The 2D pore network is used as a flow channel by OGS, which can output a map of potential stresses of the analysed 2D slice. The sample used in this section has not been part of any travertine experimental work presented in chapter 5, and was flooded as part of preliminary tests (and presented by Brondolo et al. (2018a)). The experimental matrix was based on a 'in step' variable effective stress, while $\triangle P$ was recorded through the use of two differential pressure placed on both ends of the Hassler cell (figure 3.1). The high initial permeability of the sample as well as the uncertainties surrounding the $\triangle P$ acquisition and reliability has compelled us to exclude this dataset from the comparative work presented in chapters 4, 5, and 6. Nevertheless, the experiment observed the following characteristics:

- The sample was highly heterogeneous.
- The sample contained macropores.

- The sample has been flooded for several days and at an average effective stress of 30 MPa.
- The injection/formation fluids were identical to the one used in the other studies presented in this thesis.

Figure 8.17a display the selected pre-experimental 2D slices from a travertine sample, while figures 8.17b and 8.17c show the post-experimental result and distribution of tensional and compressional stresses along the slice. The stresses have been calculated using a mesh of the slice and the 2D network of pore connection, both generated by the ICCR-Macropore. Several interesting features can be seen on the interpreted slice (figure 8.17):

- The 2D network is used in OGS as a mesh where each tube represents a fluid connection between pores. On this example, the ICCR-Macropore has generated a network of fluid flow that picks the main features of what later became the dissolution path-way (figure 8.17b). This example partially validates the network of pores as a 2D representation of 3D flow.
- The pores under tension or compression are the one part of a connected network of flow. Although obvious from the standpoint of the theory of Terzaghi (1951), it appears clear on the interpreted slice (figure 8.17c) that pores part of a global network of fluid flow have seen their walls withstanding variable stress states. Both fluid flow and effective stress could have contributed to the dissolution.
- The last feature validates the assumption of an heterogeneity and vug-driven dissolution. This hypothesis is based on the comparison of the pre- and post-experimental slices of the connected pores which were part of the main network, along with the 'unconnected' pores (marked by a red arrows in figure 8.17a). Little to no dissolution was observed within these 'unconnected' pores. This completes the validation of the 2D network

assessment of pore connectivity. Indeed, the few pores which have not been included into the main network of fluid flow by the ICCR-Macropore have been relatively preserved from any kind of dissolution. Moreover, this analysis supports the idea that heterogneities are an important driver for fluid flow, and hence for carbonate dissolution.

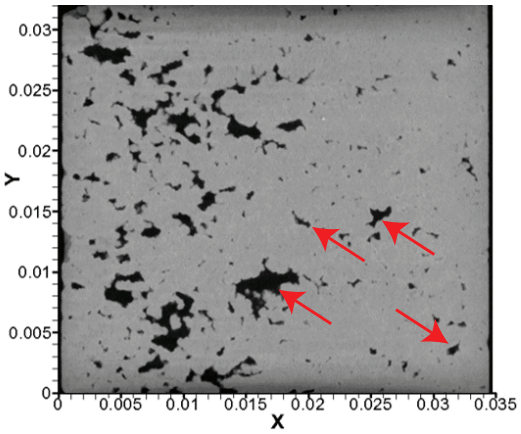

(a) Travertine: pre-exp.

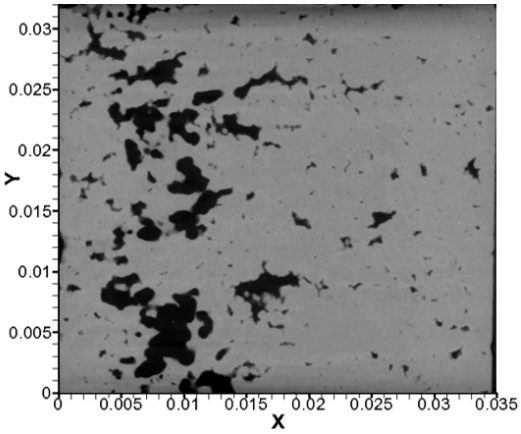

(b) Travertine: post-exp.

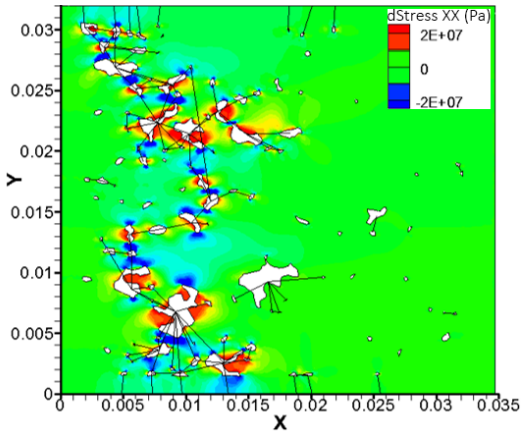

(c) Stress map & 2D network

Figure 8.17: Comparison between pre- and post-experimental 2D slice of image stack, and the stress map. The interest of this 2D model is two-fold: 1) it validates the 2D network of pore presented in chapter 3, and 2) it validates the impact that the heterogeneities have on the fluid flow.

8.2.4 Energy balance model

A study based on the energy analysis during experimental flooding is available in appendix L. In this work, the channels formations observed during this project, as well as the rate of permeability development, are reported being functions of the cumulative energy input into the samples. During Indiana limestone experiments, it was found that a cumulative energy input of 6.22 $\times 10^{-9}$ J.s.m^{-1} ($\pm$12 %) was necessary before triggering a breakthrough. This value has been used in the modelling approach to determine the dominant flow regime. The flow rate in an experiment remained constant, therefore a change in the permeability of the samples is represented by a change in the differential pressure across the sample. The experimental set-up used throughout this PhD led to a variation of the effective stress along the length of the sample.

Following analysis of the experimental data, it was found that the point at which the permeability started to increase (Indiana limestone), as well as the magnitude of increase post wormhole formation (travertine), could be correlated with the amount of energy which had been expended in the sample during each flow test. This cumulative energy input is directly related to the $\triangle P$ by a power law of the form $y = ax^b$, which is related to the interplay of the fluid velocity at the inlet of the sample and the sample initial permeability. This relationship seems valid for both Indiana limestone and travertine. The energy model is expressed by the equation 8.1 which describes the empirical model:

$$\frac{dk_n}{dt} = a\left(\frac{dP_d}{dx}\right)^b_{t=0} \tag{8.1}$$

Where $\frac{dk_n}{dt}$ is the rate of change of the normalized permeability (k/k_0), $\frac{dP_d}{dx}$ is the differential pressure measured across the sample at t=0 min, and a and b are constants. The a and b coefficients given by the $y = ax^b$ power law for each equation can be further described by a single power law relationship, so that

a pre-wormhole formation would be given by equation 8.2 while equation 8.3 characterizes travertine rocks (or post-wormhole results).

$$\begin{aligned} a &= 0.07 \left(\frac{dP_d}{dx}\right)_{t=0} \\ b &= -6.7955 \left(\frac{dP_d}{dx}\right)_{t=0}^{-0.294} \end{aligned} \tag{8.2}$$

$$\begin{aligned} a &= 0.0112 \left(\frac{dP_d}{dx}\right)_{t=0} - 0.011 \\ b &= -0.0093 \left(\frac{dP_d}{dx}\right)_{t=0} + 0.0449 \end{aligned} \tag{8.3}$$

Following a similar workflow to the one described in sections 4.5.1.1 and 5.5.1.1 (figures 4.9 and 5.14), the constants used in each of the above equations are based on the examination of the pressure gradient across the sample and the rate of change of the permeability. Figures 8.18b and 8.19b are the permeability results using the energy model, while 8.18a and 8.19a are the experimentally measured k/k_0. The pre-wormhole model describes perfectly the magnitude and amplitude of Indiana limestone rocks. This means that the pre-breakthrough phases of these rocks were dominated by an energy-related process, whose proxy can be linked to the flow-rate.

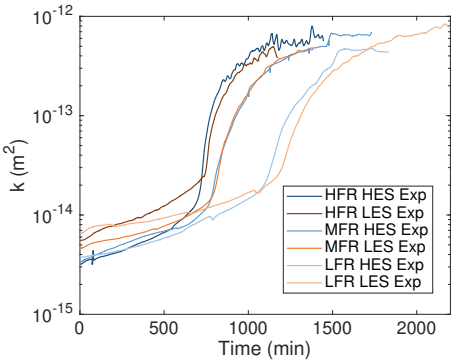

(a) Indiana limestone - exp.

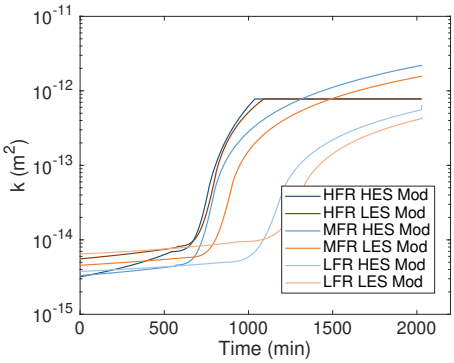

(b) Indiana limestone - model

Figure 8.18: Comparison between the experimental permeability and the model-based permeability for Indiana limestone. The model renders well the curves ordering as well as the relative magnitude until $\triangle P$ becomes too low (end of an experimental flooding).

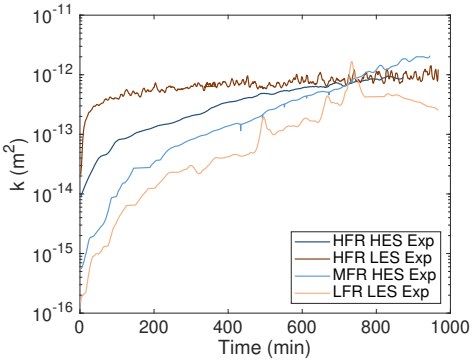

(a) Travertine - exp.

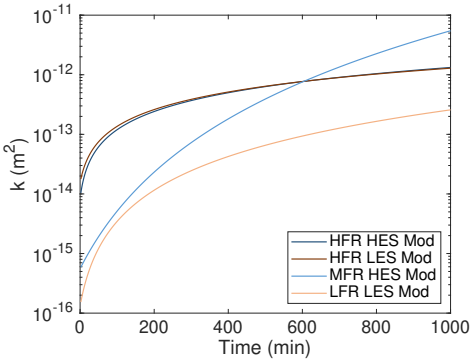

(b) Travertine - model

Figure 8.19: Comparison between the experimental permeability and the model-based permeability for travertine. While the model catches the mains trends (difference of magnitude between higher and lower PV_{rate}), it fails in finding the relative ordering between the $LFR\ LES$ and $MFR\ HES$ experiments.

Chapter 9

Conclusion and future work

9.1 Conclusion

9.1.1 Introduction

Maximizing recovery during underground fluid production has become more and more important due to technical, economical an societal issues (Al Adasani and Bai, 2011; Kamari et al., 2014). Injection and production of fluids imply large changes in pressure within a reservoir (Al-Harthy et al., 1998a; İşcan et al., 2006). Understanding the role of effective stress during carbonate reservoir flooding appears crucial as it can directly affect the permeability, the hydraulic conductivity, and the overall rock alteration. The injection of water into carbonates can lead to porosity enhancement and creation of preferential flow-paths (termed wormholes) whose sizes can range from pores throat enlargement to creation of meters large caves. Experimental flooding on small core samples aim in recreating fluid flow while highlighting the key variables responsible for carbonates alteration and what leads to a better inter-connection of the pre-existing porosity. Several factors can affect the way a wormhole propagates within a carbonate rock. One important variable driving most of the fluid flow is the heterogeneous porosity (e.g. vugs within the rock matrix). Other variables such as the variation of the

confining pressure, variable rock composition, and injection rate also appears to be responsible for variation in carbonate alteration during fluid flow. While most studies have well constrained the impact of the above mentioned variables on wormhole formation and morphology, very few experiments looking at the effect of the stress sate under steady state condition of P-T have been done. Previous studies have focused on the pressure-dependence of the permeability evolution in fractured media (Polak et al., 2004; Tian et al., 2014) on the relationship between confining/pore pressure changes and porosity and permeability evolution through triaxial tests (i.e. focusing on the elastic response of the matrix at any given combination of confining and pore pressures and/or applying stress cycles to the rocks - Yale et al. (1998); Zhou et al. (2011)), on the stress-path induced permeability changes (Khan et al., 2000), and more generally on the influence of acidifying treatment over limestone dissolution (Frick et al., 1994b; Bazin et al., 1995; Fredd et al., 1996; Fredd and Fogler, 1998; Golfier et al., 2002; Egermann et al., 2006; Luquot and Gouze, 2009; Menke et al., 2015; Ott and Oedai, 2015; Barri et al., 2016; Luquot et al., 2016; Teles et al., 2016; Zhang et al., 2016).

The novelty of our experimental work resided in observing the effect of effective stress on rock alteration during constant flooding of a pH neutral injection fluid. A change in confining pressure as a way to vary the effective stress seemed unrealistic in case of injection or draw-down phases in a geological reservoir. Therefore, we have based our effective stress calculations on changes in pore pressure, and by keeping a constant confining pressure. The experimental matrix used for all core testing has allowed us to cross-compare physical, chemical, and µCT imaging outputs, as a way to isolate the effect of the reservoir stress state during production. We have also interpreted µCT images using machine learning by using the data gathered during the experimental runs on travertine rocks (chapter 5). While the experimental work gave us the opportunity to weight the contributions of injection rate and effective stress over rock alteration, this

modelling approach allowed us to study the large impact of the pre-existing heterogeneities on the fluid flow and wormhole generation.

9.1.2 Experimental and numerical development

Our experiments have been conducted at hydrostatic reservoir conditions of pressure and temperature ($P_c = 50$ MPa - $T = 60$ °C). Six homogeneous Indiana limestone rocks, four heterogeneous travertines, and two heterogeneous Pre-salt core samples have been flooded at different PV_{rate} and effective stresses using a pH neutral artificial seawater. Effective stress and PV_{rate} were varied between experiments while kept constant during an experimental flooding.

Several numerical tools have been developed over the course of this PhD project:

- A C++ solution has been developed, based on the preliminary work of Dr. Chris McDermott (ICCR-Macropore - cf. chapter 3). The software is used as an µCT images interpreter. The tool generates geometrical outputs (used for analysis and modelling works), as well as mesh files of 2D slices rock samples and 2D network of pore connectivity (used for stress analysis in OpenGeoSys). The meshes have been used by Dr. Chris McDermott and Dr. Andrew Fraser-Harris for 2D modelling of fluid flow through heterogeneous carbonates. Their work completes the research undertaken during this PhD as it highlights the role of the heterogeneity and porosity, as well as the predictability of poro-permeability development.

- A software named 'Slice Picker' has been developed, and uses the pre-existing functions of the ICCR-Macropore. The purpose of this software is to run a quick analysis of a stack of µCT images, and provides the user with a formatted set of data for running the Artificial Neural Network analysis (third tool of this PhD project).

- A solution using the Deep Learning Toolbox of Matlab has been developed

with the help of Phil Cilli (PhD candidate within the International Centre of Carbonate Research - University of Edinburgh). This numerical work uses the ICCR-Macropore and the Slice Picker as pre-processors of experimental results in order to study the effect of heterogeneities on poro-permeability development.

9.1.3 Findings

We assessed three main variables as proxies for carbonate alteration:

- The injection rate (termed as PV_{rate}), and the effective stress (σ').
- The volume (Ω - dimensionless - cf. chapter 2) and concentration of calcium and magnesium ([C] in mol/m^3) within the effluent fluid.
- The creation of pore space and its spread within the core samples.

9.1.3.1 Injection rate

Through experimental observations, we confirmed the large and dominating influence of the PV_{rate}, which related to the $\frac{dP}{dx}$ at the inlet of the core sample during flooding. For a given effective stress, a larger amount of fluid injected through a porous medium per amount of time have generated more permeability (k), dissolution (Ω), and has positively increased the overall porosity. Despite using a non-acidic injection fluid, our results correlated with different studies using low pH fluids (Hoefner and Fogler, 1988; Daccord et al., 1989; Steefel and Lasaga, 1990; Frick et al., 1994a; Bazin et al., 1995; Fredd et al., 1996, 1999; Golfier et al., 2002; Kang et al., 2003; Egermann et al., 2006; Siddiqui et al., 2006; Bemer and Lombard, 2010; Izgec et al., 2010; McDuff et al., 2010; García-del Cura et al., 2012; Ott and Oedai, 2015; Walle et al., 2015; Barri et al., 2016; Teles et al., 2016; Zhang et al., 2016; Aman et al., 2018). We observed the following:

- A large PV_{rate} played a driving role for Indiana limestone k/k_0, Ca-Mg, and pore space creation and spreading.

- Travertine rocks have seen their permeability (k) evolution linked to the PV_{rate}, where most k was generated at large PV_{rate} values. Interestingly, once normalized against k_0, the permeability evolution seemed to be driven by the slowest PV_{rate} value.
- No conclusion can be drawn for Pre-salt experiments due to the use of a similar PV_{rate}.

9.1.3.2 Effective stress

The effective stress appeared to play a role on the permeability (k/k_0), chemical dissolution ($\frac{\Omega}{PV_{rate}}$ and [C]), and porosity evolution and spreading during seawater flooding. We noticed that this role was rock-dependent. For any given PV_{rate}, we observed the following:

- Indiana limestone have seen their k/k_0 permeability, calcium and magnesium dissolution, and porosity spreading being increased by the use of a high effective stress.
- Travertine samples have reacted in an opposite way, where a low effective stress have resulted in a greater k/k_0 permeability generation, chemical dissolution, and porosity creation and spread.
- Due to limitations in Pre-salt core sample availability, the following conclusions have been drawn from two experiments and might not be fully representative of the Pre-salt strata. We could not entirely correlate the k/k_0 evolution to a reversed process (i.e. observed during travertine flooding). The largest apparent permeability evolution during the low effective stress experiment could be due to the presence of a pre-existing flow-path within the rock. Conversely, this early and largest permeability evolution could be due to the positive impact of a higher pore pressure, helping the fluid to flow through the porous medium. We also observed larger calcium/magnesium dissolution at high effective stress.

9.1.3.3 Heterogeneity

The last variable we observed related to the heterogeneity of the core sample. Due to our µCT scanning resolution limitations, we have only been able to resolve the macroporosity within travertine-like rocks. Our artificial neural network solution, developed for the purpose of alteration and dissolution prediction, has effectively been able to constrain the likelihood and intensity of dissolution within travertine and Pre-salt samples (cf. chapters 6, 7, 8, and appendix K). This proved that local heterogeneities, pre-existing flow-path(s), and macropores were driving parameters for carbonate alteration during our experiments. Our 2D analysis of the porous media has allowed us to isolate four main key geometrical parameters having had a large impact over heterogeneous carbonate alteration during fluid flow: the amount of pores, the mean pore perimeter, and, assuming the ellipse shape of the pores, the small and large ellipse perimeter. the ellipses termed 'small' and 'large' referred here to either the area equivalent ellipse shape of a pore, or the enlarged ellipse representing the influence of a pore on the neighbouring region. We believe that the influence of the heterogeneities within the macroporosity is in fact so important that we managed to predict the dissolution pathways in carbonate sample independently of the need of specific chemical parameters, while only using geometrical features as input data. The impact of heterogeneities in a porous media seemed to overtake any other variables, and the local pressure gradients generated by the presence of macropores, or vugs, is here presented as the main driver for permeability, chemistry, and porosity evolution.

9.2 Future work

The experimental and numerical work undertaken during this PhD have allowed to draw a conclusion on the driving parameters during carbonate fluid flow. While

some work has been done, not all options have been covered due technical or time limitations. Some ideas are presented in this chapter.

9.2.1 Experimental work

We ran experimental flooding using a cross-comparable matrix, and while this has allowed us to better understand how both homogeneous and heterogeneous carbonates react under different stress state, more effort could be put in order to refine the results:

- A PV_{rate} of 2.5 or 3 seems unrealistic in the context of in-situ reservoir flooding (especially as the fluid front move away from the injection point). Future experimental matrix could be designed to study the effect of lower PV_{rate} values on carbonate alteration. Considering PV_{rate} values orders of magnitude different could allow to observe new couplings between effective stress and flow rate.

- We studied the effect of seawater injection during a WAG phase (no CO_2). One important future step relates the investigation of two phase flow (CO_2-seawater) through carbonate rocks, while studying the impact of effective stress during WAG injection.

- We found a limitation in the absence of syn-flooding µCT imaging. This is due to the experimental rig and the µCT facilities being located in two separate rooms. A large improvement would reside in re-designing a Hassler cell that would allow easy loading and unloading of the samples for µCT imaging. The future researchers could think of LabVIEW controlled functions that would safely unload the confining and pore pressures, hence keeping the sample intact during the scanning phase.

- Most of the rig re-development done in this PhD was focusing on the

analogue-to-numerical recording of the variables throughout an experimental flooding. A large development phase including testings had already been done by McCraw (2016) and the delivered rig was fully proven and functional. One conclusion of this thesis concerns the processes leading to rock dissolution under different stress state, and while it appears clear the stress state did affect rocks of different nature in different way, it is still unclear how. One way to better isolate the processes in place would be to add a set of filters at the outlet of the Hassler cell which would act as a fine-catcher. Further visual analyses would permit to quantify and characterize the dissolution process undergone by the rock, in particular erosion processes.

- A last experimental improvement of this work would be to enlarge the experimental matrix vertically, by adding more effective stress case scenario.

9.2.2 Modelling work

The ANN analysis (chapter 7) showed that heterogeneities amongst a rock are of prime importance for calcite dissolution and wormhole development. Due to µCT resolution limitations, we have not been able to extent the analysis to the homogeneous Indiana limestone. Further investigations with a high resolution µCT imaging and a smaller ROI would be of interest in order to weight the limits of applicability of this tool.

9.3 Technical recommendations

There follow some ideas of development or re-development which, have not been put in place due to time limitation. The development of numerical tools has taken a large part of this PhD. While working, some tools contains bugs, and/or certainly have room for improvement.

9.3.1 ICCR-Macropore

While fully functional, the tool, counting ∼10,600 lines of code distributed across 10 files, contains unfixed bugs which have not been solved yet. Although they do not prevent the software from working properly, at terms they should be investigated. One major bug arises when a specific type of slice is scanned, which prevent the ICCR-Macropore from continuing the analysis. Troubleshooting has been done, unfortunately, the issue has not been isolated yet. A temporary solution consists in erasing the non-conforming slice(s), once spotted, as well as removing their names from the name file before re-running the ICCR-Macropore.

One reason for the development of the Slice-Picker (cf. section 3.3.4) concerned a misconception of the ICCR-Macropore which led to a memory drain. This memory leak is observed when several hundreds of slices are scanned by the tool, which translates to a saturation of the RAM, leading to a complete freeze of the computer. It is recommended to scan no more than 200 slices for a 8 Mo RAM computer. Few investigations have been done in order to avoid this memory build-up, and this issue has been partially resolved through a better use of C++ pointers. One evolution of the software would concern a complete re-working of the structures and functions. One repercussion of this redesign would be to integrate the Slice-Picker as a sub-function of the ICCR-Macropore.

The ICCR-Macropore is able to interpret SVG format files. As described in section 3.3.3, a possible evolution of the software implies the introduction of several input formats, such as .eps, .ai, and .pdf.

One last improvement focuses on the output files dimensions. Most of the outputs are either in pixel or cm (or related sub-units). It would be interesting to let the user decide what format the output results should be converted in.

9.3.2 LabVIEW controller

Two main improvements can be done on the LabVIEW controller.

The first main change concerns a major flaw spotted during a pressure sensor calibration. The differential pressure transducer needs to be calibrated every year. A factory reset costing approximately $350 plus shipping fees, it remains easier and less time-consuming to do a in-house re-calibration using the LabVIEW controller and one ISCO pump as a delivery pump: one side of the transducer is set to atmospheric pressure while the desired pressure is applied on the other side by the ISCO pump. A flaw in the code provokes a sudden and massive surge in pressure from the ISCO pump, reaching a critical limit of 70 MPa, endangering the user and the hardware. Several membranes have been damaged before understanding part of the problem: while still unclear, an involuntary command seems to be sent to the ISCO pump. This command tells the ISCO to reach an infinite pressure. This command override can only be provoked if a mathematically impossible operation is realized. The main issue relates to the reading of the confining pressure sensor during the calibration of the transducer. Usually, no rock is put in place during any calibration of the equipment, therefore, no confining pressure has to be applied. Nevertheless, the confining pressure sensor reads a pressure, which when 0 Pa of pressure is applied, fluctuates around zero. If, at any point, a function catches a perfect 0 Pa of confining pressure, this function might behave unexpectedly and overrides every possible factory and software securities. While I tried reaching and solving the bug, the function triggering that behaviour has not been isolated yet. Solving the bug remains hard due to the non-repeatability of the error without severely damaging the hardware. A way to accommodate this bug is to send the transducer for re-calibration to Validyne, or to avoid using the labVIEW controller

during this calibration phase. Options include using the ISCO pump manually while the output voltage of the transducer can be controlled with a voltmeter.

A second improvement relates to the pore pressure setting. An effective stress control function can be added, based on the reading of the confining pressure sensor. Indeed, due to changes in atmospheric pressure and room temperature, the confining stress fluctuates over time (up to ∼2.5 MPa). Overnight-break phases would also cause the confining pressure to drop slightly. Confining pressure readjustments were done manually throughout each experimental flooding. One way to fill this gap would be to create a function that reads the confining pressure sensor value and automatically adapts the pore pressure in order to create the desired effective stress, and in the case of this project, a low or a high one.

9.3.3 Data treatment improvement

Several changes can be done to improve or complete the data treatment:

- The PV_{rate} across all study is kept constant and is based on the pre-experimental triple weighing of each sample. Keeping that value constant implies few assumptions, such as no dissolution, or a linear increase of the dissolution during flooding. While widely assumed amongst researcher, this constant PV_{rate} can be slightly improved by using the relationship between porosity increase and Ca-Mg dissolution (Luquot and Gouze, 2009).

- The above also implies to redefine the fluid sampling method. During this project, the rate of fluid sampling was based on the time, while a sampling rate based on the amount of pore volume injected seems to be a more reliable method. Here again, this implies the definition of a syn-flooding constant PV_{rate} due to the limitation of the experimental set-up preventing the user from having syn-flooding porosity evolution.

Appendix A

Formation water composition

Compound	Ion	Quantity (g/L)
NaCl	Na	65.76
	Cl	101.4
$CaCl_2$	Ca	13.53
	Cl	23.95
$SrCl_2$	Sr	2.64
	Cl	2.13
$MgCl_2$	Mg	1.84
	Cl	5.38
KCl	K	1.2
	Cl	1.08
KBr	K	0.35
	Br	0.71

Table A.1: Processed formation water chemical composition.

Appendix B

Petrological analysis of the Indiana formation

Laminations can be found within the Indiana limestone. They are alternating carbonate sand-sized grains and micrite layers. Their sizes range from 2 mm to 20-40 cm. Units also display an alternation of bioturbated and unbioturbated rock which refers to a dynamic system following the seasonal restriction.

Baxter (1960) has studied the fossils present in the outcrops of Illinois (USA). Most of the carbonate part is composed of several types of fossil:

- Crinoids are marine animals belonging to the Echinoderma phylum. They can be found nowadays at shallow levels (Zmarzly, 1985) as well as greater depth (Oji et al., 2009). They live attached to the seafloor during their adult life. Within the Indiana limestone, plates of crinoid occur as crystallized units. Most fossils are in broken pieces and have been fragmented and abraded. The crinoid fossils are mildly sorted. Most fragments are 0.2 to 1.5 mm large.

- Bryozoan are a common constituent of limestones. They are small aquatic organisms (less than 1 mm) living in colonies of interconnected individuals.

Some encrust the surface of rocks or shells, while others form tree-like branching colonies. Indiana limestone's ones belong to Fenestella, Polypora and Sulcoretipora. They display a better preservation than the crinoids. The size of some fragments can be as large as several millimetres, and are for the most part no longer than 0.1 mm.

- Endothyra is an extinct organism which belonged to the still-existing subphylum Foraminifera. They were marine single-celled protists living in a shell (test) which can be found unbroken amongst the stratigraphy. They are usually found in the upper part of the formation. Sizes range from 0.2 to 0.5 mm.

- Oolites are not stricto-sensus fossil of organism, but consist of single or multi-layered deposits of calcite surrounding a nucleus. They are common in beds presenting foraminifera. Noticeably, single layered oolites generally display a large Foraminifera or a fossil debris (i.e. crinoid fragment) as a nucleus. Smaller fragmented fossils (bryozoan fragments, crinoid parts, small foraminifera) might be found as nuclei for multi layered oolites.

The carbonate cement of the formation is a crystalline calcite which envelop the fossil debris (Baxter, 1960). The remaining, non-carbonate part, of the formation is made of:

- Chert: stiff silica usually white and present in globules. They are usually sand-sized.

- Quartz: appears in the form of replacement material in fossils, or as sand grains (very localized in the Kidd sub-member).

- Silt: most prominent residue, and is uniformly distributed over the entire formation.

- Clay: material finer than 4 microns, represents a minor constituent of the formation.

Appendix C

Indiana formation stratigraphic presentation

Baxter (1960) split the Indiana formation into four sub-members displaying different depositional dynamics and fossil contents. Figure C.1 shows the stratigraphic nomenclature that contains the Indiana limestone (referred to as Salem formation). Within the Salem formation, and by decreasing order of age, the following sequences can be found:

- Kidd: Grey to Brown limestone composed of Crinoid columnals and bryozoan parts. The unit shows a variable $CaCO_3$ content with inserts of clay in some layers followed by very pure calcite units. Most of the unit is made of calcarenite (mostly pure sand-sized carbonate rock).

- Fults: period of unstable conditions. Displays a low-clay calcite (calcarenite) alternatively deposited with high-clay content calcite (calcilulite). The clay and was probably provided by a nearby land. This period is associated with variations in the velocity of currents in a shallow bay.

- Chaflin: begins with calcilulite, followed by an extensive (locally oolitique) biocalcarenite. Through the end of this phase the calcarenite deposition

gradually stopped leaving place to a calcilulite. The bed locally contains plant fossils and algal limestone.

- Rocher: mostly made of calcarenitic limestone composed of Endothyra, usually fragmented and layered to form oolites.

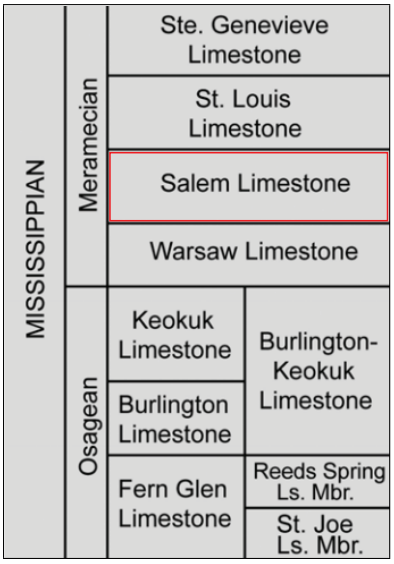

Figure C.1: Detailed Mississippian stratigraphic nomenclature. The Salem formation correspond to the Indiana limestones .After: Ramaker et al. (2015).

Appendix D

Travertine shrub morpho-types

While travertines can display different facies depending on the dynamics of the system (figures D.1 and D.2 - Claes et al. (2017)), the environmental instabilities that control the rapid changes in hydrodynamic conditions, with episodes of stagnancy or evaporation (Guo and Riding, 1994), eventually influence the complex shrub morpho-types (Soete et al., 2015; Rezende and Pope, 2015; Erthal et al., 2017):

- Microbialites and stromatolites form at shallow to moderate water level.
- Sallow waters level and sub-aerial exposure:
  - Dendriform shrubs correspond to moderate to low energy water flows:
    - Narrow Dendriform: fast flow rates which also reduces/stops the microbial activities. They are characterized by a pronounced vertical stem. The branches are distributed in tight packing fashion with elongated and straight framework of pore.
    - Wide Dendriform: intermediate flow rates. The branches are arranged in a broad and open pack spreading away from the stem ('open hand' structure). The pore framework is more patchy, displaying less elongated pore shape.

    - Filli Dendriform: slow flow rates. The branches are thin and elongated. The porosity framework is elongated as well.

  - Arborescent-Arbustiform-Pustular shrubs correspond to very slow to steady flows. These facies are characterised by very thin or absent branches. The pustular like shrubs have been described as pisoid by Guo and Riding (1998).

- Others: travertines present a variety of other facies that display megapores, or vugs. The main ones encountered within both Pre-salt and Saturia travertines are (Chafetz, 2013):

  - Raft: crust or ice. They form on the surface highly calcite saturated waters.

  - Foam: could be exclusive to travertine deposits. They are vertically oriented cylindrical tubes that form when a forced stream of rising gas pushes and drags upwards microbial mats into vertical orientation.

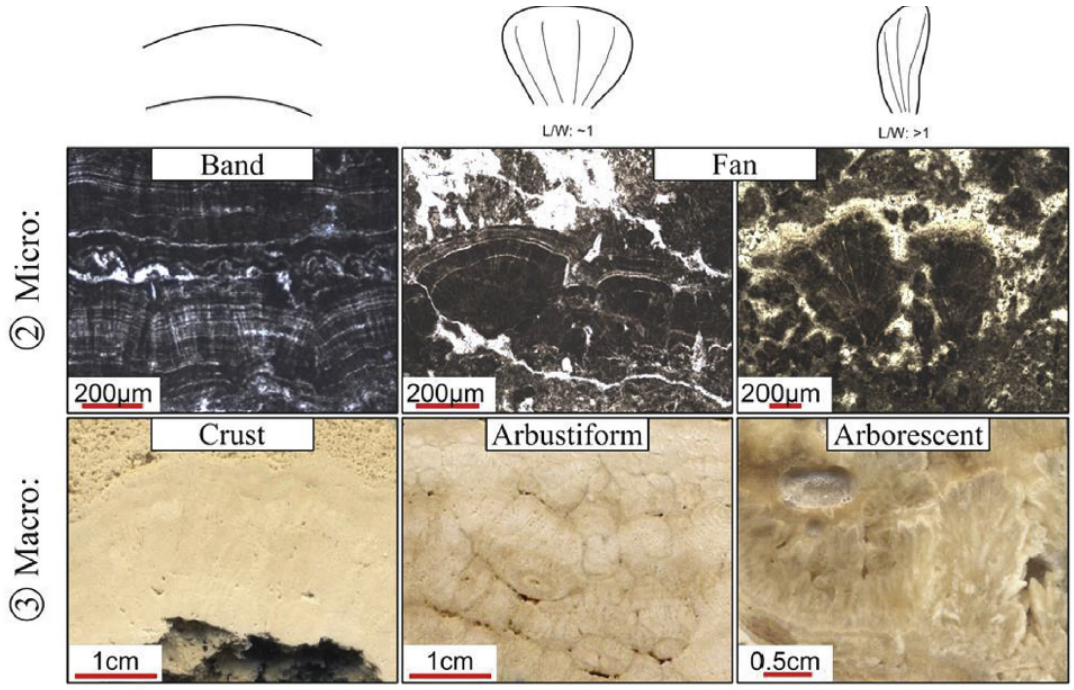

Figure D.1: 1/2 - Classification of shrubs' morphology (micro and macro scale). Shrub samples from Denizli, Turkey. After Claes et al. (2017).

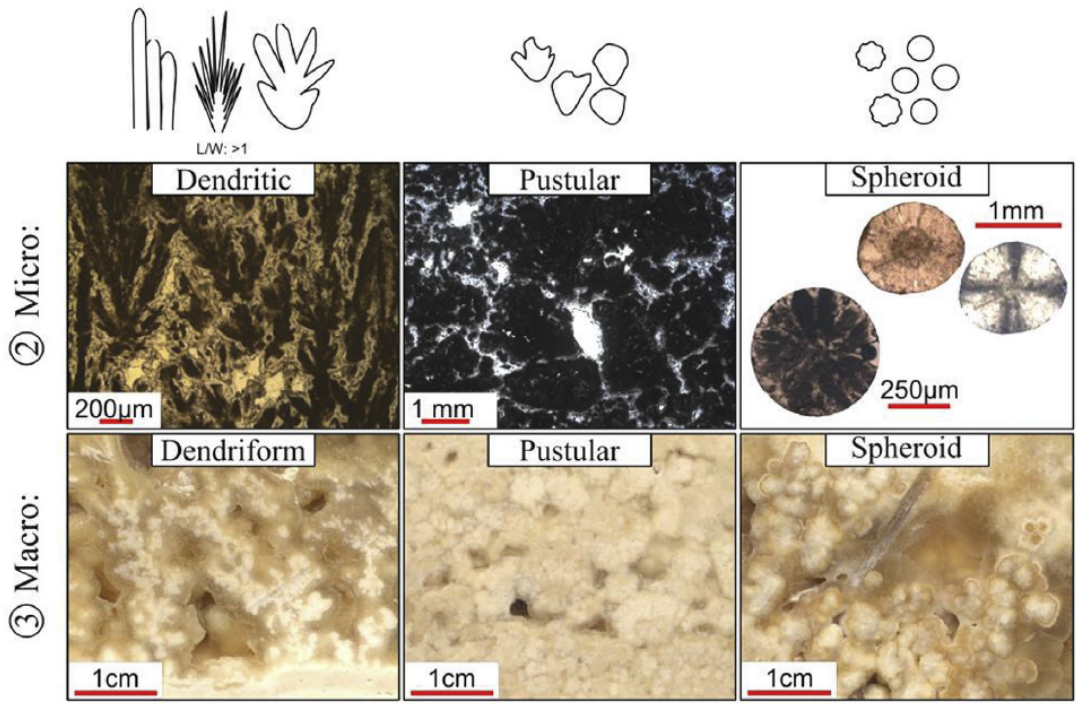

Figure D.2: 2/2 - Classification of shrubs' morphology (micro and macro scale). Shrub samples from Denizli, Turkey. After Claes et al. (2017).

Appendix E

List variables for the CNT file (ICCR-Macropore)

The main variables of a CNT file are described below, and should be set according to the level of interpretation desired by the user:

- Determine porosity distribution 1: Boolean (0/1). Indicates a porosity distribution is needed.
- Determine porosity distribution 2: Double (mm). Indicates the step size of infilling used to determine the porosity distribution.
- Bezier point density: Double (-). Indicates the initial density to interpret svg curves with. This is then adjusted to the minimum point spacing below.
- Min area tolerance: Double (svg file size^2). The pores smaller than this value are ignored.
- Max area tolerance: Double (svg file size^2). The pores larger than this value are be ignored.
- Box tolerance: Double (%). Defines an extra box around the generated mesh with $\triangle x$ and $\triangle y$ as a function of the overall size of the input image.

- Mesh quality min acute angle: Double (degree). Value of the sharpest angle allowed of the pore contour.

- Mesh density: Double (mm by default). This value defines the size of the element within the generated mesh.

- Mesh spacing: Double (mm). Minimum point spacing along voids, this overrides the Mesh density.

- Min void width: Double (mm). This variable is a beta test and should be used carefully. The variable sets an acceptable minimum void width within a pore.

- Min polygon spacing: Double (mm). If macropores (referred to as polygons) are too close, the smallest one is ignored. Not yet functioning properly, and is used as a check for no overlap between surfaces.

- Process: Boolean (0/1). Switch between original coordinate system and no processing for debug mode.

- Angle check: Boolean (0/1). Switch for angle check. Set to true by default.

- Distance check: Boolean (0/1). Switch for distance check. Set to true by default.

- Void space correct: Boolean (0/1). Switch for void space correction. This variable can be used if the distance check is in use and adjusts the void space minimally.

- Cross over: Boolean (0/1). Switch for void space correction.

- Output OGS gli file: Boolean (0/1). This variable allows the ICCR-Macropore to output .gli files (used for OGS 2D modelling).

- Coefficient for area of influence for connections: Double (-). The area of the ellipse shape of a pore is multiplied by this coefficient in order to generate a two dimensional area of influence of a pore.

Appendix F

ICCR-Macropore and Slice Picker (executables)

Link for download:

https://drive.google.com/open?id=1f0SMfY_Op2-BT4cYql3RuZwX2sMH4ib4

Appendix G

SVG Converter: workflow

The steps below summarize the workflow from 3D volumes of µCT image stacks to SVG files:

- Under Avizo® 9: the 3D rendering of a core sample is saved under the 2D TIFF format.
- The stack of 2D TIFF is opened with Fiji (Schindelin et al., 2012). For our need we should reslice the 3D volume in the desired direction. The resliced stack of images is saved under the PNG format.
- The stack of PNG images is then loaded into the SVG Converter. The user selects the amount of thresholding, smoothing, and detail level to apply during the processing of the PNG as well as the resizing parameters (original width and length of the slice). By default those parameters are respectively set to 70, 10, and 100%. A direction of slicing can be selected, which will rename the output SVG file accordingly (for example, if 'Z' is selected in the drop-down list, each image will be named 'Zxxx', with 'xxx' being the slice number).
- By clicking 'Convert', the user automatically converts the stack of PNG to a stack of SVG file. The SVG converted will also create a text file of input names.

Appendix H

LabVIEW programming architecture

This appendix describes the general working pattern of the software. Each function written and used throughout an execution are not described in this thesis. The code is divided in five loops:

1. The Command loop is the first loop of the system (figure H.1). It is designed following the Event-Driven and Producer-Consumer architectures. The loop catches an event (eg. mouse click), and translates the button clicked into an order which is read by the second loop. This order is transmitted under the form of a data cluster. Figure H.1 shows the loop 1. Under a): the LabVIEW enqueuing functions. They gather the user's order(s) and enqueue them before sending the data cluster to the loop 2 (purple arrow); b): drop-down list of pre-defined events (eight in total). Event 0 (as displayed on figure H.1) represents a click on the 'ISCO run' button (which initiate the back-pressuring of the rig). Under c): the actions to be triggered, in this case the creation of a data cluster. Once the user clicks a button, the event case creates a data packet containing a simple string order ('ISCO RUN' in this case), with a Boolean (set to 'false' in case of

user event detected). The string command and the Boolean are further used by the loop 2. This loop iterates once at every user action.

2. The Sampling loop is the second loop of the system. It is designed as a slave of loop 1, and a master for loop 3, 4, and 5. This loop is also a consumer from loop 1, and a producer of data from equipment reading. According to the State-Machine architecture, this loop would represent the 'action' case, that comes after a user 'event' (loop 1). Loop 2 iterates at a frequency of 2 cycles per second. Figure H.2 shows a simplified version of the design of the loop. The red area (top) represents the equipment inputs: three equipment, associated with three data queues. The data queues send the readings of the equipment towards the loops 3, 4, and 5 for further display and logging. The State-Machine logic of this section is represented by two 'if' structures (b). The larger structure is set to 'true' by default, which represents a non-intervention of the user. In this case the loop performs regular readings of the equipment before queuing the data and sending them towards the down loops (3, 4, and 5). If a user-event is caught by the loop 1, the data cluster is received by the loop 2 (a), and sets the structure b1 to false, while the second 'if' structure (b2) catches the action associated with the user event (in the case of the action 'ISCO RUN'). The two functions displayed under c) are then temporarily wired to the the data-flow (in this case: switching on the ISCO pump and sending a message to the user interface). The three wires sent towards the three down loops contain data clusters whose formats depend on the targeted loop:

   - Loop 3 receives a complex data cluster containing all important variables to be displayed on the GUI.
   - Loop 4 receives a data cluster made of two strings.
   - Loop 5 receives a data cluster containing all available variables for logging.

3. The Display loop is the third loop of the system. No frequency is imposed to this loop which iterates as fast as it can. The frequency should, by definition, be imposed and restricted by its master loop (loop 2). Figure H.3 presents the structure of the loop. While dense, it is, with loop 4, the simplest structure of the software, as little to no logical operation is done here. The data clusters are received from loop 2 and dequeued before being dispatched towards their LabVIEW GUI structures (a). Simple functions are called within this loop (b: on-the-fly permeability calculation, and volume of fluid injected). These functions have been put in this loop as a way to unload loop 2 from these non-logged calculations.

4. The Pumps Display loop is the fourth structure on the system (figure H.4). It follows the same programming logic as the loop 3 while it focuses on displaying state messages sent by the back-pressure pump and the injection pump. The data cluster is made of two strings (a), which are displayed in a State-Machine structure-like (b).

5. The Data recording loop is the fifth and final structure of the software (figure H.5). It receives the denser data cluster as it is composed by all possible variables that can be transmitted from the equipment. A text file is created with a header naming all the variables (a), while the second function (b) performs an averaging of the data received before saving it in a text file (1 min of log = 120 logs averaged). Text files have been preferred over Excel files as a power outrage would result in losing all data, while a text file can be saved and updated as the experiment runs. We have opted for an averaging of our data for two reasons:

    - The large amount of data received from loop 2 (120 logs per minute) may crash the computer by creating an extremely large text file. Each minute of log is saved in cache memory, before averaging the variables.
    - A way to calculate the pore volume rate per minute requires to known

the volume injected per minute of flooding (cf. section 3.5 - equation 3.7). The injection pump outputs a rate in cm^3/min, which can eventually be simplified to cm^3 per minute logged.

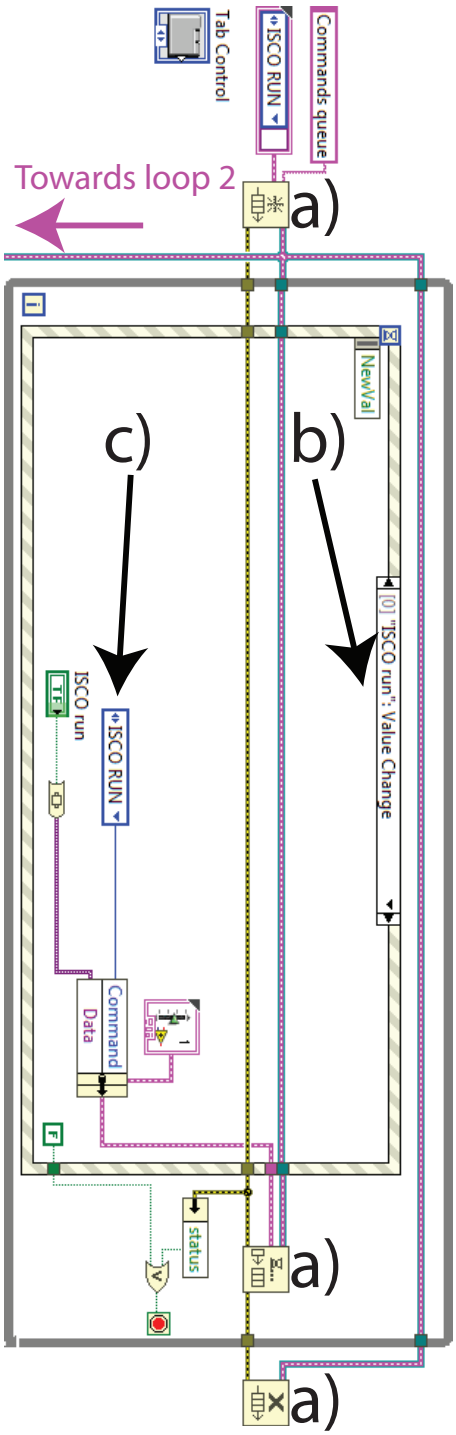

Figure H.1: Loop 1: Event-Driven and producer loop. The user's physical action are caught by this structure, before sending an order to the loop 2. a) LabVIEW queuing functions; b) pre-defined user events; c) data-cluster generation.

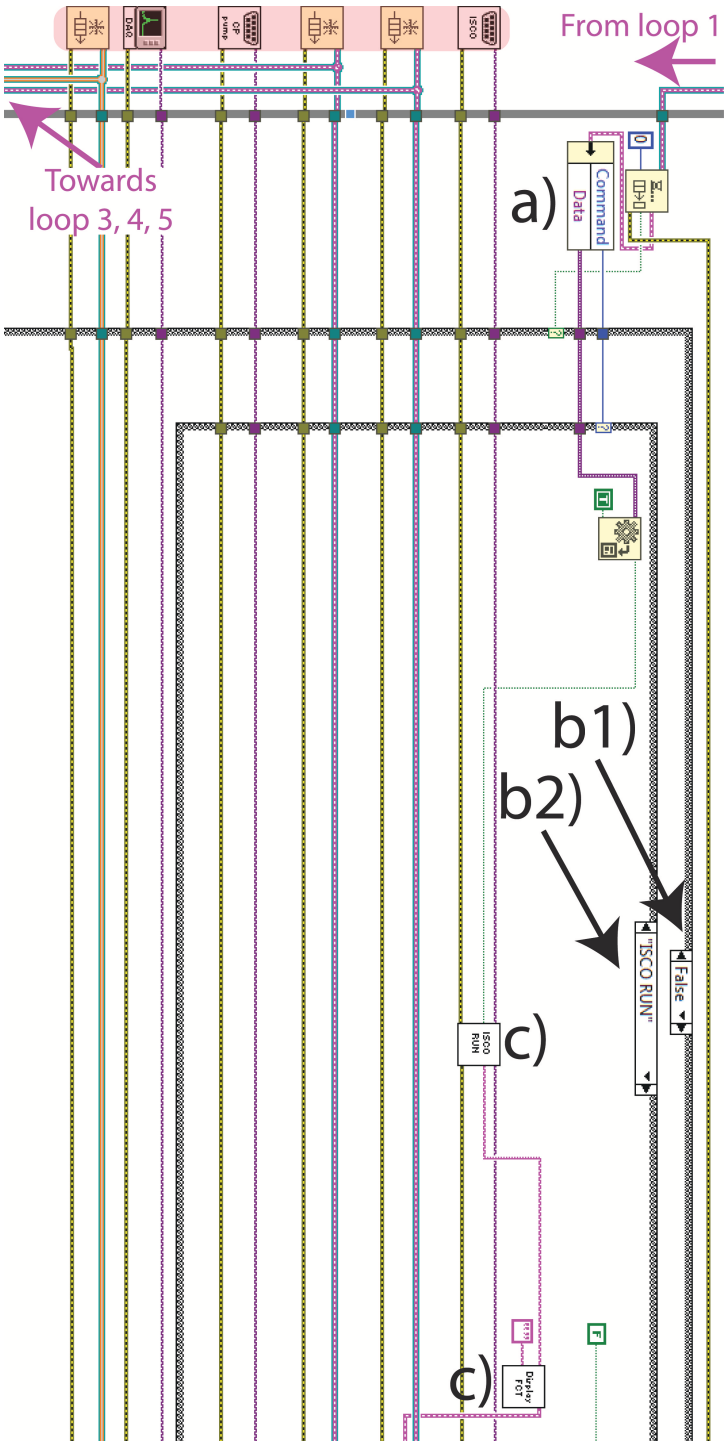

Figure H.2: Loop 2: consumer of loop 1 and producer of down loops. This structure represents a State-Machine whose actions are triggered according to the data-clusters received from the loop 1. a) data-cluster dequeued and split in two variables (a Boolean and a string command); b) 'if' structures; c) tailored functions. Red area: equipment and enqueue initialisation.

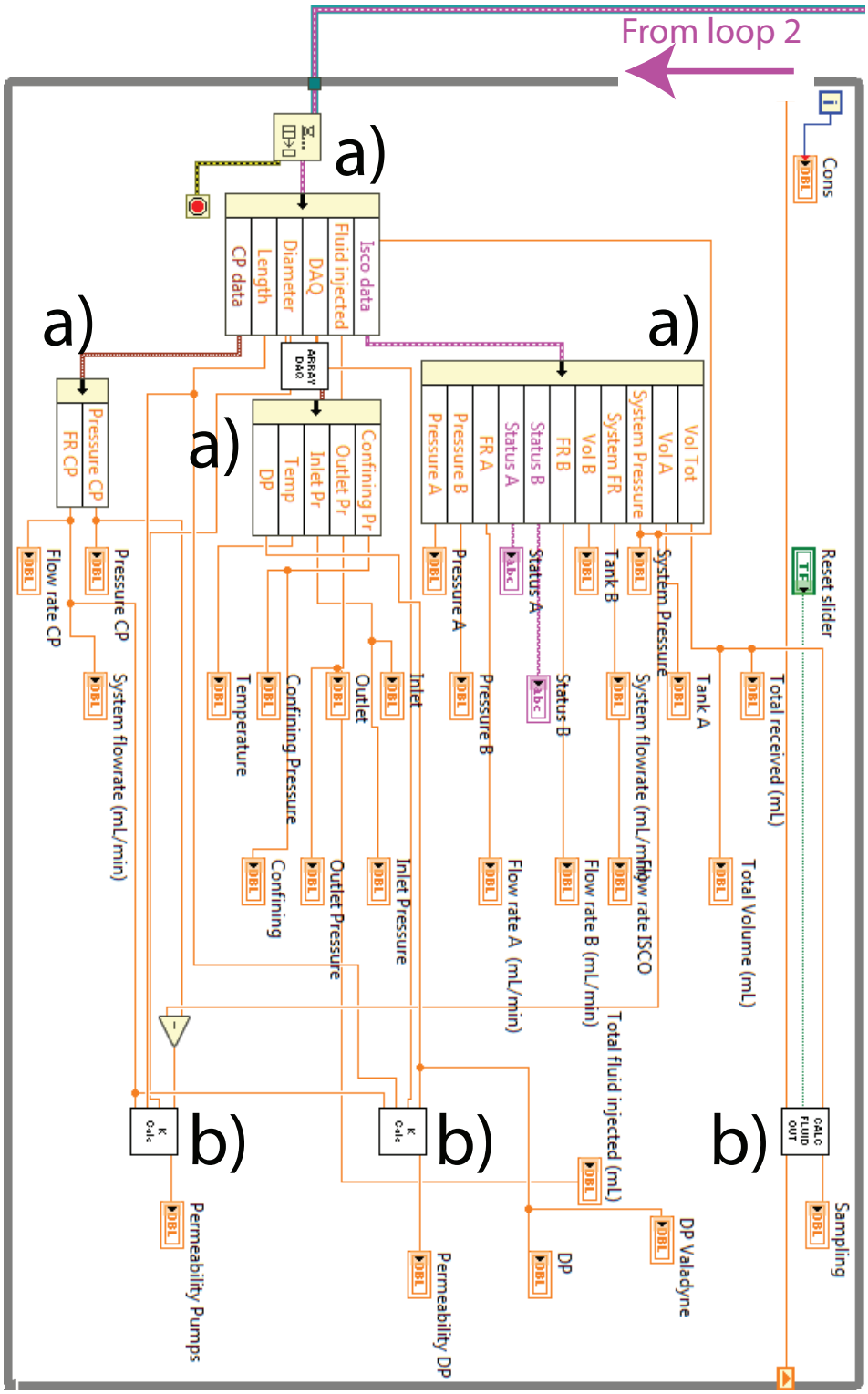

Figure H.3: Loop 3: first of the two display loops. This loop consumes the data generated by the loop 2 before displaying them in GUI structures. a) data-cluster dequeued and split into variables; b) tailored functions.

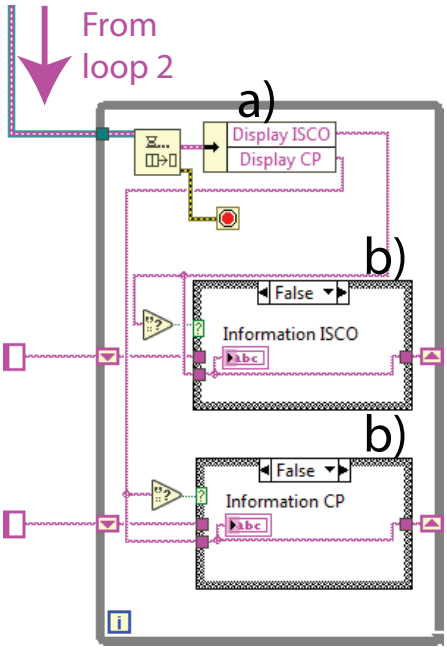

Figure H.4: Loop 4: second of the two display loops. This loop consumes the data generated by the loop 2 before displaying them in GUI structures. a) data-cluster dequeued and split into variables; b) 'if' structures.

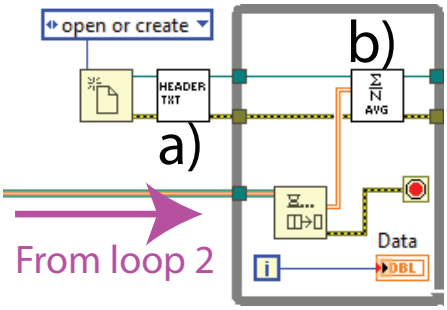

Figure H.5: Loop 5: the recording loop consumes the data generated by the loop 2, and save them in a text file. a) creation of the text file; b) tailored data averaging function.

Appendix I

LabVIEW Graphical User Interface (GUI)

The GUI is split into two main panels: the control panel (figure I.1), and the reading panel (figure I.2). The user's actions are caught by the control panel, where tasks can be set (eg. running a pump, priming a pump, setting a minimum allowed line pressure), and the most important variables are displayed (eg. line pressure, injection rate, volume of fluid within an ISCO tank). The reading panel displays secondary (i.e. control) variables (eg. permeability evolution, temperature of the system), and does not allow the user to communicate with the equipment.

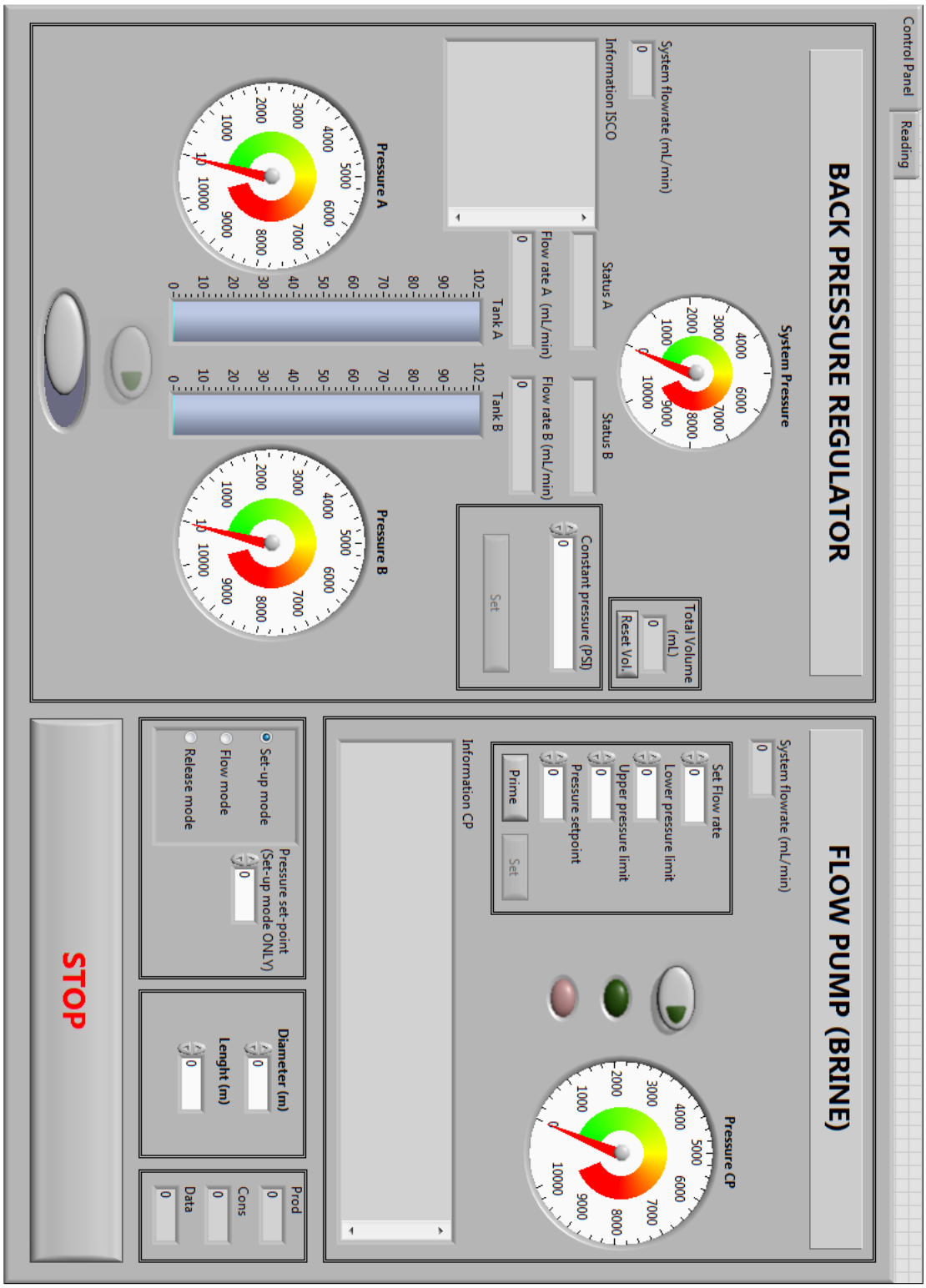

Figure I.1: Control panel of the tailored LabVIEW software.

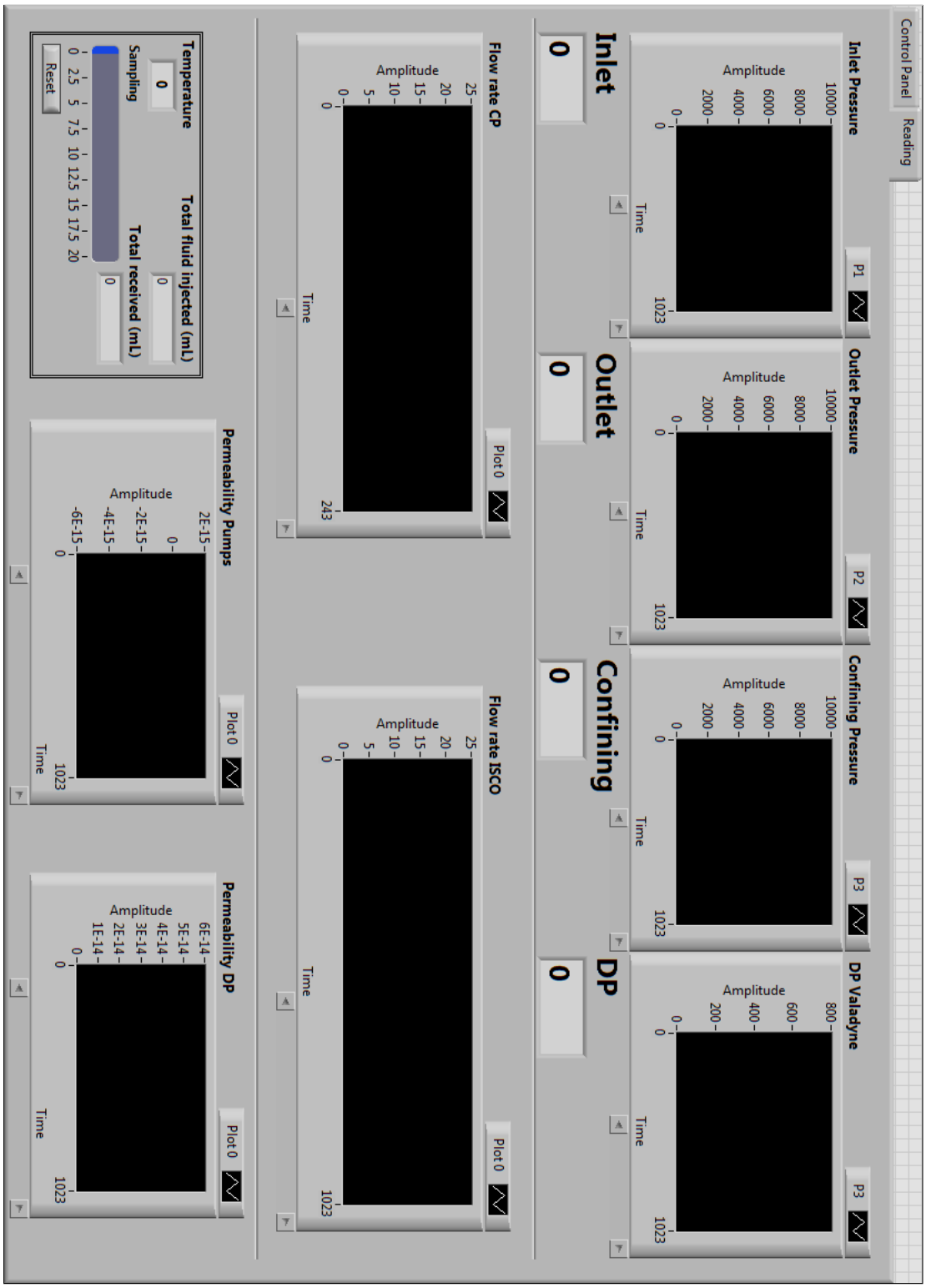

Figure I.2: Reading panel of the tailored LabVIEW software.

Appendix J

Experimental observation of wormhole formation at variable effective stress and injection rate on carbonate samples

Link for pdf download:

https://drive.google.com/drive/folders/1-EaiFj_zWrwsQL0FHLsbBoVspaa_R54g?usp=sharing

Appendix K

Prediction of wormhole formation in heterogeneous rocks using μCT imaging and machine learning

Link for pdf download:

https://drive.google.com/open?id=1S-SMweBKMcIqnl3b1G0xjkT0x3uTqPHK

Appendix L

Importance hydro-mechanical coupling for fluid flow driven wormhole formation in carbonate rocks

Link for pdf download:

https://drive.google.com/open?id=1zP4-w8GaWRSF9yI9OMeMtl6OidWMsAzo

References

Al Adasani A, Bai B. Analysis of eor projects and updated screening criteria. Journal of Petroleum Science and Engineering 2011;79(1-2):10–24.

Al-Harthy S, Dennis J, Jing X, Marsden J, et al. Petrophysical properties under true-triaxial stress for hydrocarbon recovery prediction. In: SPE Permian Basin Oil and Gas Recovery Conference. Society of Petroleum Engineers; 1998a. .

Al-Harthy S, Dennis J, Jing X, Marsden J, et al. Petrophysical properties under true-triaxial stress for hydrocarbon recovery prediction. In: SPE Permian Basin Oil and Gas Recovery Conference. Society of Petroleum Engineers; 1998b. .

Alabi G, Kasten R, Chitale V, Yadavalli S, Piccoli L, et al. The value of petrophysical measurements across multiple scales–a lacustrine carbonate example from campos basin, brazil. In: SPWLA 55th Annual Logging Symposium. Society of Petrophysicists and Well-Log Analysts; 2014. .

Alexeev A, Shapiro A, Thomsen K. Modeling of dissolution effects on waterflooding. Transport in Porous Media 2015;106(3):545–62.

Alves IAS, Aragao AFL, Bastos BL, Falcao JL, Fartes E, et al. Pre-salt santos basin c: well construction learning curve acceleration. In: Offshore Technology Conference. Offshore Technology Conference; 2009. .

Aman M, Espinoza DN, Ilgen AG, Major JR, Eichhubl P, Dewers TA. Co2-induced chemo-mechanical alteration in reservoir rocks assessed via batch reaction experiments and scratch testing. Greenhouse Gases: Science and Technology 2018;8(1):133–49.

Baechle GT, Weger R, Eberli GP, Massaferro JL. The role of macroporosity and microporosity in constraining uncertainties and in relating velocity to permeability in carbonate rocks. In: SEG Technical Program Expanded Abstracts 2004. Society of Exploration Geophysicists; 2004. p. 1662–5.

Balouga J. Unconventional oils: The 21st century rescuer? International Association for Energy Economics 4th Quarter Review 2012;:27–31.

Barilaro F, De Bernardo A, Verwer K, Lapponi F, Della Porta G. Pore structure, porosity and permeability of continental carbonates: A case study of pleistocene travertine (southern tuscany, italy). In: AAPG HEDBERG Conference Microbial carbonate Reservoir Characterization. 2012. .

Barri A, Mahmoud M, Elkatatny S. Evaluation of rock mechanical properties alteration during matrix stimulation with chelating agents. Journal of Energy Resources Technology 2016;138(3):032907.

Basheer IA, Hajmeer M. Artificial neural networks: fundamentals, computing, design, and application. Journal of microbiological methods 2000;43(1):3–31.

Baxter JW. Salem limestone in southwestern illinois. Circular no 284 1960;.

Bazin B, Roque C, Bouteca M, et al. A laboratory evaluation of acid propagation in relation to acid fracturing: Results and interpretation. In: SPE European Formation Damage Conference. Society of Petroleum Engineers; Society of Petroleum Engineers; 1995. .

Bear J. Dynamics of fluids in porous media. dover, new york. Dynamics of fluids in porous media Dover, New York 1972;.

Beasley C, Fiduk J, Bize E, Boyd A, Frydman M, Zerilli A, Dribus J, Moreira J, Pinto AC. Brazil's presalt play. Oilfield Review 2010;22(3):28–37.

Beglinger SE, Doust H, Cloetingh S. Relating petroleum system and play development to basin evolution: West african south atlantic basins. Marine and Petroleum Geology 2012;30(1):1–25.

Bekri S, Thovert J, Adler P. Dissolution of porous media. Chemical Engineering Science 1995;50(17):2765–91.

Bemer E, Lombard J. From injectivity to integrity studies of co2 geological storage-chemical alteration effects on carbonates petrophysical and geomechanical properties. Oil & Gas Science and Technology–Revue de l'Institut Français du Pétrole 2010;65(3):445–59.

Bernabe Y, Brace W, Evans B. From injectivity to integrity studies of co2 geological storage-chemical alteration effects on carbonates petrophysical and geomechanical properties. Oil & Gas Science and Technology–Revue de l'Institut Français du Pétrole 2010;65(3):445–9.

Berryman JG. Effective stress for transport properties of inhomogeneous porous rock. Journal of Geophysical Research: Solid Earth 1992;97(B12):17409–24.

Biot MA. Theory of elasticity and consolidation for a porous anisotropic solid. Journal of applied physics 1955;26(2):182–5.

Birch F. The velocity of compressional waves in rocks to 10 kilobars: 1. Journal of Geophysical Research 1960;65(4):1083–102.

Borghi L, Corbett PW, et al. Lacustrine carbonates-for the purpose of reservoir characterization are they different? In: OTC Brasil. Offshore Technology Conference; 2013. .

Bouchelaghem F. A numerical and analytical study on calcite dissolution and gypsum precipitation. Applied Mathematical Modelling 2010;34(2):467–80.

Boyd A, Souza A, Carneiro G, Machado V, Trevizan W, Santos B, Netto P, Bagueira R, Polinski R, Bertolini A, et al. Presalt carbonate evaluation for santos basin, offshore brazil. Petrophysics 2015;56(06):577–91.

Brondolo F, Fraser-Harris A, Edlmann K, Butler I, McDermott C. Experimental observation of channel propagation and dissolution forecasting on calcite samples at different effective pressure. In: 80th EAGE Conference and Exhibition 2018. 2018a. .

Brondolo F, McDermott C, Edlmann K, Fraser-Harris A. Experimental observation of channel propagation at variable effective stresses on carbonate samples. In: SEG Technical Program Expanded Abstracts 2018. Society of Exploration Geophysicists; 2018b. p. 3623–7.

Brown MA, Archer AW, Kvale EP. Neap-spring tidal cyclicity in laminated carbonate channel-fill deposits and its implications; salem limestone (mississippian), south-central indiana, usa. Journal of Sedimentary Research 1990;60(1):152–9.

Bruggeman VD. Berechnung verschiedener physikalischer konstanten von heterogenen substanzen. i. dielektrizitätskonstanten und leitfähigkeiten der mischkörper aus isotropen substanzen. Annalen der physik 1935;416(7):636–64.

Buijse M, et al. Mechanisms of wormholing in carbonate acidizing. In: International Symposium on Oilfield Chemistry. Society of Petroleum Engineers; Society of Petroleum Engineers; 1997. .

Carminatti M, Dias J, Wolff B, et al. From turbidites to carbonates: breaking paradigms in deep waters. In: Offshore Technology Conference. Offshore Technology Conference; 2009. .

Carminatti M, Wolff B, Gamboa L, et al. New exploratory frontiers in brazil. In: 19th World Petroleum Congress. World Petroleum Congress; 2008. .

Chafetz HS. Porosity in bacterially induced carbonates: Focus on microporesmicroporosity after bacterial decay. AAPG bulletin 2013;97(11):2103–11.

Chafetz HS, Folk RL. Travertines; depositional morphology and the bacterially constructed constituents. Journal of Sedimentary Research 1984;54(1):289–316.

Chafetz HS, Guidry SA. Bacterial shrubs, crystal shrubs, and ray-crystal shrubs: bacterial vs. abiotic precipitation. Sedimentary Geology 1999;126(1-4):57–74.

Chauhan S, Rühaak W, Khan F, Enzmann F, Mielke P, Kersten M, Sass I. Processing of rock core microtomography images: Using seven different machine learning algorithms. Computers & Geosciences 2016;86:120–8.

Chen Y, Fambrough J, Bartko K, Li Y, Montgomery C, Ortoleva P, et al. Reaction-transport simulation of matrix acidizing and optimal acidizing strategies. In: International Symposium on Oilfield Chemistry. Society of Petroleum Engineers; Society of Petroleum Engineers; 1997. .

Chitale VD, Alabi G, Gramin P, Lepley S, Piccoli L, et al. Reservoir characterization challenges due to the multiscale spatial heterogeneity in the presalt carbonate sag formation, north campos basin, brazil. Petrophysics 2015;56(06):552–76.

Choquette PW, Pray LC. Geologic nomenclature and classification of porosity in sedimentary carbonates. AAPG bulletin 1970;54(2):207–50.

Churcher P, French P, Shaw J, Schramm L, et al. Rock properties of berea sandstone, baker dolomite, and indiana limestone. In: SPE International Symposium on Oilfield Chemistry. Society of Petroleum Engineers; Society of Petroleum Engineers; 1991. .

Cilli P, Brondolo F, Butler I, Edlmann K, McDermott C. Location and magnitude of preferential flow path formation in carbonate rocks, forward prediction from pre-experimental ct-scan using machine learning. In: AGU Fall Meeting Abstracts. 2018. .

Claes H, Erthal MM, Soete J, Özkul M, Swennen R. Shrub and pore type classification: Petrography of travertine shrubs from the ballık-belevi area (denizli, sw turkey). Quaternary International 2017;437:147–63.

Cleary MP, Lee SM, Chen IW. Self-consistent techniques for heterogeneous media. Journal of the Engineering Mechanics Division 1980;106(5):861–87.

Compton RG, Pritchard KL, Unwin PR. The dissolution of calcite in acid waters: mass transport versus surface control. Freshwater Biology 1989;22(2):285–8.

Cortina-Januchs M, Quintanilla-Dominguez J, Vega-Corona A, Tarquis A, Andina D. Detection of pore space in ct soil images using artificial neural networks. Biogeosciences 2011;8(2):279–88.

Coto B, Martos C, Peña JL, Rodríguez R, Pastor G. Effects in the solubility of caco3: Experimental study and model description. Fluid Phase Equilibria 2012;324:1–7.

Coyner KB. Effects of stress, pore pressure, and pore fluids on bulk strain, velocity, and permeability in rocks. Ph.D. thesis; Massachusetts Institute of Technology; 1984.

Crawford B, Yale D, et al. Constitutive modeling of deformation and permeability: relationships between critical state and micromechanics. In: SPE/ISRM Rock Mechanics Conference. Society of Petroleum Engineers; 2002. .

García-del Cura MÁ, Benavente D, Martínez-Martínez J, Cueto N. Sedimentary structures and physical properties of travertine and carbonate tufa building stone. Construction and Building Materials 2012;28(1):456–67.

Daccord G, Lenormand R, Lietard O. Chemical dissolution of a porous medium by a reactive fluid—i. model for the "wormholing" phenomenon. Chemical Engineering Science 1993a;48(1):169–78.

Daccord G, Lietard O, Lenormand R. Chemical dissolution of a porous medium by a reactive fluid—ii. convection vs reaction, behavior diagram. Chemical engineering science 1993b;48(1):179–86.

Daccord G, Touboul E, Lenormand R, et al. Carbonate acidizing: toward a quantitative model of the wormholing phenomenon. SPE production engineering 1989;4(01):63–8.

Davies CW, Shedlovsky T. Ion association. Journal of The Electrochemical Society 1964;111(3):85C–6.

Davies J, Davies D, et al. Stress-dependent permeability: characterization and modeling. In: SPE Annual Technical Conference and Exhibition. Society of Petroleum Engineers; 1999. .

De Boever E, Varloteaux C, Nader FH, Foubert A, Békri S, Youssef S, Rosenberg E. Quantification and prediction of the 3d pore network evolution in carbonate reservoir rocks. Oil & Gas Science and Technology–Revue d'IFP Energies nouvelles 2012;67(1):161–78.

De Marsily G. Quantitative hydrogeology. Technical Report; Paris School of Mines, Fontainebleau; 1986.

Den Ouden L, Nasralla R, Guo H, Bruining H, van Kruijsdijk C. Calcite dissolution behaviour during low salinity water flooding in carbonate rock. In: IOR 2015-18th European Symposium on Improved Oil Recovery. 2015. .

Dierick M, Masschaele B, Van Hoorebeke L. Octopus, a fast and user-friendly tomographic reconstruction package developed in labview®. Measurement Science and Technology 2004;15(7):1366.

Edlmann K, Haszeldine S, McDermott C. Experimental investigation into the sealing capability of naturally fractured shale caprocks to supercritical carbon dioxide flow. Environmental earth sciences 2013;70(7):3393–409.

Egermann P, Bekri S, Vizika O, et al. An integrated approach to assess the petrophysical properties of rocks altered by rock-fluid interactions (co2 injection). Petrophysics 2010;51(01).

Egermann P, Bemer E, Zinszner B. An experimental investigation of the rock properties evolution associated to different levels of co2 injection like alteration processes. paper SCA 2006;34:12–6.

Ehrenberg S, Nadeau P. Sandstone vs. carbonate petroleum reservoirs: A global perspective on porosity-depth and porosity-permeability relationships. AAPG bulletin 2005;89(4):435–45.

Emig WH. Travertine deposits of Oklahoma. Oklahoma Geological Survey, 1917.

Endoh K, Suga H. Phase diagram of salt–water system determined by tg-dta. Thermochimica acta 1999;327(1-2):133–7.

Erthal MM, Capezzuoli E, Mancini A, Claes H, Soete J, Swennen R. Shrub morpho-types as indicator for the water flow energy-tivoli travertine case (central italy). Sedimentary geology 2017;347:79–99.

ESA . Impress - supporting education across europe. http://www.spaceflight.esa.int/impress/text/education/Mechanical%20Properties/MoreModuli.html; 2009. [Online accessed 1-March-2019].

ExxonMobil . Impress - supporting education across europe. exxonmobil.com/energyoutlook; 2018. [Online accessed 31-March-2019].

Folk RL. Practical petrographic classification of limestones. AAPG Bulletin 1959;43(1):1–38.

Formigli JM, Pinto C, Carlos A, Almeida AS, et al. Ss: Santos basin's pre-salt reservoirs development: The way ahead. In: Offshore Technology Conference. Offshore Technology Conference; 2009. .

Fouard C, Malandain G, Prohaska S, Westerhoff M. Blockwise processing applied to brain microvascular network study. IEEE transactions on medical imaging 2006;25(10):1319–28.

Fouke BW, Farmer JD, Des Marais DJ, Pratt L, Sturchio NC, Burns PC, Discipulo MK. Depositional facies and aqueous-solid geochemistry of travertine-depositing hot springs (angel terrace, mammoth hot springs, yellowstone national park, usa). Journal of Sedimentary Research 2000;70(3):565–85.

Fourar M, Radilla G, Lenormand R, Moyne C. On the non-linear behavior of a laminar single-phase flow through two and three-dimensional porous media. Advances in Water resources 2004;27(6):669–77.

Fournier F, Leonide P, Biscarrat K, Gallois A, Borgomano J, Foubert A. Elastic properties of microporous cemented grainstones. Geophysics 2011;76(6):E211–26.

Fraser-Harris A, McDermott C, Couples G, Edlmann K, Brondolo F, Lightbody A, Fazio M, Sauter N. Experimental investigation of hydraulic fracturing and stress sensitivity of fracture permeability under changing true-triaxial conditions. Submitted.

Fredd C, Fogler H, et al. Optimum conditions for wormhole formation in carbonate porous media: Influence of transport and reaction. Spe Journal 1999;4(03):196–205.

Fredd C, Fogler HS, et al. Alternative stimulation fluids and their impact on carbonate acidizing. In: SPE Formation Damage Control Symposium. Society of Petroleum Engineers; Society of Petroleum Engineers; 1996. .

Fredd CN, Fogler HS. Influence of transport and reaction on wormhole formation in porous media. AIChE journal 1998;44(9):1933–49.

Freire-Gormaly M, Ellis JS, MacLean HL, Bazylak A. Pore structure characterization of indiana limestone and pink dolomite from pore network reconstructions. Oil & Gas Science and Technology–Revue d'IFP Energies nouvelles 2016;71(3):33.

Frick T, Mostofizadeh B, Economides M, et al. Analysis of radial core experiments for hydrochloric acid interaction with limestones. In: SPE Formation Damage Control Symposium. Society of Petroleum Engineers; Society of Petroleum Engineers; 1994a. .

Frick TP, Kurmayr M, Economides MJ, et al. An improved modeling of fractal patterns in matrix acidizing and their impact on well performance. SPE Production & Facilities 1994b;9(01):61–8.

Garcia-Rios M, Cama J, Luquot L, Soler JM. Interaction between co2-rich sulfate solutions and carbonate reservoir rocks from atmospheric to supercritical co2 conditions: Experiments and modeling. Chemical Geology 2014;383:107–22.

Gardner G, Wyllie M, Droschak D. Hysteresis in the velocity-pressure characteristics of rocks. Geophysics 1965;30(1):111–6.

Garing C, Luquot L, Pezard PA, Gouze P. Electrical and flow properties of highly heterogeneous carbonate rocks. AAPG Bulletin 2014;98(1):49–66.

Geuzaine C, Remacle JF. Gmsh: A 3-d finite element mesh generator with built-in pre-and post-processing facilities. International journal for numerical methods in engineering 2009;79(11):1309–31.

Ghabezloo S, Sulem J, Guédon S, Martineau F. Effective stress law for the permeability of a limestone. International Journal of Rock Mechanics and Mining Sciences 2009;46(2):297–306.

Gobran B, Brigham W, Ramey Jr H, et al. Absolute permeability as a function of confining pressure, pore pressure, and temperature. SPE Formation Evaluation 1987;2(01):77–84.

Golfier F, Zarconne C, Bazin B, Lenormand R, Lasseux D, QUINTARD M. On the ability of a darcy-scale model to capture wormhole formation during the dissolution of a porous medium. Journal of fluid Mechanics 2002;457:213–54.

Gomes PO, Kilsdonk B, Minken J, Grow T, Barragan R. The outer high of the santos basin, southern são paulo plateau, brazil: pre-salt exploration outbreak, paleogeographic setting, and evolution of the syn-rift structures. American Association of Petroleum Geologists Search and Discovery Article 10193 2009;.

Guo L, Riding R. Aragonite laminae in hot water travertine crusts, rapolano terme, italy. Sedimentology 1992;39(6):1067–79.

Guo L, Riding R. Origin and diagenesis of quaternary travertine shrub fabrics, rapolano terme, central italy. Sedimentology 1994;41(3):499–520.

Guo L, Riding R. Hot-spring travertine facies and sequences, late pleistocene, rapolano terme, italy. Sedimentology 1998;45(1):163–80.

Gurevich B. A simple derivation of the effective stress coefficient for seismic velocities in porous rocks. Geophysics 2004;69(2):393–7.

Hall C, Tharakan P, Hallock J, Cleveland C, Jefferson M. Hydrocarbons and the evolution of human culture. Nature 2003;426(6964):318.

Handhal AM. Prediction of reservoir permeability from porosity measurements for the upper sandstone member of zubair formation in super-giant south rumila oil field, southern iraq, using m5p decision tress and adaptive neuro-fuzzy inference system (anfis): a comparative study. Modeling Earth Systems and Environment 2016;2(3):111.

Hart DJ, Wang HF. Laboratory measurements of a complete set of poroelastic moduli for berea sandstone and indiana limestone. Journal of Geophysical Research: Solid Earth 1995;100(B9):17741–51.

Haykin S. Neural networks: a comprehensive foundation. Prentice Hall PTR, 1994.

Heid J, McMahon J, Nielsen R, Yuster S, et al. Study of the permeability of rocks to homogeneous fluids. In: Drilling and production practice. American Petroleum Institute; 1950. .

Hoefner M, Fogler HS. Pore evolution and channel formation during flow and reaction in porous media. AIChE Journal 1988;34(1):45–54.

Huang T, Hill A, Schechter R, et al. Reaction rate and fluid loss: the keys to wormhole initiation and propagation in carbonate acidizing. In: International Symposium on Oilfield Chemistry. Society of Petroleum Engineers; Society of Petroleum Engineers; 1997. .

Huang T, Zhu D, Hil A. Prediction of wormhole population density in carbonate matrix acidizing. In: SPE European Formation Damage Conference. Society of Petroleum Engineers; Society of Petroleum Engineers; 1999. .

Hudson Beale M, Hagan MT, Demuth HB. Impress - supporting education across europe. 2018. URL: https://uk.mathworks.com/help/pdf_doc/deeplearning/nnet_ref.pdf.

Hung K, Hill A, Sepehrnoori K, et al. A mechanistic model of wormhole growth in carbonate matrix acidizing and acid fracturing. Journal of petroleum technology 1989;41(01):59–66.

İşcan A, Kök M, Bagcı A. Estimation of permeability and rock mechanical properties of limestone reservoir rocks under stress conditions by strain gauge. Journal of petroleum science and engineering 2006;53(1-2):13–24.

Isdale J, Spence C, Tudhope J. Physical properties of sea water solutions: viscosity. Desalination 1972;10(4):319–28.

Izgec O, Zhu D, Hill AD. Numerical and experimental investigation of acid wormholing during acidization of vuggy carbonate rocks. Journal of Petroleum Science and Engineering 2010;74(1-2):51–66.

Jaeger JC, Cook NG, Zimmerman R. Fundamentals of rock mechanics. John Wiley & Sons, 2009.

Jones B, Renaut RW. Calcareous spring deposits in continental settings. Developments in Sedimentology 2010;61:177–224.

Jowitt S, Osborn R, Thomas R, Naden J, Gunn A, Herrington R, Nicolaides S. T-type mineralisation—a pseudo-epithermal style of vhms associated gold mineralisation, cyprus. In: Mineral Deposit Research: Meeting the Global Challenge. Springer; 2005. p. 635–7.

Kalia N, Balakotaiah V. Effect of medium heterogeneities on reactive dissolution of carbonates. Chemical Engineering Science 2009;64(2):376–90.

Kamari A, Nikookar M, Sahranavard L, Mohammadi AH. Efficient screening of enhanced oil recovery methods and predictive economic analysis. Neural Computing and Applications 2014;25(3-4):815–24.

Kang Q, Zhang D, Chen S. Simulation of dissolution and precipitation in porous media. Journal of Geophysical Research: Solid Earth 2003;108(B10).

Kele S, Demény A, Siklósy Z, Németh T, Tóth M, Kovács MB. Chemical and stable isotope composition of recent hot-water travertines and associated thermal waters, from egerszalók, hungary: Depositional facies and non-equilibrium fractionation. Sedimentary Geology 2008;211(3-4):53–72.

Kester DR, Duedall IW, Connors DN, Pytkowicz RM. Preparation of artificial seawater 1. Limnology and oceanography 1967;12(1):176–9.

Khan M, Teufel L, et al. The effect of geological and geomechanical parameters on reservoir stress path and its importance in studying permeability anisotropy. SPE Reservoir Evaluation & Engineering 2000;3(05):394–400.

Kitano Y. Geochemistry of calcareous deposits found in hot springs. The Journal of earth sciences, Nagoya University 1963;11(1):68–100.

Kittridge MG. Investigating the influence of mineralogy and pore shape on the velocity of carbonate rocks: Insights from extant global data sets. Interpretation 2015;3(1):SA15–31.

Klinkenberg L, et al. The permeability of porous media to liquids and gases. In: Drilling and production practice. American Petroleum Institute; 1941. .

Kok MV, Iscan AG, Ulker EB. Effect of axial stresses on reservoir rocks. Energy sources 2002;24(10):915–20.

Kolditz O, Bauer S, Bilke L, Bottcher N, Delfs J, Fischer T, Gorke U, Kalbacher T, Kosakowski G, Mcdermott C, Park C, Radu F, Rink K, Shao H, Shao H, Sun F, Sun Y, Singh A, Taron J, Walther M, Wang W, Watanabe N, Wu Y, Xie M, Xu W, Zehner B. Opengeosys: an open-source initiative for numerical simulation of thermo-hydro-mechanical/chemical (thm/c) processes in porous media. Environmental Earth Sciences 2012;67(2):589–99. doi:10.1007/s12665-012-1546-x.

Kumar M, Han Dh. Pore shape effect on elastic properties of carbonate rocks. In: SEG Technical Program Expanded Abstracts 2005. Society of Exploration Geophysicists; 2005. p. 1477–80.

Lager A, Webb KJ, Collins IR, Richmond DM, et al. Losal enhanced oil recovery: Evidence of enhanced oil recovery at the reservoir scale. In: SPE Symposium on Improved Oil Recovery. Society of Petroleum Engineers; 2008. .

Lai P, Moulton K, Krevor S. Pore-scale heterogeneity in the mineral distribution and reactive surface area of porous rocks. Chemical Geology 2015;411:260–73.

Landis EN, Keane DT. X-ray microtomography. Materials characterization 2010;61(12):1305–16.

Lapedes A, Farber R. How neural nets work. In: Proceedings of the 1987 International Conference on Neural Information Processing Systems. Cambridge, MA, USA: MIT Press; NIPS'87; 1987. p. 442–56. URL: http://dl.acm.org/citation.cfm?id=2969644.2969691.

Lasaga AC. Chemical kinetics of water-rock interactions. Journal of geophysical research: solid earth 1984;89(B6):4009–25.

Liu X, Ormond A, Bartko K, Ying L, Ortoleva P. A geochemical reaction-transport simulator for matrix acidizing analysis and design. Journal of Petroleum Science and Engineering 1997;17(1-2):181–96.

Lucia FJ. Rock-fabric/petrophysical classification of carbonate pore space for reservoir characterization. AAPG bulletin 1995;79(9):1275–300.

Luquot L, Gouze P. Experimental determination of porosity and permeability changes induced by injection of co2 into carbonate rocks. Chemical Geology 2009;265(1-2):148–59.

Luquot L, Hebert V, Rodriguez O. Calculating structural and geometrical parameters by laboratory measurements and x-ray microtomography: a comparative study applied to a limestone sample before and after a dissolution experiment. Solid Earth 2016;7(2).

Maheshwari P, Balakotaiah V, et al. Comparison of carbonate hcl acidizing experiments with 3d simulations. SPE Production & Operations 2013;28(04):402–13.

Marques Erthal M. Travertine shrub structures: origin, diagenetic modifications and petrophysical characteristics - tivoli case (central italy). 2018. URL: https://lirias.kuleuven.be/retrieve/487062$$DMarcelleMarques_Thesis.pdf.

Maurer J, Tabeling P, Joseph P, Willaime H. Second-order slip laws in microchannels for helium and nitrogen. Physics of Fluids 2003;15(9):2613–21.

Mavko G, Mukerji T, Dvorkin J. The rock physics handbook: Tools for seismic analysis of porous media. Cambridge university press, 2009.

Mavko G, Nur A. The effect of a percolation threshold in the kozeny-carman relation. Geophysics 1997;62(5):1480–2.

McCraw C, Edlmann K, McDermott C. Experimental investigation of the effect of coupled processes (thermo-hydro-mechanical-chemical) on co2 flow through fractured caprock. In: EGU General Assembly Conference Abstracts. volume 15; 2013. .

McCraw CA. Supercritical co2 flow through fractured low permeability geological media: experimental investigation under varying mechanical and thermal conditions. 2016.

McDuff D, Shuchart CE, Jackson S, Postl D, Brown JS, et al. Understanding wormholes in carbonates: Unprecedented experimental scale and 3-d visualization. In: SPE Annual Technical Conference and Exhibition. Society of Petroleum Engineers; Society of Petroleum Engineers; 2010. .

McGuire P, Chatham J, Paskvan F, Sommer D, Carini F, et al. Low salinity oil recovery: An exciting new eor opportunity for alaska's north slope. In: SPE Western Regional Meeting. Society of Petroleum Engineers; 2005. .

Menke HP, Bijeljic B, Andrew MG, Blunt MJ. Dynamic three-dimensional pore-scale imaging of reaction in a carbonate at reservoir conditions. Environmental science & technology 2015;49(7):4407–14.

Millero FJ, Milne PJ, Thurmond VL. The solubility of calcite, strontianite and witherite in nacl solutions at 25 c. Geochimica et Cosmochimica Acta 1984;48(5):1141–3.

Misra KC. Introduction to geochemistry: principles and applications. John Wiley & Sons, 2012.

Mondol NH, Jahren J, Bjørlykke K, Brevik I. Elastic properties of clay minerals. The Leading Edge 2008;27(6):758–70.

Moré JJ. The levenberg-marquardt algorithm: implementation and theory. In: Numerical analysis. Springer; 1978. p. 105–16.

Morse JW, Arvidson RS. The dissolution kinetics of major sedimentary carbonate minerals. Earth-Science Reviews 2002;58(1-2):51–84.

Nakano CMF, Pinto C, Carlos A, Marcusso JL, Minami K, et al. Pre-salt santos basin-extended well test and production pilot in the tupi area-the planning phase. In: Offshore Technology Conference. Offshore Technology Conference; 2009. .

Naveiro JT, de Oliveira AP, et al. Developing mega projects simultaneously: The brazilian pre-salt case. In: Offshore Technology Conference. Offshore Technology Conference; 2015. .

Nelson PH, et al. Permeability-porosity relationships in sedimentary rocks. The log analyst 1994;35(03).

Norris A. A differential scheme for the effective moduli of composites. Mechanics of materials 1985;4(1):1–16.

Nur A. Critical porosity and the seismic velocities in rocks. EOS Transactions AGU 1992;73:66.

Oji T, Ogawa Y, Hunter AW, Kitazawa K. Discovery of dense aggregations of stalked crinoids in izu-ogasawara trench, japan. Zoological science 2009;26(6):406–9.

Ott H, Oedai S. Wormhole formation and compact dissolution in single-and two-phase co2-brine injections. Geophysical Research Letters 2015;42(7):2270–6.

Panga MK, Ziauddin M, Balakotaiah V. Two-scale continuum model for simulation of wormholes in carbonate acidization. AIChE journal 2005;51(12):3231–48.

Panthi S. Carbonate chemistry and calcium carbonate saturation state of rural water supply projects in nepal. In: Proceedings of the Seventh International Water Technology Conference, Cairo, Egypt. 2003. p. 1–3.

Peng C, Crawshaw JP, Maitland GC, Trusler JM. Kinetics of calcite dissolution in co2-saturated water at temperatures between (323 and 373) k and pressures up to 13.8 mpa. Chemical Geology 2015;403:74–85.

Pentecost A. The formation of travertine shrubs: mammoth hot springs, wyoming. Geological Magazine 1990;127(2):159–68.

Pentecost A. Formation of laminate travertines at bagno vignone, italy. Geomicrobiology Journal 1994;12(4):239–51.

Pentecost A. The quaternary travertine deposits of europe and asia minor. Quaternary Science Reviews 1995;14(10):1005–28.

Pentecost A. Travertine. Springer Science & Business Media, 2005.

Pizarro JODS, Branco CCM, et al. Challenges in implementing an eor project in the pre-salt province in deep offshore brasil. In: SPE EOR Conference at Oil and Gas West Asia. Society of Petroleum Engineers; 2012. .

Plummer LN, Busenberg E. The solubilities of calcite, aragonite and vaterite in co2-h2o solutions between 0 and 90 c, and an evaluation of the aqueous model for the system caco3-co2-h2o. Geochimica et cosmochimica acta 1982;46(6):1011–40.

Pokrovsky OS, Golubev SV, Schott J. Dissolution kinetics of calcite, dolomite and magnesite at 25 c and 0 to 50 atm pco2. Chemical Geology 2005;217(3-4):239–55.

Pokrovsky OS, Golubev SV, Schott J, Castillo A. Calcite, dolomite and magnesite dissolution kinetics in aqueous solutions at acid to circumneutral ph, 25 to 150 °c and 1 to 55 atm pco2: New constraints on co2 sequestration in sedimentary basins. Chemical Geology 2009;265(1-2):20–32. doi:10.1016/j.chemgeo.2009.01.013.

Polak A, Elsworth D, Liu J, Grader AS. Spontaneous switching of permeability changes in a limestone fracture with net dissolution. Water Resources Research 2004;40(3).

Powell W. Indiana limestone. http://academic.brooklyn.cuny.edu/geology/powell/613~webpage/NYCbuilding/IndianaLimestone/IndianaLimestone.htm; 2004. [Online accessed 21-september-2018].

Ramaker EM, Goldstein RH, Franseen EK, Watney WL. What controls porosity in cherty fine-grained carbonate reservoir rocks? impact of stratigraphy, unconformities, structural setting and hydrothermal fluid flow: Mississippian, se kansas. Geological Society, London, Special Publications 2015;406(1):179–208.

Ramanujan S. Modular equations and approximations to π. Quart J Math 1914;45:350–72.

Revil A. Pervasive pressure-solution transfer: A poro-visco-plastic model. Geophysical Research Letters 1999;26(2):255–8.

Rezende M, Pope M. Importance of depositional texture in pore characterization of subsalt microbialite carbonates, offshore brazil. Geological Society, London, Special Publications 2015;418:SP418–2.

Robinson RA, Stokes RH. Electrolyte solutions. Academic Press Inc., 1955.

Rocha LAS, Junqueira P, Roque J, et al. Overcoming deep and ultra deepwater drilling challenges. In: Offshore Technology Conference. Offshore Technology Conference; 2003. .

Rochelle-Bates N, Schröder S, Dixon R. Characterisation of the pre-salt microbialite in the kwanza basin, angola. In: ACE 2018 Annual Convention & Exhibition. 2018. .

Rogner HH. An assessment of world hydrocarbon resources. Annual review of energy and the environment 1997;22(1):217–62.

Ronchi P, Cruciani F. Continental carbonates as a hydrocarbon reservoir, an analog case study from the travertine of saturnia, italy. AAPG Bulletin 2015;99(4):711–34.

Saar MO, Manga M. Permeability-porosity relationship in vesicular basalts. Geophysical Research Letters 1999;26(1):111–4.

Saini-Eidukat B, Yahin A. Web-phreeq: a www instructional tool for modeling the distribution of chemical species in water. Computers & Geosciences 1999;25(4):347–53.

Saller A, Rushton S, Buambua L, Inman K, McNeil R, Dickson JT. Presalt stratigraphy and depositional systems in the kwanza basin, offshore angola. AAPG Bulletin 2016;100(7):1135–64.

Salvo L, Suéry M, Marmottant A, Limodin N, Bernard D. 3d imaging in material science: Application of x-ray tomography. Comptes Rendus Physique 2010;11(9-10):641–9.

Sato M, Bitter I, Bender MA, Kaufman AE, Nakajima M. Teasar: Tree-structure extraction algorithm for accurate and robust skeletons. In: Computer Graphics and Applications, 2000. Proceedings. The Eighth Pacific Conference on. IEEE; 2000. p. 281–449.

Sawamura S, Yoshimura Y, Kitamura K, Taniguchi Y. Effects of pressure, temperature, and concentration on the viscosity of an aqueous solution of sodium chloride. The Journal of Physical Chemistry 1992;96(13):5526–9.

Schindelin J, Arganda-Carreras I, Frise E, Kaynig V, Longair M, Pietzsch T, Preibisch S, Rueden C, Saalfeld S, Schmid B, et al. Fiji: an open-source platform for biological-image analysis. Nature methods 2012;9(7):676.

Schröder S, Ibekwe A, Saunders M, Dixon R, Fisher A. Algal–microbial carbonates of the namibe basin (albian, angola): implications for microbial carbonate mound development in the south atlantic. Petroleum Geoscience 2016;22(1):71–90.

Seguin D, Montillet A, Comiti J. Experimental characterisation of flow regimes in various porous media—i: Limit of laminar flow regime. Chemical engineering science 1998;53(21):3751–61.

Selvadurai A, Głowacki A. Permeability hysterisis of limestone during isotropic compression. Groundwater 2008;46(1):113–9.

Seminar S. Cross-bedding in the salem limestone of central indiana. Sedimentology 1966;6(2):95–114.

Sharqawy MH, Lienhard JH, Zubair SM. Thermophysical properties of seawater: a review of existing correlations and data. Desalination and water treatment 2010;16(1-3):354–80.

Shi Y, Wang CY. Pore pressure generation in sedimentary basins: overloading versus aquathermal. Journal of Geophysical Research: Solid Earth 1986;91(B2):2153–62.

Siddiqui S, Nasr-El-Din HA, Khamees AA. Wormhole initiation and propagation of emulsified acid in carbonate cores using computerized tomography. Journal of Petroleum Science and Engineering 2006;54(3-4):93–111.

Sippel RF, Glover ED. The solution alteration of carbonate rocks, the effects of temperature and pressure. Geochimica et Cosmochimica Acta 1964;28(9):1401–17.

Skempton A. Adress on effective stress in soils, concrete and rocks, pore pressure and suction in soils, conf. 1960.

Smith NM. Sedimentology of the salem limestone in indiana. 1966;.

Soete J, Kleipool LM, Claes H, Claes S, Hamaekers H, Kele S, Özkul M, Foubert A, Reijmer JJ, Swennen R. Acoustic properties in travertines and their relation to porosity and pore types. Marine and Petroleum Geology 2015;59:320–35.

Sonmez H, Gokceoglu C, Nefeslioglu H, Kayabasi A. Estimation of rock modulus: for intact rocks with an artificial neural network and for rock masses with a new empirical equation. International Journal of Rock Mechanics and Mining Sciences 2006;43(2):224–35.

Soraya B, Malick C, Philippe C, Bertin HJ, Hamon G, et al. Oil recovery by low-salinity brine injection: Laboratory results on outcrop and reservoir cores. In: SPE Annual Technical Conference and Exhibition. Society of Petroleum Engineers; Society of Petroleum Engineers; 2009. .

Steefel CI, Lasaga AC. Evolution of Dissolution Patterns; American Chemical Society. p. 212–25. URL: https://pubs.acs.org/doi/abs/10.1021/bk-1990-0416.ch016. doi:10.1021/bk-1990-0416.ch016.

Stokes GG. On the effect of the internal friction of fluids on the motion of pendulums. volume 9. Pitt Press Cambridge, 1851.

Sun Y, Xie L, He B, Gao C, Wang J. Effects of effective stress and temperature on permeability of sandstone from co2-plume geothermal reservoir. Journal of Rock Mechanics and Geotechnical Engineering 2016;8(6):819–27.

Swann DH, Willman HB. Megagroups in illinois. AAPG Bulletin 1961;45(4):471–83.

Szymczak P, Ladd A. Wormhole formation in dissolving fractures. Journal of Geophysical Research: Solid Earth 2009;114(B6).

Teles A, Machado A, Pepin A, Bize-Forest N, Lopes R, Lima I. Analysis of subterranean pre-salt carbonate reservoir by x-ray computed microtomography. Journal of Petroleum Science and Engineering 2016;144:113–20.

Terra G, Spadini A, Franca A, Sombra C, et al. Carbonate rock classification applied to brazilian sedimentary basins. Boletin Geociencias Petrobras 2010;18:9–29.

Terzaghi K. Theoretical soil mechanics. Chapman And Hall, Limited.; London, 1951.

Thompson DL, Stilwell JD, Hall M. Lacustrine carbonate reservoirs from early cretaceous rift lakes of western gondwana: Pre-salt coquinas of brazil and west africa. Gondwana Research 2015;28(1):26–51.

Tian Y, et al. Experimental study on stress sensitivity of naturally fractured reservoirs. In: SPE annual technical conference and exhibition. Society of Petroleum Engineers; 2014. .

Tsukrov I, Kachanov M. Solids with holes of irregular shapes: effective moduli and anisotropy. International Journal of Fracture 1993;64(1):R9–.

Tutolo BM, Tosca NJ. Experimental examination of the mg-silicate-carbonate system at ambient temperature: Implications for alkaline chemical sedimentation and lacustrine carbonate formation. Geochimica et Cosmochimica Acta 2018;225:80–101.

Vairogs J, Hearn C, Dareing DW, Rhoades V, et al. Effect of rock stress on gas production from low-permeability reservoirs. Journal of Petroleum Technology 1971;23(09):1–161.

Vasquez GF, Vargas Junior EdA, Ribeiro CJB, Leão M, Justen JCR. Experimental determination of the effective pressure coefficients for brazilian limestones and sandstones. Revista Brasileira de Geofísica 2009;27(1):43–53.

Versfelt JW, et al. South atlantic margin rift basin asymmetry and implications for pre-salt exploration. In: International Petroleum Technology Conference. International Petroleum Technology Conference; 2009. .

Virgone A, Broucke O, Held AE, Lopez B, Seard C, Camoin G, Swennen R, Foubert A, Rouchy JM, Pabian-Goyheneche C, et al. Continental carbonates

reservoirs: the importance of analogues to understand presalt discoveries. In: IPTC 2013: International Petroleum Technology Conference. 2013. .

Walle L, Papamichos E, et al. Acidizing of hollow cylinder chalk specimens and its impact on rock strength and wormhole network structure. In: 49th US Rock Mechanics/Geomechanics Symposium. American Rock Mechanics Association; American Rock Mechanics Association; 2015. .

Wang Y, Hill A, Schechter R, et al. The optimum injection rate for matrix acidizing of carbonate formations. In: SPE Annual Technical Conference and Exhibition. Society of Petroleum Engineers; Society of Petroleum Engineers; 1993. .

Weijermars R. Principles of rock mechanics. Alboran Science Publishing, 1997.

Whitaker S. Flow in porous media i: A theoretical derivation of darcy's law. Transport in porous media 1986;1(1):3–25.

Wilkins SJ, Compton RG, Taylor MA, Viles HA. Channel flow cell studies of the inhibiting action of gypsum on the dissolution kinetics of calcite: a laboratory approach with implications for field monitoring. Journal of colloid and interface science 2001;236(2):354–61.

Wright M, Dillon P, Pavelic P, Peter P, Nefiodovas A. Measurement of 3-d hydraulic conductivity in aquifer cores at in situ effective stresses. Groundwater 2002;40(5):509–17.

Wright VP. Lacustrine carbonates in rift settings: the interaction of volcanic and microbial processes on carbonate deposition. Geological Society, London, Special Publications 2012;370:SP370–2.

Wright VP, Barnett AJ. An abiotic model for the development of textures in some south atlantic early cretaceous lacustrine carbonates. Geological Society, London, Special Publications 2015;418:SP418–3.

Xu S, Payne MA. Modeling elastic properties in carbonate rocks. The Leading Edge 2009;28(1):66–74.

Yagiz S. Predicting uniaxial compressive strength, modulus of elasticity and index properties of rocks using the schmidt hammer. Bulletin of Engineering Geology and the Environment 2009;68(1):55–63.

Yale DP, Crawford B, et al. Plasticity and permeability in carbonates: dependence on stress path and porosity. In: SPE/ISRM Rock Mechanics in Petroleum Engineering. Society of Petroleum Engineers; 1998. .

Zeebe RE. An explanation of the effect of seawater carbonate concentration on foraminiferal oxygen isotopes. Geochimica et Cosmochimica Acta 1999;63(13-14):2001–7.

Zhang D, Kang Q. Simulation of coupled flow, transport, and reaction in porous media by lattice boltzmann method. In: AGU Fall Meeting Abstracts. 2004. .

Zhang Y, Sarmadivaleh M, Lebedev M, Barifcani A, Rezaee R, Testamantia N, Iglauer S, et al. Geo-mechanical weakening of limestone due to supercritical co2 injection. In: Offshore Technology Conference Asia. Offshore Technology Conference; Offshore Technology Conference; 2016. .

Zhou X, Zeng Z, Liu H. Stress-dependent permeability of carbonate rock and the implication to co2 sequestration. In: This paper was presented at the 45th US Rock Mechanics/Geoemechanics symposium help in San Francisco, CA June. 2011. p. 26–9.

Zhou Z, Cui X, Zhang W. The relationship between formation temperature and permeability in a heavy oil reservoir. Petroleum Science and Technology 2016;34(1):31–6.

Ziarani AS, Aguilera R. Knudsen's permeability correction for tight porous media. Transport in porous media 2012;91(1):239–60.

Zimmerman RW. Compressibility of sandstones. volume 29. Elsevier, 1990.

Zmarzly D. The shallow-water crinoid fauna of kwajalein atoll, marshall islands: ecological observations, interatoll comparisons, and zoogeographic affinities 1985;.

Zoback MD, Byerlee J. Permeability and effective stress: Geologic notes. AAPG Bulletin 1975;59(1):154–8.

Zoback MD, Byerlee JD. Effect of high-pressure deformation on permeability of ottawa sand. AAPG Bulletin 1976;60(9):1531–42.